Three Dimensional Passivated-electrode Insulator-based Dielectrophoresis (3D PiDEP)

Phillip Zellner

Dissertation submitted to the faculty of the Virginia Polytechnic Institute and State University in partial fulfillment of the requirements for the degree of

Doctor of Philosophy

In

Electrical Engineering

Masoud Agah, Chair
Mantu K. Hudait
Sanjay Raman
Amy J. Pruden-Bagchi
Bahareh Behkam

June 26, 2013

Blacksburg, Va

Keywords: MicroElectroMechanical Systems (MEMS), Dielectrophoresis (DEP), Microfabrication, Three Dimensional (3D), Reactive Ion Etch (RIE), RIE lag, *Escherichia coli* (*E. coli*), *Staphylococcus aureus (S. aureus),* Off-chip Passivated-electrode Dielectrophoresis (OπDEP), Embedded Passivated-electrode Dielectrophoresis (EπDEP)

Copyright 2013, Phillip Zellner

Abstract

The focus of this research is the isolation of waterborne pathogens which are one of the grand challenges to human health, costing the lives of about 2.5 million people worldwide each year. The aim was to develop new microfluidic techniques for selectively concentrating and detecting waterborne pathogens. Detection of microbes in water can greatly help reduce deaths; however, analytical instruments cannot readily detect them due to the extreme dilution of these microbes, and hence, require significant sample concentration. Current methods are expensive and either require days to process or are not sufficiently robust for water monitoring. Microfluidic chips based on insulator-based dielectrophoresis (iDEP) provide a promising solution to these problems and have been previously used to selectively concentrate biological particle such as bacteria.

The microfluidic devices in this work were created with a 3D mircofabrication technique, which we also developed as part of this project. The core process of the technique is the etching of 3D structures in silicon with a single plasma etch utilizing an effect known as reactive ion etch lag (RIE lag). Using this unique process, 3D devices are fabricated in both silicon and the polymer polydimenthylsiloxane (PDMS). Using both numerical modeling and experimental results, we show how these 3D structures enhance the performance of the dielectrophoretic devices. The main findings indicate that 3D structures can help reduce Joule heating in the devices and lower the applied voltage necessary to operate the devices.

Additionally, within this work, we develop a new dielectrophoresis technique called off-chip passivated-electrode, insulator-based dielectrophoresis microchip (OπDEP). This technique combines the sensitivity of electrode-based dielectrophoresis (eDEP) with the high-throughput and inexpensive device characteristics of insulator-based dielectrophoresis. The result is a cartridge based system which is accessible, economical, high-performance, and high-throughput technologies allowing timely detection of pathogenic bacteria.

To My Family and the United States of America

Acknowledgements

I would like to thank my advisor, Dr. Masoud Agah, for seeing this project to the end. Throughout this work, there were many difficulties, however, Dr. Agah was still supportive of me through the hard times. His guidance helped me overcome both the technical issues and politics of modern day research. As an expert in the field of MEMS, Dr. Agah helped me to quickly gain a thorough understanding of the subject. But most importantly, he has always had my best interest at heart and has done everything in his power to prepare me to be a successful researcher.

I would like to thank the current and former members of the VT MEMS Lab. In particular, I would like to thank Mr. Shree Narayanan whose personal and professional help to me throughout my entire graduate school career cannot be exaggerated. A great man you will be and a better friend, there is none. To those who worked directly with me; Mr. Tyler Shake, Mr. Yahya Hosseini, and Mr. Zaki Hasnain; thank you for all the hours that you put in to make this possible. I could not have completed this work without your help. I would like to thank my other VT MEMS colleagues for their friendship, advice, and technical assistance: Mr. Liam Renaghan, Ms. Vaishnavi Srinivasaraghavan, Dr. Jeannine Strobl, Mr. Amin Zareian, Mr. Mehdi Nikkhah, Mr. Bassam Alfeeli, Mr. Syed Ali, Mr. Alperen Ketene, Mr. Hamza Shakeel, Mr. Muhammad Akbar, and Hesam Babahosseini.

I would like to thank the Via Family for the Bradley Fellowship for funding the first half of my graduate studies. Your generosity gave me the opportunity to go to graduate school in the first place and also the freedom to choose any research lab and research topic. I certainly would not have been able to work on this project at all if it were not for this immense flexibility. I sincerely hope that you consider the fruits of my labor here at Virginia Tech, worthy of your award. I would also like to thank the SMART program for funding the second half of my graduate studies. Thank you for believing in me. Because of you I was able to focus on my research with no financial concerns. This allowed me to bring this project to a very satisfying conclusion. Additionally, I have you to thank for starting my professional career in the exact field of my interest. I look forward to making your investment in me a good one. Wherever I go, I will endeavor to honor the names of the Bradley Fellowship and the SMART

Scholarship and to represent all that these awards stand for. I firmly believe that all that you have given me are not simply gifts, but debts to be paid back to society.

I would like to thank my family for all the love and support you have given me and continue to give me throughout my life. A special thanks goes to my mother, Donna Zellner and my brothers Benjamin Zellner and Timothy Zellner. Your faith in me has been and continues to be an inspiration and a motivation to me. Most importantly, I sincerely thank my father, Daniel Zellner, for showing me both in word and in deed, how to live a life of purpose. Because of him, I fear no man and no obstacle. Because of him, I never quit until the job is done. Because of him, I strive every single day to be the best person I can be.

Phillip Zellner

June 2013

Table of Contents

1 Introduction and Background 1
1.1 Significance and Background 1
1.2 Theory 9
1.3 Three Dimensional Fabrication 15
1.4 Objective and Outline of Dissertation 19

2 A Fabrication Technology for Three Dimensional Micro Total Analysis Systems 21
2.1 Introduction 21
2.2 Fabrication 23
2.3 Results and Discussion 25
2.3.1 Burying the Channels 25
2.3.2 Channels with Varying Dimensions 30
2.3.3 Applications 35
2.4 Conclusions 37

3 Silicon Insulator-Based Dielectrophoresis Devices for Minimized Heating Effects 39
3.1 Introduction 39
3.2 Materials and Methods 41
3.2.1 Silicon Device Fabrication 41
3.2.2 PDMS Device Fabrication 43
3.2.3 iDEP Experiments 44
3.2.4 Temperature Measurements 45
3.3 Theory 46
3.3.1 DEP 46
3.3.2 Fluid Flow 48
3.3.3 Heat Transfer 49
3.3.4 Numerical Modeling 49
3.4 Results 51
3.4.1 Trapping 51

3.4.2 Thermal Measurements ... 53
3.4.3 Numerical Modeling ... 54
3.5 Discussion ... 56
3.6 Conclusion ... 59
3.7 Extra Numerical Results ... 60

4 A Single-Mask Process for 3D Microstructure Fabrication in PDMS ... 62
4.1 Introduction ... 62
4.2 Fabrication Process ... 64
4.3 Results and Discussion ... 67
4.3.1 Glass Reflow Factor ... 67
4.3.2 3D Pattern Transfer from Silicon to Glass and PDMS ... 70
4.3.3 PDMS Devices with 3D Properties ... 72
4.4 Conclusion ... 75

5 3D Insulator-based Dielectrophoresis using DC-Biased, AC Electric Fields for Selective Bacteria Trapping ... 77
5.1 Introduction ... 77
5.2 Theory ... 79
5.3 Experimental Procedure ... 81
5.3.1 Device Fabrication ... 81
5.3.2 Experimental Setup ... 82
5.3.3 Sample Preparation ... 83
5.4 Results ... 84
5.4.1 Characterization of Particles ... 84
5.4.2 Separation of Particles ... 86
5.5 Discussion and Concluding Remarks ... 88

6 Off-chip Passivated-electrode, Insulator-based Dielectrophoresis (OπDEP) ... 91
6.1 Introduction ... 91
6.2 Theory ... 92

6.3 Methods and Materials 94
6.3.1 Device Designs 94
6.3.2 Numerical Modeling 95
6.3.3 Device Fabrication 96
6.3.4 Cell Preparation 97
6.3.5 Experimental Setup 97
6.4 Results and Discussion 99
6.4.1 Numerical Modeling 99
6.4.2 Frequency Response 101
6.4.3 Flow Rate Tests 104
6.4.4 Selective Concentration 105
6.5 Conclusion 106

7 Three Dimensional Passivated-electrode Insulator-based Dielectrophoresis (3D-πDEP) 109
7.1 Introduction 109
7.2 Theory 109
7.3 Methods and Materials 111
7.3.1 Numerical Device Modeling 111
7.3.2 Device Fabrication 111
7.3.3 Cell Preparation 114
7.3.4 Experimental Setup 115
7.4 Results and Discussion 116
7.4.1 Numerical Modeling 116
7.4.2 Frequency Response 118
7.4.3 Low Voltage Operation 120
7.4.4 Flow Rate tests 121
7.5 Conclusion 122

8 Conclusions and Future Work 124
8.1 Summary 124

8.2 Off-chip Impedance Sensing....124
8.2.1 Introduction....124
8.2.2 Methods and Materials....125
8.2.3 Results and Discussion....127
8.2.4 Conclusions and Outlook....129
8.3 Embedded Passivated-electrode Insulator-based Dielectrophoresis (EπDEP)....131
8.3.1 Introduction....131
8.3.2 Methods and Materials....132
8.3.3 Results and Discussion....135
8.3.4 Conclusions and Outlook....135
8.4 Other Future Directions....136
8.5 Dissertation Significance and Contribution....137
8.5.1 Microfabrication Thrust....137
8.5.2 Dielectrophoresis Thrust....138

Bibliography....142

List of Figures

Figure 1-1 (Top) Schematic of early eDEP device (Bottom) Photo of yeast collection on an electrode of the early eDEP device [13]. 3

Figure 1-2 Separation of live and dead yeast cells in a microfabricated eDEP device [20]........ 4

Figure 1-3 Schematic of a cell fusion system which was the first microfluidic device to utilize iDEP [23]. 5

Figure 1-4 Manipulation of fluorescent spheres in iDEP devices with microposts [24]. 6

Figure 1-5 Selective trapping of bacteria in a micropost iDEP device [31]. (A) Trapping of *Escherichia coli* from a mixture containing *Bacillus subtilis* (B) Trapping of both *Escherichia coli* and *Bacillus subtilis* (C) Trapping of *Bacillus megaterium* from a mixture containing *Bacillus cerus* (D) Trapping of both *Bacillus megaterium* and *Bacillus cereu.* 7

Figure 1-6 Reported implementations of electrode-based and insulator-based dielectrophoresis techniques for separating live (green) and dead (red) bacteria [30, 32]. 8

Figure 1-7 Coulomb force balance for polarized neutral particle. The yellow regions are electrodes with the indicated electric potentials. The black arrows indicate the electric field lines. (A) uniform applied electric field (B) nonuniform applied electric field 9

Figure 1-8 Schematic representation of dielectrophoresis of two dissimilar, polarized, neutral particles. 11

Figure 1-9 Diagram Schematic representation of how a cell can be simplified into a homogenous particle with effective permittivity ε_p* [40]. 12

Figure 1-10 (A)Diagram of the ellipsoid multishell model for bacteria cells (B) Model of the typical frequency response of a biological cell in a low conductivity electrolytic solution [35]. The crossover frequencies are labeled fc1 and fc2. A decrease in the dielectric parameters in each case produces the changes in the modeled plot as indicated by arrows in the different frequency regions. 13

Figure 1-11 Microfabricated Lens using the MEMSNAS process [71]. 17

Figure 1-12 The range of possible depth to width aspect ratios for a 30 min etch duration. SEM photos show typical results for each section on the plot [73]........ 18

Figure 2-1. Process flow for 3D buried channels. (Top) Mask layout (1-3) Sealable channels (4) Gradually varying depth design (5) Unsealable mask window for access holes or nano-scale holes in oxide layer (6) Non-uniform channel. 23

Figure 2-2. Optical images of the oxide lattice structures of Designs 1 (right) and 10 (left). The window patterns in oxide are clearly visible. In both images Channel 1 is above Channel 2. 24

Figure 2-3. Important parameters in the window patterns present on the photolithographic mask. 25

Figure 2-4. Buried channel dimensions falling underneath the curves are achievable... 26

Figure 2-5. SEM images of buried microchannel networks (Upper Left) Network with intersections (Lower Left) Close up image of a 90° intersection (Upper Right) Top view of 8 channel intersection with mask oxide removed (Lower Right) Cross section of buried 8 channel intersection along the dotted line........ 27

Figure 2-6. SEM images of a width and depth varying microchannel (Top) Microchannel before sealing. The mask oxide has been removed here for visibility. (Bottom) Microchannel after sealing........ 28

Figure 2-7. Top view of SEM image of 600 nm holes in the oxide layer. 29

Figure 2-8. SEM images of the transition region of microchannels in Design 1 (B) and Design 10 (A) The left images show the cross-sections of the channels while the right images show the top view of the channels. 31

Figure 2-9. Depth profiles of the transition region of the microchannels in Design 1 (bottom) and Design 10 (top) right images show the top view of the channels. 32

Figure 2-10. Measured transition angles between the two connecting channels........ 33

Figure 2-11. Settling distance from 2% of the lower channel's depth to 2% of the upper channel's depth. 34

Figure 2-12. Cross-sections of non-symmetric channels (A) 190 μm deep channel (B) 90 μm deep channel. 34

Figure 2-13. SEM Images of a DEP trapping device. A 125 μm deep channel is connected to six 20 μm deep channels (Left) 45° angle view (Right) Top view........ 35

Figure 2-14. (Left) Optical image of a flow cytometery device (Right) SEM image of depth transition. 36

Figure 2-15. SEM images of a microreactor. 9 features of distinct depth from 100μm to 20μm are present (Left) Optical image of device (Right) Image showing side channel.36

Figure 3-1 Device fabrication process flow for 3D devices (Left) and 2D posts (Right). (A) Top view of DRIE lag mask design (B) Oxide deposition (C) Pattern oxide/photoresist mask (D) DRIE lag 3D silicon etch (E) Pattern of backside photoresist (F) Anisotropic

DRIE of backside of silicon to create ports (G) Thermal oxide growth (H) Anodic bonding of pyrex wafer, attach reservoirs, and insert electrodes. Not to scale. 41

Figure 3-2 Images of the iDEP microchannels. (a) Top and perspective views, respectively, of device A (b1 and b2) Top and perspective views, respectively of device B (c) Optical image of top view of device C. All images except (c) are SEM images .. 43

Figure 3-3 Trapping experiments of 1µm (green) and 2µm (orange) beads in iDEP devices. Fluid flow is from right to left. (a) Separation of beads at V_{app}=1.0x10^2 V in device A with polarity of the applied potential shown. (b) Separation of beads at V_{app}=3.0x10^2 V in device B 51

Figure 3-4 Performance measurments of iDEP devices. Voltages are applied over 1cm. (a) Trapping efficiencies of iDEP devices (n=5). (b) Selective concentration efficiencies of silicon iDEP devices (n=5). (c) Temperature Measurements after 30 seconds (n=3). Error bars shown for 1 standard deviation... 52

Figure 3-5 Simulation results for microchannels fabricated in both silicon and PDMS. Plot shows the maximum temperature in the microchannel as a function of time. The conductivity of the medium is 0.02 S/m. The minimum voltage required for operation is used: 100 V for Device A (Silicon Cone) and 300 V for both Device B (Silicon Posts) and Device C (PDMS Posts). 60

Figure 3-6 Simulation results for Device A (Silicon Cone). Plot shows the maximum temperature in the microchannel as a function of time. The conductivity of the medium is varied. The minimum voltage required for operation is used: 100 V. 60

Figure 3-7 Simulation results for Device B (Silicon Posts). Plot shows the maximum temperature in the microchannel as a function of time. The conductivity of the medium is varied. The minimum voltage required for operation is used: 300 V. 61

Figure 3-8 Simulation results for Device C (PDMS Posts). Plot shows the maximum temperature in the microchannel as a function of time. The conductivity of the medium is varied. The minimum voltage required for operation is used: 300 V. 61

Figure 4-1 Process flow of fabrication of 3D structures in glass and elastomers. (a) photomask layout to induce RIE lag (b) silicon isotropic RIE SF_6 plasma etching, (c) anodic-bonding of silicon and glass in vacuum, (d) glass reflow, (e) silicon etch to release the glass device, and (f) pouring PDMS prepolymer, curing, and peeling PDMS replica from the glass master. 65

Figure 4-2 3D structures fabricated in silicon utilizing RIE lag. These structures comprising more complex structures that contain channels with different width and depth, depth transition, and other geometries that might not be simple to achieve utilizing multiple steps of 2D lithography (a) microposts for use in insulator-based dielectrophoresis as well as CTC trapping, (b) 40 µm-deep channel connecting two 100 µm-deep channels together, (c) a flow-cytometry chamber, 40 µm-deep in the narrow

section and 90 μm-deep in the deeper section. 66

Figure 4-3. (a) glass surface after heat treatment at 760 °C for 8 hours and (b) glass surface after heat treatment at 800 °C for 20 minutes. Reboiling effect has caused the formation of small bubbles on the surface of both wafers. 68

Figure 4-4. SEM images of glass structure after heat treatment at 760 °C for 8 hours and silicon removal (a) Glass master device with bubbles spread around and (b) close-up view of bubbles on the surface of glass master. 68

Figure 4-5 Bonded surface of glass and silicon after reflow process. The device was placed in a furnace at 720 °C for 4 hours and then at 760 °C for 30 minutes. 69

Figure 4-6. SEM images of several glass device prototypes after silicon release. The glass structures include replica of channels/cavities with different height and width.(a) capillary network, (b)micro-flow cytometry chamber, (c)spiral, and (d)cell migration passageways. Scale bar represents the actual dimension only in lateral-direction as the images are tilted in vertical-direction. 70

Figure 4-7. SEM images of several 3D microfluidic devices made in PDMS using the master structures depicted in Figure 6. (a) capillary network, (b) micro-flow cytometry chamber, (c) spiral, and (d) cell migration passageways with the inset showing 90° rotated image. Scale bar represents the actual dimension only in lateral-direction as the images are tilted in vertical-direction. 71

Figure 4-8 Trapping and release of 2 μm beads. (A) No voltage (B) 150 V is applied (C and D) Voltage is turned off and particles are released. 73

Figure 4-9 Trapping and release of 0.5 μm beads. (A) No voltage (B) 350 V is applied (C and D) Voltage is turned off and particles are released. 74

Figure 5-1 Device fabrication process flow. (A) Top view of DRIE lag mask design (B) Pattern oxide mask (C) DRIE lag 3D silicon etch (D) Anodic bonding of pyrex wafer (E) Melt pyrex into silicon mold (F) Etch all silicon with KOH (G) Pour PDMS over pyrex master and cure (H) Remove PDMS from glass master and punch ports (I) Plasma bond to glass slide, attach reservoirs, and insert electrodes 82

Figure 5-2 (A) SEM of a iDEP device comprised of 3D microposts. (B) SEM of the cross section of the posts showing the depth change of the structures 83

Figure 5-3 *E. coli* trapping at α =19 and VACpp = 190 by (A) nDEP at 2kHz (B) pDEP at 400kHz. Fluid flow is from left to right (C) Frequency response of trapping of *E. coli,* live *S .aureus,* dead *S .aureus* and beads as function of frequency 190VACpp offset by10 VDC (α =19) (n=10)... 85

Figure 5-4 Quantification of selective trapping as a function of α for (A) nDEP at 2kHz (pDEP) at 400kHz. (n=10) 87

Figure 5-5 Fluid flow is from left to right (A) Selective trapping of *E. coli* (green) from red 1μm beads with an applied signal 180Vpp at 2kHz offset by 20VDC. (B) The AC signal is removed and the cells are released. (C) Trapping of both live (green) and dead (red) *S. aureus* with an applied signal of 150VACpp at 2kHz offset by 50VDC. (D) Selective trapping of live *S. aureus* cells from dead *S. aureus* cells with an applied signal of 180VACpp at 2kHz offset by 20VDC. 88

Figure 6-1 Schematic of the OπDEP device. (A) Isometric view of the device with the disposable fluidic section separated from the reusable electrodes (B) Device under operating conditions with the two parts assembled (C) Close-up view of the functional region of the device showing the relevant forces and dimensions. During operation, the microposts within the channel are aligned with the electrodes as shown. 93

Figure 6-2 COMSOL simulations of electric field gradients in the OπDEP devices. The PDMS roof of the devices has been removed from the figure for clarity (A) ∇(E•E) at 300 kHz in previously reported Device 1 without microfluidic structures (B) ∇(E•E) at 300 kHz in OπDEP Device 2 (C) Maximum values of ∇(E•E) as a function of frequency 100

Figure 6-3 Observed DEP trapping of *E. coli* in the OπDEP devices for an applied AC signal at 400Vpp and a flow rate of 400μL/hr. Trapping images are shown for Device 2. (A)10kHz signal (B) 100kHz signal (C) 300kHz signal (D) Quantized light intensity in the trapping region as a function of frequency (n=10)... 103

Figure 6-4 Observed DEP trapping of *E. coli* in the OπDEP devices for an applied AC signal at 400 Vpp at 300 kHz and variable flow rates. Trapping images are shown for Device 3. (A) 500 μL/hr (B) 900 μL/hr (C) 1200 μL/hr (D) Capture efficiency as a function of flow rate (n=10 sweeps). Error bars shown for 1 standard deviation......... 104

Figure 6-5 Selective trapping of *E. coli* (green) from 1 μm beads (red) with a fluid flow rate of 400 μl/hr. (A) No applied voltage (B) 400 Vpp at 300 kHz is applied for 30 seconds (C) Voltage is turned off and the concentrated bacteria is released (D) After trapped bacteria are released, none remain on the microposts.................................... 105

Figure 8-1 Device fabrication process flow. (A) Top view of DRIE lag mask design (B) Pattern oxide mask and then use RIE lag 3D silicon etch (C) Remove oxide lattice structure with BOE (D) Anodically bond to pyrex wafer under vacuum (E) Melt pyrex into silicon mold (F) Etch all silicon with KOH (G) Pour PDMS over pyrex master and cure (H) Remove PDMS from glass master and punch ports (I) Plasma bond to glass slide (J) Evaporate electrodes on separate substrate (K) Align electrodes and microfluidic device 112

Figure 7-2 Optical image of 3D πDEP device. (Top) Disposable microfluidic cartridge (Bottom) Reusable electrodes 113

Figure 7-3 SEM of a πDEP device comprised of 3D microposts. (A) Top view of

device (B) Magnified top view showing 3D posts (C) Cross section of the posts showing the depth change of the structures (D) Magnified cross section showing constriction.. 114

Figure 7-4 COMSOL simulations of electric fields in 3D πDEP devices. (A) Side view of ∇(E•E) profile at 400Vpp, 300kHz (B) Top view of ∇(E•E) profile at 400Vpp, 300kHz (C) Maximum values of ∇(E•E) as a function of frequency 117

Figure 7-5 Fluid flow is from left to right. Experimentally observed DEP trapping of *E. coli* and *S. aureus* in 3D πDEP devices for an applied AC signal at 400Vpp and a flow rate of 400μL/hr. Images are of *S. aureus* trapping (A) 300 Hz signal (B) 3kHz signal (C) 30kHz signal (D) 300kHz (E) Trapping efficiency as a function of frequency (n=10).. 119

Figure 7-6 Minimum signal amplitude for 100% trapping efficiency in 3D πDEP devices with a constant flowrate of 400 μl/hr. (n=10 sweeps). Error bars shown for 1 standard deviation.. 120

Figure 7-7 Fluid flow is from left to right. Observed DEP trapping trapping of *S .aureus* in 3D πDEP devices for an applied AC signal at 400Vpp at 300 kHz and variable flow rates. (A) 600μL/hr (B) 1000μL/hr (C) 1500μL/hr (D) Capture efficiency as a function of flow rate (n=10 sweeps). Error bars shown for 1 standard deviation . 121

Figure 8-1: Off-chip cell impedance sensing device. (A) Layout for the photomask of the device. The yellow layer is the electrode layout and the red layer is the microfluidic layout. (B) Larger view of the main area of interest in the layout (C) Optical image of device with the microfluidic cartridge loaded onto the reusable electrodes 126

Figure 8-2: Electrical schematic for the off-chip cell impedance sensing device of EπDEP device. The large black dots denote the connection terminals of the reusable electrodes... 127

Figure 8-3: Fluorescent microscopy of the off-chip cell impedance sensing device in operation. *E. coli* are stained green. Fluid flow is from left to right. (A) The cells are trapped onto the preconcentrator posts. (B) The relay is switched to the impedance detection electronics and the the bacteria are released from the posts. (C) The bacteria continue down the channel into the narrow constriction and the impedance analyzer registers sees a drop in impedance. (D) All of the bacteria passed through the narrow constriction 128

Figure 8-4: Performance of the off-chip cell impedance sensing device. It should be noted that all impedance changes were negative, however the absolute value of the change is displayed here for clarity. Error bars are shown for 1 standard deviation (n=3) 129

Figure 8-5: Conceptual images of the proposed 3D-πDEP platform for waterborne pathogenic bacteria isolation and enrichment. 130

Figure 8-6: Schematic of EπDEP device. (A) Isometric view (B) Top view showing how the electrodes are aligned such that they straddle the insulating structures within the

microchannel. (C) Side view showing material composition. 132

Figure 8-7: The effect of different passivation layer thicknesses on the DEP force. Thinner passivation layers lead to larger electric field gradients. 133

Figure 8-8: Fabrication process flow for EπDEP devices. (A) Photomask pattern. (B) DRIE silicon etch (C) Cure PDMS in silicon mold (D)Remove PDMS from mold (E) Deposit gold onto glass substrate (F) Spin PDMS over electrodes (G) Align and plasma the two substrates together.. 134

Figure 8-9: DEP trapping of *Salmonella typhimurium* (ATCC 14028) with 40 Vpp at (A) 10 kHz (B) 100 kHz (C) 300 kHz 135

Figure 8-10: Diagram of the microfabrication thrusts presented in this work. The squares bordered in green denote the original research presented in this dissertation 138

Figure 8-11: Diagram of the DEP thrusts presented in this work. The squares bordered in green denote work performed in this dissertation... 141

List of Tables

Table 2-1. PECVD Deposition Parameters 24

Table 2-2 DRIE Etch Parameters 24

Table 2-3.Geometric parameters for window patterns in the transition regions 30

Table 2-4. Geometric parameters of window patterns for the connecting silicon channels 31

Table 3-1 Simulation results for microchannels fabricated in both silicon and PDMS 54

Table 4-1 Reflow temperature and time effect on the formation of bubbles on the surface of glass 69

Table 6-1 Design parameters for each of the different devices. 95

1 Introduction

1.1 Significance and Background

Drinking-water-borne pathogens kill more than 2.5 million people a year world-wide [1]. Practical and effective tools for waterborne pathogen monitoring are urgently needed to advance protection of public health and to enable immediate action in response to bioterrorism threats. Development of such tools has remained an elusive challenge, even into the current age of biotechnology. According to the World Health Organization [2], the isolation in culture of pathogenic bacteria from the environment has not significantly changed since the 1960s, when methods for chemical treatment of samples to remove background organisms were first implemented. Current water quality regulations remain focused on culturing of fecal-indicators, which are sub-optimal targets because they are not actually pathogens, do not necessarily correlate directly with pathogens, and can require days to yield results. Molecular-based methods, however, have failed to meet their promise as a feasible alternative. While they can provide high specificity to target pathogens and results in only a few hours, they suffer greatly from limitations in recovery efficiency of sufficient high quality DNA or RNA from water samples. Distinguishing live from dead pathogens as well as overall ease of use are also major challenges for molecular methods.

Microelectromechanical systems (MEMS) systems are miniaturized structures which are used as small scale sensors and actuators. The corner stone of MEMS devices was the rise of the semiconductor industry and in particular, the microfabrication tools that resulted. Using standard semiconductor processing tools such as physical vapor deposition, reactive ion etching, and photolithography, researchers were given the ability to reliably create devices with micron and submicron scale features. One goal of MEMS is to achieve micro total analysis systems (μTAS) which perform a wide variety of functions normally reserved for bulky and expensive laboratory equipment. The first analytical laboratory equipment miniaturization was demonstrated by Terry et al., who developed a gas chromatography system on a silicon microchip[3]. Many researchers have realized the benefits of uTAS such as increased sensitivities, higher efficiencies, higher reproducibility, and decreased cost[4]. MEMS

are particularly useful for working at small length scale, such as those of a biological cell. When length scales are reduced drastically, the influence of different physical factors change. For example, at the human scale (~1 m), inertia and gravity are very strong factors while surface tension and electrostatic forces are often negligible. However, when the scale is reduced to that of a biological cell (~10^{-6} m), inertia and gravity are negligible factors while surface tension and electric forces are dominant.

Microanalytical electrokinetic (EK) techniques, a group of methods that take advantage of the large role electric forces play at small scales, are emerging as a promising alternative for rapid analysis of microorganisms. EK techniques take advantage of distinct signatures in the electrical properties unique to each microorganism. The elements of a microorganism, including the cytoplasm, plasma membrane, wall, and outer membrane, all have an associated electrical permittivity and conductivity. The size, shape, and chemical composition of these elements determine these values. Thus, biological cells are composed of a series of adjacent structures of materials which have different electrical properties as described by the shell model [5]. When nonuniform electric fields are applied, these interfaces cause large polarizations in cell which in turn lead to motion of the cell. This EK technique is known as dielectrophoresis (DEP).

It is well known that dielectrophoresis was discovered by Dr. Herbert Pohl in 1951[6]. Pohl showed that with this technique, uncharged particles could be motivated by a nonuniform electric field and he originally used DEP to suspend droplets of water air. DEP has been shown to be particularly useful for characterizing biological cells. The small size of cells (~1-10 μm) allow for the necessary high electric fields to be generated with relatively low applied voltages. Another strength of DEP is that it allows for many independent variables, such as signal magnitude, signal frequency, signal waveform, and electrode spacing to be used to control the manipulation. This results in a very flexible technique with a wide range of applications including bacteria[7], yeast[8], mammalian cells[9], viruses[10], and proteins[11].

Traditionally, electrode-based DEP (eDEP) devices create nonuniform fields with electrode designs including sharp electrodes and narrowly spaced electrodes. In 1966 Pohl was the first to apply dielectrophoresis to living organisms and he did so

using eDEP[12]. In one instance of his early work, Pohl used separated electrodes were used to create nonuniform electric fields and separate live and dead yeast cells[13]. As Figure 1-1 shows the device used was a simple petri dish with sharp platinum electrodes on either side. During operation, a signal would be applied to the electrodes and the yeast cells would be attracted to them. Pohl observed that the yeast cells response in the DEP device was greatly dependent on their viability. Additionally, the behavior of the cells varied with the media conductivity and the frequency of the applied signal. Since then many DEP studies have been performed with eDEP designs [14-19] and for decades eDEP was the only manner to achieve dielectrophoresis. Electrode based designs were popular because they provided a straightforward method to generate the high electric fields necessary for DEP. However, these designs put the suspended particles in close proximity to the electrodes which can be a problem if the electrode material is not chemically inert. Additionally, eDEP devices can be expensive to fabricate.

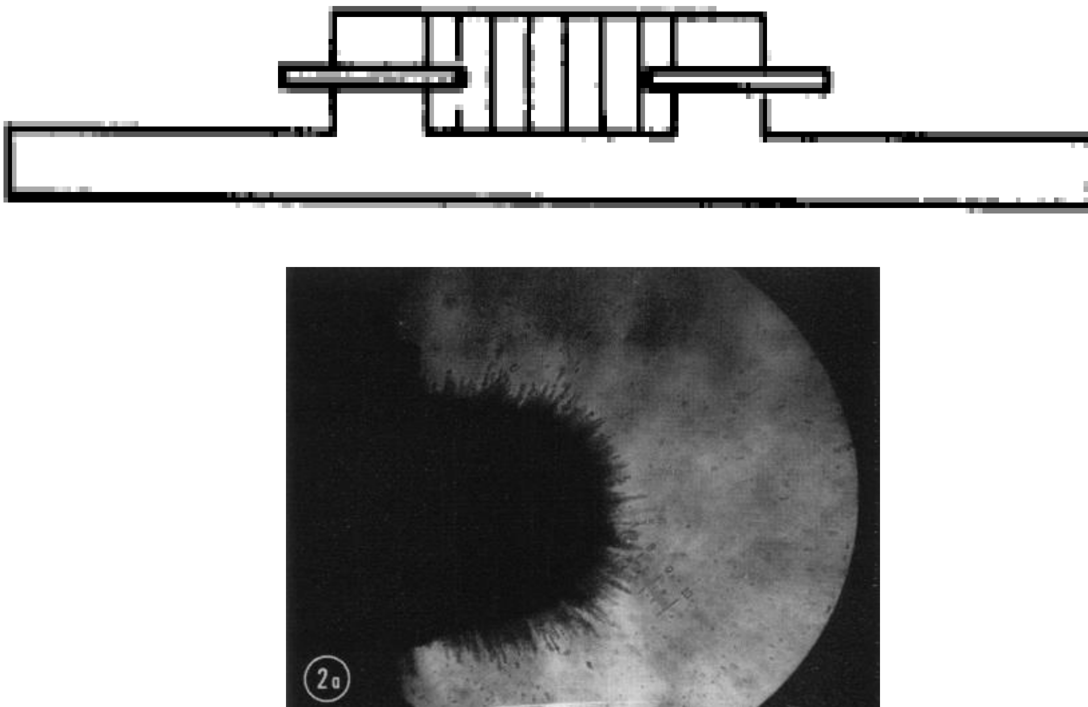

Figure 1-1 (Top) Schematic of early eDEP device (Bottom) Photo of yeast collection on an electrode of the early eDEP device [13]. Used under the Fair-Use Provision of Copyright Law.

The capabilities of eDEP devices were significantly improved by using semiconductor fabrication tools to create micron scale electrodes. The most common electrode design used is the interdigitated electrode design as it allows for very large DEP forces to be created with small applied voltages. An early example of this was by Markx and Pethig in 1994 [20]. As Figure 1-2 shows, by applying a 5Vpp 10MHz signal to the device, they were able to attract live yeast cells and repel dead yeast cells. This creates an excellent viability detector. Microfabricated eDEP designs such as this are easy to actuate with standard lab equipment and are very sensitive. However, the requirement of the particles to be in close proximity to the electrodes, which is a result of the dissipating electric field gradients inherent in eDEP design, also restrictions the depth of the microchannels to ~20-50 μm [21, 22]. Thus these devices rely primarily on a monolayer of cells being around the electrodes, which limits the throughput greatly. Additionally, electrolysis at the electrodes limits the operational frequencies and voltages, particularly at low frequencies where the devices are most sensitive to differences in the cell membrane and cell wall.

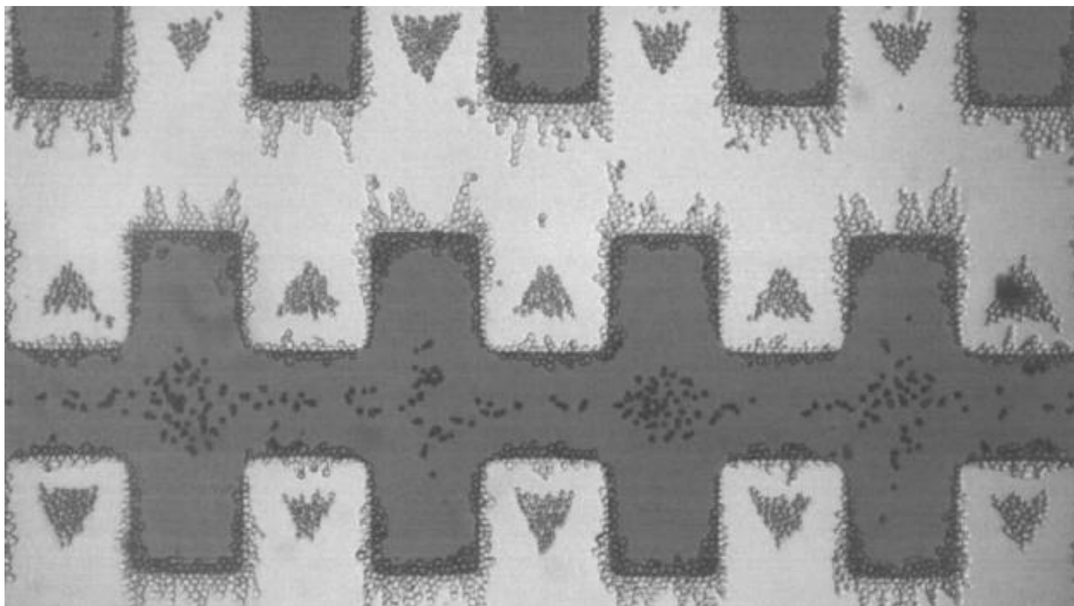

Figure 1-2 Separation of live and dead yeast cells in a microfabricated eDEP device [20]. Used under the Fair-Use Provision of Copyright Law.

Alternatively, insulator-based DEP (iDEP) uses insulating structures rather than electrode arrays to produce the nonuniform fields needed to drive DEP and to remove

the threat of gas evolution due to electrolysis. The first iDEP device was developed by Masuda et al. in 1989[23]. In that work, a single insulating constriction was used to create nonuniform electric fields to hold two cells in place for fusion (Figure 1-3). By applying a 2MHz signal across the width of the channels, the cells were shown to be attracted to the constriction. While the electrodes were fabricated on this device their size and shape were unimportant to generating the electric fields. It was the design of the constriction that provided the operating electric fields.

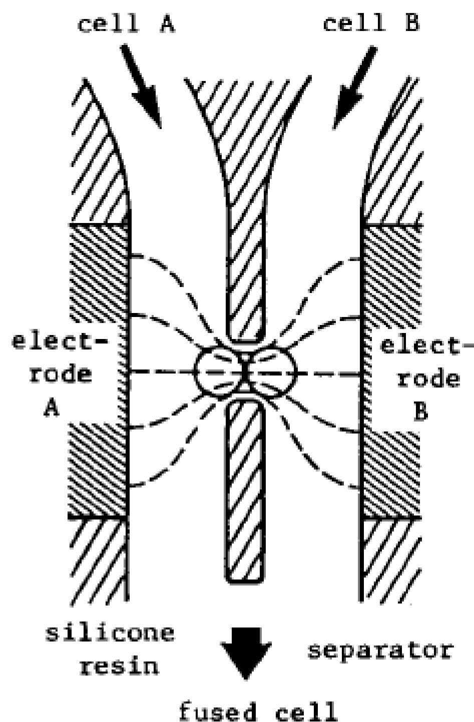

Figure 1-3 Schematic of a cell fusion system which was the first microfluidic device to utilize iDEP [23]. Used under the Fair-Use Provision of Copyright Law.

Researchers soon realized that it was not necessary to have microfabricated electrodes on the device at all. In 2003, Cummings and Singh created a microfluidic device in which the fluid flow and DEP manipulation was generated simply by have electrodes contact the resevoirs at the fluidic inlet and outlet[24]. The generated fluid flow was electroosmotic flow, which is generated by a DC potential on the electrodes. The DEP forces within the channel were created by the DC electric fields being curved by the insulating structures. As result of the applied voltage being used for both fluid

flow and DEP force, they reported two iDEP operation regimes (Figure 1-4). When the DEP force on a particle is not strong enough to completely overcome the electroosmotic flow, streaming DEP occurs and particles are deflected but continue moving downstream. When the DEP force on a particle is strong enough to completely overcome the electroosmotic flow, trapping DEP occurs and particles are held in place rather than move downstream. These results showed that iDEP devices had a degree of flexibility with operating ranges and applications.

The micropost iDEP design has been shown to be easy to fabricate as they require no metals and the only material requirement is that dielectrics are used. It is noteworthy that inexpensive dielectrics for these devices are plentiful. For example, iDEP devices have been demonstrated on glass and polymer substrates [25, 26]. The downside to this design is that it requires the use of large applied electric potentials (~1x103 V) to generate eletroosmotic flow and to trap particles. iDEP microfluidic devices have been used to trap and sort a large variety of biological particles[26-29].

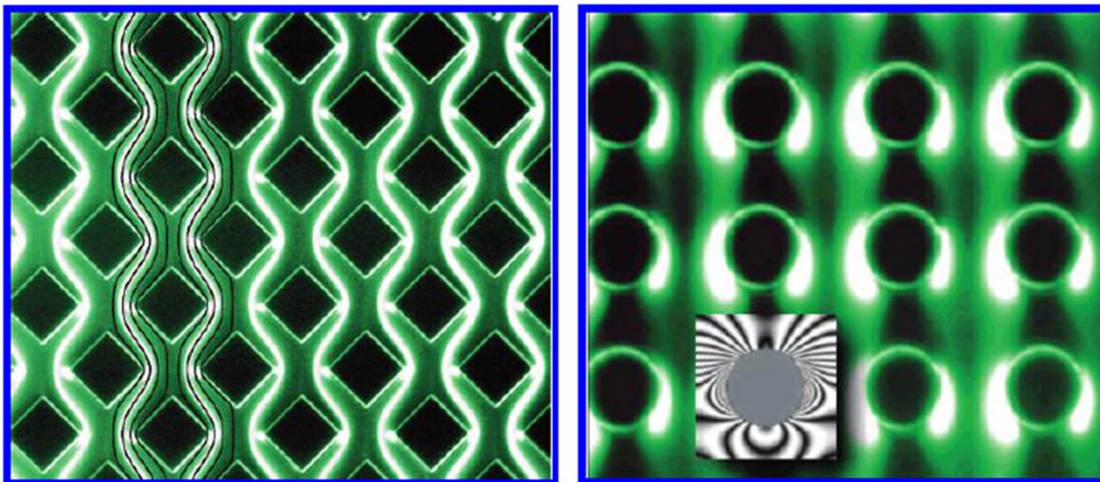

Figure 1-4 Manipulation of fluorescent spheres in iDEP devices with microposts[24]. (Left) Streaming DEP (Right) trapping DEP. Used under the Fair-Use Provision of Copyright Law.

Using the micropost iDEP design Lapizco-Encinas et al. showed that different species of bacteria could be separated[30]. In this work, the trapping voltages of four different bacteria were compared. When the trapping voltages were found to be different for all of the species, the bacteria were stained different colors, mixed, and then separated using the micropost iDEP device in the trapping regime. As Figure 1-5

shows, the devices were operating in the negative dielectophoresis trapping mode. When a cell was trapped, it was held by the DEP force upstream of the posts. As a large number of bacteria trapped, they formed semi-circular bands in the trapping region. The particles that were not being targets would simply pass through the channel freely however. Using this technique, all of the bacteria that were tested were shown to be separable from each other. These results showed that while simple to fabricate, the micropost iDEP devices cold discriminate different bacteria species. Interestingly enough, only DC voltages were used in this work whereas the DEP force on a cell is known to be very dependent on frequency. Thus even finer separation may be possible with these devices if more complex signals are used.

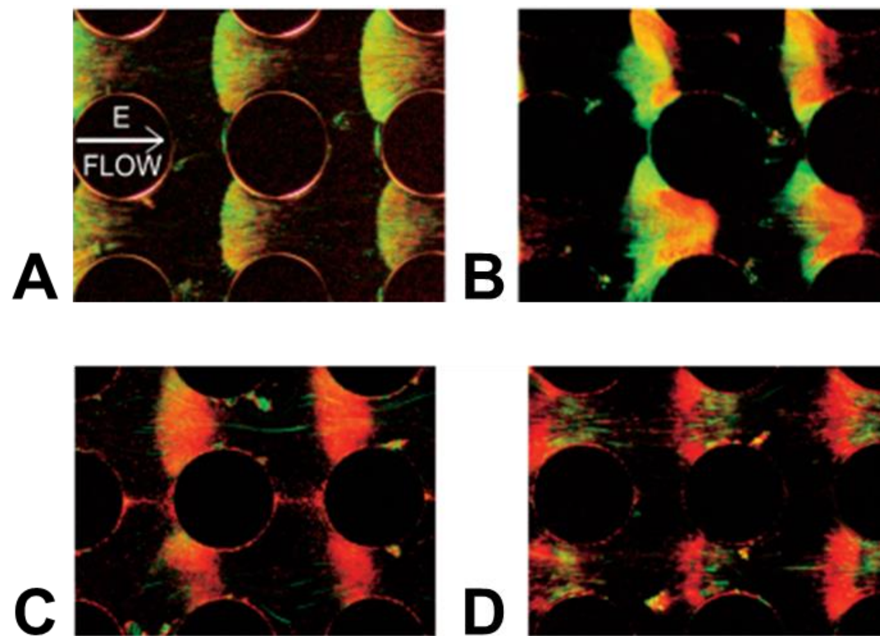

Figure 1-5 Selective trapping of bacteria in a micropost iDEP device [31]. (A) Trapping of *Escherichia coli* from a mixture containing *Bacillus subtilis* (B) Trapping of both *Escherichia coli* and *Bacillus subtilis* (C) Trapping of *Bacillus megaterium* from a mixture containing *Bacillus cerus* (D) Trapping of both *Bacillus megaterium* and *Bacillus cereu.* Used under the Fair-Use Provision of Copyright Law.

Figure 1-6 illustrates the difference between eDEP and iDEP devices. In both images, live and dead bacteria are being separated. However, for the eDEP devices, this separation occurs as the electrodes (the horizontal lines in the picture) while for the iDEP devices, the separation occurs at insulating structures within the microchannel

(the circular posts in the picture). In fact for this iDEP device, the electrodes are 1 cm apart and completely outside of the microchannel. Thus any fouling or gas evolution occurs far away from the region of interest.

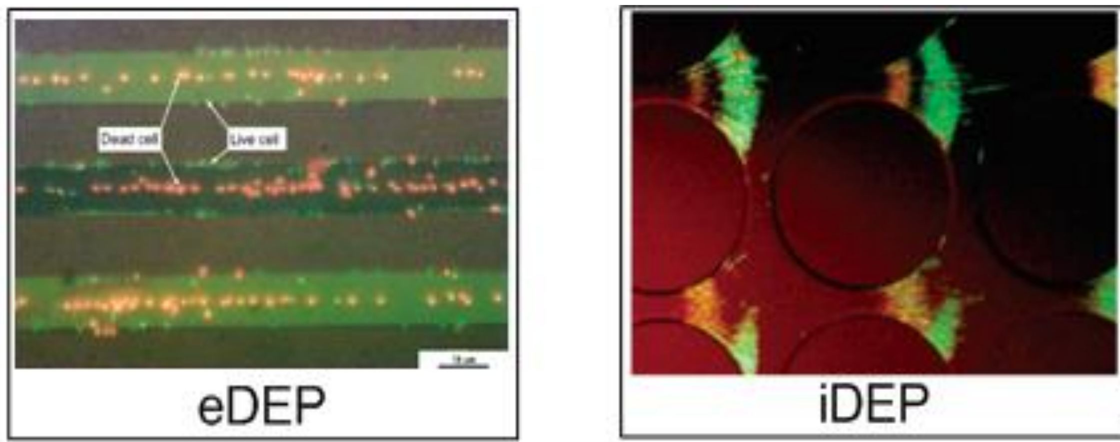

Figure 1-6 Reported implementations of electrode-based and insulator-based dielectrophoresis techniques for separating live (green) and dead (red) bacteria [30, 32]. Used under the Fair-Use Provision of Copyright Law.

Regardless of the method that DEP forces are generated, alterations to the physiology of the cell will change their dielectrophoretic response. In particular, many bacteria have been shown to have distinguishable differences in electrical properties and hence may be separated by DEP[33]. There has been much research recently on the DEP manipulation of bacteria. DEP microdevices have been used to separate *Escherichia coli* and polystyrene beads [21, 34]; live and dead *Escherichia coli* and *Listeria monocytogenes*, [15, 30], and to distinguish among different species of bacteria (*Escherichia coli, Bacillus subtilis, Bacillus cereus*, and *Bacillus megaterium*) [31]. DEP techniques have also been used to characterize the differences between different strains of the same *E. coli[35]*, although high-throughput separation has not been demonstrated. The abilities of DEP to manipulate bacteria with precision and speed, have resulted in DEP being a prime candidate for pathogen detection[36] and anti-bioterrorism[37].

The DEP-based techniques that are the focus of this research effort hold great promise for rapid and specific detection of live pathogens. In this work, we present new dielectrophoresis techniques which are highly tunable, high throughput, modular, robust, sensitive, and inexpensive.

1.2 Theory

Dielectrophoresis (DEP) is the motion of polarizable particles that are suspended in a dielectrically dissimilar media when subjected to a spatially nonuniform electric field [6]. Unlike electrophoresis, particles do not need to have any net charge to be effected by DEP. Instead, for a particle to be affected by DEP, it needs to be polarizable. Figure 1-7 illustrates the effect of placing a polarizable neutral particle in two different electric fields. In Figure 1-7A a uniform electric field is applied. The charges within the particle align with the electric field, creating an induced dipole. However, the distribution of the positive charges directly mirrors the distribution of negative charges. Thus the net Coulomb force on the particle is zero. In Figure 1-7B a nonuniform electric field is applied. When the charges within the particle align with the electric field, the charge distributions do not mirror each other. Instead, the positive charges are more focused to the right side of the particle than the negative charges are focused to the left. Thus for this case, the vector sum of the Coulomb forces on the

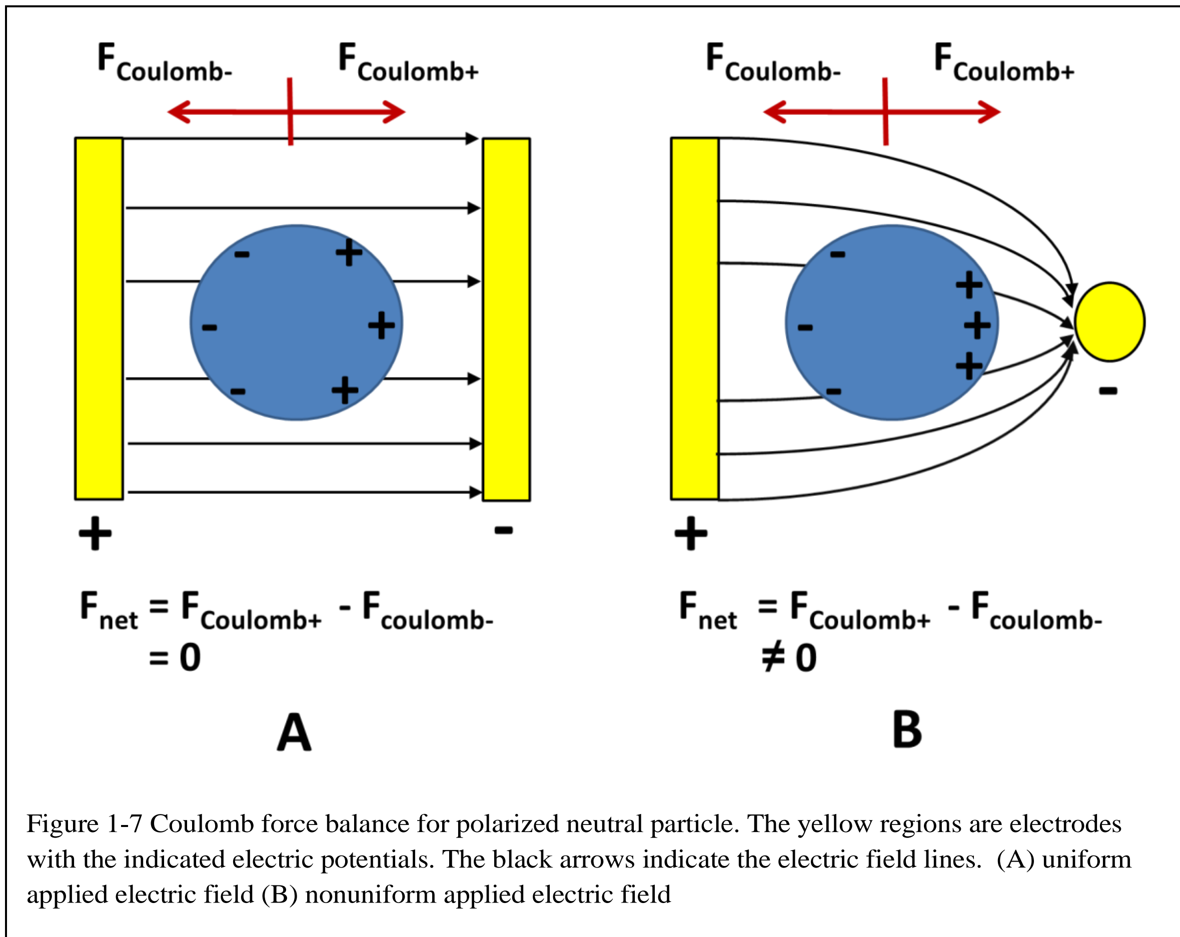

Figure 1-7 Coulomb force balance for polarized neutral particle. The yellow regions are electrodes with the indicated electric potentials. The black arrows indicate the electric field lines. (A) uniform applied electric field (B) nonuniform applied electric field

particle is not zero. For the shown case, the particle will travel toward the negative electrode. This nonzero Coulomb force on an uncharged polarizable particle in a nonuniform field is known as dielectrophoresis.

The resulting force felt by the particle is due to an induced dipole as described by the Maxwell-Wagner (MW) theory[38]. The dielectrophoretic force on a sphere can be derived directly from the induced dipole model[39, 40]. The time average DEP force felt by a spherical particle suspended in a medium is:

$$F_{DEP} = 2\pi R^3 \varepsilon_m Re[f_{CM}] \nabla |E_{RMS}|^2 \quad (1\text{-}1)$$

where R is the radius of the particle, ε_m is the permittivity of the medium, E_{RMS} is the local electric field. This equation can be derived theoretically for the case of a homogenous or inhomogeneous sphere[40]. $Re[f_{CM}]$ is the real part of the Clausius-Mossotti factor. The Clausius-Mossotti factor includes complex parameters which can be used to describe a biological cell fit to a multishell model. The factor which is:

$$f_{CM} = (\varepsilon_p^* - \varepsilon_m^*)/(\varepsilon_p^* + 2\varepsilon_m^*) \quad (1\text{-}2)$$

where ε_p^* and ε_m^* are the complex permittivities of the particle and the medium, respectively. Complex permittivity is defined as:

$$\varepsilon^* = \varepsilon + \sigma/(j\omega) \quad (1\text{-}3)$$

where ε and σ are the real permittivity and conductivity, j =sqrt(-1) and ω is the angular frequency of the applied potential signal. For DC-field iDEP experiments the complex permittivity becomes the low frequency limit of this equation which is simply the conductivity. Thus, the Clausius-Mossotti factor for DC is:

$$f_{CM} = (\sigma_p - \sigma_m)/(\sigma_p + 2\sigma_m) \quad (1\text{-}4)$$

Figure 1-8 illustrates the consequences of these equations. In this figure an electric field is created by applying a sinusoidal signal with a frequency of ω. Assume that there are two geometrically identical particles p1 and p2 with complex permittivities ε_1^* and ε_2^*, respectfully, suspended in a medium with a complex permittivity ε_m^* such that $\varepsilon_1^* > \varepsilon_m^* > \varepsilon_2^*$. For this situation, $Re[f_{CM}]$ will be positive for particle p1, thus p1 will be attracted to the region with the highest electric field

gradient. This is known as positive DEP. Conversely, Re[f_{CM}] will be negative for particle p2, thus p2 will be repelled from the region with the highest electric field gradient. This is known as negative DEP. Thus the material properties of a particle play a large role in its dielectrophoretic behavior.

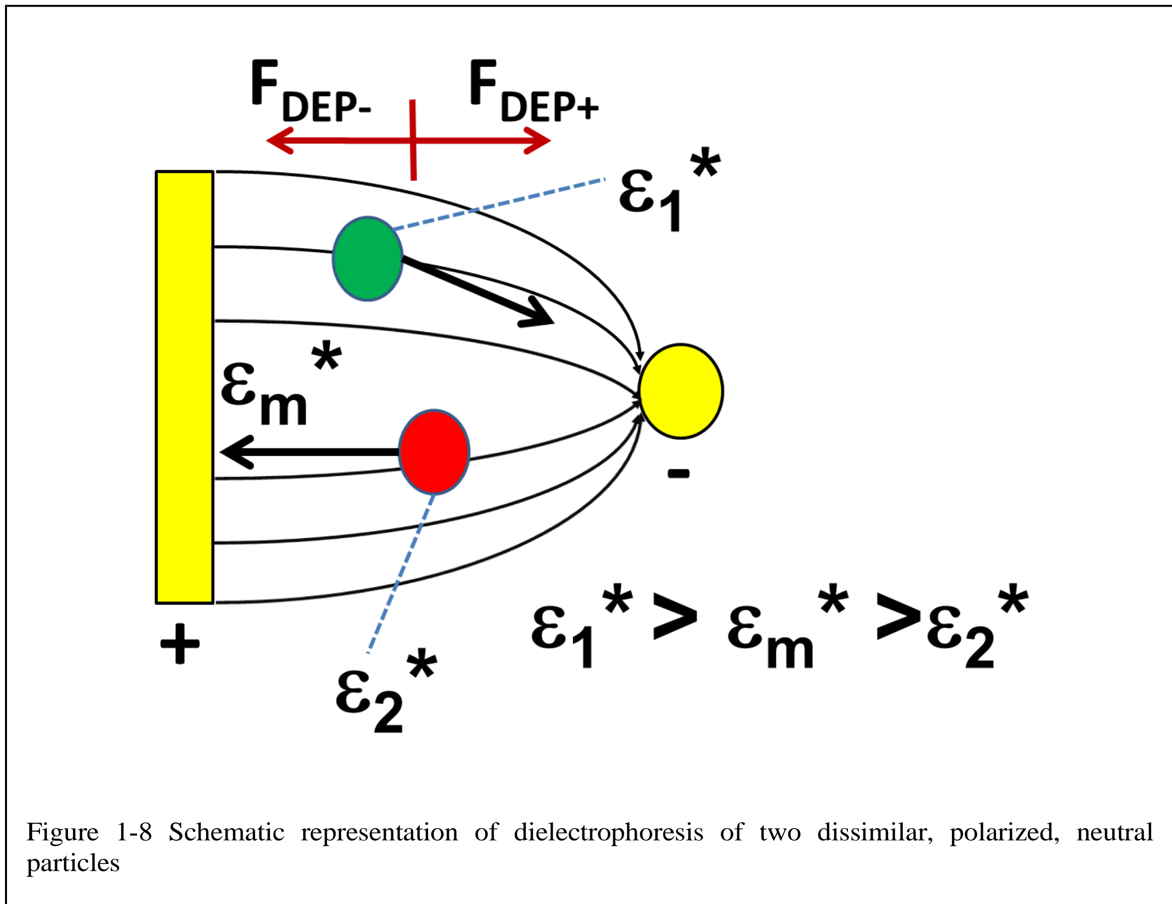

Figure 1-8 Schematic representation of dielectrophoresis of two dissimilar, polarized, neutral particles

To explain the response of biological particles to applied electric fields, the shell model of a cell was developed. In the single shell model, a cell is described as a sphere of highly conductive cytoplasm encased by a highly insulating membrane[41]. In order to more accurately model the complex cell structure, the single shell model of the cell can be refined by considering a sphere contained in another sphere[5]. This process can be repeated until the cell's behavior is adequately described and is known as the multishell model (Figure 1-9). The relevant information is conserved each iteration by using "effective" complex parameters to describe particle in the Clausius-Mossotti factor as described below. While for this work, we will treat all of the particles as spherical, this theory can be extended to nonspherical particles[35, 42]. The

main differences between spherical and nonspherical behavior concern the alignment of the nonspherical cells due to the torques that develop.

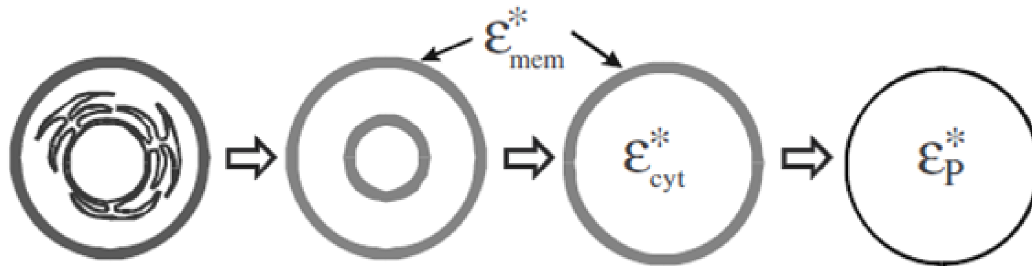

Figure 1-9 Diagram Schematic representation of how a cell can be simplified into a homogenous particle with effective permittivity ε_p*[40]. Used under the Fair-Use Provision of Copyright Law.

The DEP force magnitudes will be different for particles of different size and material makeup Figure 1-10A[35]. These differences in particle conductivity and size result in different DEP force magnitudes. This allows for selectivity among particles. Additionally the presence of mobile ions, bounded by various dielectic layers leads to different MW relaxation timescales. The result is that the DEP force on a particle is frequency dependent, especially for inhomogeneous particles such as biological cells (Figure 1-10B). For the low frequency/DC case, the only dielectrophoretic differences between particles are their size and conductivity. Also, the permittivity and conductivity of the medium affects the DEP force. For example, in our DC iDEP experiments, the particles are polystyrene beads with very low conductivities (~10^{-16} S/m) and the media is DI water (~10^{-3} S/m) or a mixture of DI and PBS (~10^{-2} S/m). Since the media conductivities are higher than the particle conductivity, the DEP force is negative, thereby motivating the particles away from high gradients in the electric field within the channels. This is known as negative DEP. For biological particles, which more complex than a solid sphere, the low conductivities of the cellular membrane dominate the particle conductance. It should be noted that for biological cells the membrane conductivity (σ_{mem}) is typically a few orders of magnitude lower than DI water (~10^{-6} S/m)[35]. Thus, biological cells also exhibit negative dielectrophoresis as low frequencies.

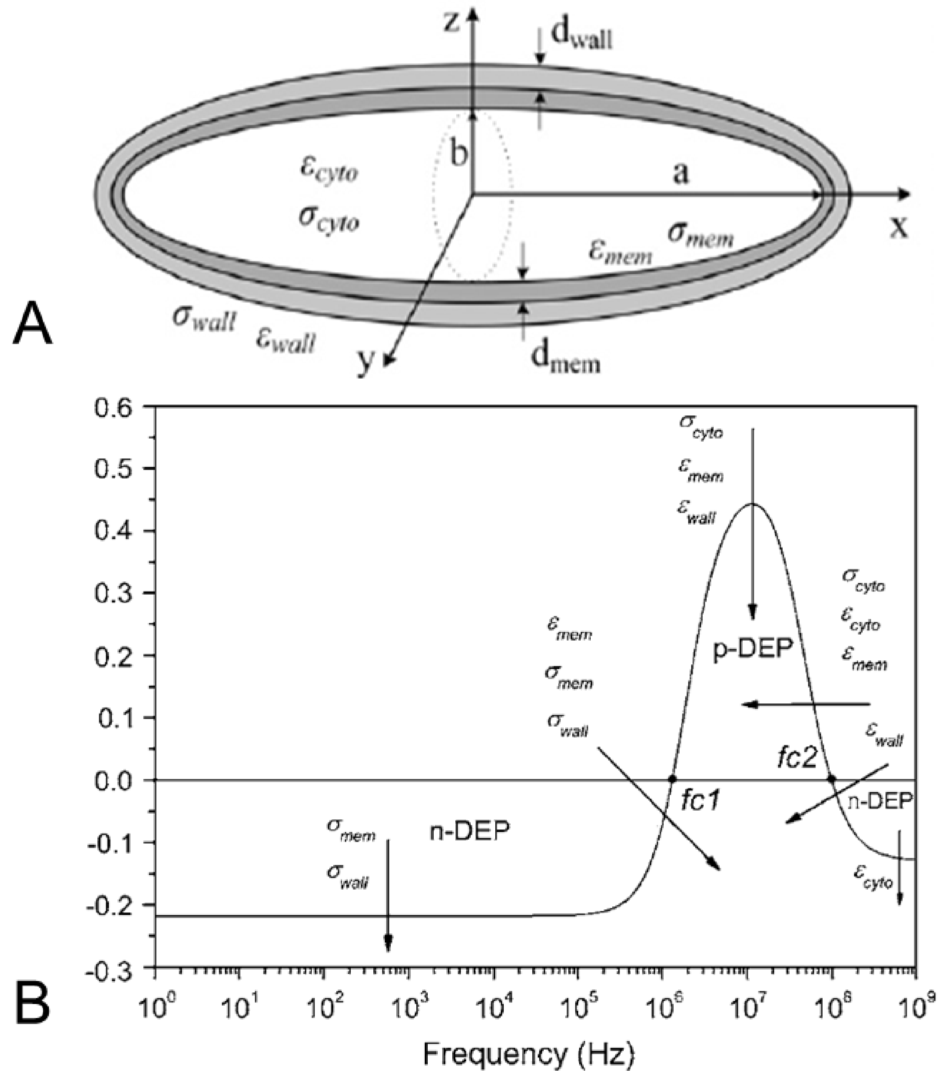

Figure 1-10 (A)Diagram of the ellipsoid multishell model for bacteria cells (B) Model of the typical frequency response of a biological cell in a low conductivity electrolytic solution[35]. The crossover frequencies are labeled fc1 and fc2. A decrease in the dielectric parameters in each case produces the changes in the modeled plot as indicated by arrows in the different frequency regions. Used under the Fair-Use Provision of Copyright Law.

For higher frequencies ($\omega > 10^3\pi$ rad/s) the complex structure of the particle plays a larger role in the DEP response. The permittivities of the membrane (ε_{mem}) and cell wall (ε_{wall}) become increasing important. As a result, there is a frequency region in which f_{CM} will be positive. This results in the particle being pulled toward the regions with high electric field gradients. Finally in the highest frequency regime, ($\omega > 10^7\pi$ rad/s) the conductivity of the cytoplasma (σ_{cyto}) dominates and to a lesser degree the conductivity of the cytoplasma (σ_{cyto}), the permittivity of the cell wall (ε_{wall}), and the permittivity of the cell wall (ε_{mem}) are significant. In this regime, f_{CM} becomes negative

again resulting in negative DEP. It should be noted the experiments in this work are limited below 10MHz and thus the effects of this regime are not seen. Figure 1-3B shows two points labeled fc1 and fc2. These are the first and second crossover frequencies. At these frequencies a particle experiences no net DEP force regardless of the magnitude of the electric field gradients. The value of these frequencies are dependant on the properties of the particle and thus a straightforward strategy for separation of particles is to operate at a frequency near one particles crossover frequency and only manipulate particles of a different type with DEP.

Fluid flow in the devices can be generated by electroosmotic (EO) flow. For this configuration, a DC electric field is applied at the fluidic ports of the DEP device. Typically the interface of a solid and an electrolyte leads to a net charge fixed charge on either side of the interface. This forms an electric double layer of ions, known as a Debye layer[43, 44]. When an electric field is applied, the ions on the electrolyte side of the interface are moved by the Coulomb force. Since the flow is motivated at the walls of the channel, the velocity profile is very uniform, or plug like, across the width of the channel. Thus EK flow can be implemented with just a DC voltage, and move the solution and the particles through the device alleviating the need for the pumps required for the pressure-driven mechanism [25, 26, 29, 31, 36, 45-59]. For a particle to become trapped in these devices, the DEP force must be larger than all the other forces acting on the particle. Mathematically, this is [26, 31]:

$$\frac{u_{DEP} \cdot u_{EK}}{u_{EK} \cdot u_{EK}} = \frac{\mu_{DEP}}{\mu_{EK}} \frac{\nabla(E \cdot E)}{E \cdot E} \cdot E > 1 \quad (1\text{-}5)$$

where $u_{DEP} = \mu_{DEP}\nabla(E \bullet E)$ and μ_{DEP} are the DEP velocity and mobility of the particle, respectively. The electrokinetic (EK) effects of electroosmosis and electrophoresis have been combined into a single term for simplicity. Thus, $u_{EK}=(\mu_{EO} - \mu_{EP})E$ and $\mu_{EK}=\mu_{EO} - \mu_{EP}$ are the EK velocity and mobility of the particle, respectively. From this, we can see that as the electric field strength increases, the DEP force increases as the gradient of the square of the electric field while EK motion increases linearly with the field. Thus, for low electric fields, EK motion dominates but if the voltage is increased, DEP will gradually become more dominant and the particle will

be trapped.

Alternatively, another operational mode of our DEP devices is to use pressure driven flow to move the solutions through the functional components. A pump, typically a syringe pump, is used to create a pressure difference between the fluidic ports of the DEP device, thus moving the fluid. Trapping occurs when the DEP force overcomes the drag force on the particle[60]. For this configuration, a particle is trapped when:

$$\frac{u_{DEP}}{u_f} = \frac{\mu_{DEP} \nabla (E \cdot E)}{\mu_f} > 1 \quad (1\text{-}6)$$

where μ_{DEP} is the DEP mobility of the particle and u_f is the velocity of the fluid. For this setup, the electric fields and fluid flow rate are completely independent and may be adjusted arbitrarily.

1.3 Three Dimensional Fabrication

Microelectromechanical systems (MEMS) offer a wide range of functionality in a very compact package. In order to operate at peak performance, however, MEMS devices often require specific 3D geometries, making the flexibility of the fabrication process critical. Fortunately, using standard micromachining techniques, it is very often possible to create 3D structures with a series of patterned depositions or etches[61-64]. Unfortunately, fabricating 3D structures in this manner is very costly and time consuming due to the number of fabrication steps needed for even basic 3D shapes such as a tetrahedron. Thus, the simplicity of the fabrication process has become important as researchers look to make 3D MEMS devices that are practical to fabricate. One promising method to do this is to limit the process to one photolithographic patterning step and then performing a single etch.

Two methods currently exist for fabricated complex 3D structures with a single photolithographic: gray scale lithography and reactive ion etch (RIE) lag. Gray scale lithography utilizes a photolithographic mask with many gray levels from opaque to transparent[65]. The mask is used to allow varying intensities of light to a layer of

photoresist. During exposure and development, the levels of opacity translate into different surfaces heights of the photoresist. A blank physical etch is then used to transfer these varying heights to the substrate. The downside to this technique is that it is very sensitive to the conditions of the exposure, development, and etching.

The other technique for obtaining complex 3D microstructures with a single mask is RIE lag[66-68]. When a substrate is being etched with DRIE, trenches with a smaller diameter have been observed to etch slower than trenches with a large diameter. This phenomenon is known as RIE lag. In order to remove substrate material, reactive particles must come into contact with the substrate surface. These particles must travel though openings in an etch mask to arrive at the substrate surface. As the size of the openings in the masking layer decreases, the rate at which species can be transferred though the opening to the substrate also decreases. This reduced transportation rate of reactive particles results in a decrease in etch rate. For large mask features, this effect is negligible. However, mask features on the order of 10µm, will experience strong RIE lag.

Other factors affect etch rates in DRIE such as aspect ratio dependent etching (ARDE) and microloading. ARDE is the decrease in etch rate that is observed with an increase in the aspect ratio of an etched trench. Etchant species require more time diffuse to the substrate surface for a high aspect ratio structure than for a low aspect ratio structure. This effect is pronounced in anisotropic etching, as the etch rate of trench decreases as the trench becomes deeper. Microloading is used to refer to the variation in the etch rate due to the variation in exposed substrate in a local area. If the exposed substrate surface is very high in particular area, the etch rate will suffer due to the limited availability of etching species. Conversely, areas with low densities of exposed substrate surface will etch at a higher rate to an abundance of etching species. Macro loading is similar to microloading, with the exception that macroloading refers to variations in etch rate across the entire substrate wafer. RIE lag is sometimes used interchangeably with ARDE, microloading, and macroloading. However, in this work, the term RIE lag will be used to describe the dependence of etch rate on mask feature size.

Traditionally, RIE lag has been considered a parasitic effect, as it prevented anisotropic etches from have a uniform depth. However, in 2002 Chou and Najafi were

the first to report the use of RIE lag for single mask 3D fabrication[69]. Their goal was to create curved electrodes for electrostatic actuators. To accomplish this, a single mask would be used to create an etched surface that varied in depth. The mask contained openings that varied from 2 μm to 50 μm. First anisotropic channels were etched, using the Bosch process. Then an isotropic etch was used to remove the pillars but leaving a curved bottom profile. The surface was made smooth by thermal oxidation and then oxide removal. The resulting features varied in depth by 20 μm.

Following the Chou and Najafi work, Bourouinia et al. developed another RIE lag based fabrication process which they named the Microloading Effect for Micromachining 3D Structures of Nearly All Shapes (MEMNAS)[70]. This process is similar to the Chou and Najafi process with the exception that no anisotropic etches are used. The mask consists of an array of circular openings whose centers are equally spaced. Differences in

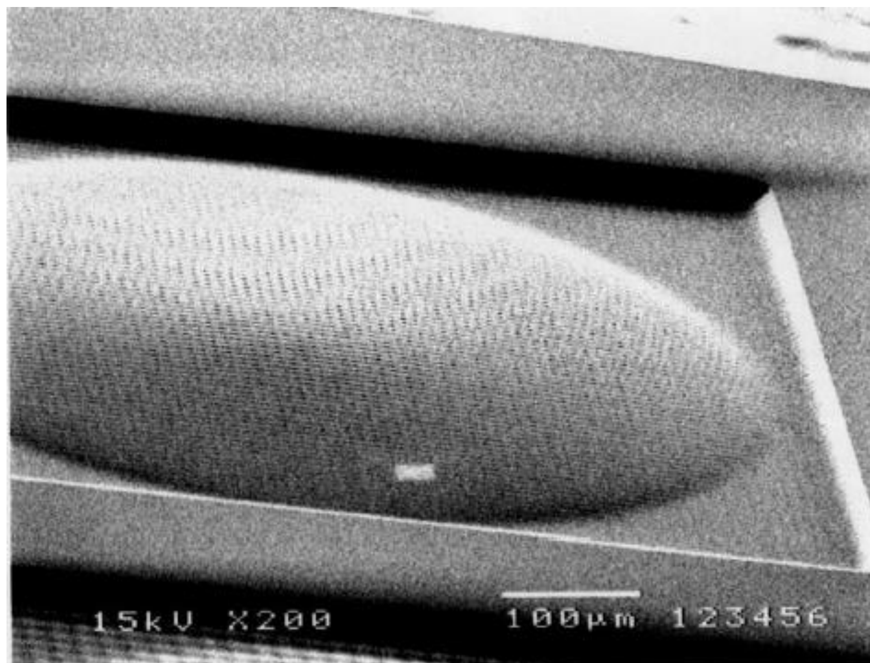

Figure 1-11 Microfabricated Lens using the MEMSNAS process [71]. Used under the Fair-Use Provision of Copyright Law.

etch depth are achieved by changing the diameter of the circles. Bourouinia et al. developed a model to predict the etch depth as a function of circle diameter. In the MEMNAS process, an isotropic RIE etch is performed through the openings in the mask. Then the mask is removed and another isotropic etch is used to smooth the surface. Using this method, structures were created with depths ranging from 20 μm to 100 μm with a

surface roughness as low as 25 nm. While not quantified in the work, the maximum achievable aspect ratios and slopes can be very low. Also the minimum feature size is 50 μm. Figure 1-11 shows a microlens which has been fabricated in silicon with the MEMSNAS process.

Rao et al. introduced a modified version of the Chou and Najafi process, with the goal of achieving smaller feature sizes[72]. Anisotropic trenches were etched using the Bosch process. In this case, the walls between trenches were on the order of 1 μm. Then the walls are removed by growing and removing thermal oxide. The minimum feature size for this technique was on the order of 5 μm.

Gantz et al. introduced a comprehensive model for creating microfluidic channels using RIE lag[73]. While previous works modeled etch depth solely as a function of feature size, Gantz et al used the size, shape, spacing, and number of features to determine the depth and width of the created channel. Their process flow included a single isotropic RIE etch through an array of rectangular opening in a mask. Due to the extended list of parameters, a large range of channel depths and widths is attainable Figure 1-12. The minimum feature size was on the order of 10 μm.

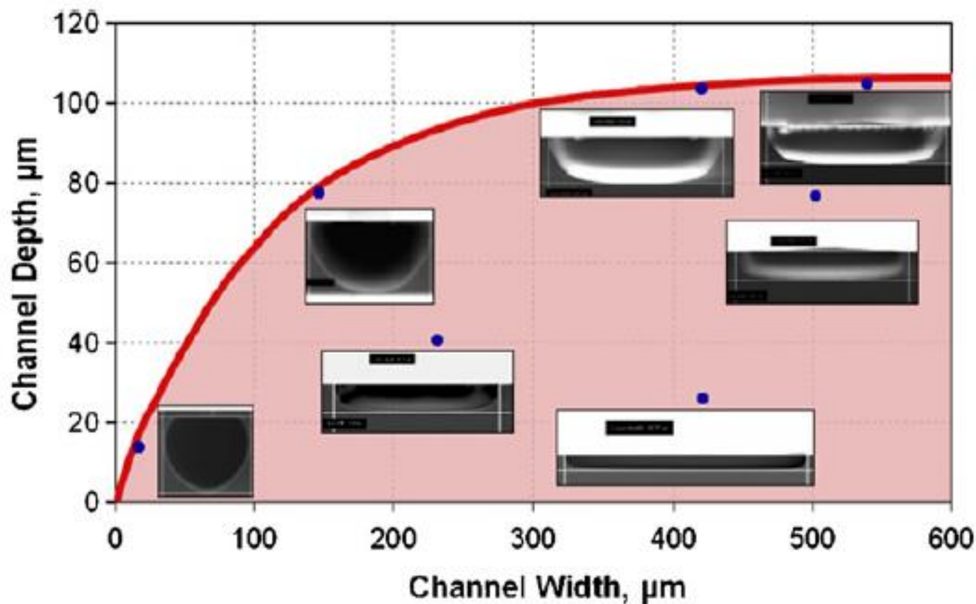

Figure 1-12 The range of possible depth to width aspect ratios for a 30 min etch duration. SEM photos show typical results for each section on the plot[73]. Used under the Fair-Use Provision of Copyright Law.

The works mentioned here all provide a mechanism for fabricating three dimensional structures in silicon with a single mask. These papers demonstrate the usefulness and cost saving potential of RIE lag as a three-dimensional microfabrication technique. However, with the exception of the Gantz et al. study, the only output parameter that is studied is depth. Gantz et al. consider depth and width as output parameter, but the channel cross-sections were all symmetric and the channels maintained a constant cross-section along their length. By contrast, this document studies the attainable slopes along the length of a channel as well as channels with symmetric and non-symmetric cross-sections.

1.4 Objective and Outline of the Dissertation

The main objective of this research is to use MEMS based fabrication techniques to develop three dimensional insulator-based dielectrophoresis (iDEP) devices. Within the scope of this research are two secondary focuses, 3D microfabrication for microfluidics and insulator-based DEP devices. Many of the fabrication techniques and process flows presented in this work are either completely new or highly modified for this application. It will be shown how the developed fabrication techniques greatly enhance the capabilities of the iDEP devices. The DEP-based devices in this work are designed to address several of the important issues in the field including lowering the operating voltages, decreasing Joule heating, and increasing throughput. Additionally, great strides have been made to retain benefits of the DEP devices including being highly tunable, inexpensive to fabricate in large quantities, modular with other microfluidic components, and very sensitive to small differences in biological cells. The application of interest is pathogen detection, however the presented techniques may be modified for other bioparticle applications such as protein, circulating tumor cell, or stem cell enrichment.

This report covers the experimental and theoretical works performed during the term of the project. Below is a brief outline of the dissertation:

Chapter 2 covers development of a fabrication technology for three dimensional (3D)

micro total analysis systems. Silicon microstructures are created with a single mask and a single etch that vary in all three dimensions. The ability to create varying depth transitions is studied as well as the ability to enclose any of the structures as a buried channel.

Chapter 3 details the use of the 3D fabrication developed in chapter 2 to create the first silicon iDEP devices. The investigation reveals the thermal benefits of using silicon devices. Additionally the effects of using 3D iDEP devices are studied.

Chapter 4 is focused on the development of a single-mask process for 3D microstructure fabrication in PDMS. This allows identical structures to be fabricated in either silicon or PDMS. It should be noted that this chapter was co-authored with Yahya Hosseini. For this work Yahya developed the glass reflow process and Phillip designed the 3D structures and tested the 3D iDEP devices.

Chapter 5 reports development of 3D PDMS iDEP devices which utilize DC biased-AC electric fields.

Chapter 6 describes the development of the first off-chip electrode insulator based dielectrophoresis (OπDEP) device.

Chapter 7 presents 3D πDEP. This technique combines 3D structures with OπDEP device architecture. The resulting device has a greatly improved performance with no added fabrication or operation cost.

Chapter 8 discusses the main conclusions from this work, concept devices, and future research directions

2 A Fabrication Technology for Three Dimensional Micro Total Analysis Systems

2.1 Introduction

Analytical systems based on microfluidics, also known as “lab-on-a-chip” or “micro Total Analysis Systems” (μTAS), represent a fast-developing area of research aimed at low cost, powerful, portable, and high throughput systems for a wide variety of applications including biomedicine, environmental monitoring, The creation and networking of microfluidic channels or microchannels is at the heart of the functionality of microfluidic systems. These microchannels direct fluid and particles through the system and allow for the manipulation of many different substances [74, 75]. For example, microchannels have been used for the small scale transport of cells[30], serve as gas chromatography columns[76], and provide cooling to microchips[77].

High levels of integration of fluidic elements with other types of elements (optical, electrical, etc.) is of paramount importance when considering lab-on-a-chip systems as miniaturized instruments that perform all chemical functions and detection in a monolithic device. From different substrate materials used to fabricate microfluidic channels such as PDMS, silicon, glass, and SU-8, silicon is intriguing in that it enables the integration of various functionalities into a monolithic device due to the fact that most micromachining techniques are still silicon based. In addition, onboard electronics for system control, signal processing, and computing can be integrated on silicon-based μTAS if fabricated using a CMOS-compatible process. Another advantage of silicon, which will be demonstrated in this paper, is its capability to produce complex three-dimensional (3D) microfluidic structures using a single-mask, single-etch process. Three dimensional designs on other substrate materials (and silicon as well) may be obtained by using multiple photolithographies and etching steps. However, the number of distinct depths that can be achieved on a single substrate is equal to the number of photolithography steps. Thus, systems with intricate features that vary in three dimensions become particularly costly to produce.

The common approach for the fabrication of silicon-based microchannels is to

selectively etch silicon (isotropic or anisotropic, wet or dry) and then seal the channels. The problem associated with wet etching techniques of silicon whether anisotropic (KOH, TMAH or EDP) or isotropic (HNA) is the dependence of the etch process on agitation, temperature, and the composition of the mixture; thereby, making it difficult to control [78-80]. In addition, wet etching is not favorable in the variety of geometry that can be created. Dry etching techniques offer a stable and reproducible alternative. Deep Reactive Ion Etching (DRIE) is a dry etch which utilizes high energy inductively coupled plasma (ICP). DRIE can be used to create three dimensional patterns in silicon. The etch rate in DRIE processes depends on a phenomenon known as "RIE lag" in which etching of a small trench lags behind a large trench [81-84]. The effect of RIE lag was first discovered on deep or high-aspect ratio trench formation using the Bosch process. Several studies have examined the relationship between the geometrical patterns and RIE lag for isotropic etching using ICP DRIE tools [72, 85-87]. Our group has been the first to investigate the use of RIE lag for microfluidic applications. In a recent study done by Gantz and Agah [73], RIE lag has been modeled and used to create microchannels in silicon with predictable dimensions. Geometric patterns in the masking layer were used to create distinct microchannel cross sections. Microchannels with many different cross sections were created on the same substrate with a single etch process and then sealed by anodic bonding the silicon substrate to a Pyrex wafer.

This paper reports for the very first time a single-mask CMOS-compatible process for creating three dimensional (3D) buried channels (3DBCT) in a silicon substrate. Silicon microchannels are created with control in all three dimensions with a single mask and a single etch step of the substrate leading to a low-cost rapid process. Complex 3D μTAS are formed comprising microchannels and cavities with varying depths and widths and with symmetric and non-symmetric cross sections. Also, because the entire process is fabricated on silicon and is CMOS compatible, 3D buried channel devices can be integrated with microelectronics allowing for a very diverse set of applications. It is notable that previous work on buried channels has focused on 2D geometries without a change in the cross section [88-90] In this work, however, microchannels are created which change in depth along the length of the channel. Also junctions are created between channels with controlled transitions between depths. Furthermore, the flexibility of our technique along with the characterization of channel

sealing properties using PECVD dielectrics presented herein allows for the creation of predictable nano-scaled holes on the substrate surface.

2.2 Fabrication

The fabrication process (Figure 2-1) starts by depositing 5600Å silicon dioxide on a <100> silicon wafer. This oxide acts both as a masking layer during the etch process and as a structural support during channel sealing. The oxide layer is deposited by plasma enhanced chemical vapor deposition (PECVD) at relatively low temperatures (250-400ºC). For this work, oxide deposition was performed in a Trion Orion II PECVD machine and under the conditions listed in Table 2-1. The oxide layer is then patterned using RIE with a photomask containing rectangular windows with different dimensions, spacing, and numbers in order to harness RIE lag.

After oxide patterning, the substrate is isotropically etched using SF_6 plasma to create 3D channels. The etching was performed with an Alcatel AMS-100 Deep Reactive Ion Etcher (DRIE) with the process parameters given in Table 2-2. The highly selective process etches silicon while leaving the oxide masking layer suspended above the channels creating a thin lattice structure with micron-sized windows (Figure 2-2). A second PECVD oxide deposition was then utilized to seal the channels. The

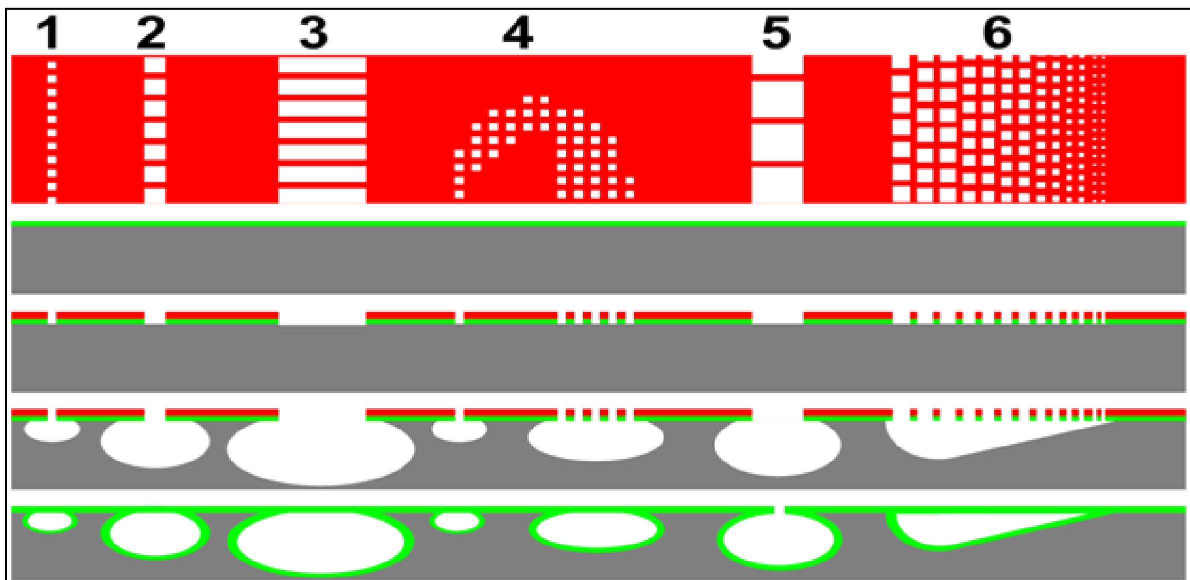

Figure 2-1. Process flow for 3D buried channels. (Top) Mask layout (1-3) Sealable channels (4) Gradually varying depth design (5) Unsealable mask window for access holes or nano-scale holes in oxide layer (6) Non-uniform channel.

Temperature (°C)	300
Pressure Set (mbar)	900
ICP Power Set (W)	175
RIE Power Set (W)	50
Silane(2%) Flow Rate (sccm)	3000
N_20 Flow Rate (sccm)	71

Table 2-1. PECVD Deposition Parameters

Flow Rate SF6 (sccm)	400
Chamber Pressure (mbar)	1.10E-03
Source Power (W)	2200
Helium Pressure (mbar)	1.00E+01
SH position from Source (mm)	200

Table 2-2. DRIE Etch Parameters

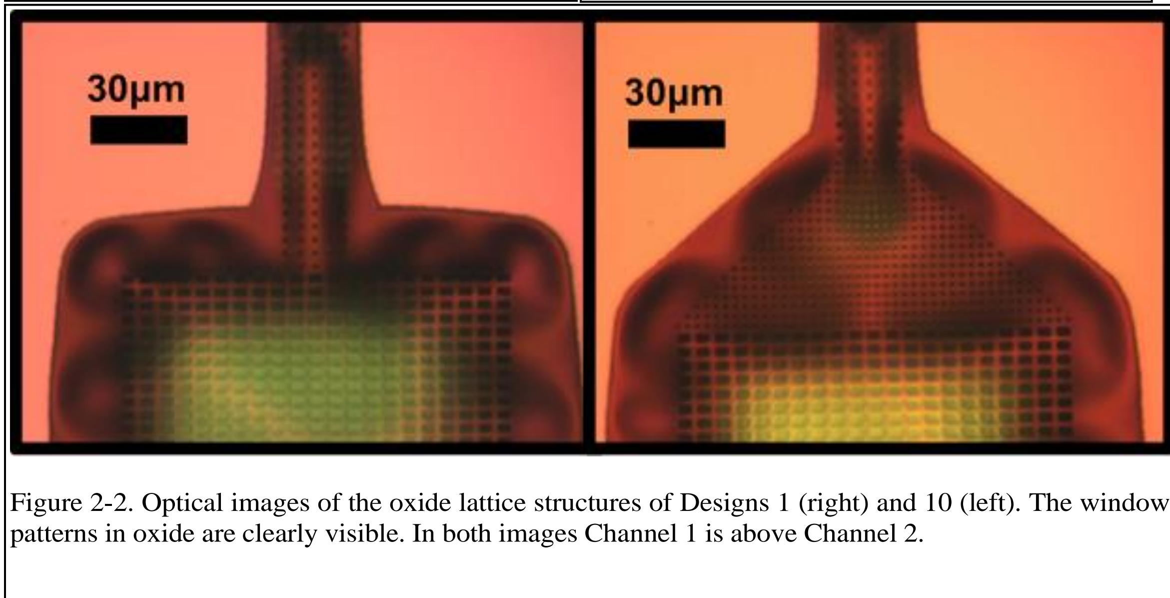

Figure 2-2. Optical images of the oxide lattice structures of Designs 1 (right) and 10 (left). The window patterns in oxide are clearly visible. In both images Channel 1 is above Channel 2.

relatively conformal nature of PECVD oxide coats the sidewalls of the silicon channels and causes the windows in the oxide lattice to close, thereby sealing and burying the channels. To achieve a more conformal coating, PECVD tetraethoxysilane (TEOS) may be used as shown previously [91]. The amount of oxide for channel sealing depends on the size of the windows. It is noteworthy that all oxide deposition is performed at low temperature (<400ºC) making the entire process CMOS-compatible. In addition, silicon can be etched from the backside to release sealed structures as previously presented [89].

Three dimensional structures are achieved in this process by utilizing RIE lag [73]. Small features on a mask yield a lower etch rate than large features. By changing the relationship between the windows patterned on the oxide masking layer, RIE lag can be tuned to create channels with varying depths and widths. In order to enhance the effect of RIE lag, the designs in the photolithographic mask are divided into a grid of rectangular openings or windows. The window patterns can be described by a series of

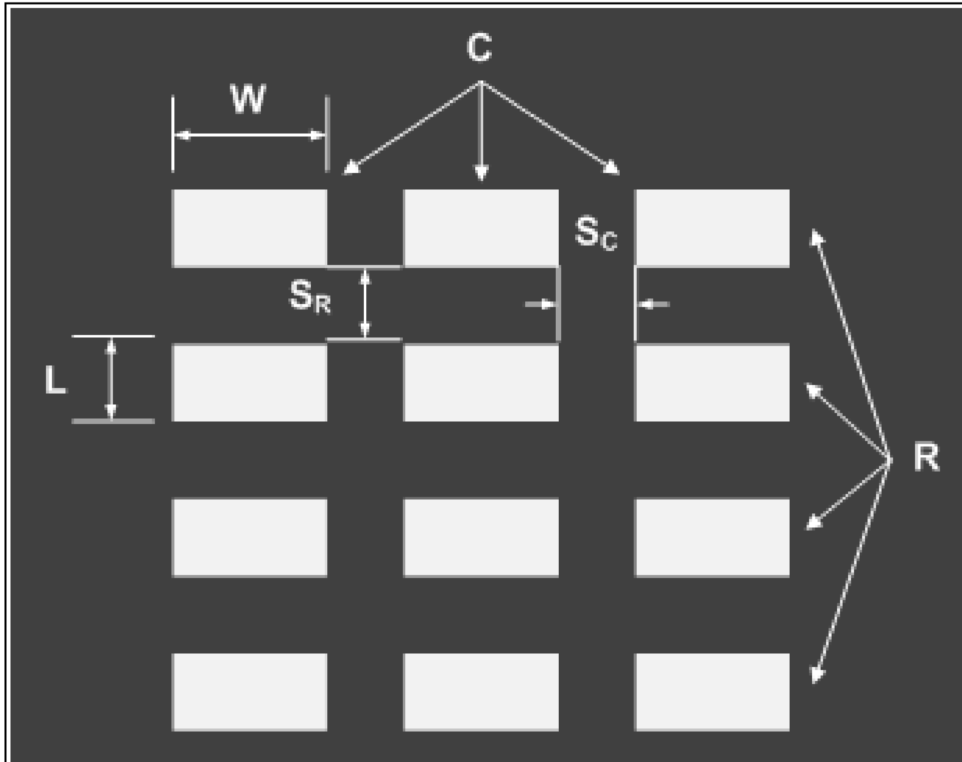

Figure 2-3. Important parameters in the window patterns present on the photolithographic mask.

parameters that play a role in defining the etch profile (Figure 2-3). Each window has a length of L and a width of W. The windows are divided into a number of rows (R) and columns (C). The spacing between the rows and columns are represented by S_R and S_C. These parameters alter the amount of the silicon substrate in a given area that is exposed to plasma etching. This, in turn, affects the local etch rate via RIE lag. By keeping the window pattern constant for a given length, the substrate can be etched to form a silicon channel with a constant cross section. Also, by varying these parameters in a particular direction, the RIE lag effect can be adjusted to create channels that vary in cross section.

2.3 Results and Discussion

2.3.1 Burying the Channels

Our ability to seal a window in the mask was largely dependent on the minimum

feature size of the window and the amount of oxide deposited. Using 3.5µm of PECVD oxide, we were able to seal 2 µm x 10 µm rectangular windows, whereas depositing 4.7 µm of oxide sealed 3 µm x 10 µm windows and 6.3 µm of oxide sealed windows up to 4 µm x 10 µm dimensions. The dimensions of the fabricated microchannels are also related to the window size. Thus, the achievable geometries are bound by the minimum and maximum window sizes. According to RIE lag models developed by our group [73], using windows ranging from 2 µm x 2 µm to 4 µm x 10 µm, buried channels can be created with depths ranging from 4 µm to 290 µm. Figure 2-4 shows the range of achievable depths and widths for several different opening sizes.

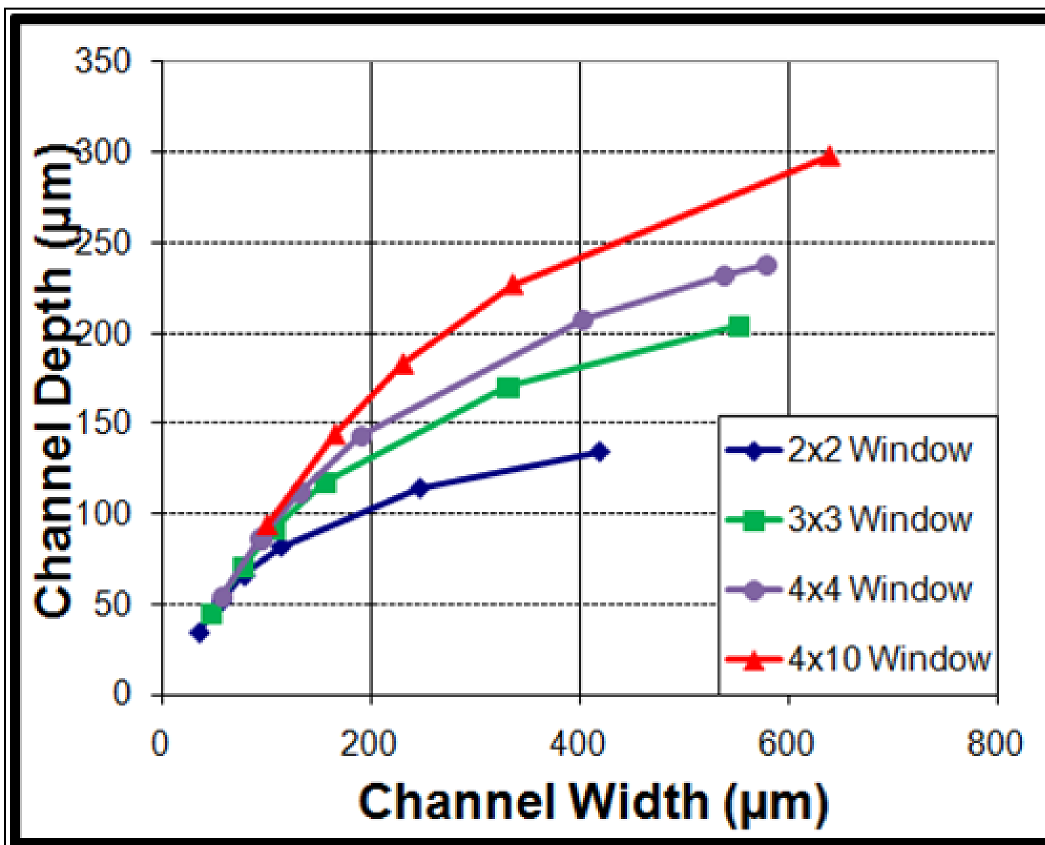

Figure 2-4. Buried channel dimensions falling underneath the curves are achievable.

We demonstrated the flexibility of this new technology by creating a series of buried microchannel networks. These structures consisted of channels with cross sections as small as 4 µm in diameter and contained networks of channels with arbitrary connections (Figure 2-5). Scanning electron microscopy (SEM) images clearly show that the microchannels were sealed without any unwanted holes or defects. As

seen in Figure 5, the etch step leaves scallops on the bottom of the channels. These scallops result from isotropic etching of the discrete windows and are on the order of a micron in size. Due to their small size, these features become more apparent in the smaller channels (~4 μm) than in the larger ones. It is worth mentioning that in these

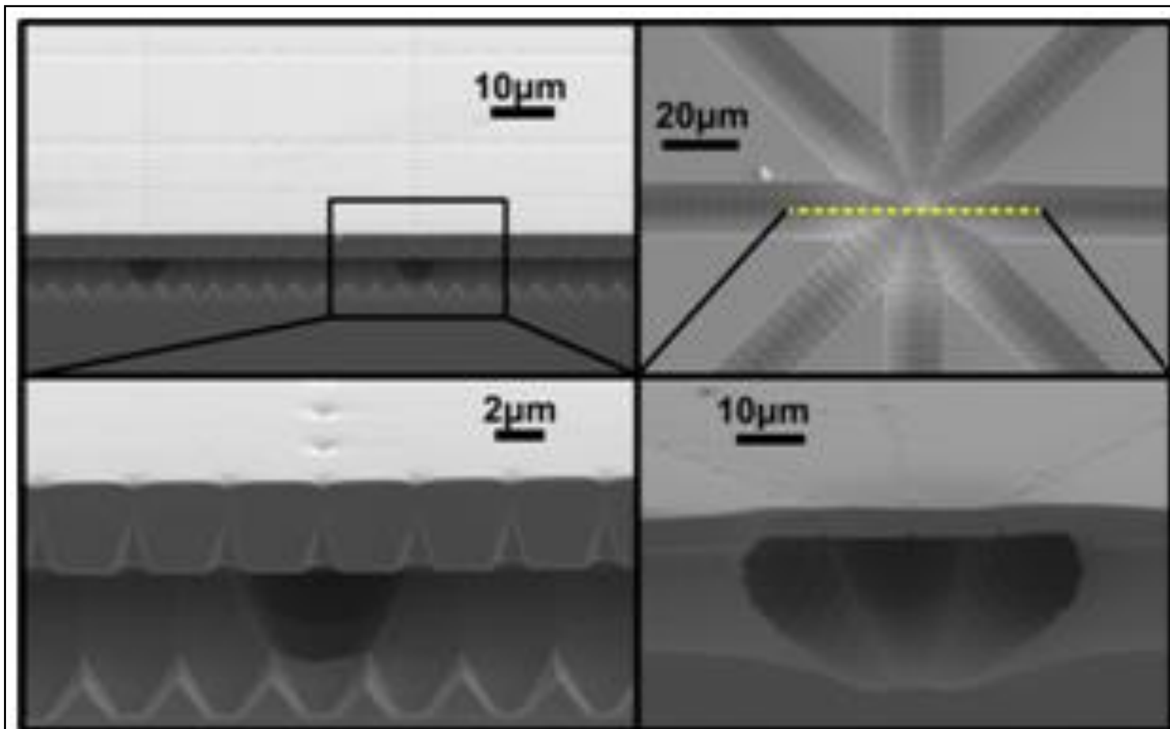

Figure 2-5. SEM images of buried microchannel networks (Upper Left) Network with intersections (Lower Left) Close up image of a 90° intersection (Upper Right) Top view of 8 channel intersection with mask oxide removed (Lower Right) Cross section of buried 8 channel intersection along the dotted line.

structures containing a network of identical microchannels, the depth at the intersection was found to be slightly larger than the depth of the network. At the intersection point, several window patterns appear in close proximity. Thus, the amount of exposed silicon substrate is larger in this region, leading to a faster etch rate due to RIE lag.

The microchannels created by this technique can vary in depth within the same channel. In order to demonstrate the 3D versatility of this approach, a buried microchannel that smoothly transitions in width from 20 μm to 45 μm and in depth from 20 μm to 85 μm was created (Figure 2-6). The gradual depth change was achieved by slowly varying the number of windows present in the masking layer along the length of the microchannel. Alternatively, changes in depth can be produced by varying the size and spacing of the windows. This is the first time that a microchannel with

varying cross section along its length has been created. Fabricating such microchannels is not feasible with conventional micromachining processes in which multiple lithography and etch steps are utilized to achieve multiple levels of depth. Figure 2-6 also shows a perspective SEM image of the channel after it was sealed. The waviness of the channel sealing is due to residual stress of the deposited oxide layer. This can be eliminated if a stress-free PECVD dielectric material is deposited to seal the channels as demonstrated before [89].

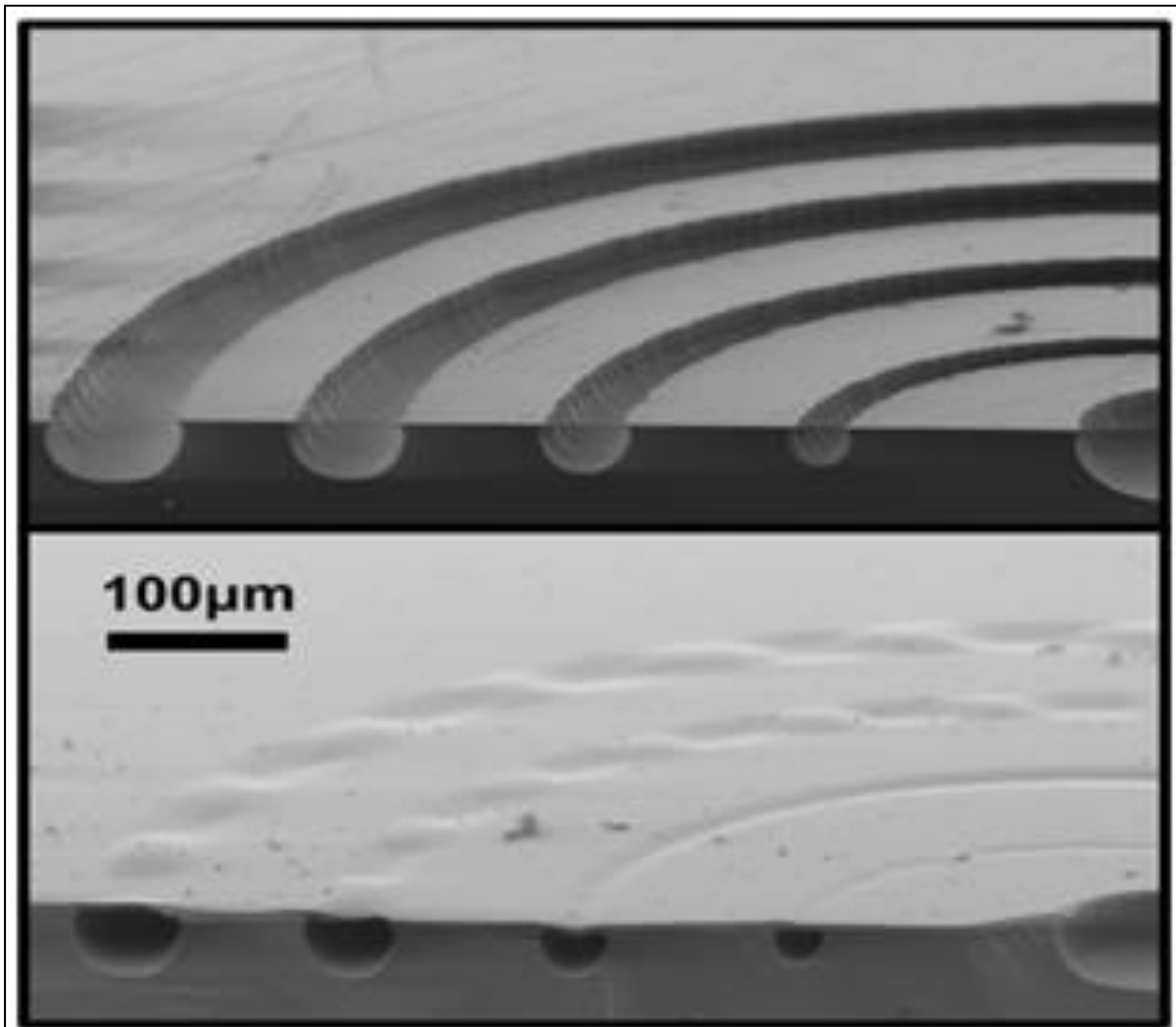

Figure 2-6. SEM images of a width and depth varying microchannel (Top) Microchannel before sealing. The mask oxide has been removed here for visibility. (Bottom) Microchannel after sealing.

Microfluidic ports are also needed for the interface of microchannels and the outside world. In order to create ports to the microchannels, the mask layout should contain windows sizes which are outside of the sealable range. The PECVD oxide

deposition can only seal window sizes of a few microns, thus larger windows remain unsealed. Large, unsealable mask windows (~1 mm) can be used to create access ports to the buried channel networks. Since the window size and deposition rate are known, the microfluidic ports can be created to an arbitrary dimension. If a window size is chosen to be slightly larger than the sealable range, nanometer-scale holes can be created. We demonstrated that holes as small as 600 nm can be easily formed from a 3 μm square window when depositing 3.5 μm of PECVD oxide (Figure 2-7). These nano-holes may be used to create a nano-scale interface for chemical and biological applications.

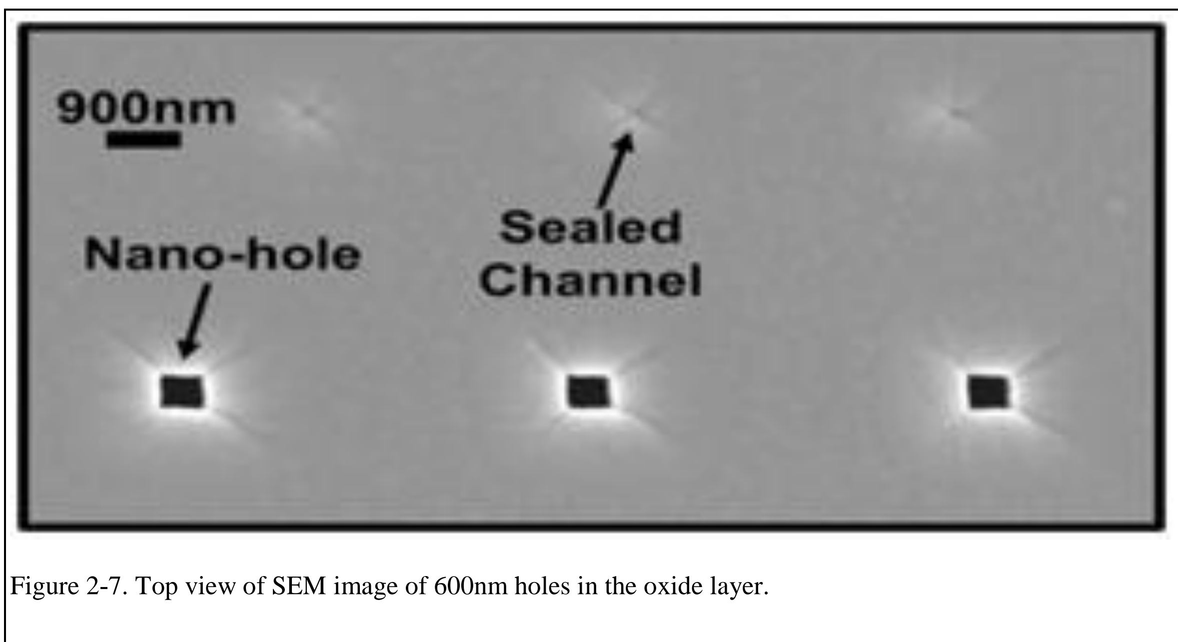

Figure 2-7. Top view of SEM image of 600nm holes in the oxide layer.

It is important to note that during channel sealing, the interior of microchannels are completely covered by a layer of oxide offering several advantages. For example, the oxide layer electrically insulates the microchannels. Therefore, techniques that require electrically insulating walls such as electrophoresis and dielectrophoresis can be performed in these channels [92]. The electrical insulation also protects electronics present on the substrate from any electric fields generated in the channels. For biomedical and microbiology applications, the oxide coating provides a biologically compatible surface for in vitro and in vivo studies [93, 94].

2.3.2 Channels with Varying Dimensions

Using our 3DBCT process, the transition slope at the junction of two dissimilar channels can also be controlled. Figure 2-8 shows a silicon structure connecting a microchannel with dimensions of 26 µm (depth) x 40 µm (width) and a microchannels with dimensions of 104 µm (depth) x 160 µm (width). The photolithographic patterns used to connect the channels is given in Table 2-3 and the patterns to create the channels are given in Table 2-4. At the junction of the two channels, 10 different mask patterns were designed to alter the profile at the transition region between the two channels, two of which are shown in Figure 2-2. The different slopes were produced by gradually or sharply altering the number and size of windows in the masking layer. The chosen pattern had 2 µm x 2 µm windows spaced 2 µm apart. The number of windows in each row varied from 8 to 42. Each design consisted of a different number of rows. The number of rows was varied linearly from 18 increments in Design 1 to 0 increments in Design 10 (Table 2-3). Figure 2-8A shows Design 10 which has a steep slope connecting the two channels, whereas in Figure 2-8B (Design 1) the slope is more gradual.

Design Number	Minimum C	Maximum C	Rows
1	8	42	18
2	10	40	16
3	12	38	14
4	14	36	12
5	16	34	10
6	18	32	8
7	20	30	6
8	22	28	4
9	24	26	2
10	N/A	N/A	0

Table 2-3.Geometric parameters for window patterns in the transition regions

Parameter	Channel 1	Channel 2
S_R and S_C	4.5	2
W	2	6
L	2	4
C	5	21

Table 2-4. Geometric parameters of window patterns for the connecting silicon channels

Depth profiles of the designs were obtained with a Veeco NT 2000 optical profilometer in vertical scanning interferometry (VSI) mode (Figure 2-9). The profiles were verified by comparing them with SEM images taken from cross sections of the channels. Missing points on the profiles indicate large slopes that are outside of the detectable range of the profilometer. The outputs from the profilometer showed that the transitions created between two channels have several interesting features (Figure 2-9). Because of the isotropic nature of the etch process, the channels take a finite distance to settle to a steady depth. Also, bulges in the profile are present at points P1 and P2.

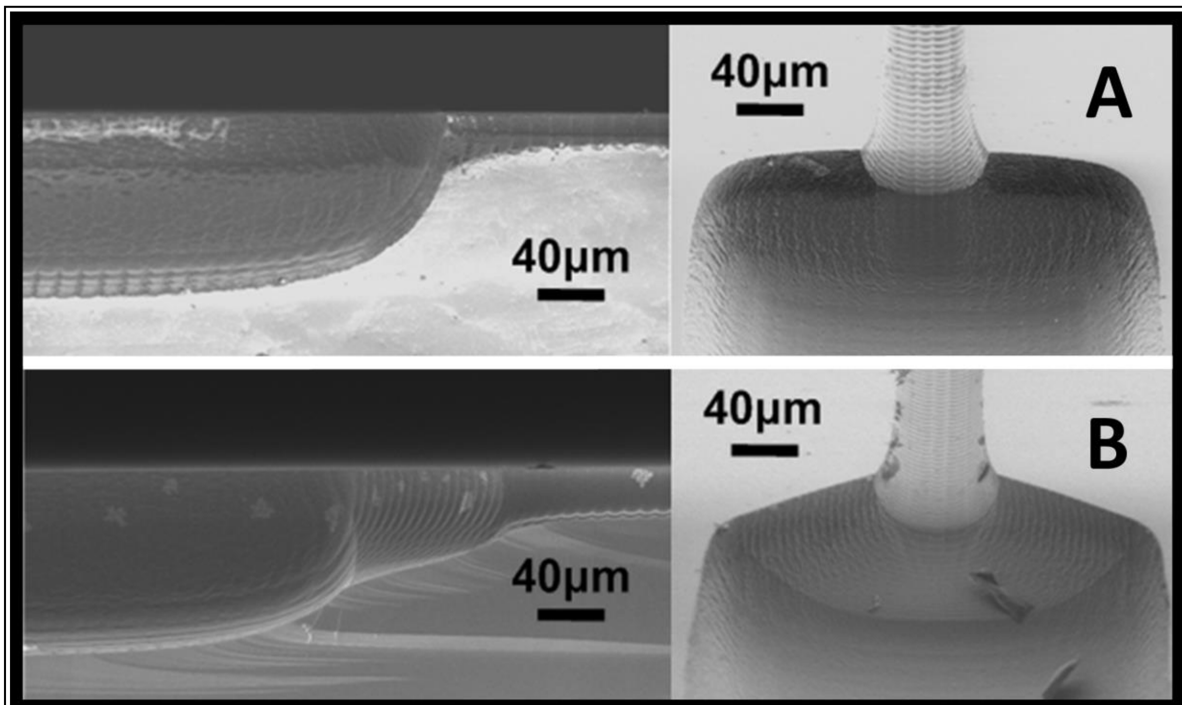

Figure 2-8. SEM images of the transition region of microchannels in Design 1 (B) and Design 10 (A) The left images show the cross-sections of the channels while the right images show the top view of the channels.

These bulges occur due to a rapid change in the mask patterns, leading to strong RIE lag effects. The bulges can be diminished if the mask pattern is altered such that the change in the window parameters is more gradual. For example the bulge at P1 is created at the point on the mask where the window pattern abruptly changes from widows that are 4 µm x 6 µm with 2 µm spacing, the pattern for Channel 2, to windows that are 2 µm x 2 µm with 2 µm spacing, the beginning of the transition pattern. This spike may be reduced if a few rows of windows were inserted between the mask

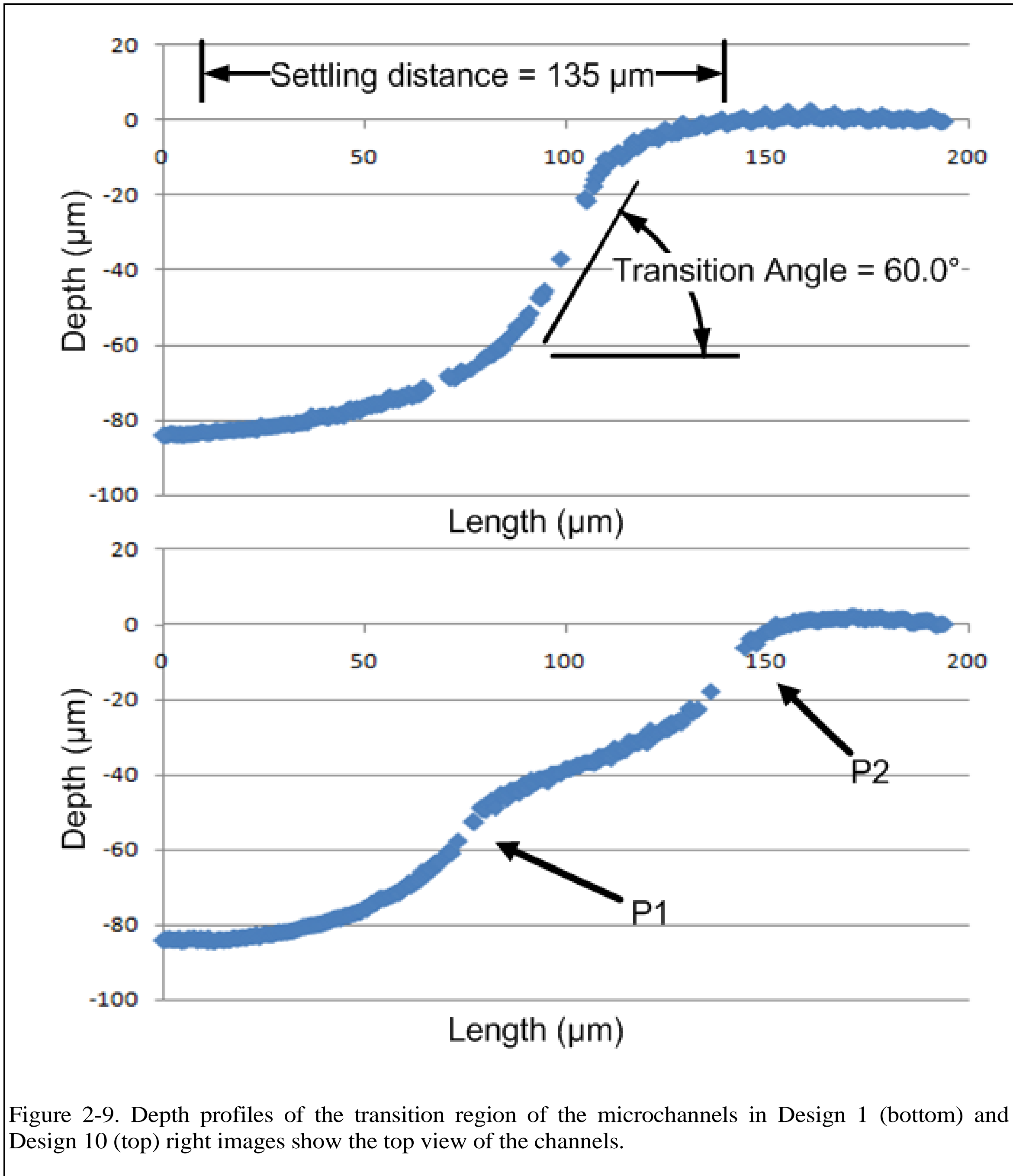

Figure 2-9. Depth profiles of the transition region of the microchannels in Design 1 (bottom) and Design 10 (top) right images show the top view of the channels.

patterns with a spacing of 2 μm and with sizes gradually changing from 4 μm x 6 μm to 2 μm x 2 μm.

Profiles were obtained of 8 replications of each microchannel and analyzed using MATLAB in order to quantify the depth profiles. The transition angle is defined by the slope of the linear regression line of the data lying between 15% and 85% of the maximum depth in order to ignore the rounding near the corners. The transition angles in the studied channels ranged from 40° to 60° with an error of +/-1° (Figure 2-10). The angles appeared to saturate at 60°, however, the data did not indicate a lower bound for the transition angle. In fact, structures were fabricated on the same wafer with transition angles much lower than 40°, an example of which was shown before in Figure 2-6. The settling distance is defined as the distance between the point where the depth profile is within 2% of the upper and lower depth of the channel. As the transition angle is increased, the settling distances decreased (Figure 2-11). The minimum settling distance was found to be 135 μm when the transition angle was 60°. This measurement is particularly important because it defines the total distance that

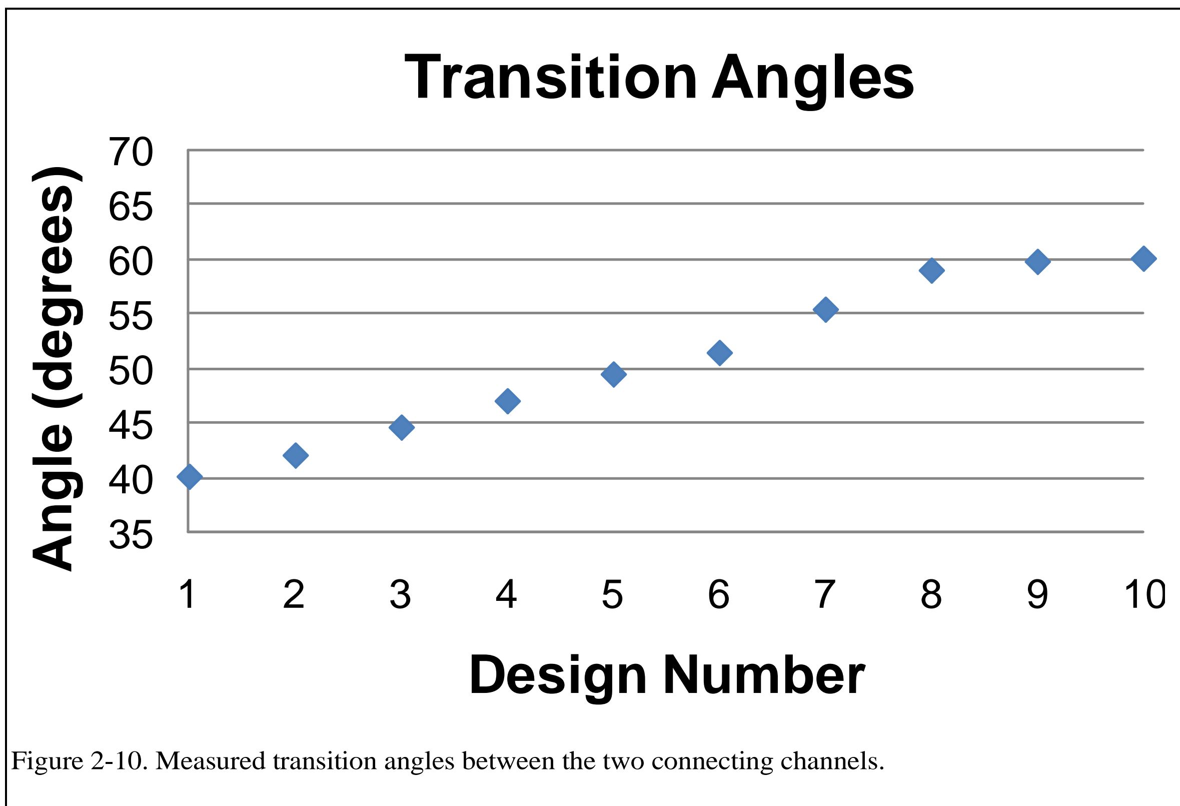

Figure 2-10. Measured transition angles between the two connecting channels.

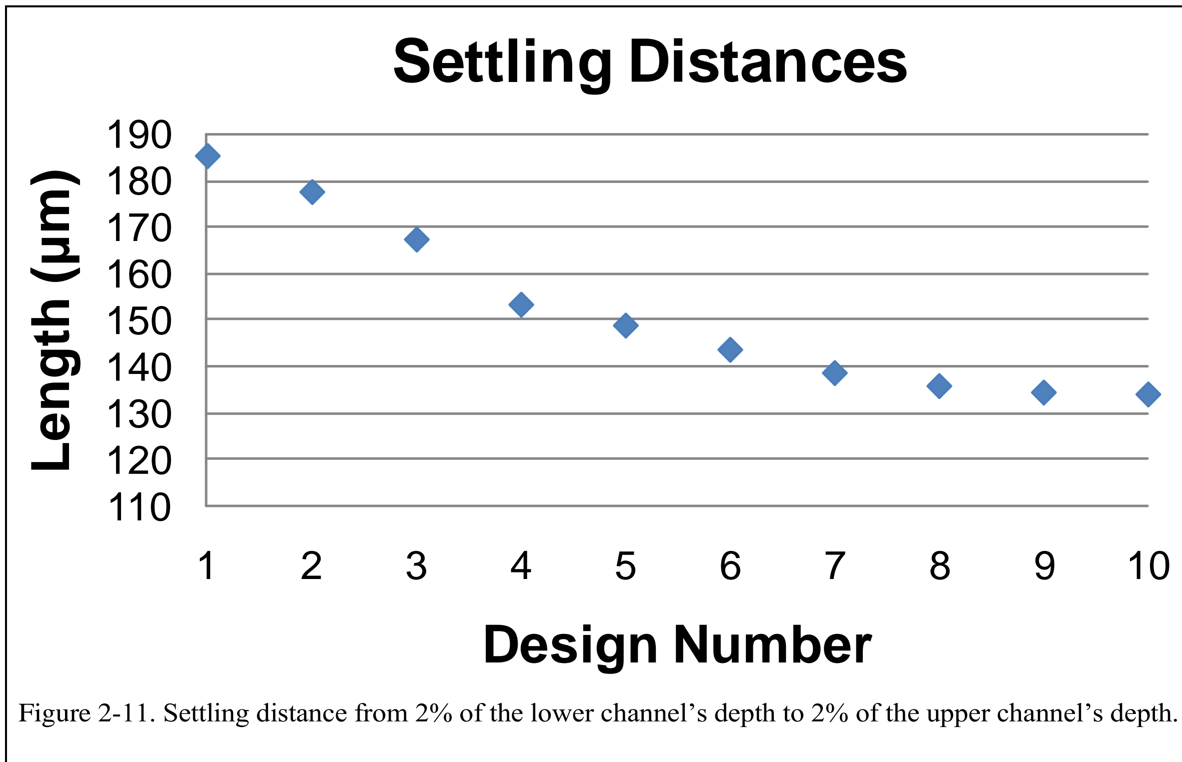

Figure 2-11. Settling distance from 2% of the lower channel's depth to 2% of the upper channel's depth.

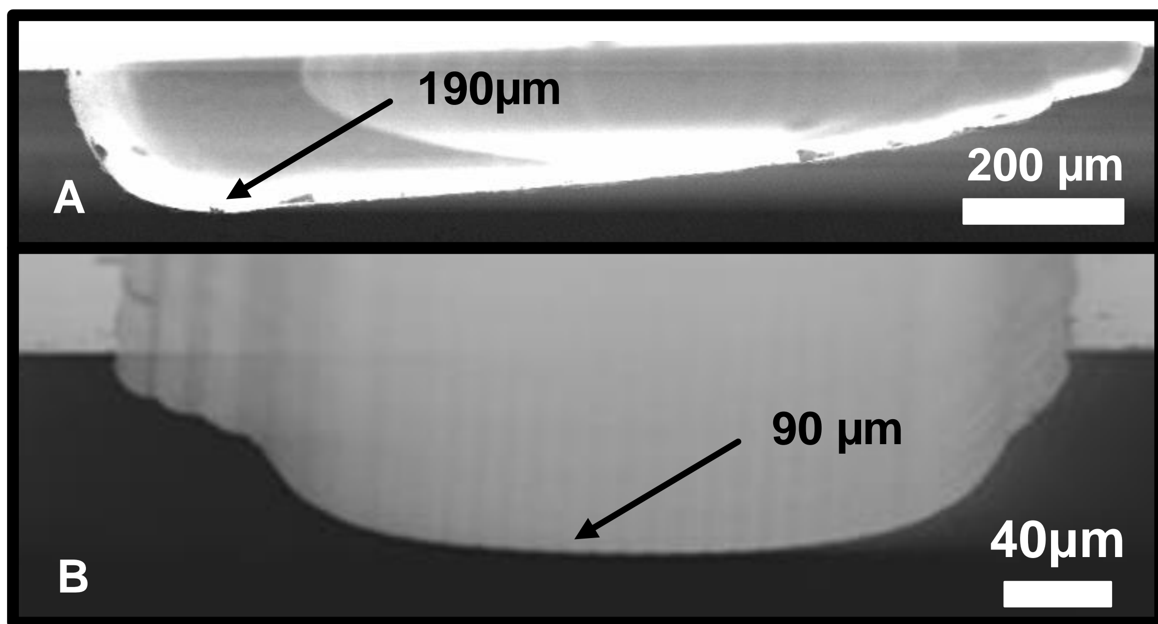

Figure 2-12. Cross-sections of non-symmetric channels (A) 190 µm deep channel (B) 90 µm deep channel.

must be provided to complete the transition between two depths. Thus any feature to be placed in the channel must be outside of the settling point range in order to avoid altering the profile of the junction.

Using our fabrication process, channel with non-symmetric cross sections were

also fabricated for the first time. These non-symmetric channels were achieved by changing the size of the openings in the mask along the width of the channel. Figure 2-12a shows such a structure created by square windows ranging from 10 µm to 2 µm. The structure is 1 mm-wide and 210 µm-deep at its deepest point. The non-uniform channels can also be fabricated by varying the spacing or number of window across the width of the channel as demonstrated in Figure 2-12b.

2.3.3 Applications

The 3DBCT process provides a versatile platform for µTAS development for applications including cell manipulation, cytometry, gas chromatography, chip cooling, flow sensors, and micro-scale chemistry reactors. To prove this point, microfluidic devices for cell handling and analysis were fabricated on a single wafer. These devices

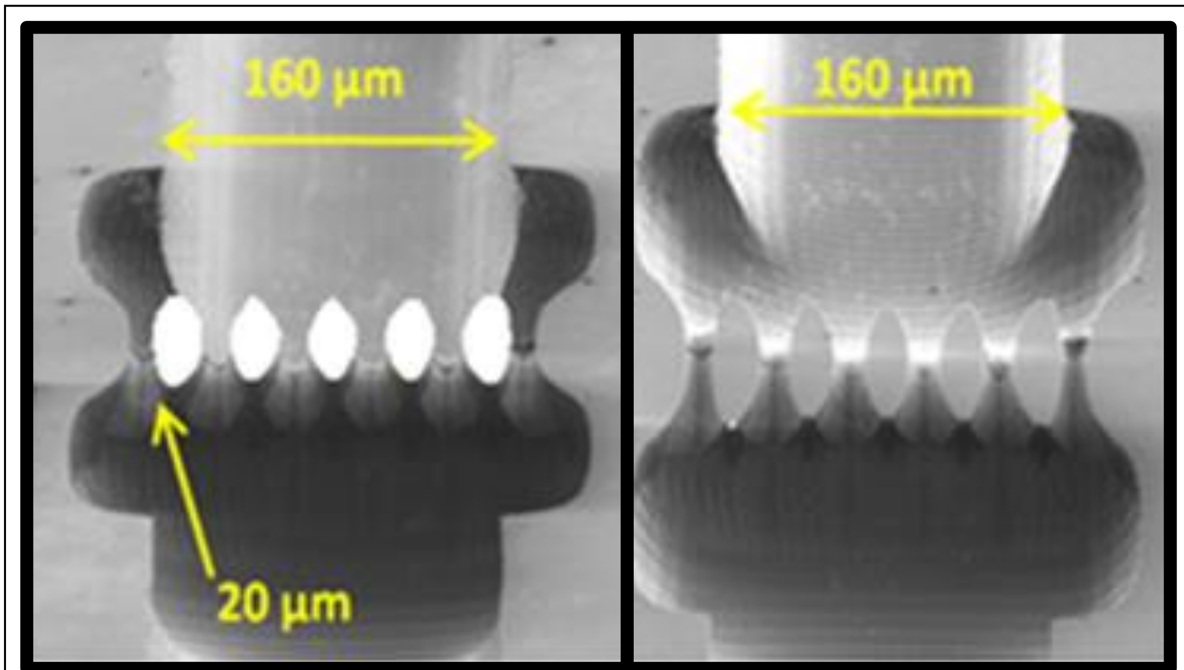

Figure 2-13. SEM Images of a DEP trapping device. A 125µm deep channel is connected to six 20 µm deep channels (Left) 45° angle view (Right) Top view.

included an insulator-based dielectrophoretic trapping device, a flow cytometer, and a microreactor. It is worth mentioning that these microstructures include channels with different depths and that the slope of the transition at the junction of different channels varies.

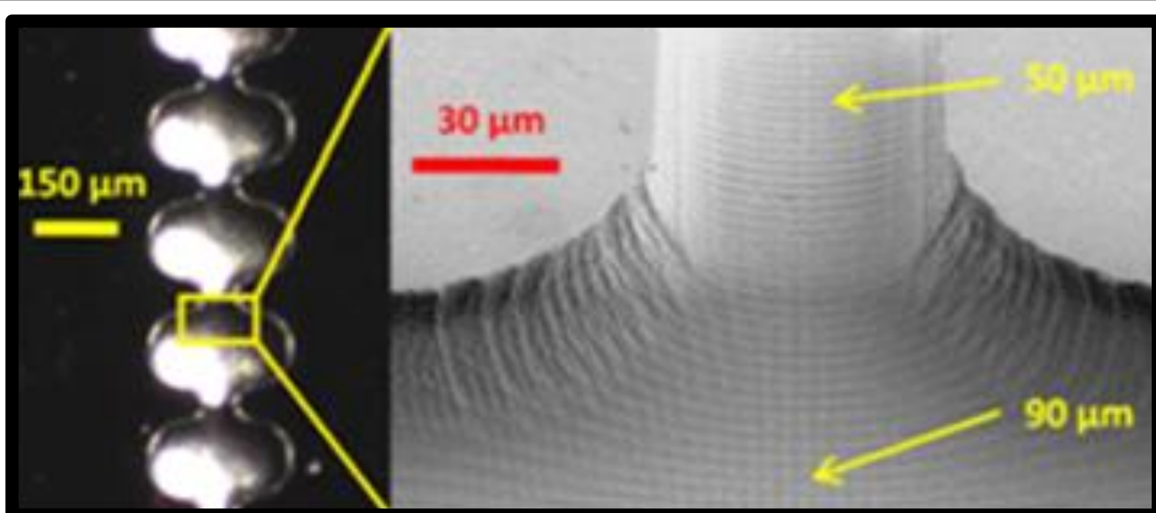

Figure 2-14. (Left) Optical image of a flow cytometery device (Right) SEM image of depth transition.

Insulator-based dielectrophoretic (iDEP) devices utilize non-uniform electric fields to trap particles of interest while allowing other particles to pass by [92, 95]. An electric potential is applied across the length of the channel. The non-uniform electric fields are generated by rapidly changing the cross section along the length of the channel. Similar to the devices in literature, our fabricated device (Figure 2-13) branches from a relatively large channel (160 µm by 125 µm) to a series of smaller channels (20 µm by 20 µm). 3D fabrication provides additional capability for the devices and has been demonstrated with channels that contain sharp depth transitions

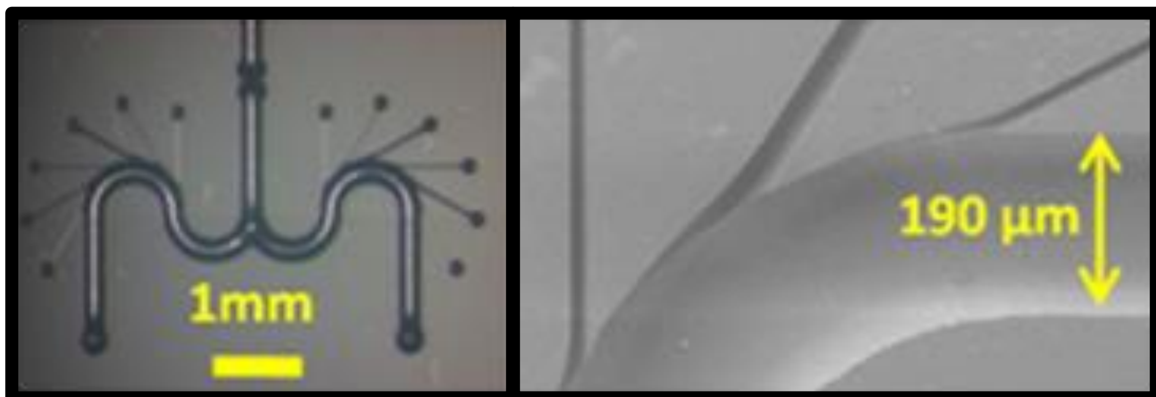

Figure 2-15. SEM images of a microreactor. 9 features of distinct depth from 100µm to 20µm are present (Left) Optical image of device (Right) Image showing side channel.

[96]. However, with 3DBCT, the slope of the transition is controllable, thus allowing greater design freedom for iDEP devices.

Flow cytometry is a technique for rapidly examining particles in a stream of fluid [97-99] (Figure 2-14). Microfluidic versions of flow cytometry can be used to examine a single particle or cell at a time. Particles from a main channel (~100 µm) are brought to a focus channel (~10 µm) where they are observed optically via a laser and a photodiode. These devices are typically fabricated with constant depth channels which constrict in width at the detection point. In our fabricated device, the depth in the constriction regions is shallower than in the other regions. This would inhibit particles from traveling above and below the particle of interest in the constriction region. The channel, however, could be connected smoothly to other microfluidic components with deeper channels.

Microreactors are used to perform chemical reactions with very limited volumes [100, 101]. Fluid may be transported by pressure-driven flow or electrokinetic forces. Reactants are introduced into the smaller channels (~20 µm) and are combined in the main channel (~100 to 300 µm). The stoichiometric ratio of the reactants can be controlled with the cross section and flow rate of each of the channels. In our fabricated device a series of channels which vary in width and depth from 20 µm to 70 µm are connected to a large 190µm-wide main channel (Figure 2-15).

2.4 Conclusion

A new process for creating three dimensionally varying buried microfluidic channels, named 3DBCT, is presented in this paper. This process requires only one mask leading to rapid and inexpensive fabrication. With a single etch, buried structures are created on a silicon wafer with varying depths and widths. The process allows for controlled transitions between depths as well as channels with symmetric and non-symmetric cross sections. The channels are sealed with depositing PECVD dielectric films, avoiding the need for wafer to wafer bonding. Interfaces and connections to the channels, with dimensions ranging from millimeters to nanometers, can also be created using larger windows in the lattice structure. A high level of integration is possible due to the fact that the process is CMOS compatible. Microelectronics circuitry can be

implemented alongside microfluidic structures on the same chip to realize a highly-efficient miniaturized system. Additionally the surface above the buried channels is relatively planar, allowing for further processing such as the creation of electrodes or sensors. The ceiling of the channels is transparent so objects inside the microsystem can be easily observed using optical microscopy. This new technology provides the building blocks for a complete 3D lab-on-a-chip system. Practical applications of 3DBCT may include: combinational chemistry, DNA analysis, and pharmacology. Structures appropriate for micromixing, flow cytometry, and dielectrophoresis were demonstrated.

3 Silicon Insulator-Based Dielectrophoresis Devices for Minimized Heating Effects

3.1 Introduction

Manipulation of micron scale particles is a topic of intense research with applications in isolating circulating tumor cells (CTCs), concentrating and detecting bacteria in drinking water, counting bacteria, separating live and dead cells, trapping viruses, sorting cells, trapping DNA and positioning cells within a microfluidic channel [25, 102-108]. Bulk techniques include centrifugation, antibody based sorting, magnetic tagging, and biochemical separation. While these techniques are high throughput, they fall short when high purity, low volume, non-tagged samples are required. For these applications, electric field based techniques are often used due to their favorable scalability, efficiency, high resolution, and sensitivity.

Dielectrophoresis (DEP) is a well-known electric field based technique for separating, moving, and trapping biological particles. The DEP effect is the motion of polarizable particles that are suspended in an electrolyte when subjected to a spatially nonuniform electric field [6]. Traditionally, electrode-based DEP (eDEP) devices create nonuniform fields with electrode designs including sharp electrodes and narrowly spaced electrodes [14-17]. These designs put the suspended particles in close proximity to the electrodes which can be a problem if the electrode material is not chemically inert. Alternatively, insulator-based DEP (iDEP) uses insulating structures rather than electrode arrays to produce the nonuniform fields needed to drive DEP and to remove the threat of gas evolution due to electroysis. iDEP microfluidic devices have been used to trap and sort bacteria, viruses, cells, and beads[26-29]. iDEP devices have been demonstrated on glass and polymer substrates [25, 26] using large applied electric potentials (~$1x10^3$ V) to generate eletrokinetic flow and to trap particles.

Joule heating is a known problem in both iDEP and eDEP devices limiting their use to sort biological cells or pathogens in high conductivity biological fluids such as blood. Varying temperatures within microfluidic devices can affect the viability of cell. It is known that temperature increases of more than 4 °C above the cells physiological temperature leads to cell death and even milder temperature increases have negative

physiological impacts [109]. Temperature effects have been reported to decrease the throughput and functionality of iDEP devices[110]. High electric fields and the resulting temperature gradients in microfluidic devices create changes in fluid motion, known as electrothermal (ET) flow [111-116]. It is known that significant (ET) flow can occur within eDEP and iDEP devices [110, 117]. This ET flow typically causes unwanted circulations in the devices which decrease performance [118].

The traditional substrates used for iDEP devices, such as PDMS and glass, intensify the problem due to their low thermal conductivity and thus inability to efficiently dissipate heat [119]. The thermal conductivities of PDMS and glass are (0.16 $Wm^{-1}K^{-1}$) [120] and (1.1 $Wm^{-1}K^{-1}$) [121], respectively. Silicon is a promising alternative to aforementioned materials by providing two orders of magnitudes higher thermal conductivity (149 $Wm^{-1}K^{-1}$)[122] and by enabling a higher flexibility in design, fabrication, miniaturization, and system-level integration.

The devices presented in this paper are fabricated using a single-mask three-dimensional (3D) microfabrication process that relies on reactive ion etch (RIE) lag. This technique allows for devices with either constant (2D) or variable (3D) depths to be fabricated on the same substrate. One geometric factor which is of particular importance to iDEP devices is the constriction ratio. This is the ratio of the largest cross sectional area of the channel to the smallest cross sectional area. Utilizing high constriction ratios, 3D iDEP devices can operate at low voltages compared to 2D designs[92, 123]. Low voltage operation decreases the Joule heating within the channel leading to lower operating temperatures. Thus, the 3D fabrication allows for iDEP devices to operate with lower applied voltages and at lower temperatures than 2D designs.

This paper presents the first reported high-performance iDEP particle trapping microchips implemented on a silicon substrate. The DEP trapping and separating experiments were performed to demonstrate device functionality. Using temperature measurements and numerical modeling, the thermal performance of silicon and PDMS devices are evaluated. Additionally, the value of the RIE lag based fabrication process is demonstrated by comparing the thermal and electrical performance of a low constriction ratio, 2D device and a high constriction ratio, 3D device.

3.2 Materials and Methods

3.2.1 Silicon Device Fabrication

The fabrication process (Figure 3-1) starts by depositing 4000 Å of silicon dioxide on a <100> silicon wafer. This oxide acts both as a masking layer during the etch process and as a structural support during channel sealing. The oxide layer is deposited by plasma enhanced chemical vapor deposition (PECVD) at 300 ºC. For this work, oxide deposition was performed in a Trion Orion II PECVD machine and silicon etching was performed in an Alcatel AMS-100 Deep Reactive Ion Etcher (DRIE). We utilize RIE lag and our previously published models [73, 124] to smoothly and arbitrarily vary the depth of the microfluidic channel in a single-etch-step process by

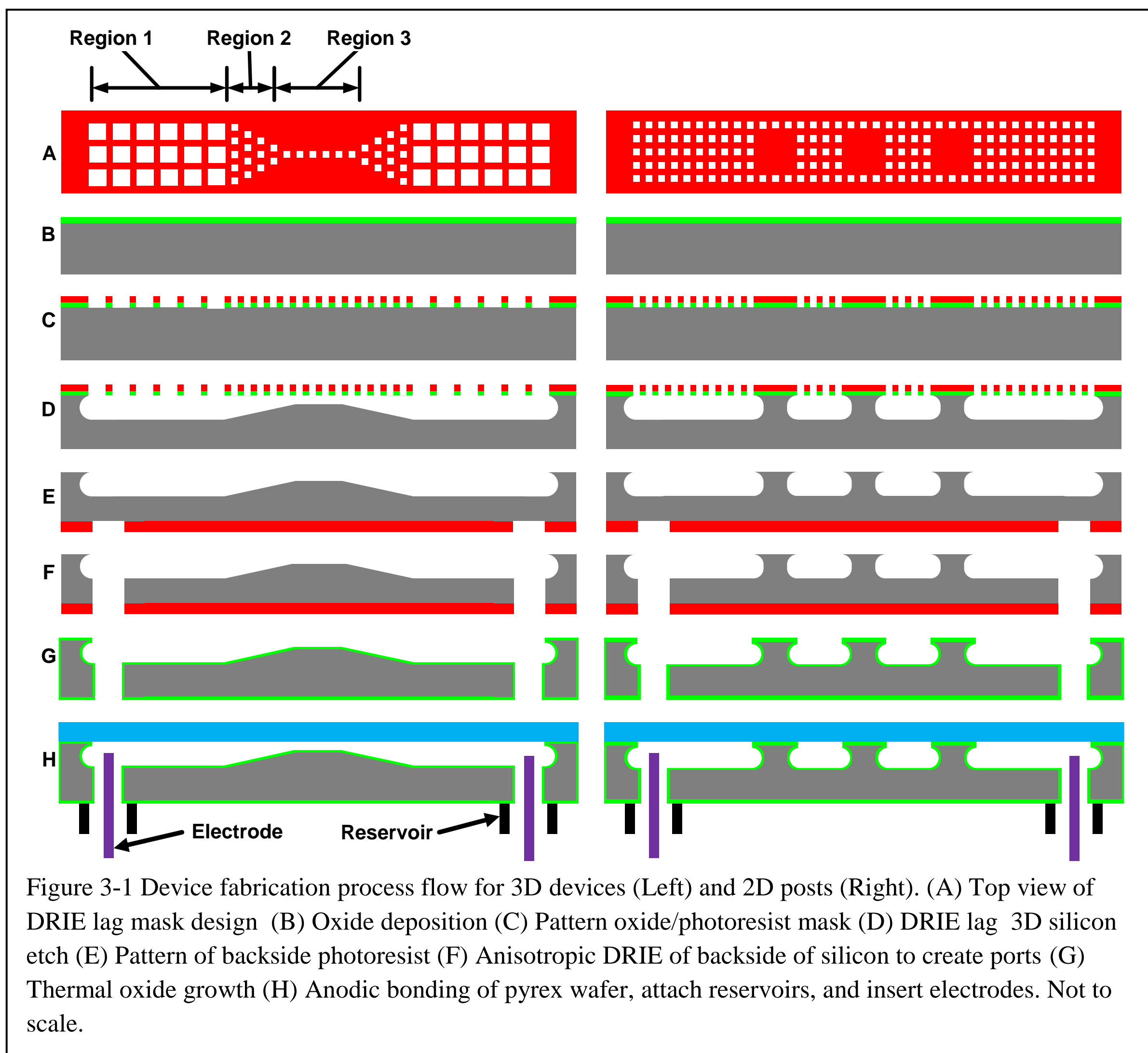

Figure 3-1 Device fabrication process flow for 3D devices (Left) and 2D posts (Right). (A) Top view of DRIE lag mask design (B) Oxide deposition (C) Pattern oxide/photoresist mask (D) DRIE lag 3D silicon etch (E) Pattern of backside photoresist (F) Anisotropic DRIE of backside of silicon to create ports (G) Thermal oxide growth (H) Anodic bonding of pyrex wafer, attach reservoirs, and insert electrodes. Not to scale.

changing the geometrical pattern on the mask layout. Different microchannel geometries can be fabricated on a single wafer using this technique, two of which are used in this work. The oxide layer is then patterned using RIE with a photomask containing square windows. In order to enhance the RIE lag during the etching process, the mask is divided into a large number of micron-scale, square window openings. In general, window patterns which expose a large amount of local surface area, etch faster than those which expose a smaller amount of local surface area. Additionally, as the number of rows of windows increases along the width the microchannel, the etch rate increases. Our 3D iDEP devices are composed of 3 regions of window patterns (see Figure 3-1). Region 1 is designed to be 90 µm deep and Region 3 is designed to be 30 µm deep. Region 2 provides a transition area between the two depths. Using this fabrication technique, channels can be obtained which vary in depth from 20 µm to 120 µm. However, as the difference between the shallowest and deepest part of the channels increases, the surface roughness of the shallowest channel increase. In order to keep the surface roughness below 0.2 µm, the channel depths for this device were designed to be 30 µm and 90 µm.

After oxide patterning, the substrate is isotropically etched using DRIE SF_6 plasma to create 3D channels. The highly selective process etches silicon while leaving the oxide masking layer suspended above the channels. The photoresist is then stripped with oxygen plasma. The oxide mask is removed with wet etch of 10:1 buffered oxide etchant (BOE) in water. The backside of the substrate is patterned and etched anisotropically using a Bosch process DRIE etch to form fluidic ports. Next, an electrical passivation layer of oxide is grown in the channels. 8000 Å silicon dioxide is grown during a wet thermal oxidation at 1000 ºC. To seal the device, a Pyrex wafer is anodically bonded to silicon. It should be noted that device operation improved with thicker passivation layers. However, the maximum oxide layer that we were able to reliably anodically bond through was 8000 Å. Fluid reservoirs are attached via epoxy to the ports into which electrodes are inserted.

Two different silicon devices were created. Device A consists of a single channel constriction in both width and depth (Figure 3-2a). The depth changes in the device from 90 µm in the main channel to 30 µm in the constriction. The width changes in both channels from 1200 µm to 70 µm. Device B is a silicon replica of a 90 µm deep

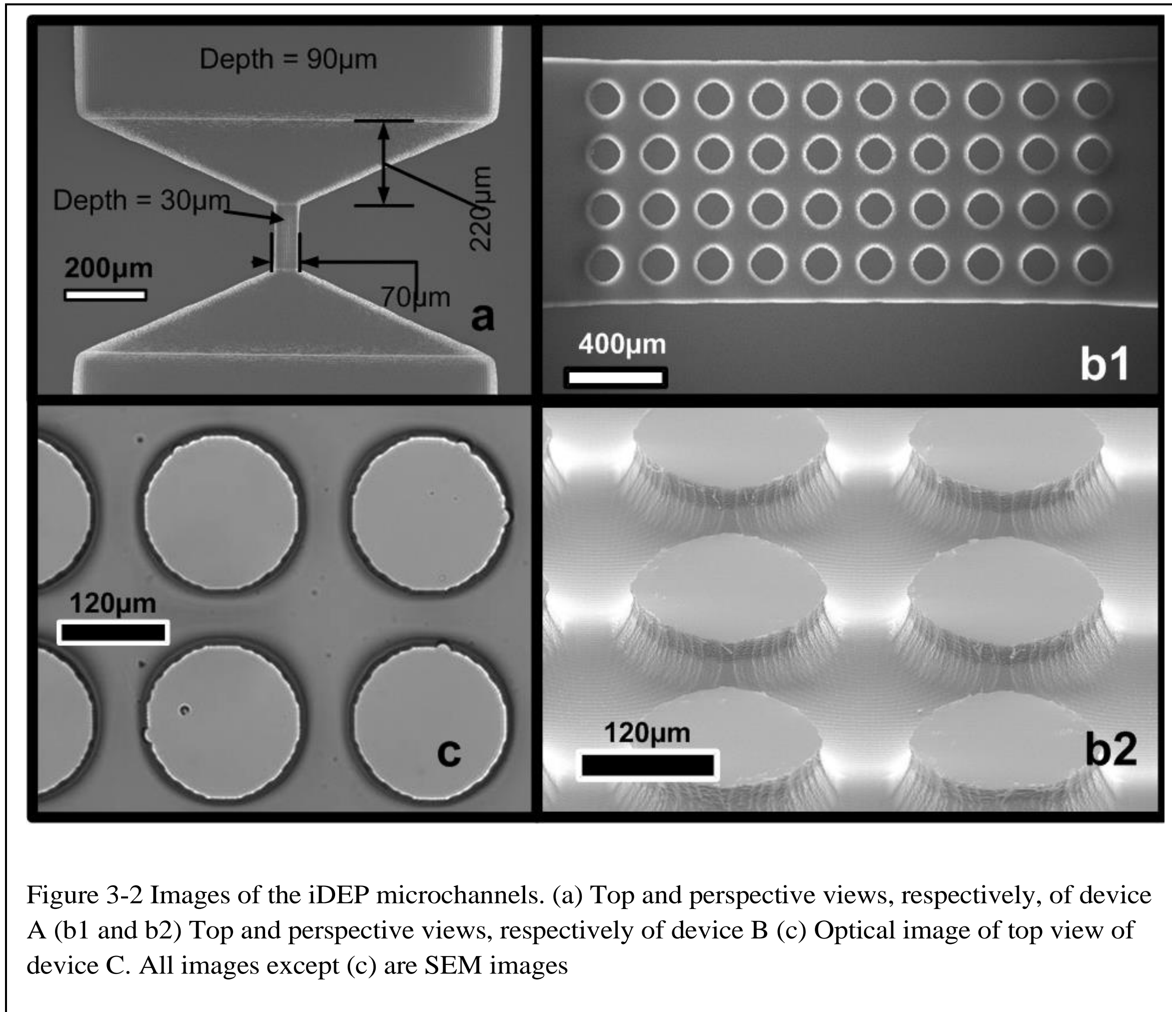

Figure 3-2 Images of the iDEP microchannels. (a) Top and perspective views, respectively, of device A (b1 and b2) Top and perspective views, respectively of device B (c) Optical image of top view of device C. All images except (c) are SEM images

PDMS micropost design (Figure 3-2b). The microposts are 170 μm in diameter and spaced 70 μm. The spacing of the fluidic ports was 1 cm to allow for comparison with previously published devices.

3.2.2 PDMS Device fabrication

PDMS devices were created as a control group for thermal experiments according to the fabrication process in [125]. A <100> silicon wafer was patterned with photoresist and etched using DRIE to obtain 90 μm-deep structures. Photoresist was stripped and the wafer was then used as a master mold for PMDS. Liquid PDMS (Sylgand 184 Silicon elastomer kit, Dow Corning, Midland, MI) was mixed to a 10:1 ratio of PDMS monomer and curing agent and poured onto the silicon mold. The setup was put into a vacuum chamber for 2 hours to remove gas bubbles and then cured for

45 min at 100 ºC. Next, 2 mm holes were punched into microchannels for fluidic ports. Finally, the PDMS was plasma bonded to a 500 µm Pyrex wafer. The PDMS devices are designated as device C (Figure 3-2c). As with the silicon micropost design, PDMS microposts are 170 µm in diameter and spaced 70 µm.

3.2.3 iDEP Experiments

Flourescent microspheres of 1 and 2 µm diameters (Flourospheres, Invitrogen, Carlsbad, CA) were used to demonstrate trapping. No surface modifications were made to the beads. The microspheres were suspended into a solution of diluted Phosphate Buffered Saline (PBS) in DI water. PBS solution (BP399-500, Fischer Scientific, Pittsburg, PA) was added to DI water until the desired conductivity of $2.00x10^{-2}$ S/m was reached. The solution was measured with a solution conductivity meter (SG7, Mettler Toledo, Scherzenbach, Switzerland) and the final solution was 1.2% PBS by volume. iDEP experiments were observed using an inverted microscope (Axio Observer Z1, Carl Ziess Inc., Oberkochen, Germany) and videos and image were acquired using the a CCD color camera (Axiocam MrC, Carl Ziess Inc., Oberkochen, Germany). A high voltage sequencer (HVS448, Labsmith, Livermore, CA) was used to apply electric potentials. Gravity-based pressure driven flow was discouraged by balancing the fluid levels in the reservoirs; however, noticeable backpressure was observed when the voltage was removed immediately following each experiment. This was due to the fluid flow during the experiment filling the downstream reservoir.

The electroosmotic mobility was measured using the current monitoring method [126]. Briefly the channels were filled with a 0.5% PBS solution. A 1% PBS solution was introduced into one reservoir and an applied potential was used to move the higher concentration solution through the channel. The time dependence of the current was measured at applied voltages from 50 V to 300 V in both the silicon and PDMS micropost channels. The time at which the current saturated was used to estimate the electroosmotic mobilities. Using this method, the electroosmotic motilities were determined for PDMS and silicon substrates to be $2.5x10^{-8}$ $m^2/(V\ s)$ and $4.3x10^{-8}$ $m^2/(V\ s)$, respectfully. The values are of the same order of magnitude and are close to those previously reported electroosmotic mobilities of electrolyte solutions in PDMS

and silica [127].

The two performance metrics, trapping efficiency (TE) and selective concentration efficiency (SCE), are defined as:

$$TE = [(T-E)/T] \times (100\%) \quad (3\text{-}1)$$

$$SCE = [(TT - UT)/TT] \times (100\%) \quad (3\text{-}2)$$

where T is the total number of particles passing through the channel, E is the number of particles that escape the trapping region of the device, TT is the total number of trapped particles, and UT is the number of unwanted trapped particles. TE indicates how many particles are trapped under given conditions whereas SCE is a measure of how well the targeted particles were concentrated. These measurements were made by counting beads in the individual frames of videos taken during the experiments. The number of particles trapped in the trapping region was determined by counting the particles going into the constriction and coming out of the constriction. The number of particles in the constriction was obtained by taking the difference of the incoming and outgoing beads. For cases where beads remained in clusters after being released, the clusters were assumed to be flat and the size of the cluster was used to estimate the number of beads in the cluster. It should be noted that if clusters had multiple beads stacked in depth then this method would underestimate the number of beads.

3.2.4 Temperature Measurements

Temperature measurements inside the iDEP devices were performed using the rhodamin B method [128-131]. Laser grade RhB (Acros Organics, Geel, Belgium) was dissolved in different conductivities of water. The dye was excited though a filter (λ~542nm) on the inverted fluorescent microscope and images were recorded with a CCD monochrome camera (Axiocam MrM, Carl Ziess Inc., Oberkochen, Germany). Electric potentials were applied with a Labsmith voltage sequencer. Measurements

were carried out under temperature-controlled conditions in an environmental chamber (Incubator XL S, Pecon GmbH, Erbach, Germany) attached to the microscope. In addition to the temperature probe monitoring the air temperature in the chamber, a type T thermocouple (COCO-001, Omega Engineering, Stamford, CT) was brought into good thermal contact with the iDEP devices with thermally conductive grease (Thermally Conductive Grease 2033, 3M, St. Paul, MN). Temperature calibrations were performed before and after testing each device. Measurements were taken after both of the temperature probes stabilized and agreed within 0.5ºC, which typically took 30min. During measurements for all devices, a small fan inside the chamber blew air on the device to increase convection. Fluorescent images were taken with an exposure time of 10ms at each temperature. The environmental chamber was set to temperatures between 20 ºC - 40 ºC and reference images were taken. Then temperature measurements were performed by applying a voltage for 30 seconds. The ambient temperature in the environmental chamber was set to 22 ºC. For the PDMS devices, the channels were exposed to light for 20 minutes prior to both calibration and experimental measurements according to [132] in order to photobleach any rhodamine B absorbed in the PDMS. New solution was added after each measurement to avoid photobleaching in the solution. Image analysis was performed with ImageJ (National Institute of Health).

3.3 Theory

3.3.1 DEP

Dielectrophoresis is the motion of polarizable particles that are suspended in a dielectrically dissimilar media when subjected to a spatially nonuniform electric field [6]. The time average DEP force felt by a spherical particle suspended in a medium is:

$$\mathbf{F}_{DEP} = 2\pi R^3 \varepsilon_m \mathrm{Re}[f_{CM}] \nabla |\mathbf{E}_{RMS}|^2 \tag{3-3}$$

where R is the radius of the particle, ε_m is the permittivity of the medium, $\mathbf{E}_{RMS}$ is the local electric field. $\mathrm{Re}[f_{CM}]$ is the real part of the Clausius-Mossotti factor which is:

$$f_{CM} = (\varepsilon_p^* - \varepsilon_m^*)/(\varepsilon_p^* + 2\varepsilon_m^*) \quad (3\text{-}4)$$

where ε_p^* and ε_m^* are the complex permittivities of the particle and the medium, respectively. Complex permittivity is defined as:

$$\varepsilon^* = \varepsilon + \sigma/(j\omega) \quad (3\text{-}5)$$

where ε and σ are the real permittivity and conductivity, j =sqrt(-1) and ω is the angular frequency of the applied potential signal. In our iDEP experiments, since the applied potential is DC, the complex permittivity becomes the low frequency limit of this equation which is simply the conductivity. Thus, the Clausius-Mossotti factor for DC is:

$$f_{CM} = (\sigma_p - \sigma_m)/(\sigma_p + 2\sigma_m) \quad (3\text{-}6)$$

For the DC case, differences in particle conductivity and size result in different DEP force magnitudes. This allows for selectivity among particles. Also, the permittivity and conductivity of the medium affects the DEP force. In our iDEP experiments, the particles are polystyrene beads with very low conductivities ($\sim 10^{-16}$ S/m) and the media is DI water ($\sim 10^{-3}$ S/m) or a mixture of DI and PBS ($\sim 10^{-2}$ S/m). Since the media conductivities are higher than the particle conductivity, the DEP force is negative, thereby motivating the particles away from high gradients in the electric field within the channels.

Fluid flow in our devices is generated by electroosmotic (EO) flow. Additionally, particles experience electrophoresis which creates motion of the particle with respect to the fluid. For a particle to become trapped in these devices, the DEP force must be larger than all the other forces acting on the particle. Mathematically, this is [26, 31]:

$$(\mathbf{u}_{DEP} \bullet \mathbf{u}_{EK})/(\mathbf{u}_{EK} \bullet \mathbf{u}_{EK}) = ((\mu_{DEP})/(\mu_{EK}))\,((\nabla\,(\mathbf{E}\bullet\mathbf{E}))/(\mathbf{E}\bullet\mathbf{E})) \bullet E > 1 \qquad (7)$$

where $\mathbf{u}_{DEP} = \mu_{DEP}\nabla(\mathbf{E}\bullet\mathbf{E})$ and μ_{DEP} are the DEP velocity and mobility of the particle, respectively. The electrokinetic (EK) effects of electroosmosis and electrophoresis have been combined into a single term for simplicity. Thus, $\mathbf{u}_{EK}=(\mu_{EO} - \mu_{EP})\mathbf{E}$ and $\mu_{EK}=\mu_{EO} - \mu_{EP}$ are the EK velocity and mobility of the particle, respectively. From this, we can see that as the electric field strength increases, the DEP force increases as the gradient of the square of the electric field while EK motion increases linearly with the field. Thus, for low electric fields, EK motion dominates but if the voltage is increased, DEP will gradually become more dominant and the particle will be trapped.

3.3.2 Fluid Flow

The steady state flow of the fluid is given by the Navier-Stokes equation and the continuity equation:

$$\rho\mathbf{u} \bullet \nabla\mathbf{u} = -\nabla\mathbf{p}+\nabla\bullet(\eta\nabla\mathbf{u})+\mathbf{F_E} \qquad (3\text{-}8)$$

$$\nabla\bullet\mathbf{u} = 0 \qquad (3\text{-}9)$$

where u is the local velocity of the fluid, p is the pressure, η is the dynamic viscosity of the fluid, and $\mathbf{F_E}$ is the time-averaged electrical body force. The electric body force is given as [133]:

$$\mathbf{F_E} = 0.5\,\mathrm{Re}(((\sigma\nabla\varepsilon - \varepsilon\,\nabla\sigma)/(\sigma + j\omega\varepsilon)\bullet\mathbf{E})\mathbf{E}^*) - 0.25\,\mathbf{E}\bullet\mathbf{E}^*\nabla\varepsilon \qquad (3\text{-}10)$$

where E and E* are the local electric field and the complex conjugate of the local electric field, respectfully. Gradients in temperature are known to cause variations in ε and σ. For electrolyte solutions in water it is known that $(1/\sigma)(\delta\sigma/\delta T) \cong 0.02\ K^{-1}$ and $(1/\varepsilon)(\delta\varepsilon/\delta T) \cong -0.004\ K^{-1}$ [133]. Thus, at DC, this equation becomes:

$$F_E = -0.5(((0.016\ K^{-1})\nabla T \bullet \mathbf{E})\ \varepsilon\mathbf{E}) + 0.5|\mathbf{E}|^2(-0.004\ K^{-1})\ \nabla T) \quad (3\text{-}11)$$

3.3.3 Heat Transfer

Joule heating is the transfer of energy from electrical to thermal domains when an electric potential is applied across a substance with a finite conductivity. The rate at which heat is produced in the channel is given by the Joule heating equation:

$$Q = \sigma|\mathbf{E}|^2 \quad (3\text{-}12)$$

where Q is the generated heat per volume (W/m^3). In our devices, this is assumed to be the only source of heating. The steady state time-averaged temperature field, T, in the fluid is governed by the following energy equation[118] :

$$\rho C_p(u \bullet \nabla T) = \nabla \bullet (k\nabla T) + \sigma\ \mathbf{E}^2 \quad (3\text{-}13)$$

where C_p is the specific heat capacity of the fluid. The ratio of axial convection to conduction within the channel is given by the thermal Peclet number:

$$Pe_L = (L\mathbf{u}\rho C_p)/k \quad (3\text{-}14)$$

where L is the characteristic length, u is the fluid velocity, ρ is the fluid density and k is the thermal conductivity. The thermal Peclet number for these experiments ranges from 10^{-1} to over 1, thus the convective heat transfer term in equation (3-12) in the fluid must be considered.

3.3.4 Numerical Modeling

In order to obtain local values of temperature and electric field within the

channels, a numerical model of the microdevices was created using COMSOL Multiphysics (COMSOL Inc., Burlington, MA). The Incompressible Navier-Stokes Module was used for fluid flow. The fluid was assumed to have the density and dynamic viscosity of water ($1.0x10^3$ kg/m^3 and 1.0 $x10^3$ (Pa s) [121]. It was assumed that there is no pressure difference between the inlet and outlet, P_{outlet} -P_{inlet}=0. The walls of the channels were assumed to provide electroosmotic flow with a μ_{EO} of $4.3x10^{-8}$ m^2/(V s) for glass and silicon dioxide walls and $2.5x10^{-8}$ m^2/(V s) for PDMS walls. In order to estimate the effect of electrothermal flow, simulations were performed with and without the electric body force.

The Conductive Media DC module was used to simulate electric fields in the devices. The fluid was assumed to have a conductivity of 0.02 S/m and a permittivity of $7.1x10^{-10}$ [121] at T_0. The channel wall and microposts were assumed to be insulating. The inlet and outlet of the channel were assumed to be at applied potentials of V_{app} and 0, respectively.

The General Heat Transfer module was used to simulate heat transfer in the devices. All of the walls were assumed to be insulating except for the upper glass substrate and the lower silicon/PDMS substrate. Since the fluid reservoirs are large compared to the fluid in the channel, fluid entering the channel is assumed to be at ambient temperature. Thus the inlet was set to a constant temperature of 295.15 K. The outlet was assumed to be insulating as it is far from the constrictions and thermal convection is strong when far away from the constriction. The upper glass wall and lower silicon/PDMS substrates were assumed to have an outward heat flux due to conduction q^{II} =-h(T-T_0), where h is the assumed heat transfer coefficient and T_0 is the ambient temperature. The magnitude of h was determined by using a parametric sweep to iterate the model until the outlet temperature in the model matched the experimental temperature measurements. For silicon devices the value of h was found to be 600 W/(m^2 K) and for PDMS devices the value was found to be 150 W/(m^2 K). For consistency, the value of H was determined for PDMS and silicon substrates using the micropost designs and remained constant for all of the designs of the same substrate. The thermal conductivity and heat capacity of the fluid were assumed to be $6.0x10^{-1}$ W/(m K) and $4.186x10^3$ J/(kg K) [121]. Joule heating was assumed to be the source of heating within the channel.

3.4 Results

3.4.1 Trapping

Selective trapping of 1 and 2 μm beads was performed in the 20.0 mS/m solution (Figure 3-3) in the iDEP devices. This conductivity was used to mimic several

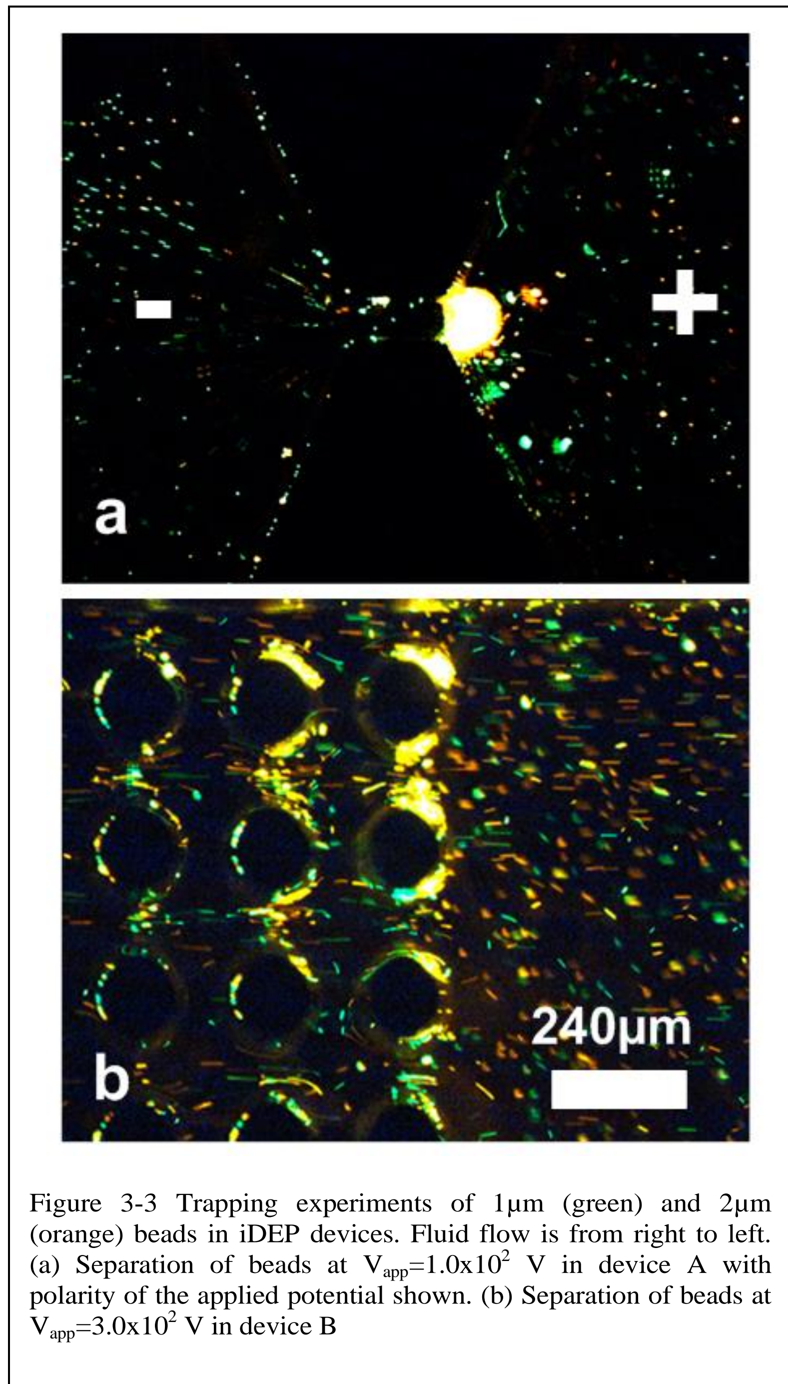

Figure 3-3 Trapping experiments of 1μm (green) and 2μm (orange) beads in iDEP devices. Fluid flow is from right to left. (a) Separation of beads at V_{app}=1.0x10^2 V in device A with polarity of the applied potential shown. (b) Separation of beads at V_{app}=3.0x10^2 V in device B

isotonic solutions with high cell viabilities used in microfluidic devices [60, 117, 134]. The devices are primed and particles are flowed into the microchannel. A voltage is then applied across the reservoirs and EO flow moves the particles. The DEP force traps the particles in the constriction region. When the voltage is removed, the particles are no longer trapped and the slight pressure difference between the reservoirs moves the released particles in a laminar fashion. The 2 µm particles require a lower electric field gradient in order to be trapped than the 1 µm and thus are concentrated during operation of the device. The smaller radius of 1 µm particles results in a lower DEP force felt by the particle for a given electric field gradient. It should be noted that no fluid circulations were observed in the channels. This indicates a lack of strong electrothermal effects under these operating conditions.

The trapping efficiencies of 2 µm of the iDEP devices are shown in Figure 3-4a. For all applied voltages the PDMS micropost (device C) design slightly outperformed

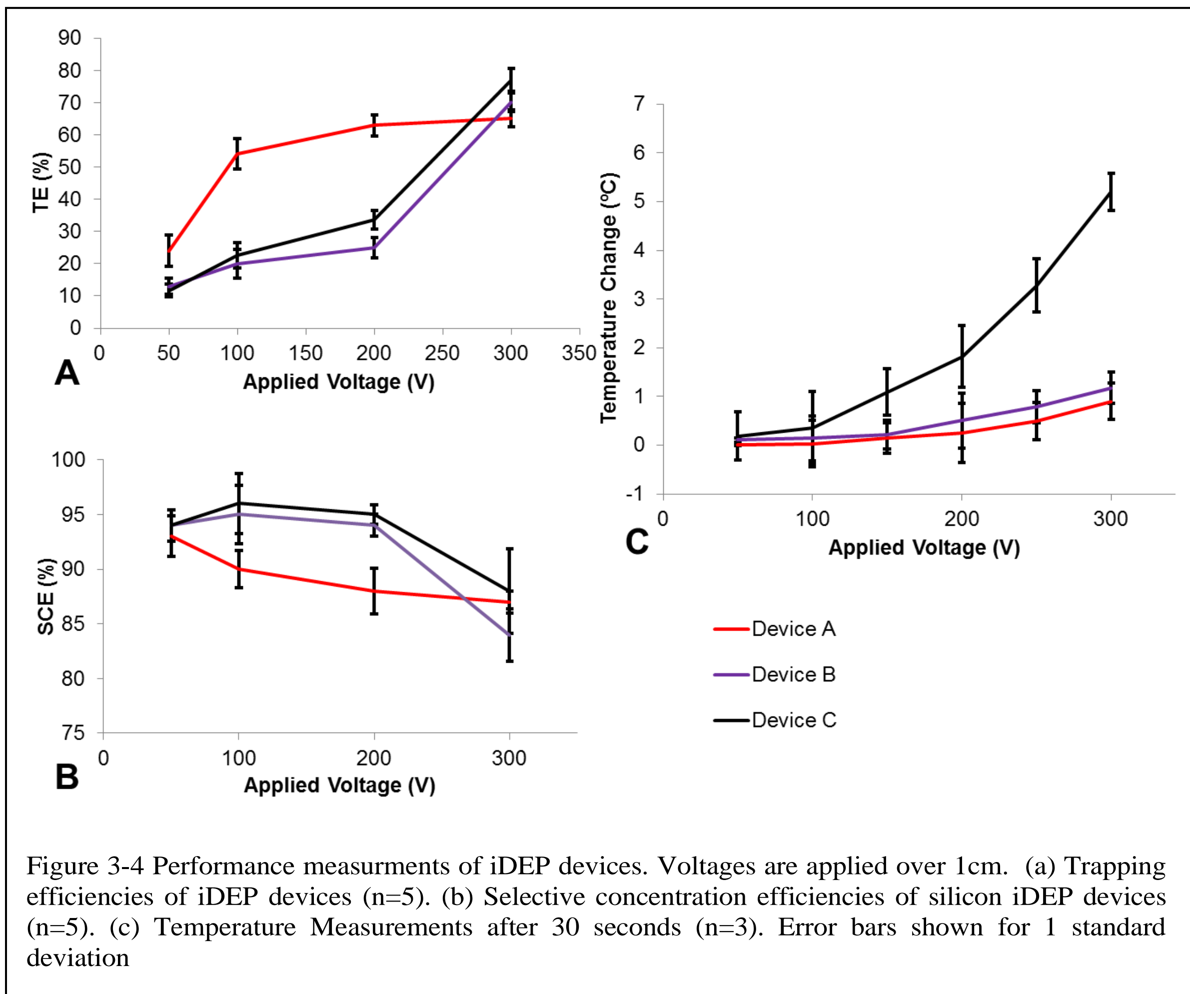

Figure 3-4 Performance measurments of iDEP devices. Voltages are applied over 1cm. (a) Trapping efficiencies of iDEP devices (n=5). (b) Selective concentration efficiencies of silicon iDEP devices (n=5). (c) Temperature Measurements after 30 seconds (n=3). Error bars shown for 1 standard deviation

the silicon micropost (device B) design in trapping efficiency. This is due to the increased electroosmotic mobility of the silicon substrate. The 3D silicon device (device A) was able to obtain trapping efficiencies over 50% at 100V while the silicon and PDMS micropost designs attained trapping efficiencies over 50% at 300 V. Thus the microposts designs required a higher applied potential to match the 3D design in trapping efficiency.

The selective concentration efficiencies of the iDEP devices are shown in Figure 4b. The figure shows that the PDMS and silicon micropost designs performed similarly with the PDMS device attaining about 5% better SCE at the trapping voltage of 300 V. While the micropost design has better numerical values than the silicon devices at low voltages, the micropost design was trapping very few particles at those voltages as shown by the TE performance. For both TE and SCE, the 3D design had comparable performance at 100 V to the micropost performance at 300 V. In fact, when 50 V was applied to device A, the SCE increased and the TE decreased dramatically just as when 200 V was applied to devices B and C.

3.4.2 Thermal Measurements

We used the temperature dependent fluorescent property of rhodamine B dye to determine the temperature inside our iDEP devices. Calibration curves were obtained for temperatures ranging from 20.0 °C to 40.0 °C. For most rhodamine B based temperature measurements, a single fluorescent intensity/temperature curve was used to interpret the results. For our devices, this is not sufficient as the intensity varies over the length and width of the channels.

To account for the nonuniform intensity plots, fluorescent intensity/temperature curves were obtained for each point along the intensity curve. The curves were fit to a decaying exponential with decay constants ranging from -0.9 %/°C to -1.5 %/°C which agrees well with previous rhodamine B experiments [128-131]. These curves were then used to interpret the intensity profiles under experimental conditions. The voltage was applied to the reservoirs of the microchannels for 30 seconds and fluorescent images were taken from the device. In order to compare the performance of all of the devices, the temperature readings at the outlet of the microchannels were averaged over the

width of the device. These measurements were taken for all the devices over a range of voltages from 50 V – 300 V as shown in Figure 4c. The results show that silicon devices are significantly better at dissipating the heat generated within the microchannels.

3.4.3 Numerical Modeling

The results from the numerical model are displayed in Table 3-1. In order to estimate the magnitude of the electrothermal flow in the channel, the velocity profiles of the channels were compared with and without the electric body force term. The results showed the maximum change in the velocity field to be below 1%. This indicates that the electrothermal flow effects are not significant for these conditions, which is consistent with the experimental observations.

	V_{app} [V]	E_{app} [V/m]	E_{max} [V/m]	$\nabla\|\mathbf{E}\|^2$ [$kg^2\ m\ C^{-2}\ S^{-4}$]	T_{out} [K]	T_{max} [K]
Device A						
	1.00E+02	1.00E+04	1.54E+05	3.52E+14	295.26	295.38
	2.00E+02	2.00E+04	3.09E+05	1.41E+15	295.60	296.06
	3.00E+02	3.00E+04	4.63E+05	3.17E+15	296.15	297.19
Device B						
	1.00E+02	1.00E+04	1.96E+04	4.82E+12	295.30	295.31
	2.00E+02	2.00E+04	3.91E+04	1.93E+13	295.77	295.79
	3.00E+02	3.00E+04	6.00E+04	4.45E+13	296.54	296.58
Device C						
	1.00E+02	1.00E+04	1.96E+04	4.82E+12	295.81	295.82
	2.00E+02	2.00E+04	3.91E+04	1.93E+13	297.77	297.83
	3.00E+02	3.00E+04	6.00E+04	4.45E+13	301.04	301.15

Table 3-1 Simulation results for microchannels fabricated in both silicon and PDMS

All devices were given applied electric potentials (V_{app}) and that matched the experimental conditions. The applied electric fields (E_{app}), which are the applied electric potentials divided by the electrode spacing (1cm) are shown for comparison with literature. For the same applied potential, device A reached local electric fields which were an order of magnitude higher than the fields generated by devices B and C. The constriction ratio is the ratio of the largest cross sectional area of the channel to the smallest cross sectional area. Devices B and C have a constriction ratio of 3:1 while device A (3D silicon chip) has a constriction ratio of 51:1. The higher constriction ratio

of device A increases the local electric field within the constriction region.

The DEP force generated by each of the devices was compared. Given identical particles and suspending media and operating frequency, the magnitude of the DEP force depends only on $\nabla|E|^2$. Thus devices were compared according to the minimum $\nabla|E|^2$ that a particle would experience as it is moved through the channel. This gradient is non-uniform near the constriction region of the devices. In this area, the gradient is very large near the walls of the microchannel and is the minimum on the line that is furthest from any walls that have changing dimensions. Larger constriction ratios benefit both from increasing total change in electric field as well as minimizing the distance that a particle can be from the insulating walls. The minimum $\nabla|E|^2$ was found on the centerline of devices B and C and along the line that was centered about the width of the channel and against the glass substrate in device A. For all applied potentials, the minimum DEP force was found to be roughly 2 orders of magnitude larger in the device A than that in devices B and C. This allows device A to trap at a lower applied electric potential.

The maximum temperature within the channels was compared. Despite devices B and C being identical in geometry, the silicon device produced less heating than its PDMS counterpart with a lower outlet temperature (Tout) and lower maximum temperature (Tmax). This was due to the increased thermal conductivity of the silicon substrate. The temperature profiles of the micropost designs were fairly uniform throughout the channels whereas device A showed the largest temperature gradient. Since the maximum electric field within device A is higher than that of devices B and C, more Joule heating occurs within a smaller space. This explains why the experimentally measured temperature of the outlet of device A was lower than that of device B at an applied potential of $3.0x10^4$ V/m, but the maximum temperature in device A was higher. However, it should be noted that the maximum temperature of device A at its operating electric potential of $1.0x10^2$ V is still lower than the maximum temperature of devices B and C at their operating electric potentials of $3.0x10^2$ V. Section 3.7 includes extra results from the numerical models showing the time dependent temperatures in the devices during operations. These results further demonstrate the thermal advantage of Devices A and B over device C as well as the

thermal advantage of Device A over Device B. Thus, the high constriction ratio 3D device decreases the temperature that the fluid reaches at the required applied electric potential while producing a larger temperature gradient within the channel. The increased temperature gradients may lead to unwanted electrothermal flows at very high voltages and media conductivities.

3.5 Discussion

In this paper, we have (1) presented the first reported silicon iDEP particle trapping microchips, (2) demonstrated that silicon devices operated at lower temperatures than identical polymer devices, (3) demonstrated that high constriction ratio 3D devices operated at low voltages compared to the traditional micropost design, and (4) performed temperature measurements and numerical modeling comparing the silicon and PDMS designs.

The silicon devices benefit from a high substrate thermal conductivity. This allows the substrate to act as a heat sink for the channels. When identical devices are fabricated in PDMS and silicon, the silicon devices operate at a lower temperature. Our temperature measurements have shown that even under low voltages (~300 V) and with a low conductivity media (~20.0 mS/m) greater than 5 °C increases in less than 30 seconds occur in PDMS-based iDEP devices. By contrast, the thermal conductivity of silicon is two and three orders of magnitude higher than that of glass and PDMS, respectively. As our results reveal, this allows for greater heat dissipation and subsequently decreases the parasitic effects arising from Joule heating. Sabounchi et al. have reported that Joule heating within iDEP devices can limit their throughput and even cause the devices to fail to trap [110].

Electrothermal (ET) flow is related to the temperature gradients within the channel. Thus, low constriction ratio designs are desirable if ET flow is to be minimized as these devices produce lower temperature gradients. However, as particles become trapped in an iDEP device, the effective constriction ratio increases as the particles are insulating. The increased thermal conductivity of the silicon devices can dissipate this heat more effectively, leading to lower operating temperatures and lower

temperature gradients. Sridharan et al. [118] experimentally demonstrated the generation of ET flow by Joule heating within iDEP devices. ET flow can diminish the device performance as it moves particles away from the trapping region and circulates them around the constriction. As the temperature gradients decrease, these undesirable effects are suppressed and become negligible. The high constriction ratio 3D device has a larger temperature gradient and is more prone to electrothermal fluid flows although this becomes noticeable at very large operating voltages. For both low and high constriction ratios, using silicon as the substrate decreases the temperature gradient and its corresponding adverse effects.

The 3D silicon device generated larger DEP forces at lower applied electric potentials. This allowed the 3D silicon chip to obtain the trapping performance of the micropost design at a lower applied electric potential, thereby requiring simpler and cheaper electronics. Many iDEP trapping devices, especially micropost designs, require applied electric potentials on the order of 10^3 V [26, 27]. Our devices provide trapping with an applied potential on the order of 10^2 V. Chen et al. [28] demonstrated a device capable of 100% trapping efficiency of 1μm particles at $4.0x10^2$ V; however, no separation was performed. Recently, Braff et al. used 3D polymeric devices for iDEP and demonstrated that the 3D structures helped to lower the applied voltage of the devices for operation[123]. Using high constriction ratio 3D devices, 10μm beads were trapped with an applied electric potential of 10 V while 1 μm particles such as *E.coli* were trapped at 50 V. Thus, our trapping voltages are among the lowest reported values. The reason for the increased performance at lower voltages in the 3D silicon chip is the high constriction ratio of the device which is achieved by varying the width and depth of the microchannel. The tradeoff is that a high constriction ratio yields a higher local electric field within the constriction region. It is also worth mentioning that errors may be introduced in the performance of the silicon devices due to the surface roughness of the microchannels that is characteristic of our 3D fabrication process [73, 124]. This surface roughness may create unwanted local electric field distributions and cause the devices to underperform. If smoothing techniques, such as repeated thermal oxidation and removal steps, are used, the operating voltage of the 3D silicon may decrease.

The silicon substrate is passivated with a thin layer of silicon dioxide. The oxide

comes into contact with the fluid and determines the electroosmotic mobility. Silicon dioxide has been known to have the same electroosmotic mobility as fused silica [135]. In our experiments, the oxide layer led to a higher electroosmotic mobility in the silicon devices than in the PDMS devices. This resulted in higher fluid velocities at identical applied electric potentials and ultimately, reduced the trapping performance compared to the identical PDMS design. This problem may be addressed by adding a surface coating to the silicon substrate to reduce the electroosmotic mobility.

In summary, PDMS iDEP devices benefit from simple and inexpensive fabrication. However, while the complexity of fabrication is increased in silicon devices, they will operate at lower temperatures and have lower thermal gradients than PDMS devices which are identical in geometry. For applications which require high conductivity solutions, silicon should be used to minimize joule heating. The decrease in the temperature gradients will lead to lower ET flow and more predictable device behavior. Additionally, temperatures increases within iDEP devices would limit their ability to maintain viability of larger, more vulnerable cell types. It is known that temperature increases of more than 4 °C above the cells physiological temperature leads to cell death and even milder temperature increases have negative physiological impacts [109]. Thus, silicon devices may be employed to increase cell viability. Using silicon fabrication techniques, high constriction ratios 3D devices can be implemented. This allows the applied potential to be effectively lowered, which reduces the cost and complexity of the supporting electronics. Additionally, the operating temperature of the 3D design is lowered. However, it produces higher electric fields, which can be damaging to some biological cells depending on the magnitude of the field required for trapping them.

In our future work, we plan to exploring silicon iDEP devices for high throughput, high viability mammalian cell trapping. In addition, peltier cooling units may be tested on the silicon devices rather than just convective cooling to achieve low heating at higher media conductivities. Finally, 3D silicon continuous flow devices will be investigated to further reduce the applied voltages.

3.6 Conclusion

High-performance microfluidic iDEP microchips, implemented on silicon, have been demonstrated to selectively trap polystyrene particles. Due to the high thermal conductivity of the silicon substrate, the silicon devices dissipate heat significantly better than identical PDMS devices. This was demonstrated with thermal measurements and numerical modeling. Additionally, silicon substrates allow for supporting electronics and MEMS devices to be fabricated on the same microchip, creating highly miniaturized systems. Using a single-mask three dimensional (3D) microfabrication process, high constriction ratio, 3D devices and low constriction ratio, 2D devices can be fabricated simultaneously. The 3D device was shown to operate at low applied voltages and temperatures. The 2D device operated at higher voltages and temperatures but had a more uniform temperature distribution and operated at lower local electric fields than the 3D device. Thus, both the substrate material and device geometry can be used to minimize heating effects in iDEP devices. These significant results demonstrate the promise of 2D and 3D silicon iDEP devices, leading to high performance trapping/sorting/concentration microsystems that have a wide range of applications.

3.7 Extra Numerical Results

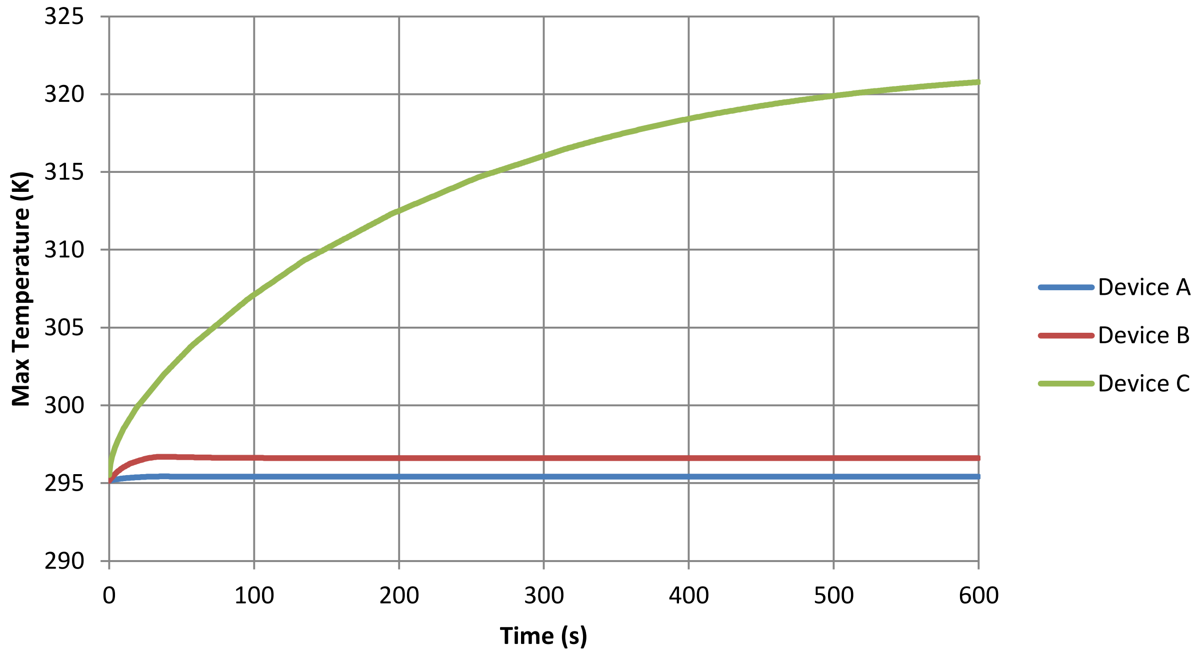

Figure 3-5 Simulation results for microchannels fabricated in both silicon and PDMS. Plot shows the maximum temperature in the microchannel as a function of time. The conductivity of the medium is 0.02 S/m. The minimum voltage required for operation is used: 100 V for Device A (Silicon Cone) and 300 V for both Device B (Silicon Posts) and Device C (PDMS Posts).

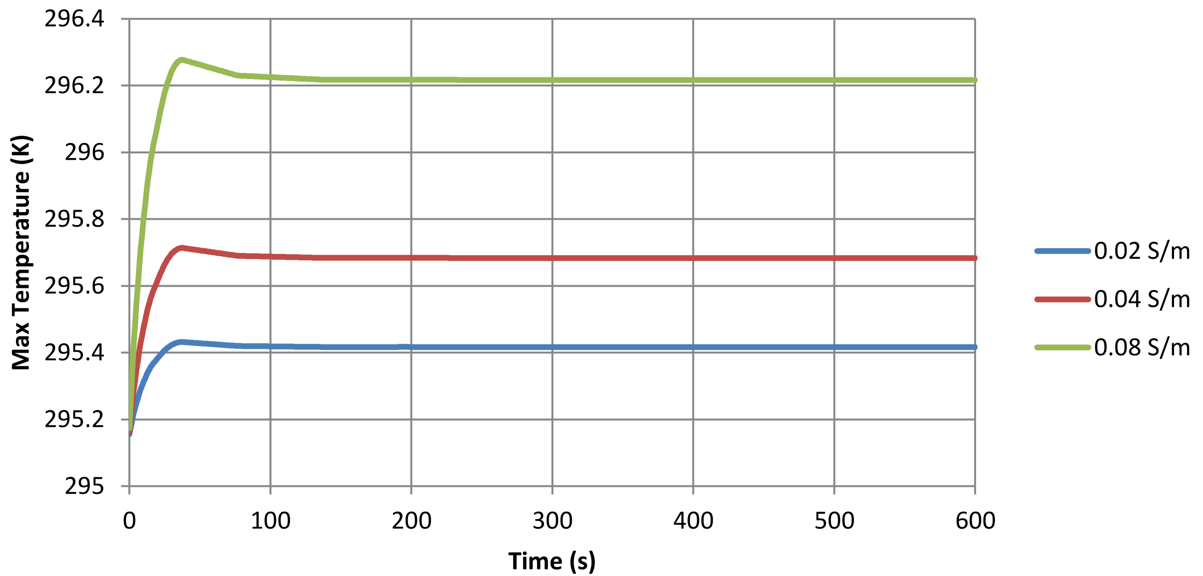

Figure 3-6 Simulation results for Device A (Silicon Cone). Plot shows the maximum temperature in the microchannel as a function of time. The conductivity of the medium is varied. The minimum voltage required for operation is used: 100 V.

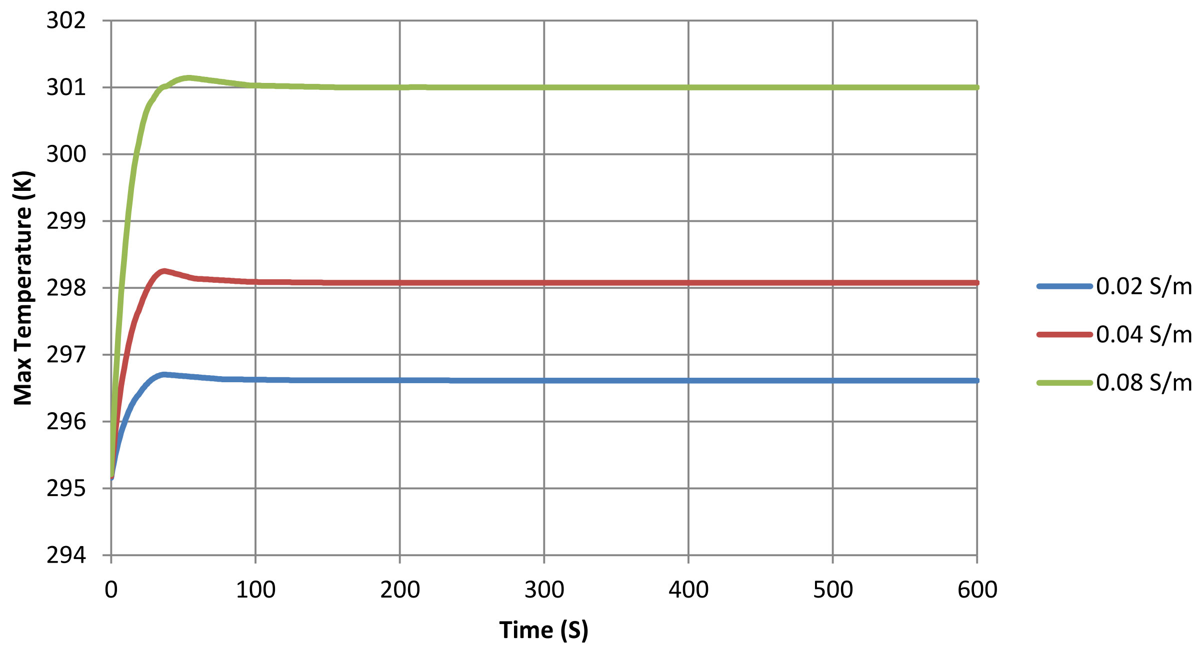

Figure 3-7 Simulation results for Device B (Silicon Posts). Plot shows the maximum temperature in the microchannel as a function of time. The conductivity of the medium is varied. The minimum voltage required for operation is used: 300 V.

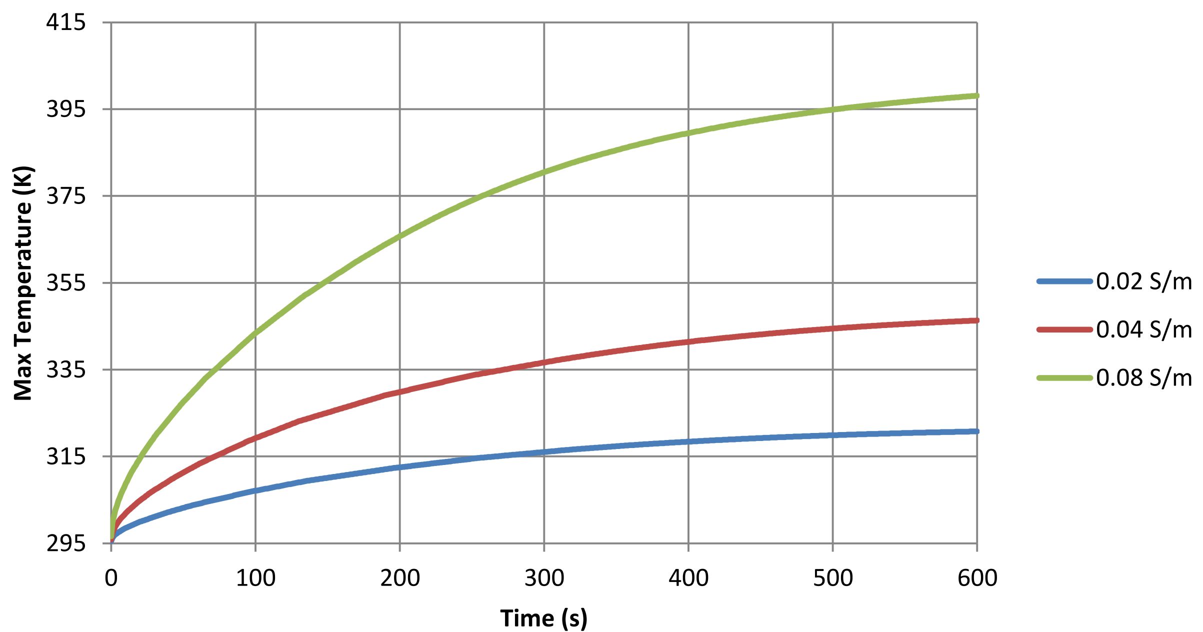

Figure 3-8 Simulation results for Device C (PDMS Posts). Plot shows the maximum temperature in the microchannel as a function of time. The conductivity of the medium is varied. The minimum voltage required for operation is used: 300 V.

4 A Single-Mask Process for 3D Microstructure Fabrication in PDMS

4.1 Introduction

Elastomers such as polydimethylsiloxane (PDMS) are widely used for lab-on-a-chip applications as they are transparent, bio-compatible, and low cost. Researchers have mainly utilized polymeric substances to develop 2D microfluidic structures due to the simplicity of the fabrication process. For many research groups, soft-lithography [136] has still remained a popular option for developing structures in elastomers due to its cost effectiveness. In this technique, the negative features of the desired patterns in 2D is transferred to a master device (e.g., SU-8) once at a time using lithography techniques. Therefore, fabricating structures with different depths requires laborious and time-consuming multiple steps of lithography. Furthermore, this technique only enables the fabrication of sharp geometries (e.g., rectangular channels), a limitation set by the lithography process and pattern transfer from the photomask to SU-8 resist.

However, realizing a comprehensive micro electro-mechanical system (MEMS) device with complex functionalities requires the development of 3D geometries in a time and resource effective manner. For instance, biologically-inspired structures such as blood vessels or respiratory systems have much more complex shape than simple rectangular microfluidic channels that can be developed utilizing basic lithographic techniques to simulate such environments. For example, in blood vessels, cells are interacting inside circular channels, with varying diameter along with multiple branching and joints, with each other and their surrounding environment. Thereby, only under such condition one can truly study the biology of cells within a system *in vitro* as it is occurring *in vivo* if the microfluidic device resembles the structures of their living conditions [137].

There have been different approaches taken to facilitate the fabrication of 3D complex structures throughout the past decades. In gray-scale lithography, masks with optical gradient contrast, unlike binary masks, have been utilized to fabricate structures with varying step profile with a single exposure [138, 139]. In direct deposition process, the scaffold of microstructures are patterned serially by a robotic arm and

infiltrated by photocurable materials. This is followed by the extraction of the scaffold to fabricate complicated networks of microfluidic channels [140]. In multi-photon absorption technique, a high energy beam is focused onto polymer resists causing the formation of highly cross-linked solid polymers which are stacked on top of each other forming a 3D structure [141, 142]. In addition, there has been a few efforts on the fabrication of circular microfluidic channels [143-145]. Fiddes et al. [144] reports the development of 3D circular channels by first filling a regular 2D rectangular channel with silicone oligomer solution and then introducing a coaxial stream of gas to form the circular-shaped channels along the gas stream. Furthermore, Song et al. [145] demonstrates the fabrication of such channels by embedding a thin wire inside the mixture of PDMS pre-polymers before polymerization and removing the wire after polymerization.

The current methods require complicated and processes and tools in order to fabricate 3D structures. Some of these techniques lack the possibility of fabricating circular channels in a robust manner [138, 139, 141, 142] and techniques developed for the fabrication of 3D channels are not suited for fabricating circular channels with constantly varying dimensions [140, 143-145]. These limitations have encouraged our group to research and establish a reliable and robust yet low cost technique for the fabrication of versatile 3D structures in PDMS.

This paper describes in details the fabrication processes of such 3D structures in PDMS based on our previous research on fabricating 3D structures in silicon, transfer of the negative replica of silicon to glass, and eventually the transfer of original patterns in silicon to PDMS utilizing the soft-lithography technique using the glass structure. In addition, as a case example, this paper demonstrates the applicability of this technique in realizing the first polymeric 3D insulator-based dielectrophoresis device that can be used to trap and enrich biological particles. The following sections discuss in details the fabrication methods utilized to achieve such 3D structures in silicon and consequently in PDMS.

4.2 Fabrication Process

RIE lag or Aspect Ratio Dependent Etching (ARDE) assists to create large features by etching multiple smaller features [146, 147]. We have previously reported on the fabrication of 3D microfluidic structures in silicon with a single-mask process taking advantage of the RIE lag effects [148, 149]. In this technique, a single mask with five independent geometric variables similar to those shown in the prior work [148] along with the etch time can determine the depth and width of the microfabricated channels. The method allows the realization of complex symmetric and non-symmetric microfluidic channels and cavities by isotropic etching of silicon in sulfur hexafluoride (SF_6) plasma using reactive ion etching (RIE) technique.

More specifically, the fabrication procedure starts by depositing 3000 Å of silicon dioxide on a silicon wafer. The oxide is deposited with a PECVD (Trion Orion II, USA) at 300 °C. In the next step, photoresist is spun and patterned with many micron-scale windows (Figure 4-1b). This window pattern enhances the RIE lag effect, allowing for large differences in depth to be achieved. The oxide layer is patterned according to the photomask. Then, silicon is etched in an DRIE (Alcatel, AMS-100, France). During the silicon etching process, the patterned oxide lattice structure remains suspended above the microchannel. The local rate of the silicon isotropic etching process is dependent on the window pattern. As a result, a 3D topography is formed by using different patterns on the photomask. As previously reported [148], the depth and width of the microchannel is related to the independent geometric values and etch time by equation (4-1)

$$\text{Depth} = \exp\left(\frac{\alpha\beta F^{\gamma}}{1+\beta F^{\gamma}}\right) \tag{4-1}$$

In this equation, α, β,and γ are a function of the etch time t and the window pattern factors c, w, l, and s. c is the number of windows in a row, s is the window spacing, w is the width of a window, and l is the length of a window. The fill factor F is given by equation (4-2)

$$F = c\left(\frac{wl}{(w+s)(w+l)}\right) \tag{4-2}$$

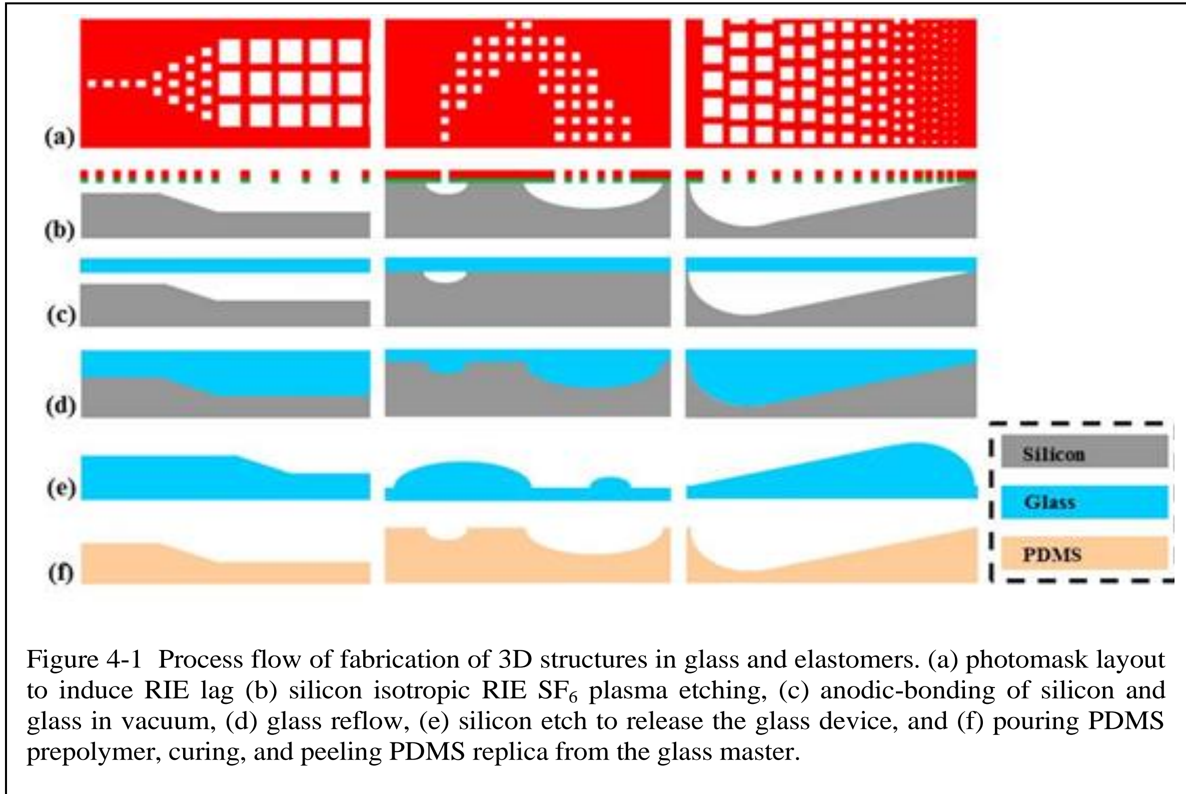

Figure 4-1 Process flow of fabrication of 3D structures in glass and elastomers. (a) photomask layout to induce RIE lag (b) silicon isotropic RIE SF_6 plasma etching, (c) anodic-bonding of silicon and glass in vacuum, (d) glass reflow, (e) silicon etch to release the glass device, and (f) pouring PDMS prepolymer, curing, and peeling PDMS replica from the glass master.

By changing the geometrical patterns, different channels with varying depths and widths can be fabricated and their dimensions can be predicted by the aforementioned models. Using such scheme, it was shown that for channels with small width (less than 30 µm), it is possible to obtain a nearly semi-circular (aspect ratio 1:1) shape, whereas increasing the channel width will decrease the aspect ratio. For very wide channels (larger than 300 µm), it is possible to obtain a rectangular cross section with nearly rounded corners. In addition, the depth profile of the transition between two different depths can be controlled by creating gradients of different window parameters. Figure 2 shows to some extend the complexity of 3D structures and quality of surfaces fabricated in silicon utilizing RIE lag using this technique.

After the fabrication of the 3D silicon device, the negative replica of silicon in glass and the positive replica of silicon in PDMS are fabricated employing the following procedures. First, both the surface of the silicon wafer comprising 3D structures and a blank 700 µm-thick Borofloat® 33 wafer are immersed in NanoStrip (Cyantek, CA, USA) for 20 minutes to remove any organic residues from the surface of the wafers. Then, silicon and Borofloat wafers are anodic-bonded under vacuum

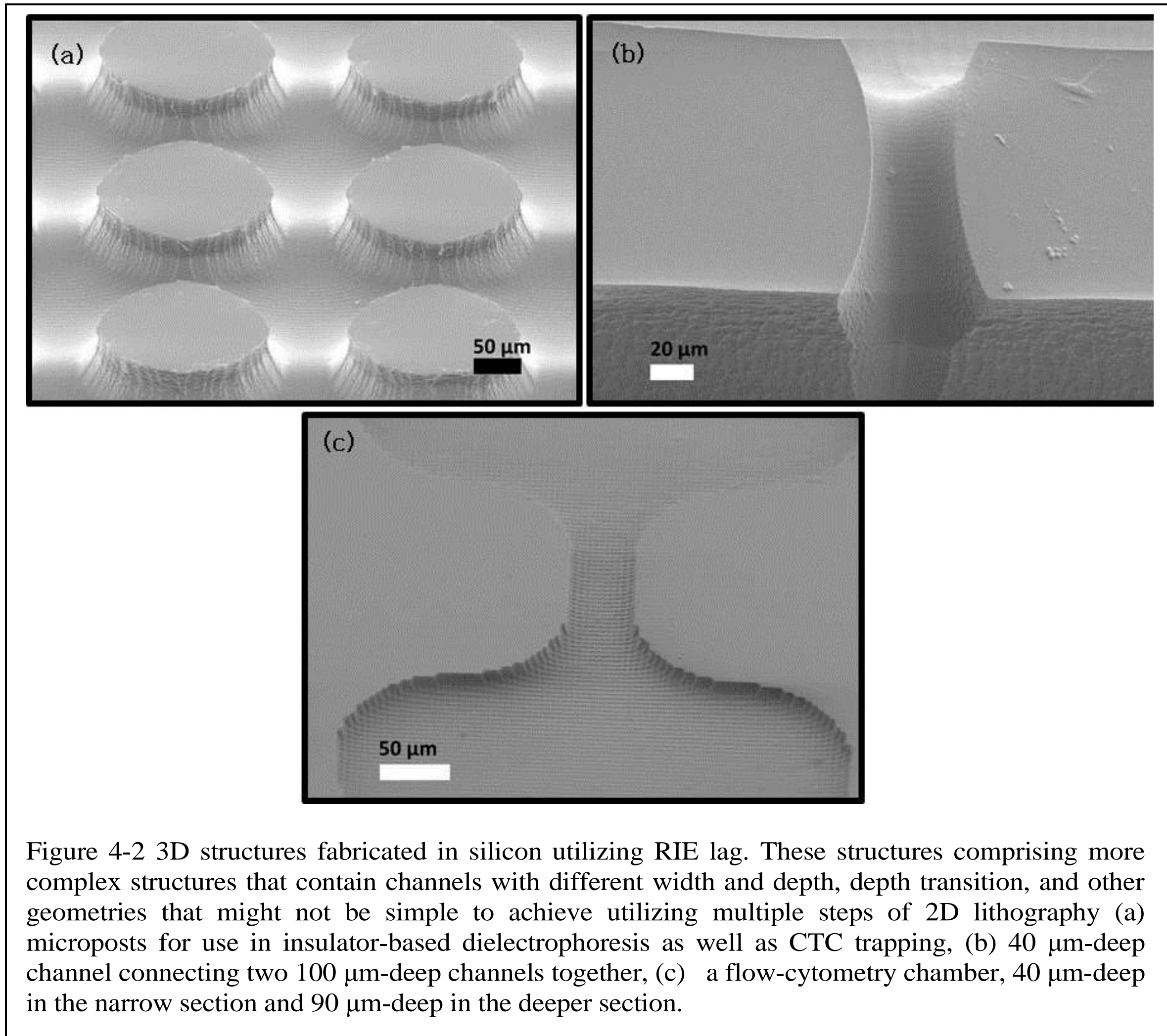

Figure 4-2 3D structures fabricated in silicon utilizing RIE lag. These structures comprising more complex structures that contain channels with different width and depth, depth transition, and other geometries that might not be simple to achieve utilizing multiple steps of 2D lithography (a) microposts for use in insulator-based dielectrophoresis as well as CTC trapping, (b) 40 µm-deep channel connecting two 100 µm-deep channels together, (c) a flow-cytometry chamber, 40 µm-deep in the narrow section and 90 µm-deep in the deeper section.

employing a substrate bonder (Karl-Suss, SB6, Germany) (Figure 1c). The bonded structure is placed in a high temperature oven and its temperature is elevated and maintained at 720 °C for about 4 hours and then is gradually increased to 760 °C with 10 °C/min. The structure is kept at this temperature for 30 minutes. Under these conditions, glass reflows and fills the channels and cavities formed in silicon (Figure 4-1d). After cooling down the melted device, the surfaces of the bonded wafers are cleaned by immersing them in a 10:1 buffered Hydrofluoric acid (BOE) to remove any oxide growth on silicon during the reflow process.

Subsequently, the silicon substrate is completely etched by Potassium hydroxide (KOH) at 95 ^{o}C leaving behind the glass microstructure device having the negative replica of the silicon structures (Figure 4-1e). In order to obtain the positive replica of the 3D structures in PDMS, the surface of the glass master is silanized by vaporizing a

couple of droplets of Trichloro(1*H*,1*H*,2*H*,2*H*-perfluorooctyl)silane (Sigma-Aldrich, MO, USA) for 2 hours inside a desiccator to ensure smooth and safe release of the PDMS mold.

Then the pre-polymer and curing agent of Sylgard 184 (Dow Corning, MI, USA) are mixed for the ratio of 10:1 and poured gently on the surface of the glass master. The device is again placed inside a desiccator and PDMS is degassed for about 1 hour. The glass master along with the uncured PDMS device is then placed in an oven at 100 °C for one hour. The PDMS structure is then separated from the glass master while replicating the same 3D features on the original silicon substrate (Figure 1f). As evident, due to isotropic etching at the beginning of the process, sharp corners and edges in the final PDSM structures are avoided.

4.3 Results and Discussion

4.3.1 Glass Reflow Factors

In order to replicate the 3D features of silicon to PDMS, while heated in furnace, glass should reflow into the cavities of silicon and fill them completely. To achieve this, the reflow temperature and duration should be properly set. In an ideal case, it is desired to ramp the furnace temperature to the softening point of Borofloat wafer (820 °C) for enough time to ensure that the glass wafer reflows and fills the cavities etched in silicon. However, as the temperature of the furnace is being increased, small bubbles start to form on the surface of the glass wafers, which at some cases can occur inside the silicon cavities, hence deforming the final shapes and geometries in glass. The presence of such bubbles on the surface of glass wafers can be attributed to the re-boiling effect, which usually occurs at high temperatures on the junction of non-well controlled surfaces (in this case, the anodic-bonded surface of glass and silicon) [15]. Bubbles appear on the surface of glass structure where it faces the silicon wafer. In this work, attempts have been taken to avoid the presence of such detrimental effects as much as possible. Figure 4-3 shows the surface images of glass wafers after being heated at 800 °C for 20 minutes and 760 °C for 8 hours. The glass wafers were bonded to blank silicon wafers prior to placing in the furnace and the

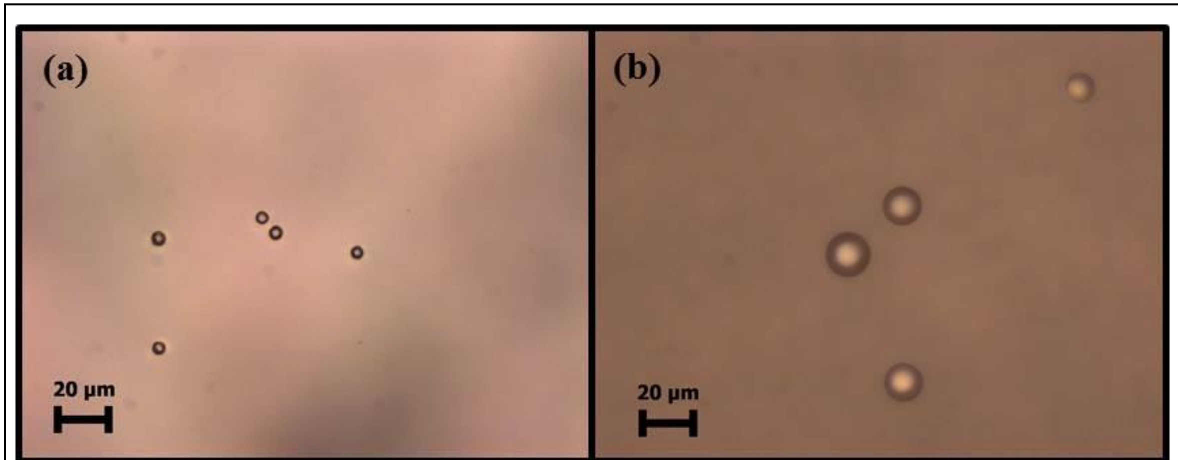

Figure 4-3. (a) glass surface after heat treatment at 760 °C for 8 hours and (b) glass surface after heat treatment at 800 °C for 20 minutes. Reboiling effect has caused the formation of small bubbles on the surface of both wafers.

silicon wafers were removed after the glass reflow procedure. Furthermore, Figure 4-4 shows the SEM images of the surface of the glass wafer, which contain some structures, after the reflow process at 760 °C for 8 hours. These defects, if untreated, will be transferred to the PDMS mold, and leave additional small and round pieces of PDMS atop the mold on the spots of the defects.

In order to alleviate the re-boiling effect, we adjusted three factors including temperature ramp rate, reflow temperature, and reflow time. The furnace temperature was ramped to the target point gradually (10 °C/min). As illustrated in Figure 4-3 and Figure 4-4, this factor solely cannot help to eliminate the defects on the surface of glass but sudden increase of the furnace temperature will result in the formation of much more bubbles. Furthermore, the furnace temperature was reduced to below the

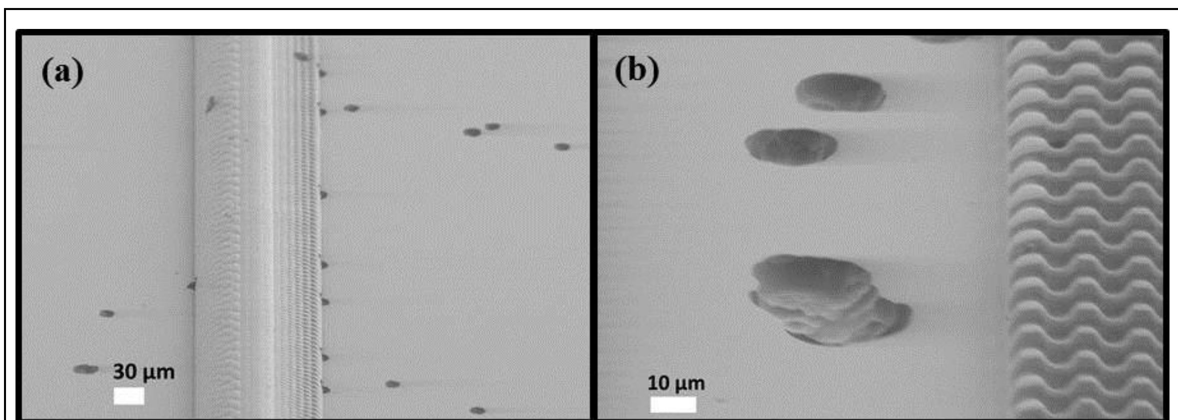

Figure 4-4. SEM images of glass structure after heat treatment at 760 °C for 8 hours and silicon removal (a) Glass master device with bubbles spread around and (b) close-up view of bubbles on the surface of glass master.

Temperature \ Time	20 MINUTES	40 MINUTES	8 HOURS
700°C	✓	✓	✓
720°C	✓	✓	✓
750°C	✓	✓	✗
770°C	✓	✓	✗
800°C	✗	✗	✗

Table 4-1 Reflow temperature and time effect on the formation of bubbles on the surface of glass

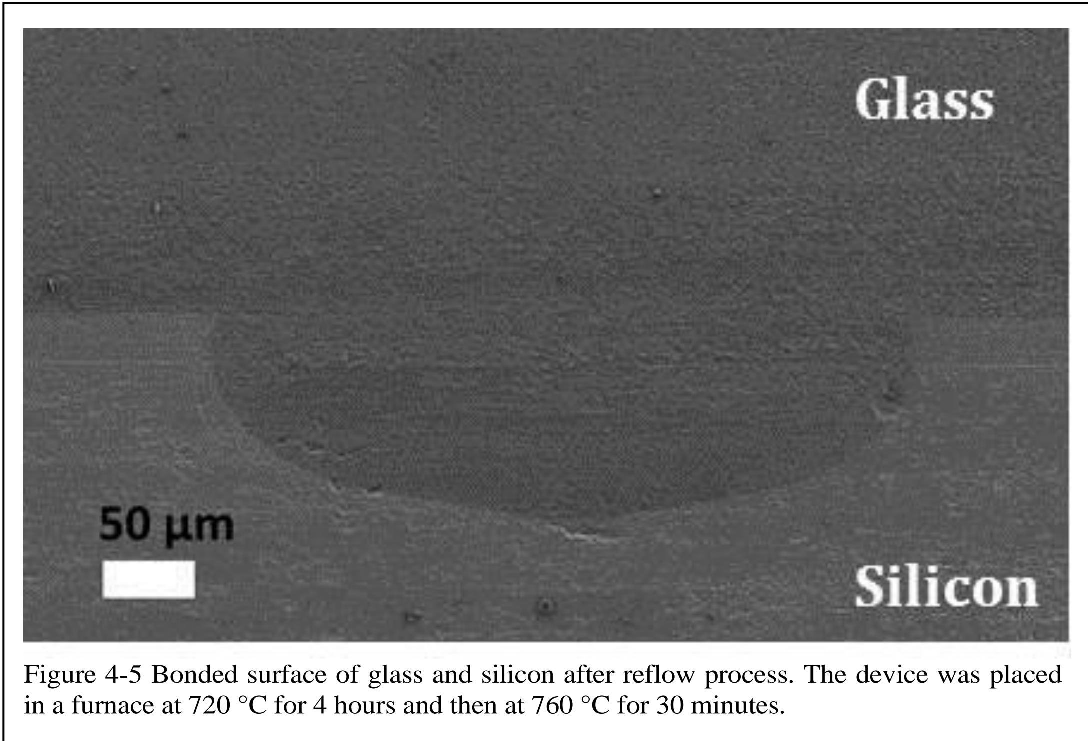

Figure 4-5 Bonded surface of glass and silicon after reflow process. The device was placed in a furnace at 720 °C for 4 hours and then at 760 °C for 30 minutes.

softening point of Borofloat for a various range of time. Then, the furnace temperature and the reflow time were recorded. Table 4-1 reports the conditions which resulted in a bubble-free glass surface with a check-mark (✓) and those which resulted in the

formation of bubbles on the surface of the glass with a cross-mark (×). In order to both obtain a bubble-free glass structure and ensure complete reflow of glass in the silicon cavities, it was chosen to first maintain the furnace temperature at 720 °C for 4 hours and then ramp the furnace temperature to 760 °C for 30 minutes. As Figure 4-5 shows, glass has completely filled the silicon cavity using the above temperature and time settings.

4.3.2 3D Pattern Transfer from Silicon to Glass and PDMS

Figure 4-6 shows images of several glass microstructures after they are released

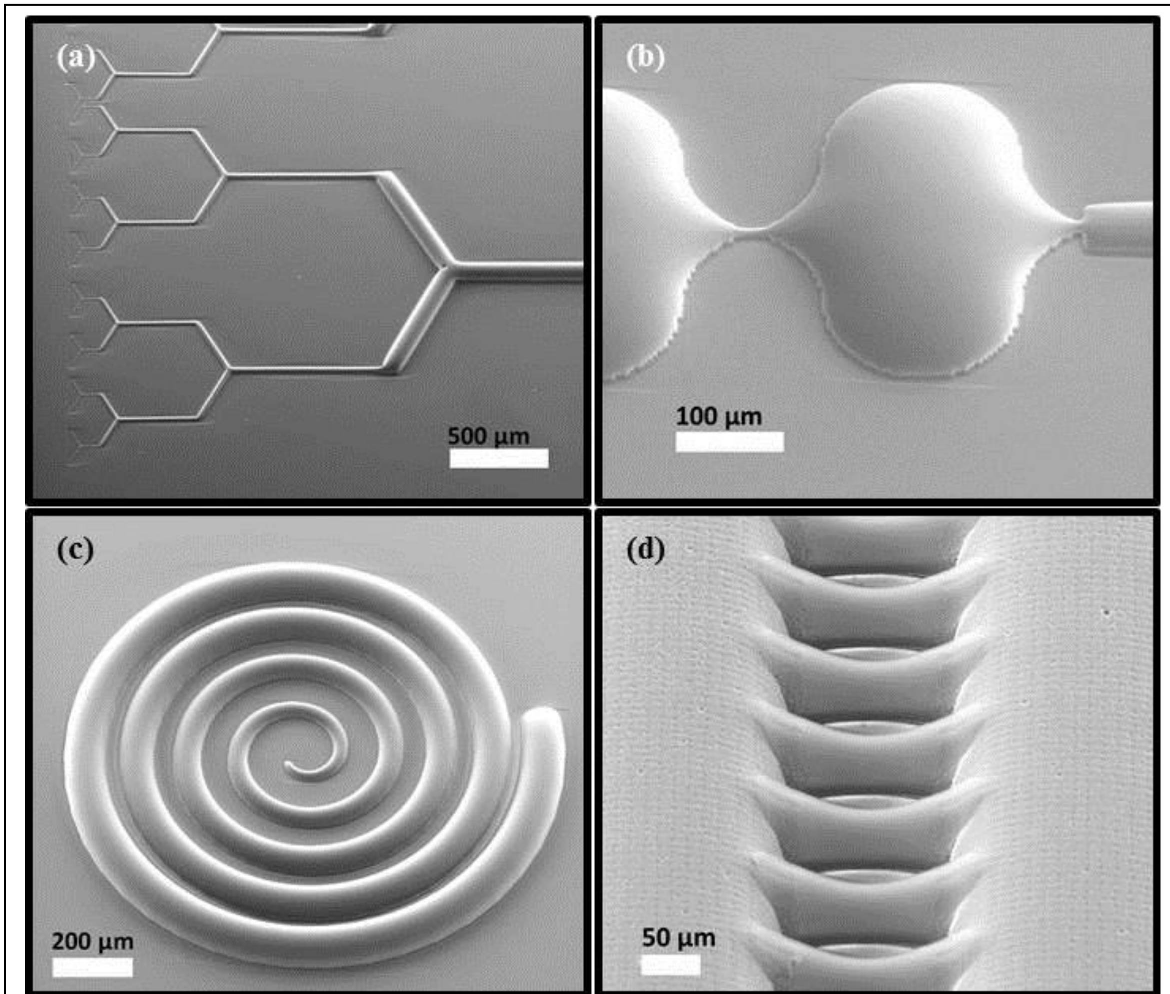

Figure 4-6. SEM images of several glass device prototypes after silicon release. The glass structures include replica of channels/cavities with different height and width.(a) capillary network, (b)micro-flow cytometry chamber, (c)spiral, and (d)cell migration passageways. Scale bar represents the actual dimension only in lateral-direction as the images are tilted in vertical-direction.

from silicon, clearly depicting out-of-plane structures with different heights and widths. Figure 4-7 shows the images of several PDMS prototypes fabricated using the glass structures as master. As the glass wafer fills the silicon cavities after the reflow process, all the features of the original structures are transferred to the PDMS mold.

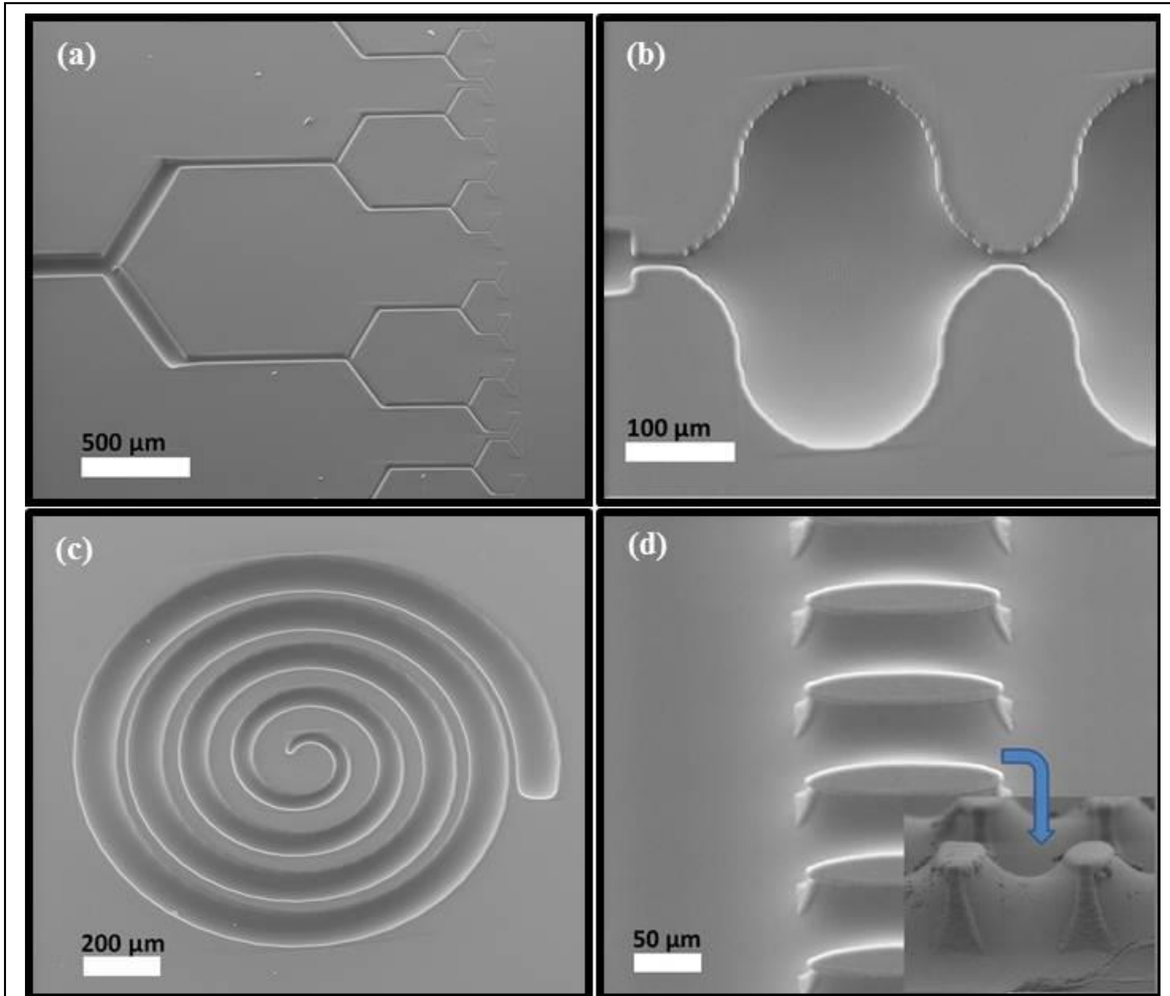

Figure 4-7. SEM images of several 3D microfluidic devices made in PDMS using the master structures depicted in Figure 6. (a) capillary network, (b) micro-flow cytometry chamber, (c) spiral, and (d) cell migration passageways with the inset showing 90^0 rotated image. Scale bar represents the actual dimension only in lateral-direction as the images are tilted in vertical-direction.

The surface of the PDMS mold is, however, very smooth on the area that the glass wafer was faced the un-etched area of the silicon wafer. These complex 3D devices can find numerous applications including microfluidic mixing, cell and particle separation and enrichment, and droplet splitting. The ability to create both constant depth and variable depth channels increases the design flexibility of all of these devices. The structure in Figure 4-7a is a capillary network with channel depths ranging from 10µm

to 80 μm which can be used to simulate blood vessels in the human body. Similar types of structure have been fabricated by melting photoresist to form the master structures [150, 151], however, this method requires additional steps of lithography to enable controlling the width and depth of the channels simultaneously. Figure 4-7b shows a microchannel composed of 400 μm-wide, 20 μm-deep chambers which are connected by smaller channels measuring 7 μm in both depth and width. This structure may be used for flow cytometry to observe a single particle at a time. Using this 3D architecture, particles from a large main channel can be brought into a small focus channel where they are positioned in width and depth for imaging. Figure 4-7c shows a spiral which varies smoothly in depth from 25 μm to 50 μm and in width from 25 μm to 100μm. In Figure 4-7d, two 50 μm deep main channels are separated by a series of smaller channels which are 15 μm-deep and 20 μm-wide. This structure may be used to study cell migration through narrow passageways.

4.3.3 PDMS Devices with 3D Properties

In order to demonstrate the versatility of this 3D fabrication process, 3D insulator-based dielectrophoresis (iDEP) devices were created and tested. iDEP microfluidic devices have been used to trap and sort bacteria, viruses, cells, and beads. Dielectrophoresis is the motion of polarizable particles that are suspended in an electrolyte when subjected to a spatially nonuniform electric field [152]. The DEP force felt by a spherical particle suspended in a medium is given by equation (4-3):

$$F_{DEP} = 2\pi R^3 \varepsilon_m \operatorname{Re}[f_{CM}] \nabla |\mathbf{E}|^2 \qquad (4\text{-}3)$$

where R is the radius of the particle, ε_m is the permittivity of the medium, $\mathbf{E}$ is the local electric field, and $\operatorname{Re}[f_{CM}]$ is the real part of the Clausius-Mossotti factor. Fluid flow in iDEP devices is generated by electrokinetic (EK) flow. For a particle to become trapped in these devices, the DEP force must be larger than the EK force on the particle. Mathematically, this is [153] given by equation (4-4):

$$\frac{u_{DEP} \cdot u_{EK}}{u_{EK} \cdot u_{EK}} = \frac{\mu_{DEP}}{\mu_{EK}} \frac{\nabla(E \cdot E)}{E \cdot E} \cdot E > 1 \tag{4-4}$$

where $u_{DEP} = \mu_{DEP} \nabla(E \cdot E)$ and μ_{DEP} are the DEP velocity and mobility of the particle, respectively, and $u_{EK} = \mu_{EK} E$ and μ_{EK} are the EK velocity and mobility of the particle, respectively. The DEP force increases as the square of the electric field while the EK increase linearly with the electric field. Thus, as the electric field strength increases, the DEP forces become dominant. When the DEP overcomes the EK flow, the particle is trapped. In iDEP, insulating structures are used to create the required

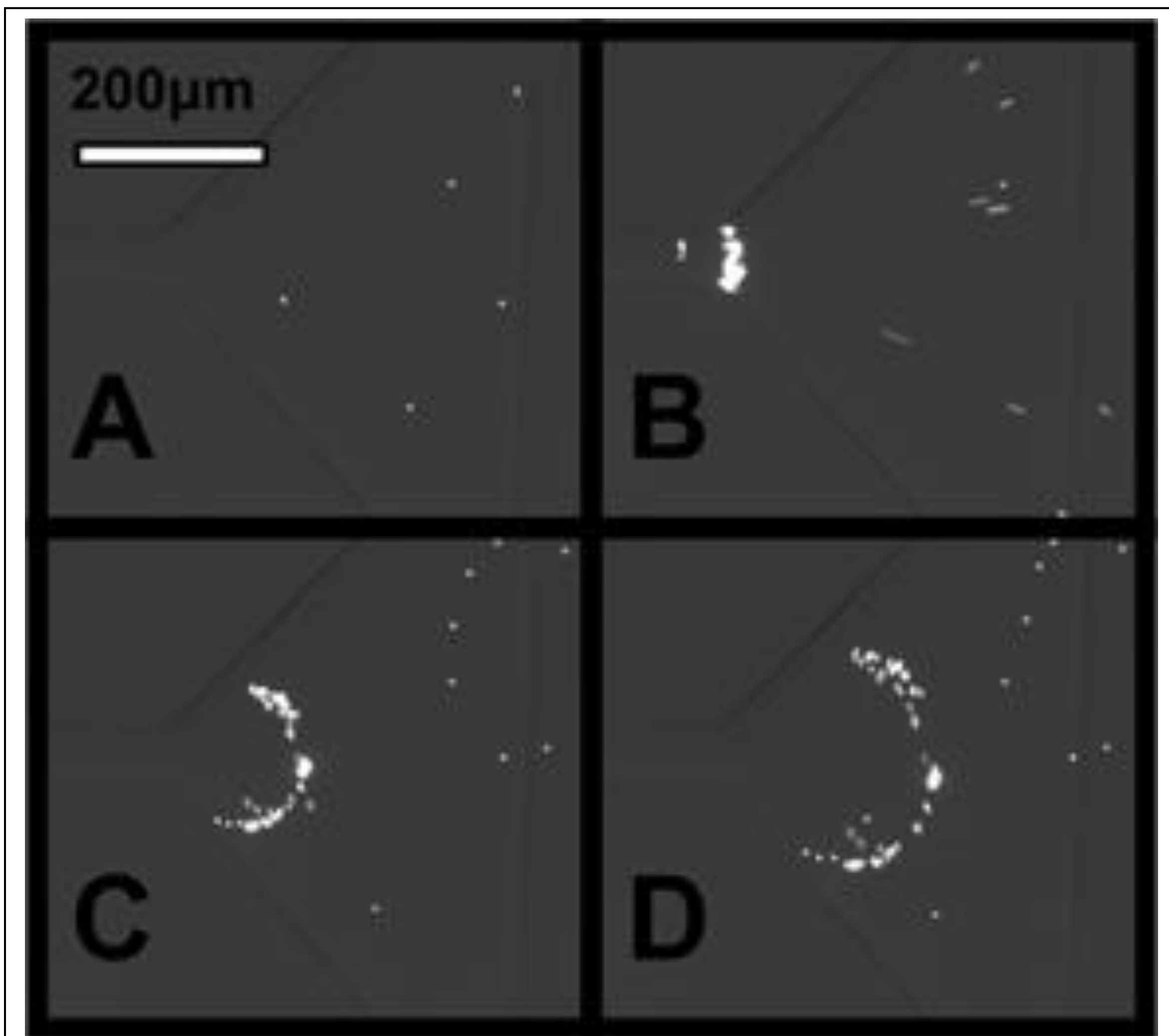

Figure 4-8 Trapping and release of 2 μm beads. (A) No voltage (B) 150 V is applied (C and D) Voltage is turned off and particles are released.

electric field gradient.

The 3D iDEP device presented herein consists of a 1.2 mm-wide, 90 μm-deep main channel and a 70 μm-wide, 30 μm-deep trapping channel. The transition between the two channels is smooth. Typical iDEP devices contain constrictions in width to create the required non uniform electric field [154, 155]. However, recently it has been shown that 3D geometries can enhance the performance of iDEP devices by decreasing the applied voltage required for operation [156, 157]. The 3D fabrication enhances the performance of the devices by creating larger gradients over wider areas when compare to those obtained in fixed depth devices. The 3D geometry allows for large cross-sectional area constrictions within a short space. These sharp constrictions create high

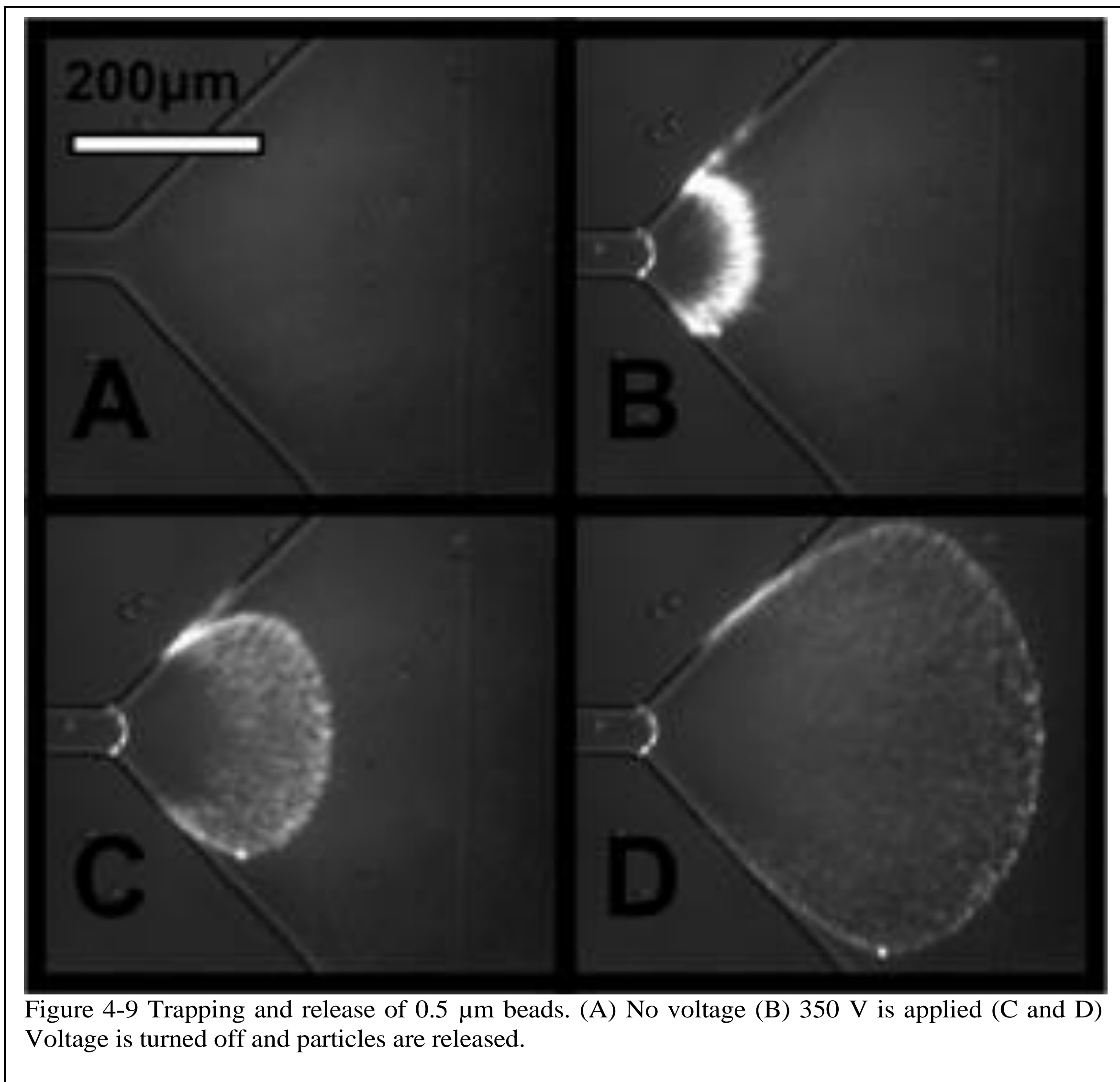

Figure 4-9 Trapping and release of 0.5 μm beads. (A) No voltage (B) 350 V is applied (C and D) Voltage is turned off and particles are released.

electric field gradients which in turn lead to high DEP forces. Thus, a 3D device is able to create stronger DEP forces than a 2D device with the same footprint. This allows for operation at lower applied fields.

For our experimental setup, 0.5 µm and 2 µm diameter polystyrene beads were suspended in DI water with a measured conductivity of 760 µS/m. The solution was flowed through the microfluidic device and voltage was applied along the length of the channel from the 1cm spaced reservoirs. Trapping of 2 µm beads was obtained at 150 V with over 90% of all particles trapped (Figure 4-8). The trapping was shown to be reversible with 100% of the trapped particles released when voltage was removed. Trapping of 0.5 µm beads was obtained at 350 V with over 85% of all particles trapped (Figure 4-9). The trapping was shown to be reversible for 90% of the particles while the remainder became fixed to the channel floor.

iDEP devices typically require applied voltages from 400 V/cm to 1200 V/cm [153, 158-161]. However, the 3D slopes in our device allowed for trapping at 150 V. Lowering the required applied voltage decreases the joule heating in the channel which can kill biological particles and can create unwanted thermal currents in the device. Additionally, lowering the operating voltage decreases the complexity and cost of the electronics needed to actuate the device. Thus, the performance of the iDEP devices is enhanced by our 3D fabrication method.

4.4 Conclusion

The presented method provides a novel, low-cost, high-yield process to develop 3D in-plane PDMS devices whose realization with other methods such as conventional multiple lithography and etching steps for forming the master is very difficult if not impossible. The width and depth of the structures can vary from a few hundred microns down to a few microns while transition between these changes can be controlled to be gradual. It is also notable that out-of-plane structures are formed in glass substrates in this technique. The main advantage of using the method described in this paper is the ease of the release of the glass master from the silicon structure. As the glass substrate contain out-of-plane structures, releasing the PDMS device is not difficult. If one wants to use an elastomer instead of glass and peel it off from the in-plane silicon substrate,

the released structures are very likely to be damaged due to the undercut features present in the isotropically etched silicon structures.

Several microfluidic structures in PDMS have been demonstrated that can be used for cellular analysis, bioparticle enrichment, and bio-inspired network formation. In particular, 3D structures were developed in PDMS for insulator-based dielectrophoresis. It was shown that these devices can operate at voltages which are at least a factor of 2 lower than voltages required to operate their 2D counterparts. Enrichment of 500 nm and 2 μm were successfully demonstrated using applied voltages of 350 V and 150 V, respectively. The trapping efficiency was measured to be more than 80%. The high-performance 3D iDEP can be used to enrich bacteria and other biological particles finding a variety of applications ranging from water and food safety to counter-terrorism.

5 3D Insulator-based Dielectrophoresis using DC-Biased, AC Electric Fields for Selective Bacteria Trapping

5.1 Introduction

Dielectrophoresis (DEP) is a well-known electric field based technique for separating, moving, and trapping biological particles. DEP devices have been shown to separate and concentrate beads, bacteria, viruses, and mammalian cells [162]. The DEP effect is the motion of polarizable particles that are suspended in a dissimilar media when subjected to a spatially nonuniform electric field [6]. Conventional microfluidic DEP techniques utilized microfabricated electrodes to generate non uniform electric fields. These electrode-based DEP (eDEP) designs utilized sharp electrodes and narrowly spaced electrodes to create large electric field gradients and thus large DEP forces [14-17]. eDEP devices put the target particles close to the electrodes, which present complications if the electrodes are not chemically inert. Additionally, adding microfabricated electrodes to a microfluidic device requires an additional photolithographic mask and deposition step, which increases the cost and somewhat complexity of the device.

An alternative microfluidic technique for generating DEP forces is insulator-based dielectrophoresis (iDEP). First proposed by Cummings and Singh, iDEP uses insulating structures rather than electrode patterns to produce the nonuniform electric fields necessary for DEP[24]. These device are very inexpensive as they lack embedded electrodes, are simple to fabricated, and can be made of a large variety of economical materials such as glass and polymers[25, 26]. iDEP devices have been used for a wide range of applications including manipulation of bacteria, viruses, cells, and beads [26-29].

iDEP devices typically utilize a large DC voltage applied to the fluidic reservoirs of the microfluidic device to operate. This creates electric fields throughout the channel which move the target particles through the channel by electroosmosis (EO) and electrophoresis (EP), as well as trap the particles with dielectrophoresis (DEP). One disadvantage of iDEP is the large voltages necessary for operation. This increases the cost and complexity of the driving equipment. Additionally, large DC

voltages lead to Joule heating within the channel. This can affect the viability and physiology of the target bioparticles [109, 163]. Also, Joule heating in microfluidic channels can create temperature gradients which lead to electrothermal (ET) fluid flow within the channel[111-116]. ET flow typically results in unwanted circulations in DEP devices which decreases performance[118].

Recently, several researchers have begun to actuate iDEP devices with DC-biased AC electric fields. Hawkin et. al demonstrated the first reported use of this type of actuation[96]. In that work, an iDEP channel was used to continuously deflect polymer beads and separate them by size. The effects of the AC to DC electric field magnitude and the constriction ratio of the channel were studied both theoretically and experimentally. Other studies have used 2D microfluidic devices to manipulate particles with DC-biased AC electric fields. Zhu and Xuan investigated the effect of the AC to DC electric fields on the ability to focus a stream of polymer beads[164]. Lewpiriyawong et. al used a modified H filter to separate polymer beads by size by deflecting them to different fluidic outlets[165]. In a different study, Lewpiriyawong et. al demonstrated device trapping of polymer beads and yeast cells in a high constriction iDEP device[166]. All of these studies also concluded that the use of DC-biased AC electric fields lowered the total voltage necessary for operation.

Another method to decrease the operating voltage of iDEP devices is to use three dimensional (3D) structures. 3D constrictions within a microfluidic channel can create high constriction ratios, which are ratios of the largest cross sectional area of the channel to the smallest cross sectional area. Previously, our group has developed a fabrication technology for creating three dimensionally varying structures with a single photolithographic mask. Utilizing a phenomenon known as reactive ion etch lag (RIE lag), a single plasma etch can create structures on a silicon substrate which vary in height, width, and depth simultaneously[124]. Using these structures, we have created high constriction ratio devices which achieve 100% trapping of 2 μm particles with an applied potential of only 100 V [167, 168], an order of magnitude lower than the potentials used to operate traditional 2D designs. Additionally, others have used 3D iDEP devices to trap bacteria with potentials as low as 50 V [123].

This paper presents the theory, fabrication, and testing of a new 3D iDEP

device. The device is fabricated using our newly developed 3D PDMS technique and used to selectively trap and separate *Escherichia coli* (*E. coli*) and 1 μm polystyrene beads as well as live and dead *Staphylococcus aureus* (*S. aureus*). The 1 μm beads were chosen because they are similar in size to *E. coli* and thus difficult to separate with only DC fields. Both negative and positive DEP was observed over a frequency range of DC to 600 kHz. This is the first reported use of DC-biased AC fields to selectively trap bacteria.

5.2 Theory

Dielectrophoresis is the motion of polarizable particles that are suspended in an electrolyte when subjected to a spatially nonuniform electric field [6]. The DEP force felt by a spherical particle suspended in a medium is:

$$\mathbf{F_{DEP}} = 2\pi R^3 \varepsilon_m Re[f_{CM}] \nabla |\mathbf{E}|^2 \quad (5\text{-}1)$$

where R is the radius of the particle, ε_m is the permittivity of the medium, **E** is the local electric field. $Re[f_{CM}]$ is the real part of the Clausius-Mossotti factor which is:

$$f_{CM} = (\varepsilon_p^* - \varepsilon_m^*)/(\varepsilon_p^* + 2\varepsilon_m^*) \quad (5\text{-}2)$$

where ε_p^* and ε_m^* are the complex permittivities of the particle and the medium, respectively. Complex permittivity is defined as:

$$\varepsilon^* = \varepsilon + \sigma/(j\omega) \quad (5\text{-}3)$$

Thus, F_{DEP} will fluctuate greatly depending on the operating frequency and can even change direction. At DC and very low frequency fields, DEP separation of bioparticles is mostly dominated by the size difference of the particles due to the cubed radius term and the low conductivity of cellular membranes. However, at high frequencies, the fields are able to penetrate the cell membrane into the electrically conductive cytoplasm. Thus cells can have a higher DEP frequency dependency than solid particles. If a particle is attracted to a region with a high electric field, it experiences positive DEP (pDEP). Conversely, if a particle is repelled by a region with

a high electric field, it experiences negative DEP (nDEP). In order for a particle to become trapped in these devices, the DEP force must overcome the electrokinetic forces. Fluid flow in these devices is driven by electroosmotic (EO) flow. Additionally particles move with respect to the fluid due to electrophoresis (EP). Under steady state, a force balance among EP, EO, DEP and Stokes drag forces results in a terminal particle velocity which can be expressed as [96]:

$$\mathbf{u} = \mu_{DEP}\nabla\mathbf{E}^2 + \mu_{EO}\mathbf{E} + \mu_{EP}\mathbf{E} \quad (5\text{-}4)$$

where μ_{DEP}, μ_{EO}, and μ_{EP} are the DEP, electroosmotic, and eletrophoretic mobilities. DC electric fields have a significant impact on the electrophoresis, electroosmosis and dielectrophoresis of a particle. However, the EO term and the EP term are linearly dependent on the electric field while the DEP term is non-linearly dependent on the electric field. Consequently, DEP trapping can be achieved by increasing the electric field until the DEP term dominates the equation; however, this can lead to very high applied potentials (~1000V) [31]. This is undesirable as it leads to increased Joule heating which complicates the fluid flow and can damage the biological particles of interest. In this work, an AC signal with a DC offset is used. The ratio of the magnitudes of the applied electric fields is α:

$$\mathbf{E} = \mathbf{E}_{DC} + \mathbf{E}_{AC} = \mathbf{E}_{DC}\,(1 + \alpha) \quad (5\text{-}5)$$

$$\alpha = |\mathbf{E}_{AC}| \,/\, |\mathbf{E}_{DC}| \quad (5\text{-}6)$$

Substituting Eq. (6) into Eq. (4). and integrating over one period of oscillation shows the time average velocity of the particle as a function of the DC electric field and α [96]:

$$\mathbf{u} = (\alpha^2 + 2)\,\mu_{DEP}\nabla\mathbf{E_{DC}}^2 + (\mu_{EO} + \mu_{EP})\mathbf{E_{DC}} \quad (5\text{-}7)$$

In this case, The DC offset still provides motion of particles through the channel as well as some DEP force. The AC electric field, however, provides only a DEP force that is tunable. As the frequency is increased, the DEP term dominates the equation and only dielectrophoresis is significant [96]. While mathematically, the AC fields

contribute to an instantaneous EO and EP velocity, these components average to zero over one period of the applied signal. As a result, their effects are negligible for high frequencies (f~1kHz). The ratio α can be used to adjust the strength of the DEP force relative to the total electric field. Therefore particle concentration can be achieved at lower voltages by increase the AC component and decreasing the DC component of the electric field signal.

In our device, the insulating 3D posts constrict the current, creating a high electric field between the posts and a low electric field away from the posts. Due to the fluid flow, particle experiencing pDEP will be trapped on the downstream end of the posts and particles experiencing nDEP will be trapped on the upstream end of the posts. By varying the frequency and α of the applied signal, particles can be selectively trapped based on their geometry and electrical properties. Additionally, the 3D geometry increases the gradient of the electric field by providing a larger change in cross sectional area for current to pass through. This allows for large DEP forces to be generated with low applied electric fields.

5.3 Experimental Procedure

5.3.1 Device Fabrication

PDMS devices are fabricated according to our recently developed 3D polymer fabrication technique [169]. Fabrication (Figure 5-1) starts by depositing and patterning an oxide layer. Silicon is etched isotropically using SF_6 plasma. We utilize reactive ion etch (RIE) lag and our published models [73, 124] to smoothly and arbitrarily vary the depth of the microfluidic channel in a single-etch-step process by changing the geometrical pattern on the mask layout. Silicon is bonded to a Pyrex wafer under vacuum and then heated to 700°C for 8 hours. The Pyrex substrate is melted and fills the cavities on silicon. Silicon is then completely etched with a KOH solution and the Pyrex wafer is used as a master mold for PDMS. Molded PDMS devices were then bonded to glass substrates after being treating with oxygen plasma. The resulting microchannels are 90μm deep containing microposts spaced 40μm with

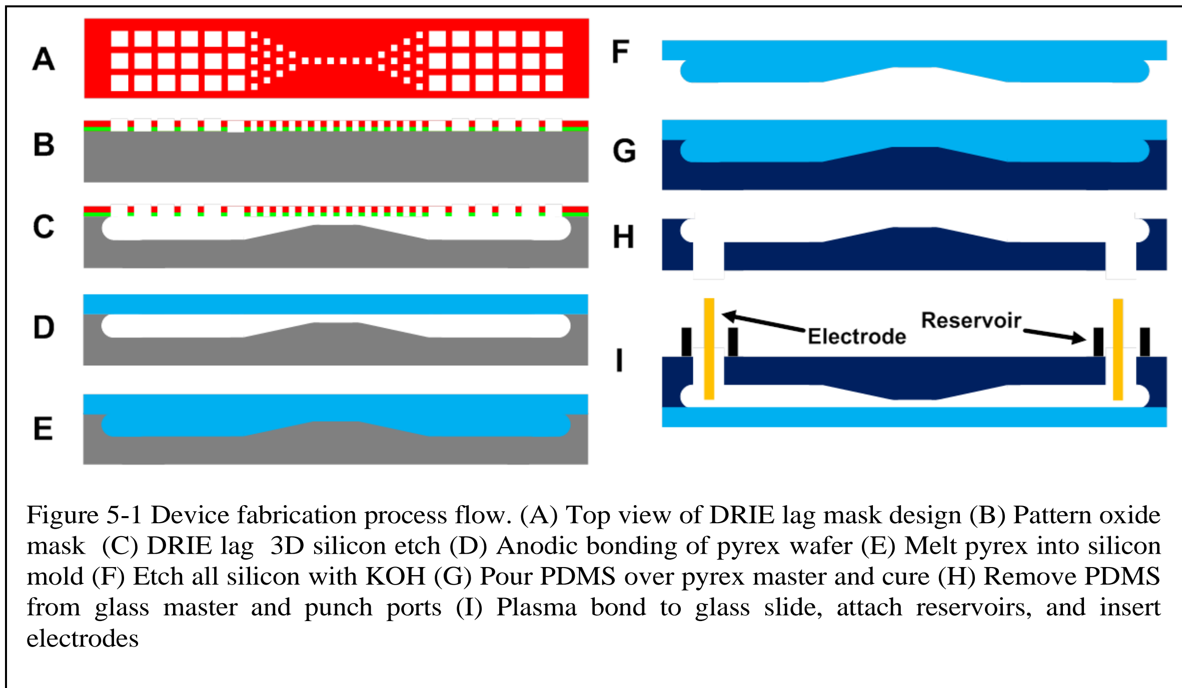

Figure 5-1 Device fabrication process flow. (A) Top view of DRIE lag mask design (B) Pattern oxide mask (C) DRIE lag 3D silicon etch (D) Anodic bonding of pyrex wafer (E) Melt pyrex into silicon mold (F) Etch all silicon with KOH (G) Pour PDMS over pyrex master and cure (H) Remove PDMS from glass master and punch ports (I) Plasma bond to glass slide, attach reservoirs, and insert electrodes

the depth of 40μm for the constriction region between the posts (Figure 5-2).

5.3.2 Experimental Setup

A function generator (4079, BK Precision) was connected to a power amplifier (EW2350, Tegam) which provided up to 200V_{p-p} across a frequency range of DC to 1MHz. An oscilloscope (DL1300A, Yokogawa) was connected to the monitor output of the amplifier to observe the applied waveforms for distortion. The PDMS-based microfluidic devices were placed in vacuum for at least 30 min before experiments were run to reduce priming issues. The electrodes were placed in the fluid reservoirs, spaced 1cm apart. Experiments were observed using an inverted fluorescent microscope (Axio Observer Z1) and videos of all trapping experiments were acquired using a CCD color camera and a dual band excitation filter. One method of quantifying the effectiveness of the DEP trap is the use of light intensity measurements. All of the particles used in this work were fluorescent. During DEP trapping experiments, as the number of particles trapped in the DEP device increased, the intensity of the light also increased. Using ImageJ (NIH), a region of interest was chosen around the microposts, where the DEP trapping occurred, and the intensity of the light in this region was

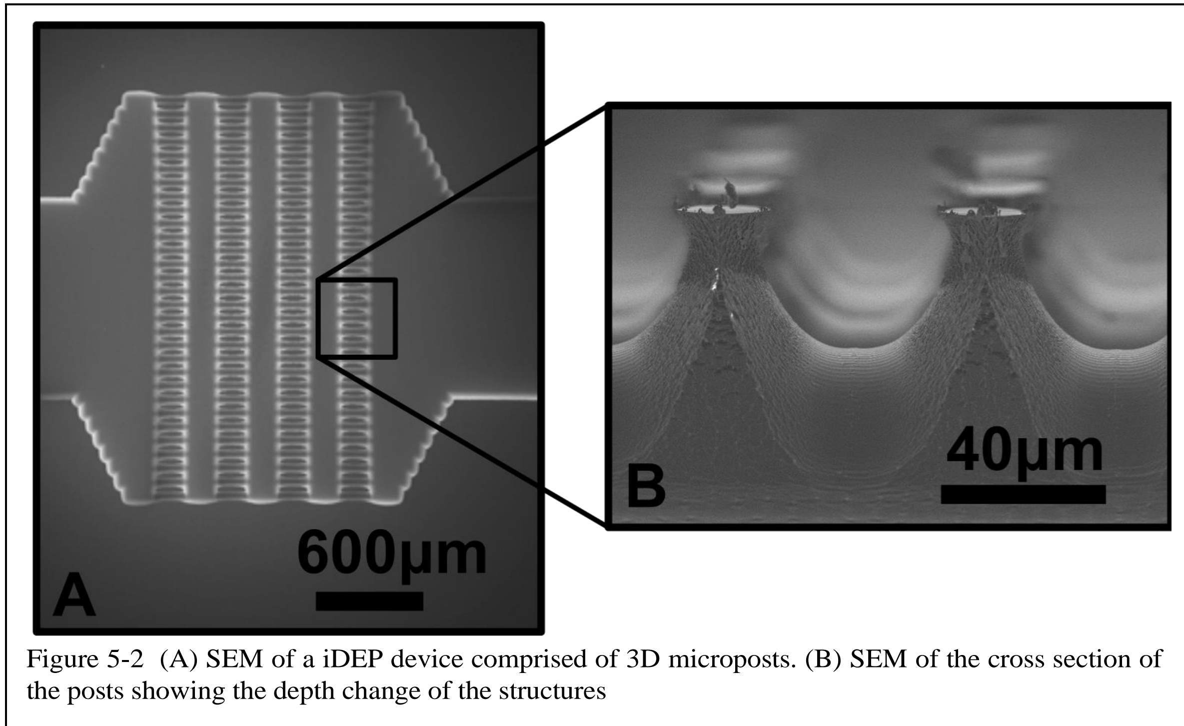

Figure 5-2 (A) SEM of a iDEP device comprised of 3D microposts. (B) SEM of the cross section of the posts showing the depth change of the structures

quantized for the last frame before the electric signal was removed. The size, shape and location of the region of interest were held constant throughout the experiments. These experiments were repeated ten times in random order and the results were averaged at each applied signal frequency.

5.3.3 Sample Preparation

Escherichia coli (E. coli) strain MG1655 was grown in LB medium containing 1% tryptone, 0.5% NaCl, and 0.5% yeast. Tetracycline was applied as the antibiotic at 5µg/mL concentration since the strain contained pHC60, a stably maintained plasmid that constitutively expresses GFP useful for fluorescent microscopy analyses. *Staphylococcus aureus (S. aureus)* (ATCC 12600) was cultured in brain heart infusion media. All controls were cultured in 100 mL of their respective broth medium at 37 °C and 165 rpm to the exponential growth phase (OD600 ~0.5). Cells were transferred into two sterile 50 ml centrifuge tubes and subjected to three washes by centrifugation (5000 × g for 10 min) and resuspension in 1X PBS. Quantification of bacteria was done microscopically using a hemocytometer (counting chamber), and by colony forming unit (CFU) counting of dilutions where colony numbers ranged between 30 and

300. For all experiments, *E. coli* cells, *S. aureus* cells, and red fluorescent polystyrene beads (Flourospheres, Invitrogen) were centrifuged and resuspended 3 times in DI water with a measured conductivity of 800 μS/m. No surface modifications were made to the beads. The DI water conductivity was measured with a solution conductivity meter (SG7, Mettler Toledo, Scherzenbach, Switzerland). The cells were diluted to a final concentration of 1×10^8 cells/mL. For experiments with a mixture of fluorescent beads and *E. coli*, the fluorescent beads were also diluted to a concentration of 1×10^8 beads/mL. For the live/dead separation experiments, dead cells were obtained by heating an aliquot of live cells for 20 min at 80°C. Live and dead *S. aureus* cells were then labeled with the Syto 9 and propidium iodide stains from the Live/Dead Baclight Bacterial Viability Kit (Molecular Probes, Eugene, OR). The solutions of live and dead cells were then mixed in equal parts.

5.4 Results

5.4.1 Characterization of Particles

E. coli, and 1 μm and 4 μm polystyrene beads suspended in DI water were placed in the channel. Particles which are different in size can be separated easily due to the cubed radius term in the DEP force shown in equation 5-1. For example, with this device, we observed 100% trapping of 4μm polystyrene beads with an applied DC potential of 30V. Both *E. coli* and 1μm polystyrene beads trapped at DC potentials of 100V. Thus, while the 4μm beads may be separated from *E. coli* with DC fields, the 1 μm beads require a more complex separation strategy.

The frequency response of the *E. coli* was evaluated by holding α constant at 19 (10 VDC and 190 VAC_{pp}) and sweeping the frequency from 1kHz to 600kHz. Under these conditions, both pDEP and nDEP trapping of *E. coli* was observed (Figure 5-3A and 5-3B). The observed nDEP trapping was able to trap 100% of the *E. coli* that passed through the constriction region; however, the pDEP trapping was much weaker and was only able to trap approximately 20% of the *E. coli*. Trapping was measured after 30 seconds of applied field by quantifying the intensity of the fluorescent in the

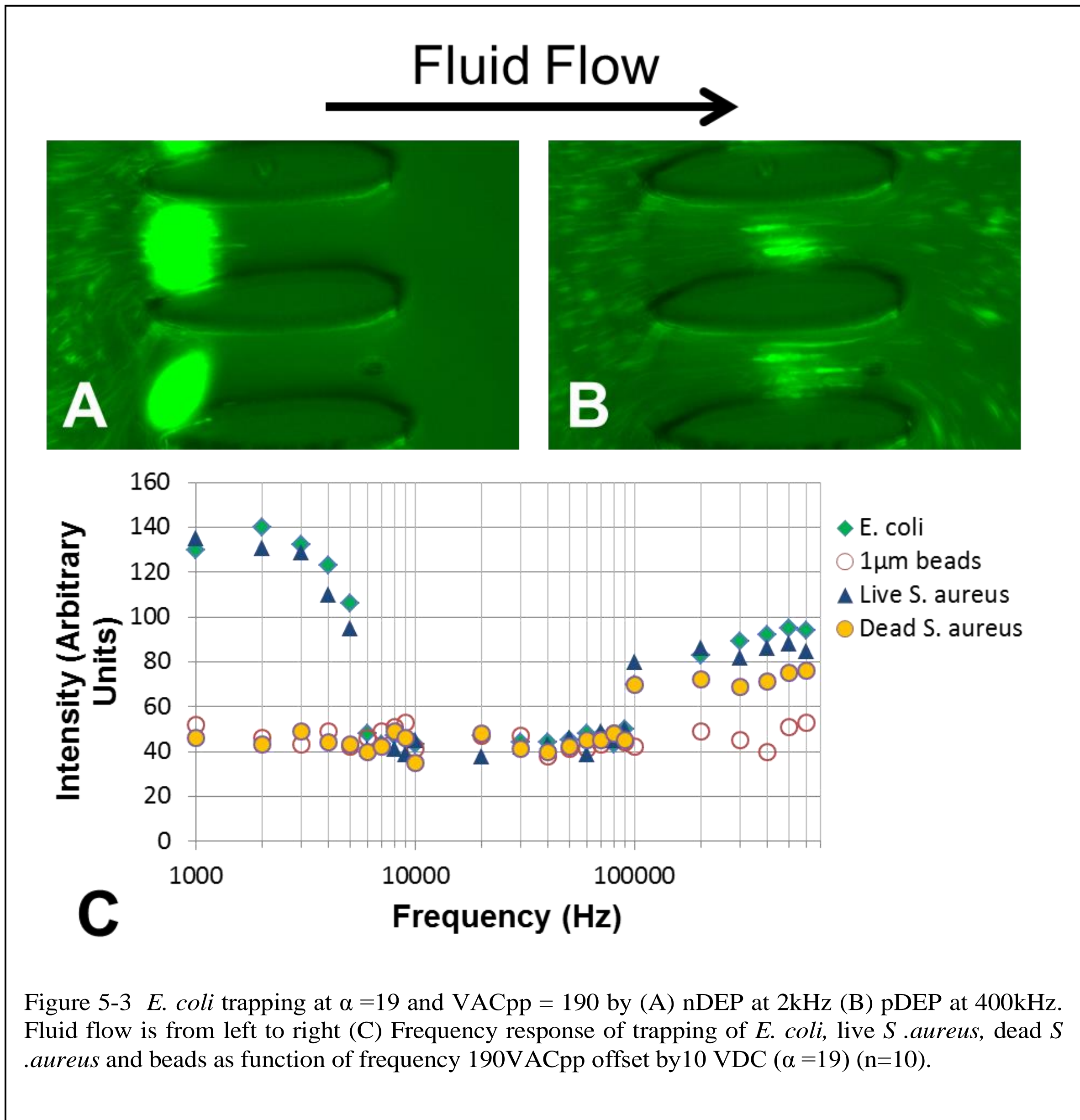

Figure 5-3 *E. coli* trapping at α =19 and VACpp = 190 by (A) nDEP at 2kHz (B) pDEP at 400kHz. Fluid flow is from left to right (C) Frequency response of trapping of *E. coli,* live *S .aureus,* dead *S .aureus* and beads as function of frequency 190VACpp offset by10 VDC (α =19) (n=10).

trapping region of the device (Figure 5-3C). As seen in Figure 5-3C, when no trapping occurred, the background fluorescent intensity observed was between 20-40 arbitrary units (AU). This resulted neither from particle trapping or fouling but from particles moving through the trapping region. In other words, only intensities above 40 AU indicate DEP trapping. Particles trapped in the upstream half of the constriction were under pDEP while those trapped in the downstream half of the constriction were under nDEP. The *E. coli* showed nDEP trapping below 5kHz and pDEP above 100kHz with no trapping between 6kHz and 90kHz, putting the DEP crossover frequency in this region. The frequency response of the polystyrene beads suspended in DI water was

evaluated with the same methodology. The beads did not show any observable response to the AC fields. This indicates that the *E. coli* are more responsive to high α DEP in this frequency range. These tests were repeated for both live and dead *S. aureus* cells as well. As shown in Figure 5-3C, it was observed that the live *S. aureus* cells behaved very similar to the *E. coli* cells in both the positive and negative DEP regimes. This is not surprising as it has been previously reported that *S. aureus* and *E. coli* have similar DEP responses below 1MHz [170]. The dead S. aureus cells, however, performed very differently. At frequencies below 10khz, there was no observable response from the dead cells. pDEP of the dead cells was observed at frequencies of 100kHz although the trapping was observed to be slightly weaker than that of live cells at high frequencies.

5.4.2 Separation of Particles

E. coli and 1μm beads were mixed into a single solution in DI water and placed in the channel. Similar, live and dead *S. aureus* were mixed into a single solution in DI water and placed in a separate channel. Separation was obtained by fixing the frequency to 2kHz for nDEP and 400kHz for pDEP to maximize *E. coli* and live *S. aureus* trapping. Holding the magnitude of the sum of VDC and VAC_{pp} constant at 200V, the value of α was varied. After 30 seconds, the intensity of the different colors were quantified in the trapping region. Figure 5-4A and Figure 5-4B show the results for operation at 2kHz and 400kHz, respectively. The background fluorescent intensity was observed to be between 20-40 AU. This means only values above 40 indicate particle consistent accumulation and trapping. The trapping of all particles increased with decreasing α due to the increased electroosmotic fluid flow and hence larger number of particles crossing the trapping region in the 30s timeframe.

For both the pDEP and nDEP frequencies, the *E. coli* separated easily from the beads for high values of α. However, for low values of α both *E. coli* and beads were trapped as the DC component of the DEP force became more dominant. If the extreme is considered, when α = 0 and only DC fields are applied, both *E. coli* and 1um beads are trapped making separation very difficult. It should be noted that all observed trapping of beads was nDEP due to the DC component of the applied signal. While there was some fouling of polystyrene beads in the channel, no beads were observed

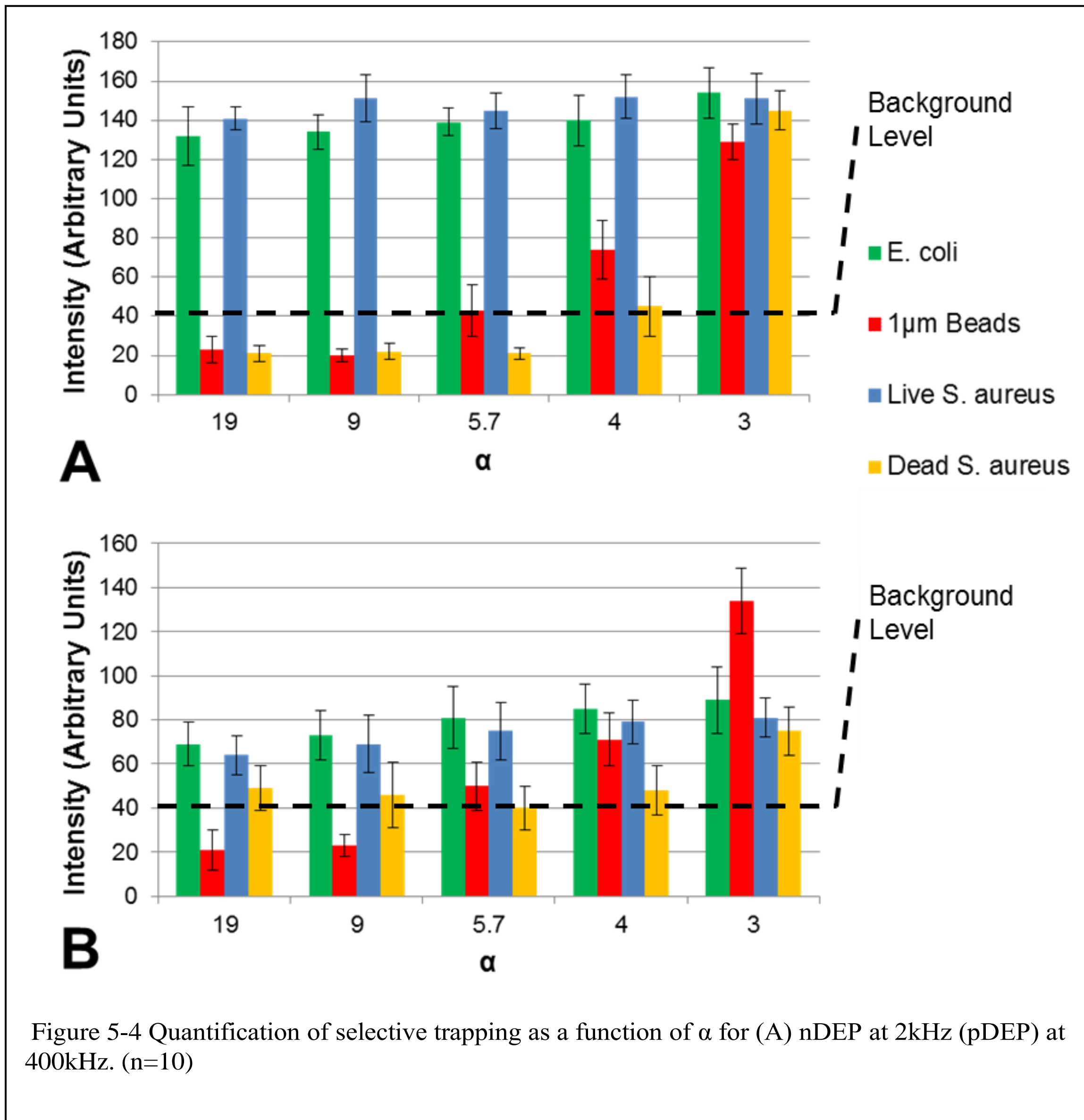

Figure 5-4 Quantification of selective trapping as a function of α for (A) nDEP at 2kHz (pDEP) at 400kHz. (n=10)

trapping at α = 9 or 19 (Figure 5-5). Figure 5-5A and 5-5B show the *E. coli* being trapped and then release back into the sample, when the AC voltage is removed. Using these operating conditions, it is possible to completely separate the *E. coli* in a sample from the beads by running the entire sample through the device to selectively trap *E. coli* and then running a clean media through the device and releasing the bacteria.

At 2 kHz, live and dead *S. aureus* separated readily for all conditions except the lowest value of α test (Figure 5-4A). For these conditions, the live cells trapped while the dead cells passed through the DEP trap, unaffected. At 400kHz, separation was much more difficult. For all values of α tested, more live cells trapped than dead cells (Figure 5-4B). However, neither the trapping of live cells nor the separation from dead

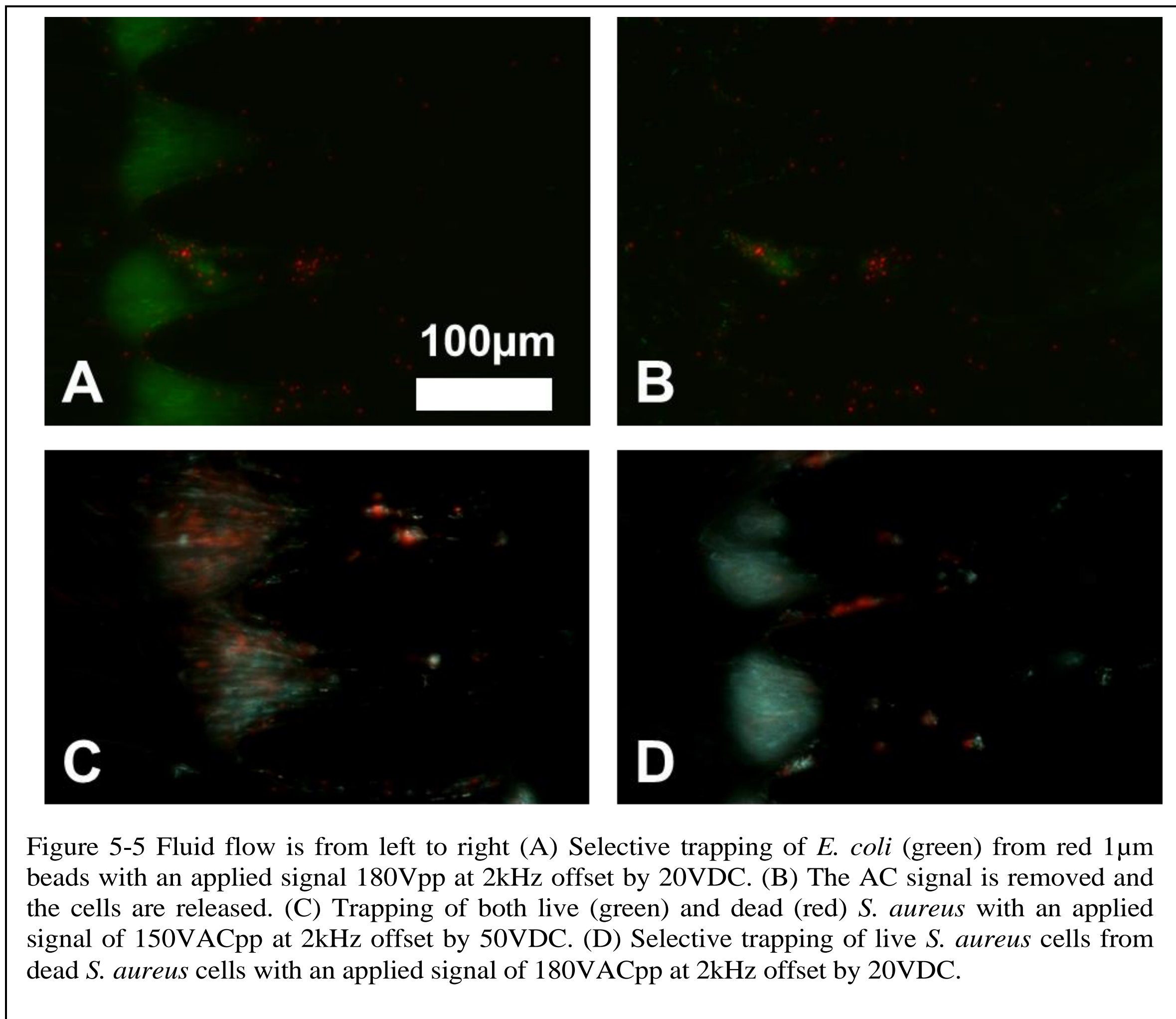

Figure 5-5 Fluid flow is from left to right (A) Selective trapping of *E. coli* (green) from red 1μm beads with an applied signal 180Vpp at 2kHz offset by 20VDC. (B) The AC signal is removed and the cells are released. (C) Trapping of both live (green) and dead (red) *S. aureus* with an applied signal of 150VACpp at 2kHz offset by 50VDC. (D) Selective trapping of live *S. aureus* cells from dead *S. aureus* cells with an applied signal of 180VACpp at 2kHz offset by 20VDC.

cells was completely efficient. Some dead cells were found to reversibly trap at all values of α. Thus separation in the nDEP regime is preferred. Figure 5-5C shows an example of an nDEP regime trapping of both live and dead *S. aureus* for a low value of α. Conversely, Figure 5-5D shows trapping of live *S. aureus* but not dead *S. aureus* for high value of α.

5.5 Discussion and Concluding Remarks

In this paper we have: (1) presented the first reported trapping based 3D DC-biased AC field iDEP device, (2) demonstrated the first reported bacteria trapping in a DC-biased AC field iDEP device, (3) performed separation of *E. coli* and polymer beads, and (4) performed separation of live and dead *S. aureus*.

The present device successfully trapped 1µm bioparticles with a total voltage of 200V which is the lowest reported for trapping with a DC-biased AC field iDEP device to date. The closest, is a work by Lewpiriyawong et al., who demonstrated trapping of 5µm diameter yeast cells in a 2D channel with a total voltage of 600V[166]. It should be noted that the yeast cells were larger than the bacteria used in this work, and thereby easier to trap according to Equation 5-1. Several others have demonstrated DC-biased AC field iDEP devices which operate at lower voltages for particle deflection, however significantly weaker DEP forces can be used for those techniques[164, 165].

The reason for the decreased operating voltage is the 3D structures. As we have demonstrated previously[168], 3D iDEP devices can operate at significantly lower voltages than 2D devices. iDEP devices create the nonuniform electric field necessary for DEP by forcing the electric current in fluidic channel to curve around insulating structures. This concentrates the current density in some areas more than others, creating electric field gradients. The larger the geometric gradient of the channel walls, the larger the electric field gradient will be. 3D fabrication provides a method to increase the geometric gradient of the channel walls for a fixed device size.

Separation of *E. coli* from polystyrene beads was found to be very easy in both the pDEP and nDEP regimes for high values of α. Thus a large AC component enables a finer control over the separation. This is due to the fact that at DC, the particles are both insulators of similar size and experience similar DEP forces. Therefore, while separation may be possible with only a DC potential, it is much more difficult. On the other hand, increasin the DC component increases the flow rate and throughput of the device. For optimum performance, the separation should be carried out at the lowest α for which no bead traps, which was experimentally found to be $\alpha = 9$.

The ability to separate live *S. aureus* cells from dead *S. aureus* cells is due to differences in the cell membrane. When a cell dies, the membrane become permeable, increasing its conductivity by four orders of magnitude [30]. This change is particularly important at low applied signal frequencies since the cell membrane dominates f_{CM} at low frequencies. This explains how the live and dead cells readily separated in the nDEP regime. At high frequencies the membrane is not as dominant, which increases the difficulty of the separation. This was reflected experimentally by a decrease in

selectivity in the pDEP regime.

These results show the feasibility of selectively trapping bio-particles with either positive or negative DEP in the same iDEP device using DC-biased AC fields. Due to the flexibility, selectivity, economy of fabrication, and portability of these devices, they have the potential to realize critical bioparticle applications such as monitoring drinking water for harmful pathogens.

6 Off-chip Passivated-electrode, Insulator-based Dielectrophoresis (OπDEP)

6.1 Introduction

Dielectrophoresis Dielectrophoresis (DEP) is a well-known electric field based technique for separating, moving, and trapping micron-scale particles. DEP has been shown to be particularly useful for characterizing biological cells. The small size of cells (~1-10 μm) allow for the necessary high electric fields to be generated with relatively low applied voltages. The other strength of DEP is that it allows for many independent variables, such as signal magnitude, signal frequency, signal waveform, and electrode spacing to be used to control the manipulation. This results in the ability to separate very similar particles. Thus, the technique has spread to a wide range of biological applications including bacteria[171], yeast[8], mammalian cells[9], viruses[10], and proteins[11].

Traditionally, electrode-based DEP (eDEP) devices create nonuniform fields with electrode designs including sharp electrodes and narrowly spaced electrodes[14-17]. Indeed, the majority of DEP devices reported in literature utilize microfabricated electrodes. The use of micropatterned electrodes allows for strong local electric fields, however, it increases the cost and complexity of fabrication. For biological applications, both avoiding contamination and device cost are a concern, thus it is desirable for the microfluidic components to be low cost and disposable.

Alternatively, insulator-based DEP (iDEP) uses insulating structures rather than electrode arrays to produce the nonuniform fields needed to drive DEP and to remove the threat of gas evolution due to electrolysis[31]. iDEP microfluidic devices have been used to manipulate a wide range of particles including bacteria, viruses, cells, and beads[26-29]. In iDEP devices, the electric voltages are applied along the entire length of the microchannels which leads to a large heat buildup[110]. Also, the electrodes must be brought in contact with the solution, which can lead to contamination issues.

In this paper, we present the first reported off-chip passivated-electrode, insulator-based dielectrophoresis microchip (OπDEP). This technique allows for inexpensive devices to create strong DEP forces with low Joule heating, leading to a

high throughput microfluidic system. Our device uses insulting structures within the channel as well as parallel electrodes to create DEP forces by the same working principle that iDEP devices use. Additionally, unlike eDEP and iDEP, no physical electric connections are made to the microfluidic chip. Thus, a new, inexpensive microfluidic chip may be used for each experiment while the electrodes may be reused. The resulting devices create DEP forces which are larger by roughly two orders of magnitude for the same applied voltage when compared to eDEP which relies on parallel electrodes alone to produce the DEP forces. In order to demonstrate this technology, we trapped Escherichia coli (*E. coli*), a known waterborne pathogen, from water samples at flow rates as high as 1200 μl/hr. We also selectively concentrated bacteria from a suspension of polystyrene beads.

6.2 Theory

A schematic of the OπDEP devices is shown in Figure 1. The device is composed of a permanent, reusable set of electrodes and a disposable, polymer microfluidic chip with microposts embedded in the channel. The microfluidic chip fits onto the electrodes as a disposable cartridge. The device operates by capacitively coupling the electric fields into the microfluidic channel. Figure 1C shows the dominant forces acting on a particle within the device. The main force balance that occurs on a particle is between the dielectrophoresis force and the hydrodynamic drag force.

Dielectrophoresis is the motion of polarizable particles that are suspended in an electrolyte when subjected to a spatially nonuniform electric field[6]. The DEP force felt by a spherical particle suspended in a medium is:

$$\mathbf{F_{DEP}} = 2\pi R^3 \varepsilon_m \mathrm{Re}[f_{CM}]\, \nabla(\mathbf{E} \bullet \mathbf{E}) \qquad (6\text{-}1)$$

where R is the radius of the particle, ε_m is the permittivity of the medium, **E** is the local electric field. $\mathrm{Re}[f_{CM}]$ is the real part of the Clausius-Mossotti (CM) factor which is:

$$f_{CM} = (\varepsilon_p^* - \varepsilon_m^*)/(\varepsilon_p^* + 2\varepsilon_m^*) \qquad (6\text{-}2)$$

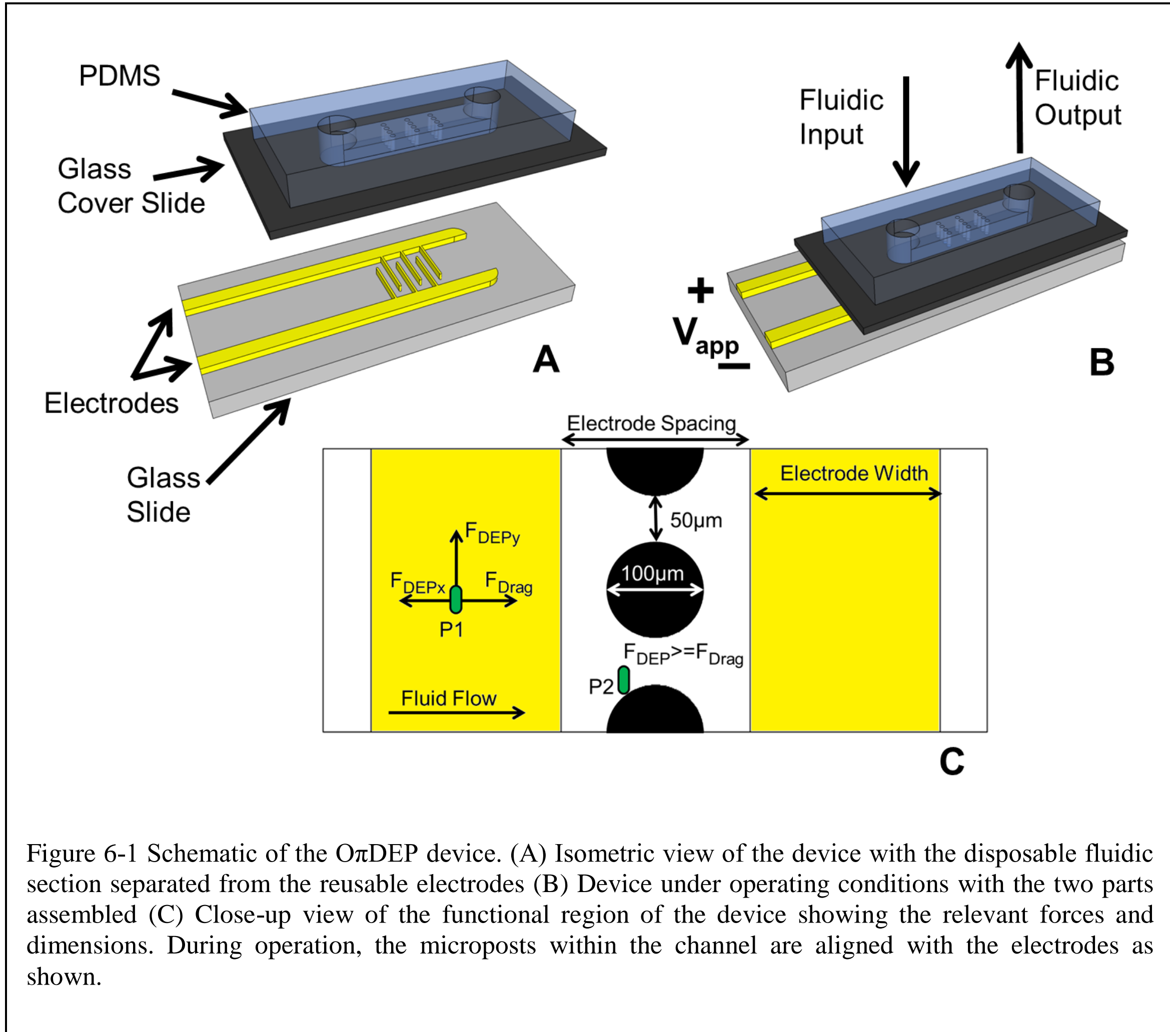

Figure 6-1 Schematic of the OπDEP device. (A) Isometric view of the device with the disposable fluidic section separated from the reusable electrodes (B) Device under operating conditions with the two parts assembled (C) Close-up view of the functional region of the device showing the relevant forces and dimensions. During operation, the microposts within the channel are aligned with the electrodes as shown.

where ε_p^* and ε_m^* are the complex permittivities of the particle and the medium, respectively. Complex permittivity is defined as:

$$\varepsilon^* = \varepsilon + \sigma/(j\omega) \qquad (6\text{-}3)$$

Thus, $\mathbf{F_{DEP}}$ will fluctuate greatly depending on the operating frequency and even change direction. At DC and very low frequency fields, DEP separation of bioparticles is mostly dominated by the size difference of the particles due to the cubed radius term and the low conductivity of cellular membranes. However, at high frequencies, the fields are able to penetrate the cell membrane into the electrically conductive cytoplasm. Consequently, cells can have a higher DEP frequency dependency than

solid particles. If a particle is attracted to a region with a high electric field, it experiences positive DEP (pDEP). Conversely, if a particle is repelled by a region with a high electric field, it experiences negative DEP (nDEP). As the DEP force on a particle passes from pDEP to nDEP or vice versa in frequency space, a frequency point exists where the DEP force on a particle is zero, regardless of the magnitude of the electric field gradients. This point is known as a crossover frequency.

Fluid is moved through the channel by a pressure driven flow. The drag force on a spherical particle in a fluid at a low Reynold's number is given by:

$$\mathbf{F}_{\mathbf{Drag}} = 6\eta R\pi(u_{pf}) \tag{6-4}$$

Where R is the radius of the particle, η is the viscosity of the fluid, and u_{pf} is the relative velocity of the particle with respect to the fluid. For a particle in our DEP devices, a force balance occurs between drag and dielectrophoresis as shown by particle P1 in Figure 1C. In order for a particle to become trapped in these devices, the DEP force must overcome the drag force on the particle ($\mathbf{F}_{\mathbf{DEP}} >= \mathbf{F}_{\mathbf{Drag}}$) as shown by particle P2 in Figure 1D. Thus, DEP trapping becomes more difficult as the fluid velocity is increased.

As Equation 1 shows, the DEP force is proportional to the gradient of the electric field squared. In our design, insulating structures within the channel enhance this gradient and greatly increase the DEP force over the interdigitated electrode design. This enables the device to operate at high flow rates and low frequencies.

6.3 Methods and Materials

6.3.1 Device Designs

Three different designs are used in this work (Table 1). The microfluidic channel for all the devices has a cross section of 2 mm x 50 µm and a length of 2 cm. Device 1 is similar to a previously reported design[172] consisting of a microfluidic channel with no features and electrodes with a width of 200 µm and a spacing of 200 µm. This design is present in this work to compare to the innovative designs. The DEP

	Electrode Width	Electrode Spacing	Microposts Present?
Device 1	200 µm	200 µm	No
Device 2	200 µm	200 µm	Yes
Device 3	4 mm	600 µm	Yes

Table 6-1 Design parameters for each of the different devices.

forces in this device rely on nonuniform fields created by the presence of the off-chip electrodes. Devices 2 and 3, which are the new designs and the focus of this study, use a microfluidic channel with 100 µm diameter PDMS posts which are spaced 50 µm apart. In these devices, the insulating structures create the nonuniform fields necessary for DEP. Device 2 uses electrodes with a width of 200 µm and a spacing of 200 µm, the same as Device 1 for evaluation purposes. Device 3 has much larger electrodes with a width of 4 mm and a spacing of 600 µm. The wider electrodes of Device 3 increase the capacitive coupling between the electrodes and the microfluidic channel, which enables DEP trapping at lower frequencies.

6.3.2 Numerical Device Modeling

In order to investigate the electric field distributions within the microchannel, a numerical model of the devices was created using COMSOL Multiphysics 3.5 (COMSOL Inc., Burlington, MA) using the AC/DC module. 3D models were created of the three devices in this study. The electrical conductivities used for PDMS, glass, air, and deionized water are 8.20×10^{-13} S/m, 1.25×10^{-9} S/m, 3.00×10^{-9} S/m, and 8.00×10^{-4} S/m, respectively. The electrical permittivities used for PDMS, glass, air, and deionized water are 2.65, 4.65, 1, and 80, respectively. As for the boundary conditions, the electrodes were given AC electric potentials and all other boundaries were set to electrical insulation. The purpose of the simulations was to evaluate the values of $\nabla|E|^2$ as a function of position and frequency. Equation 1 shows that for a given particle and medium, $\nabla|E|^2$ is proportional to the DEP force felt by a particle. Thus the performance of the device should be predicted by these simulations.

6.3.3 Device Fabrication

The two-port microchannel devices are 2 cm-long, 2 mm-wide, and 50 µm-deep fabricated in polydimethylsiloxane (PDMS). A <100> silicon wafer was patterned with photoresist (AZ9200) and etched using an Alcatel AMS-100 Deep Reactive Ion Etcher (DRIE) to obtain the structures. Photoresist was stripped and the wafer was then used as a master mold for PMDS. Liquid PDMS (Sylgand 184 Silicon elastomer kit, Dow Corning, Midland, MI) was mixed to a 10:1 ratio of PDMS monomer and curing agent and poured onto the silicon mold. The setup was put into a vacuum chamber for 2 hours to remove gas bubbles and then cured for 45 min at 100 ºC. Next, 2 mm holes were punched into microchannels for fluidic ports. Finally, the PDMS was plasma bonded to a #0 micro cover glass (Electron Microscopy Sciences) which is approximately 100 µm thick, forming the microfluidic cartridge.

On a separate Pyrex substrate, electrodes were formed using the lift-off technique. The substrate was patterned with photoresist (AZ9260, AZ Electronic Materials). Next, using e-beam evaporation (PVD-250, Kurt J. Lesker Company), a thin layer (25 nm) of chrome and then a thicker layer (200 nm) of gold was deposited. The excess metal was removed by dissolving the photoresist in acetone. As a technical note, a printed circuit board (PCB) could be used for the electrode patterning if the transparency of the substrate is not crucial.

During device operation the microfluidic cartridge is placed onto the electrode substrate and aligned such that the insulating structures in the micrchannel are visible between the electrodes. It should be noted that the alignment does not have to be very precise. As long as the microposts are present between in the electrodes, the devices will operate. The electric fields are capacitively coupled into the microfluidic channel and the nonuniform fields necessary for DEP are created by the insulating structures in the channel. After running an experiment, the PDMS microfluidic device was easily removed from the electrodes and a new device was placed on the electrodes.

6.3.4 Cell Preparation

Escherichia coli (*E. coli*) strain MG1655 was grown at 37 °C in LB medium containing 1% tryptone, 0.5% NaCl, and 0.5% yeast to a concentration of 4×10^8 cells/ml. Tetracycline was applied as the antibiotic at 5µg/ml concentration since the strain contained pHC60, a stably maintained plasmid that constitutively expresses GFP useful for fluorescent microscopy analyses. For all experiments, *E. coli* cells, red fluorescent 1 µm beads (Flourospheres, Invitrogen), or both were centrifuged and resuspended 3 times in DI water with a measured conductivity of 800 µS/m. No surface modifications were made to the beads. The DI water conductivity was measured with a solution conductivity meter (SG7, Mettler Toledo, Scherzenbach, Switzerland). The cells were diluted to a final concentration of 1×10^8 cells/ml. For experiments with a mixture of fluorescent beads and *E. coli*, the fluorescent beads were diluted to a concentration of 1×10^8 beads/ml. It should be noted that due to a lack of nutrients in the DI water, the *E. coli* cells will eventually die if they are not resuspended in a media with nutrients. However, using a flourescdent stain viabilitiy kit (Live/Dead BacLight, Invitrogen) the *E. coli* cells were found to be over 95% viable after being suspended in the DI water for 1 hour. This ensured that the experiments were being performed on live *E. coli* cells.

6.3.5 Experimental Setup

A function generator (4079, BK Precision) was connected to a power amplifier (EW2350, Tegam) which excited the reusable electrodes with an AC signal of 400 V peak to peak (V_{pp}) with frequencies from 1 kHz to 1 MHz. An oscilloscope (DL1300A, Yokogawa) was connected to the monitor output of the amplifier to observe the applied waveforms for distortion. The PDMS-based microfluidic devices were placed in vacuum for at least 30 minutes before experiments were run to reduce priming issues. During device operation, the solution was passed through the OπDEP device using a 1 ml syringe connected to syringe pump (NE-1000, New Era Pump Systems Inc) to a waste reservoir. Once the device was primed, fluid was continually moved through the channels at 50 µL/hr for 5 minutes prior to the beginning of the experiments. DEP

trapping experiments were observed using an inverted fluorescent microscope (Axio Observer Z1) and videos of all trapping experiments were acquired using either a CCD monochrome camera (Axiocam MRm) or a CCD color camera (AxioCam MRc). For experiments where red beads and green stained *E. coli* were mixed, the optical filter was changed between red and green from frame to frame to distinguish the different particles.

For a single DEP trapping experiment data point, the flow rate of interest would be applied for 15 seconds to stabilize the flow velocity. Then, the electric signal would be switched on and the DEP trapping would be recorded by video. The signal switched off after 30 seconds and bacteria were released. The microchannels were inspected before every run and cleared of fouled bacteria by increasing the flow rate of the syringe pump when necessary. Thus, each data point included only bacteria trapped during that run.

One method of quantifying the effectiveness of the DEP trap is the use of light intensity measurements. The *E. coli* cells used in this work expressed GFP which acted as a fluorescent stain. During DEP trapping experiments, as the number of *E. coli* cells trapped in the OπDEP device increased, the intensity of the light also increased. Using ImageJ (NIH), a region of interest was chosen around the microposts, where the DEP trapping occurred, and the intensity of the light in this region was quantized for the last frame before the electric signal was removed. The size, shape and location of the region of interest were held constant throughout the experiments. These experiments were repeated ten times in random order and the results were averaged at each applied signal frequency.

Another performance metric for the experiments is the capture efficiency (CE) which is defined as:

$$CE = [(I - O)/I] \times 100\% \quad (5)$$

where I is the number of incoming bacteria observed on a single frame of the trapping video, O is the number of outgoing or escaped bacteria observed on a single frame of the trapping video. These measurements were made by counting the bacteria upstream

(I) and downstream (O) of the trapping region in the individual frames of the videos taken during the experiments. The regions used for counting I and O were the identically sized rectangles and remained constant for the experiments. Ten fluid flow velocity sweeps from 100 μl/hr to 1500 μl/hr were each completed in random order. To obtain a data point representing one flow rate, values of I and O were averaged over the ten flow sweeps. For cases where bacteria remained in clusters after being released, the clusters were assumed to be flat and the size of the cluster was used to estimate the number of bacteria in the cluster. It should be noted that if clusters had multiple bacteria stacked in depth, then this method would underestimate the number of bacteria.

6.4 Results and Discussion

6.4.1 Numerical Modeling

The results from the numerical model are displayed in Figure 2. In Figure 2A and 2B, the 3D geometry used is shown next to the $\nabla(\mathbf{E}\bullet\mathbf{E})$ slice plot for an applied signal of 400 V_{pp} at 300 kHz. It should be noted that the simulation for Device 3 is not shown here as it is much larger than devices 1 and 2 due to the 4 mm electrodes. However, the electric field distribution for device 3 is virtually identical to that of device 2. Figure 2A shows the electric field gradients in Device 1 with a peak gradient of about 3.2 x 10^{13} $[(m\bullet kg^2)/(s^6\bullet A^2)]$. Figure 2B shows the electric field gradient in Device 2 with a peak gradient of about 2.3 x 10^{15} $[(m\bullet kg^2)/(s^6\bullet A^2)]$. This means for a given applied signal, the introduction of the insulating posts within the channel increases values of $\nabla(\mathbf{E}\bullet\mathbf{E})$ by two orders of magnitude when compared to the previously reported electrode-only design. This is an important result as equation 1 shows that $\nabla(\mathbf{E}\bullet\mathbf{E})$ is proportional to the DEP force on a particle. The other significant result is the location of the high field gradients. For device 1, the highest field gradients occur directly over the electrodes whereas for Device 2 the highest field gradients occur near the insulating structures and away from the electrodes. This is a common characteristic of iDEP devices[26]. The advantage of having the peak electric field gradients away from the electrodes is a practical one. Particle fouling in the

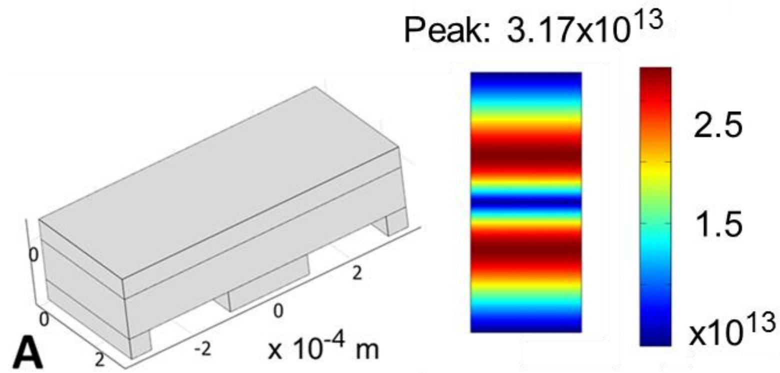

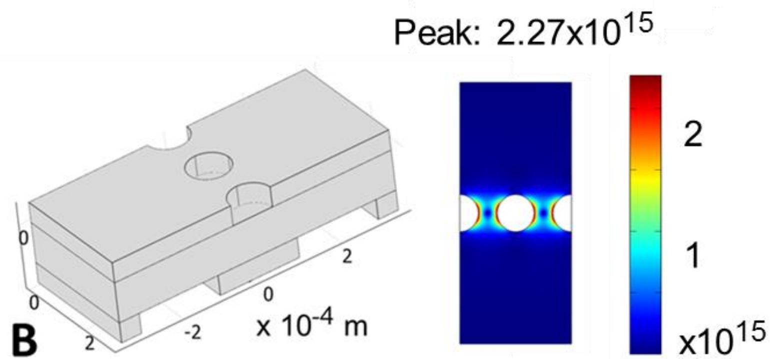

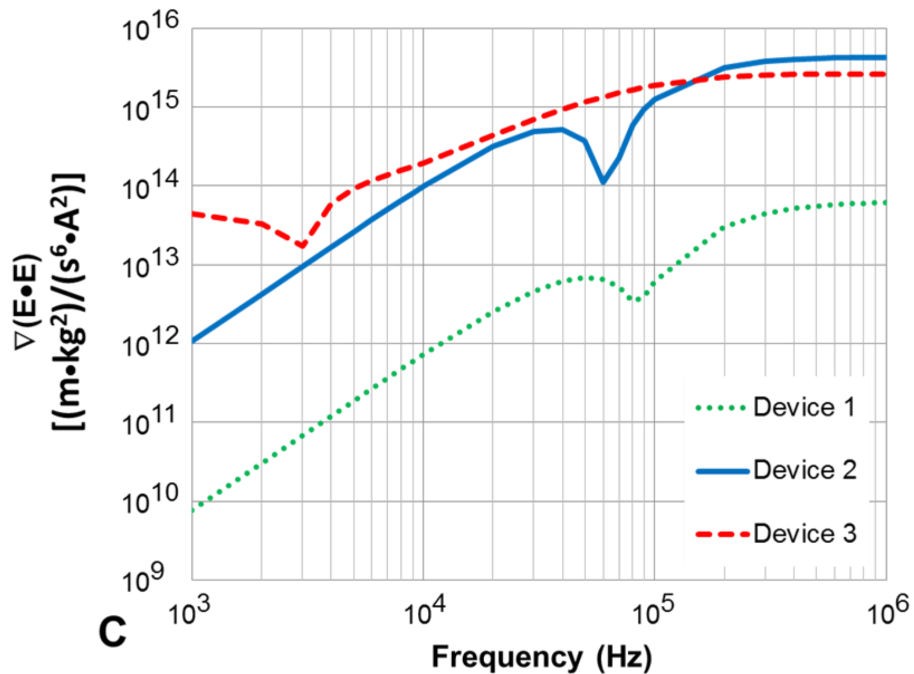

Figure 6-2 COMSOL simulations of electric field gradients in the OπDEP devices. The PDMS roof of the devices has been removed from the figure for clarity (A) ∇(E•E) at 300 kHz in previously reported Device 1 without microfluidic structures (B) ∇(E•E) at 300 kHz in OπDEP Device 2 (C) Maximum values of ∇(E•E) as a function of frequency

microchannel tends to occur in DEP devices where the strongest DEP forces are present. For eDEP devices, such as Device 1, this is at the electrodes. This can effectively add another passivation layer to the electrodes, which will weaken the electric fields and lower the performance of the device. However, for iDEP devices, such as Device 2, fouling will tend to occur at the insulating structures and not over the electrodes. Thus, the electric fields will remain high in the device until enough particles have fouled to completely clog the device.

Figure 2C shows the frequency response of the DEP devices. As the plot shows, OπDEP devices create much larger electric fields over a large frequency range. Furthermore, Device 3 creates larger electric field gradients at low frequencies when compared to Device 2. This is due to the increased capacitance of the very large electrodes for Device 3. The maximum gradient reached with Device 3 is less than that of Device 2, however, this is due to the increased electrode spacing. The larger spacing was simply a practical consideration as it made alignment simpler. This increased capacitance effectively shifts the graph of the frequency response to lower frequencies. Thus, the local minimum between 10^4 Hz and 10^5 Hz on for device 2 is moved to between 10^3 Hz and 10^4 Hz. In summary, electrode design in Device 3 yields higher electric field gradients over a wider frequency range but with the cost of a larger device size and less compactness.

6.4.2 Frequency Response

Bacteria trapping experiments were performed on all devices with the applied electric signal of 400 V_{pp}. When there was no fluid flow in the channel, bacteria in Device 1 were observed moving toward the electrodes and forming pearl chains. This is typical behavior in DEP devices operating in the pDEP regime [20, 32, 103]. However, when any fluid flow was introduced, the DEP forces inside Device 1 were not strong enough to overcome the drag force on the bacteria. Therefore, no trapping was observed in Device 1 even at the lowest applied flow rate of 10 µl/hr. Conversely, in Device 2 and 3 not only did bacteria trap with applied fluid flow, the trapping attained 100% capture efficiency with flow rates up to 400 µl/hr. This clearly demonstrates that the OπDEP devices greatly outperform the off-chip electrode based devices [172] in

DEP trapping strength.

Figure 3 shows the experimental performance of the OπDEP devices at different applied frequencies but with a fixed flow rate of 400 μl/hr. As Figures 3A-3C show, the ability of the devices to trap *E. coli* cells varied with frequency. Figure 3D shows the quantification of the light intensity in the trapping region for Device 2 and 3 as a function of frequency. Device 1 is excluded from Figure 3D as DEP trapping could not be attained with applied fluid flow. It should be noted that the amplitude of the amplified signal began to attenuate at 400 kHz due to the power amplifier limitation. This led to a decrease in DEP trapping strength at higher frequencies. For Device 2, maximum trapping occurred at 300 kHz. At this frequency, no bacteria were observed escaping the trap and thus the CE was 100%. Device 3 attained a CE of 100% at a lower frequency, 100 kHz, and maintained 100% trapping until the bandwidth limit of the amplifier was reached.

These results match well with the numerical models. In the numerical models, the highest DEP forces are shown to be close to the microposts and decrease as the distance from the posts is increased. Thus, the minimum DEP force that a particle passing through the channel will experience is along the centerline between two posts. For weak DEP forces, particles near the posts may trap but not the particles traveling along the centerline. As the magnitude of the DEP force is increased, more particles will trap, increasing the efficiency of the device. When the magnitude of the DEP force is strong enough to trap a particle along the centerline, 100% CE will be obtained. Thus, increases in the DEP forces will result in higher trapping efficiencies. Since the electric field gradients in the device are dependent on frequencies, the trapping efficiencies will be as well.

The DEP force on a particle is dependent not only on the electric field gradients but also on the properties of the particle and the suspending medium. For *E. coli* suspended in a media with a conductivity of ~1 mS/m, the CM factor has been shown to increases monotonically from DC until after 1 MHz[35] leading to a monotonic increase in DEP trapping until 1 MHz[173]. Considering the particles and medium are held constant, the differences in performance of the devices are solely based on the differences in the electric field gradients ($\nabla(\mathbf{E} \bullet \mathbf{E})$) generated in the channel.

The local minimum in $\nabla(\mathbf{E}\bullet\mathbf{E})$ in Device 2 between 10^4 and 10^5 Hz predicted by the model appears in the experimental data as decreased trapping from 10^4 to 10^5 Hz. However, in Device 3, the local minimum is predicted to be between 10^3 and 10^4 Hz, where the DEP trapping is already weak. Thus, in the experiments, Device 3 did not have decreased trapping from 10^4 to 10^5 as Device 2 did. Instead, the *E. coli* trapping increased monotonically with frequency. It should be noted that some of the increased performance of Device 3 may be due to the fact that the wide electrodes may mitigate any losses from air gaps created by slightly warped glass cover slides. The thin electrodes of Device 2, however, would not be as resilient to imperfections in the assembly.

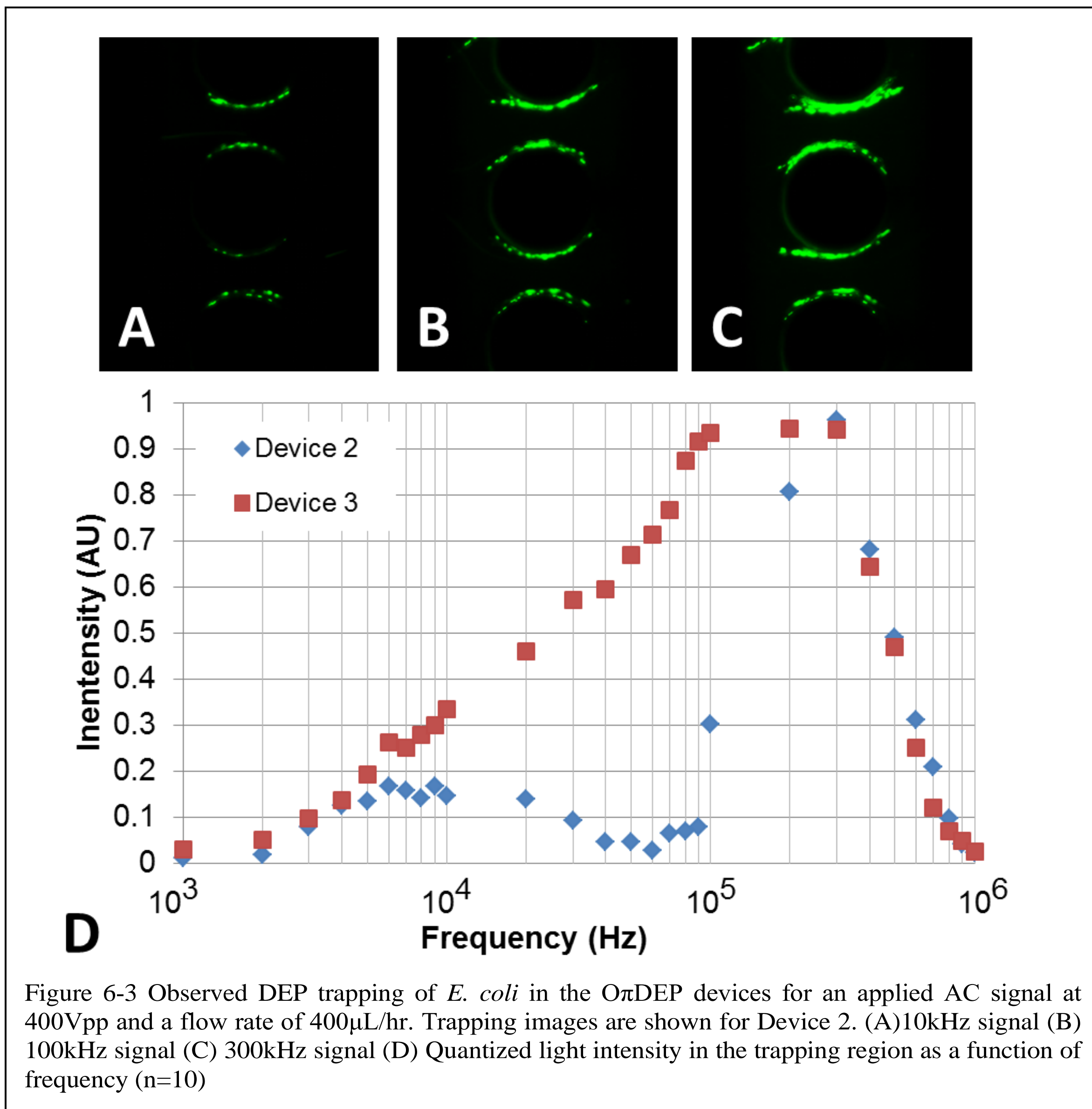

Figure 6-3 Observed DEP trapping of *E. coli* in the OπDEP devices for an applied AC signal at 400Vpp and a flow rate of 400µL/hr. Trapping images are shown for Device 2. (A)10kHz signal (B) 100kHz signal (C) 300kHz signal (D) Quantized light intensity in the trapping region as a function of frequency (n=10)

6.4.3 Flow Rate Tests

To determine the throughput of the devices, the flow rate was swept from 100 µl/hr to 1500 µl/hr. The applied electric signal was held constant at 400 V_{pp} and 300 kHz as this was the frequency at which both Device 2 and 3 experienced the highest trapping efficiency. Figure 4 shows the dependence of capture efficiency on flow rate. It should be noted that both devices performed very similarly with the mean values with 4% of each other, making the data points between the two hard to distinguish. Thus, for clarity, Figure 4D shows only the data from Device 2. The devices were able to obtain 100% CE consistently for flow rates up to 400 µl/hr. A decrease in capture

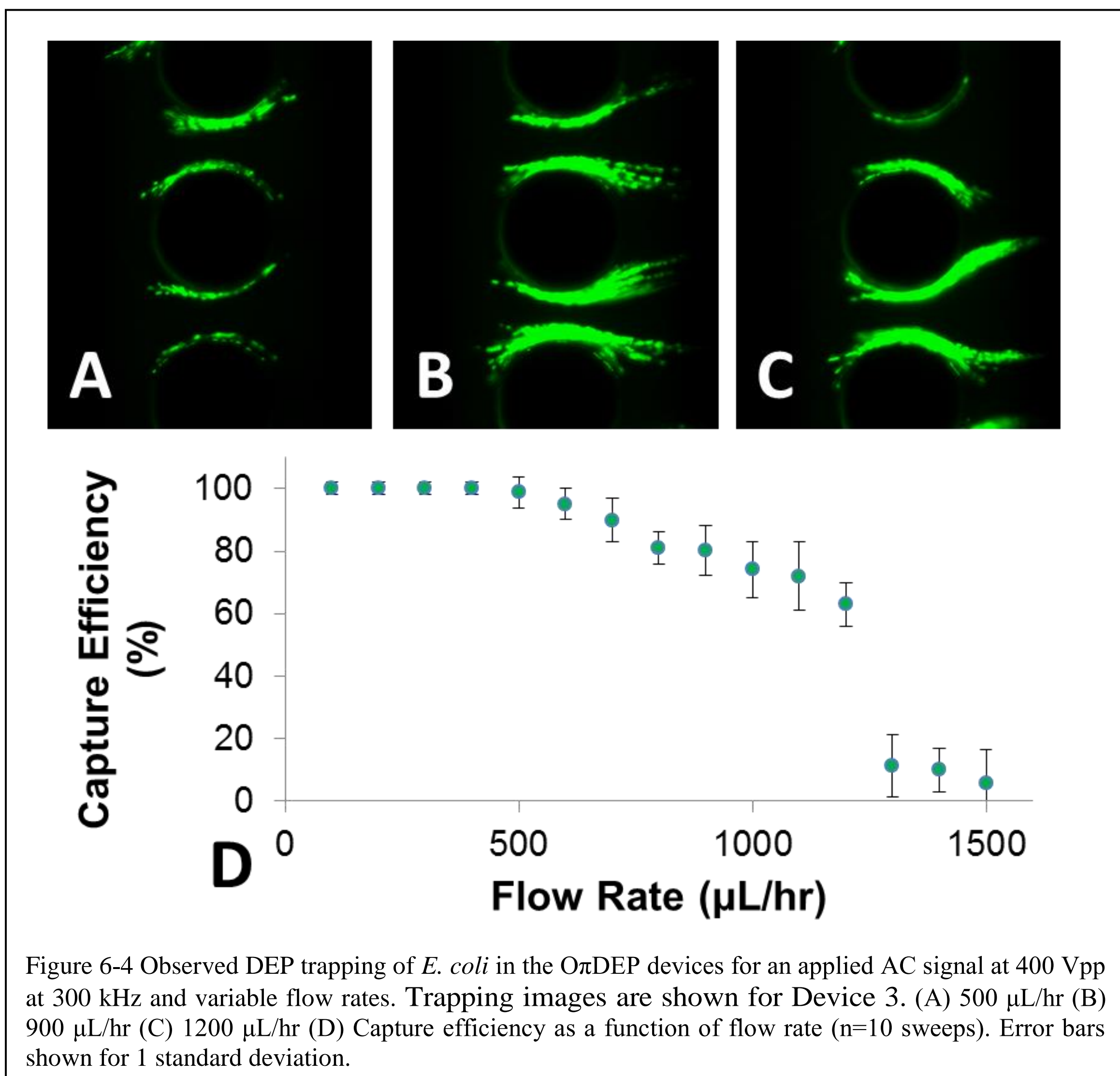

Figure 6-4 Observed DEP trapping of *E. coli* in the OπDEP devices for an applied AC signal at 400 Vpp at 300 kHz and variable flow rates. Trapping images are shown for Device 3. (A) 500 µL/hr (B) 900 µL/hr (C) 1200 µL/hr (D) Capture efficiency as a function of flow rate (n=10 sweeps). Error bars shown for 1 standard deviation.

efficiency began at 500 µl/hr, where a few of the runs had a CE of 100% but it was not consistent. From 500 µl/hr to 1200 µl/hr the capture efficiency decreased gradually in a roughly linear fashion. However, at 1300 µl/hr the CE plummeted. In the videos of the experiments, DEP trapping was still observed. However, as pearl chains of *E. coli* formed, eventually the drag force on the pearl chain would become strong enough to pull the entire group of bacteria off of the microposts. This would repeat itself throughout the experiments, leading to very little net trapping. These results show that the maximum throughput for 100% trapping is 400 µl/hr. If only concentration is desired and capture efficiency is not critical then the devices can be operated at flow rates up to 1200 µl/hr.

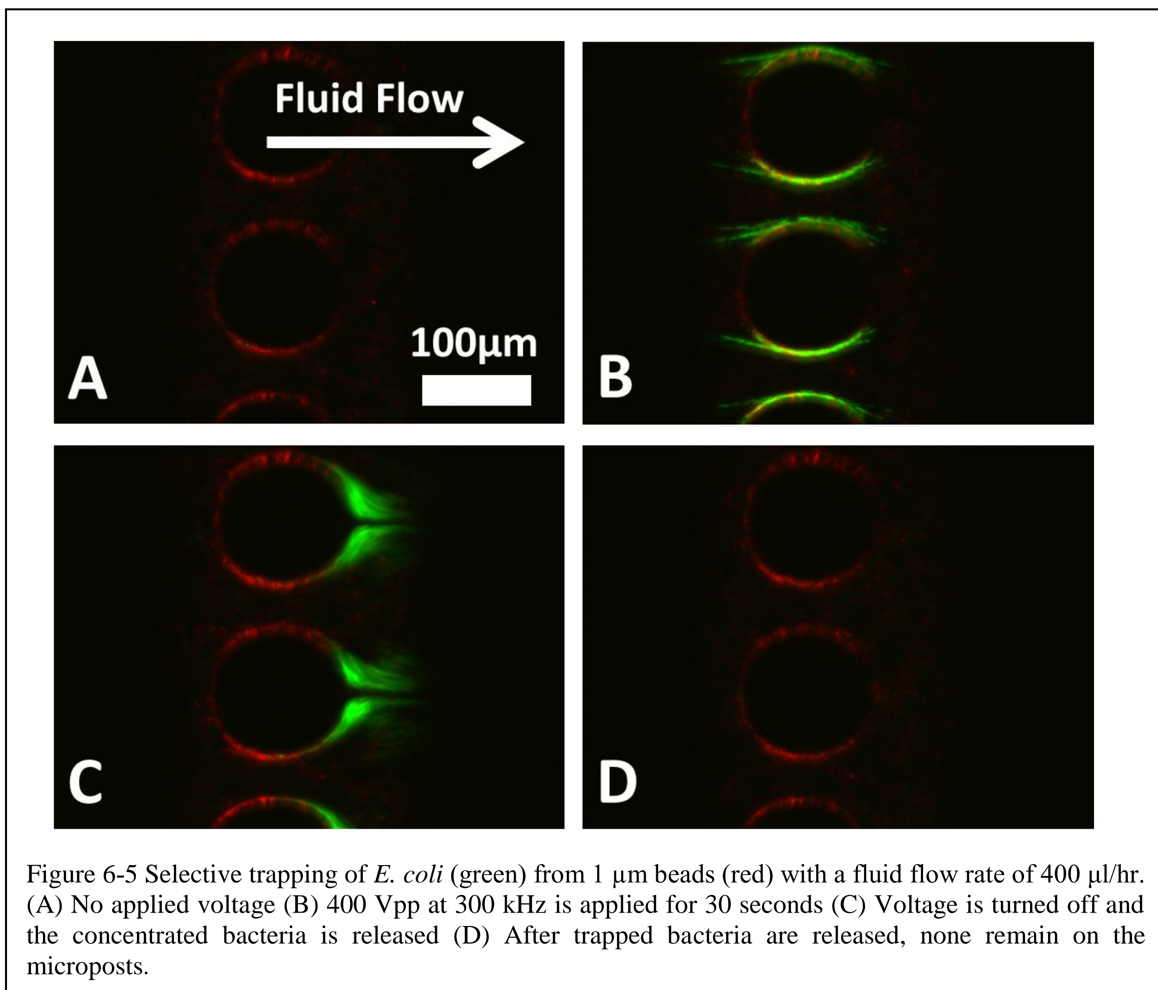

Figure 6-5 Selective trapping of *E. coli* (green) from 1 µm beads (red) with a fluid flow rate of 400 µl/hr. (A) No applied voltage (B) 400 Vpp at 300 kHz is applied for 30 seconds (C) Voltage is turned off and the concentrated bacteria is released (D) After trapped bacteria are released, none remain on the microposts.

6.4.4 Selective Concentration

To demonstrate the ability of these devices to selectively concentrate biological

samples from contaminants, *E. coli* cells were mixed with 1 μm red fluorescent beads, which were chosen because they are roughly the same size as *E. coli* cells. As Figure 5 shows, the bacteria was trapped and released on the microposts while the beads did not (see Electronic Supplementary Material Video S1). It should be noted that some of the red beads did foul to the surfaces of the device before any electric signal was applied as Figure 5A shows. However, only the bacteria were reversibly trapped with dielectrophoresis. This is evident when observing frames immediately after turning the electric signal off. As Figure 5C shows, only bacteria are present in the released sample. The bacteria are therefore completely separated from the beads, demonstrating the potential of OπDEP for selectively concentrating samples.

6.5 Conclusion

OπDEP is a recently invented method by our group to actuate iDEP devices with reusable electrodes on a separate substrate, allowing for a very scalable throughput. The OπDEP technique allows for inexpensive polymer microfluidic cartridges to be disposable while having reusable electrodes. In this paper, we have (1) presented OπDEP, the first reported iDEP devices powered by off-chip electrodes, (2) demonstrated through modeling and experiments the superior performance of OπDEP devices over the electrode-only designs, (3) demonstrated how different electrode patterns can be used to affect the trapping performance, and (4) demonstrated selective *E. coli* manipulation with the OπDEP devices.

This technique combines the advantages of traditional eDEP (tunable electrodes and strong electric fields) with those of iDEP (tunable insulating structures, no electrode fouling, and inexpensive devices). While the applied signal parameters such as the AC voltage magnitude and AC signal frequency can be tuned in real time, the physical parameters, such as electrode spacing, electrode shape, and geometrical dimensions can also be adjusted to fit the application. It is particularly important to note that due to the ability of this technology to reuse the electrodes, a toolkit of reusable electrodes can be created to suite a large range of applications. As shown in this work, the electrodes can be made very wide for better low frequency operation or vary narrow for a compact footprint. Groups of electrodes can be put in parallel for

high throughput batch processing. Alternatively, unlike traditional iDEP devices, OπDEP devices can have many independent electrodes and give each set of electrodes a different electric signal. This would create a very compact platform with multiple trapping zones in series, each with unique geometrical features tailored for multi-step filtration/isolation or for enrichment of different biological particles in a single operation.

While OπDEP relies on iDEP principles to generate trapping, it alleviates one of the main disadvantages of iDEP, which is Joule heating. iDEP devices typically have electrodes that actuate the devices at the fluid inlet and outlet. Thus, resistive heating occurs along the entire length of the channel. This heat buildup can limit the throughput of iDEP device and even result in device failure[110]. Additionally, for biological applications, higher temperatures can affect the sample or even reduce viability rates[109]. The OπDEP devices, however, greatly reduce the electrode spacing, creating electric field gradients in a very small area of the microchannel. This reduces the total electrical energy converted to heat and thus Joule heating is minimized. The result is that OπDEP compared to iDEP devices, may be able operate for longer times, with a wider range of media, and with minimized temperature effects on the biological samples.

Another advantage of OπDEP design is the throughput. As we have demonstrated, high capture efficiencies are achievable at high flow rates due to the strong DEP forces generated in OπDEP devices. It also should be noted that since the electrodes generating the field are implemented across the channel width, the channel can be made arbitrarily wide and the DEP forces will remain the same. Thus, the throughput can be increased by simply widening the microchannel. There may, however, be some practical limitations to the fabrication of very wide channels without the channels collapsing. These problems will be mitigated by the microposts within the channel acting as support columns.

OπDEP devices can be customized to meet a broad range of applications. Even though we have used microposts design, any iDEP microchannel configuration can be employed with this technology including single constrictions[174], 3D constrictions[123, 168, 175], 3D barriers[96], and filter designs[176]. DEP deflection

based devices[28, 177-179], which operate continuously with lower DEP forces, are straightforward to implement with OπDEP. Since deflection based designs do not need to completely stop particles in the channels, they can be operated with lower applied voltages.

This technology has the potential to provide rapid, reproducible, and cost effective platform of DEP particle manipulation for applications ranging from pathogen detection to cancer cell characterization. In our future work, we plan to explore devices with passivation membrane thicknesses much less than the 100 μm cover slides used in this paper. We anticipate that these devices will be able to trap at much lower applied voltages, work over a wider frequency range, and have increased throughputs. Additionally, we will explore DEP device designs with different micropost configurations to further increase the capture efficiencies at very high flow rates.

7 Three Dimensional Passivated-electrode Insulator-based Dielectrophoresis (3D πDEP)

7.1 Introduction

In this study, we present the first reported 3D off-chip passivated-electrode, insulator-based dielectrophoresis microchip (3D πDEP). Previously, we have shown an off-chip passivated-electrode, insulator-based dielectrophoresis microchip (OπDEP) device capable of DEP trapping. One of the drawback of this technique, however, is the limited frequency range due to the need for high applied frequencies in order to capacitively couple sufficient power in to the microchannel. In this work, we enhance the capabilities of OπDEP by introducing 3D structures into microchannel. These 3D structures create significantly larger electric field gradients than the previously 2D structures and consequently generate very larger DEP forces. Additionally, using our 3D PDMS fabrication technique, these devices can be produced in polymers from a glass mold, keeping the fabrication cost and time low. As with the OπDEP devices, the microfluidic channels of the 3D πDEP devices are fabricated on a disposable polymer cartridge. The electrodes are fabricated on a separate substrate and never come into contact with the experiment solution, and thus are reusable. In order to demonstrate this technology, *Escherichia coli* (*E. coli*), and *Staphylococcus aureus* (*S. aureus*) are trapped from water samples under various conditions. Trapping efficiencies of 100% were obtained at flow rates as high as 600 μl/hr and 70% at flow rates as high as 1500 μl/hr. Additionally, 100% trapping was demonstrated over a frequency range from 800 Hz to 600kHz with signals as low in amplitude as $50V_{pp}$.

7.2 Theory

Dielectrophoresis is the motion of polarizable particles that are suspended in an electrolyte when subjected to a spatially nonuniform electric field[180]. The DEP force felt by a spherical particle suspended in a medium is:

$$\mathbf{F_{DEP}} = 2\pi R^3 \varepsilon_m \mathrm{Re}[f_{CM}]\, \nabla(\mathbf{E} \bullet \mathbf{E}) \qquad (1)$$

where R is the radius of the particle, ε_m is the permittivity of the medium, **E** is the local electric field. $Re[f_{CM}]$ is the real part of the Clausius-Mossotti (CM) factor which is:

$$f_{CM} = (\varepsilon_p^* - \varepsilon_m^*)/(\varepsilon_p^* + 2\varepsilon_m^*) \qquad (2)$$

where ε_p^* and ε_m^* are the complex permittivities of the particle and the medium, respectively. Complex permittivity is defined as:

$$\varepsilon^* = \varepsilon + \sigma/(j\omega) \qquad (3)$$

Thus, $\mathbf{F_{DEP}}$ will fluctuate greatly depending on the applied frequency according to the CM factor. It is differences in the CM factor of different particles that allows for separation with DEP. Models have been developed for the CM factor of bacteria such as the multishell model [35]. These models can predict what the frequency dependant DEP force on a bacterial cell will be given the material makeup of the cell and the suspending medium.

The drag force on a spherical particle in a fluid at a low Reynold's number is given by:

$$\mathbf{F_{Drag}} = 6\eta R\pi(u_{pf}) \qquad (4)$$

where R is the radius of the particle, η is the viscosity of the fluid, and u_{pf} is the relative velocity of the particle with respect to the fluid. For a particle to trap in a DEP device, the DEP force must be greater or equl to the drag force ($\mathbf{F_{DEP}} >= \mathbf{F_{Drag}}$). As equation 4 shows, the larger the flow rate through the device, the larger the necessary DEP force to trap the particle.

The 3D πDEP device operates by capacitively coupling the electric fields from the electrode substrate into the microfluidic channel. In the middle of the microchannel, 3D insulating structures create constrictions which connect the two halves of the channel. Since PDMS has a much higher impedance than the DI water, the path of least resistance for the current is through these fluidic constrictions. Thus, the bulk of the current is compressed through the small 3D constrictions. This creates electric field gradients within the channel and is the main operating principle of iDEP devices. These electric field gradients, and thus the DEP force generated, depend on the geometric

gradient of the insulating structures. Structures which vary in all three dimensions benefit from being able to constrict the entire cross-section of the microchannel and thus obtain high geometric gradients. It has been previously demonstrated that iDEP devices with 3D gradients generate larger DEP forces than those with only 2D gradients[123, 168] enabling them to operate at very low voltages. This decreases Joule heating within channel that it often a major limiting factor in iDEP devices[110]. Additionally this limits eletrothermal flow, which is a parasitic effect that creates complications in iDEP devices[117].

7.3 Methods and Materials

7.3.1 Numerical Device Modeling

In order to investigate the electric field distributions within the microchannel, a numerical model of the devices was created using COMSOL Multiphysics 3.5 (COMSOL Inc., Burlington, MA) using the AC/DC module. 3D models were created of the three devices in this study. The electrical conductivities used for PDMS, glass, air, and deionized water are 8.20×10^{-13} S/m, 1.25×10^{-9} S/m, 3.00×10^{-9} S/m, and 8.00×10^{-4} S/m, respectively. The electrical permittivities used for PDMS, glass, air, and deionized water are 2.65, 4.65, 1, and 80, respectively. As for the boundary conditions, the electrodes were given AC electric potentials and all other boundaries were set to electrical insulation. The purpose of the simulations was to evaluate the values of $\nabla|E|^2$ as a function of position and frequency. Equation 1 shows that for a given particle and medium, $\nabla|E|^2$ is proportional to the DEP force felt by a particle.

7.3.2 Device Fabrication

Figure 7-1 shows our new process flow for the design and fabrication of 3D πDEP, implemented in PDMS. First, 0.4µm of thermal silicon dioxide is grown at 1000 °C on a <100> silicon wafer. This oxide acts both as a masking layer during the etch process and as a structural support during channel sealing. Using our silicon micromachining [R] we created a photomask layout consisting of an array of rectangular openings with different sizes (Figure 7-1A). After patterning photoresist

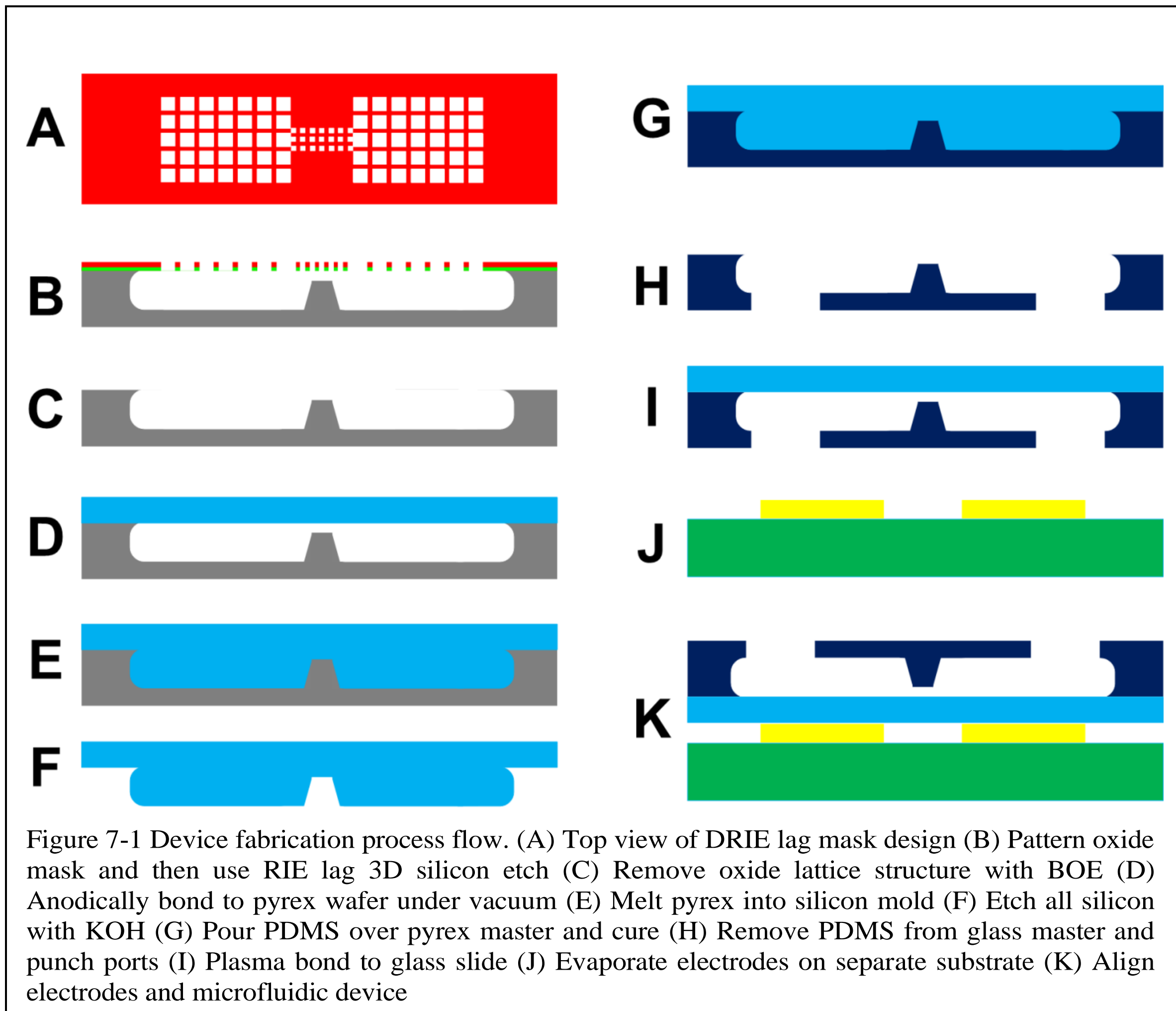

Figure 7-1 Device fabrication process flow. (A) Top view of DRIE lag mask design (B) Pattern oxide mask and then use RIE lag 3D silicon etch (C) Remove oxide lattice structure with BOE (D) Anodically bond to pyrex wafer under vacuum (E) Melt pyrex into silicon mold (F) Etch all silicon with KOH (G) Pour PDMS over pyrex master and cure (H) Remove PDMS from glass master and punch ports (I) Plasma bond to glass slide (J) Evaporate electrodes on separate substrate (K) Align electrodes and microfluidic device

(S1813), the pattern is transferred to the oxide using an Alcatel AMS-100 Deep Reactive Ion Etcher (DRIE) with CH_4 plasma. Then we isotropically etch silicon using with SF_6 plasma(Figure 7-1B). By utilizing reactive ion etch lag (RIE lag) and its dependency on the geometrical patterns of the layout, we can easily form 3D cavities and microposts. After removing photoresist, we anodically bond a Pyrex wafer to the silicon substrate under vacuum (Figure 7-1C and (Figure 7-1D). Then, the substrates are brought to a high temperature in a furnace and the liquid glass conforms to the silicon designs (Figure 7-1E) [R]**.** The silicon substrate is etched away using KOH, leaving only the glass substrate (Figure 7-1F). The glass substrate is then used as a master mold. Liquid PDMS (Sylgand 184 Silicon elastomer kit, Dow Corning, Midland, MI) was mixed to a 10:1 ratio of PDMS monomer and curing agent and poured onto the silicon mold (Figure 7-1G). The setup was put into a vacuum chamber for 2 hours to remove gas bubbles and then cured for 45 min at 100 ºC, resulting in 3D

PDMS structures. Next, the polymer was carefully pealed from the mold and 2 mm holes were punched into microchannels for fluidic ports (Figure 7-1H). The PDMS device is sealed by plasma bonding to a size #0 glass cover-slide (Electron Microscopy Sciences) (Figure 7-1I) which is approximately 100μm-thick forming the microfluidic cartridge. It is notable that we can include a large variety of designs on a single wafer and fabricate all at once. Additionally, many PDMS devices can be created from the same glass master mold, saving more resources.

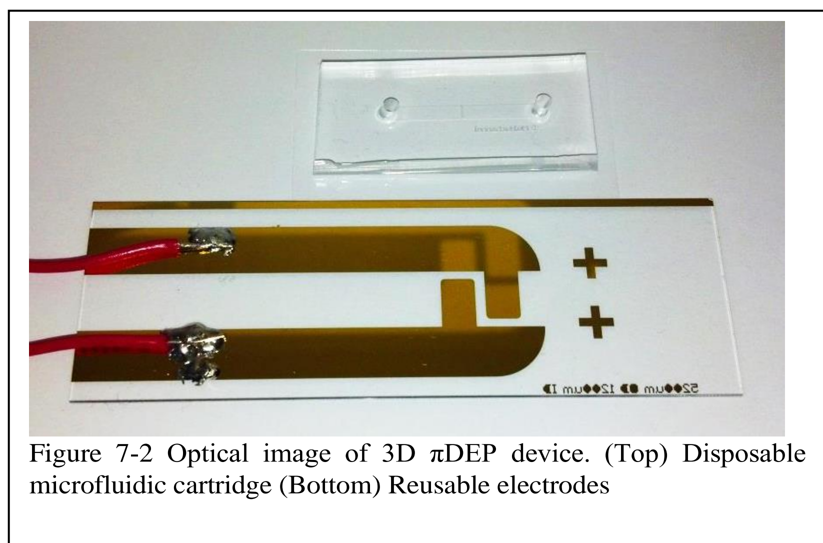

Figure 7-2 Optical image of 3D πDEP device. (Top) Disposable microfluidic cartridge (Bottom) Reusable electrodes

On a separate Pyrex substrate, electrodes were formed using the lift-off technique. The substrate was patterned with photoresist (AZ9260, AZ Electronic Materials). Next, using e-beam evaporation (PVD-250, Kurt J. Lesker Company), a thin layer (25 nm) of chrome and then a thicker layer (200 nm) of gold was deposited. The excess metal was removed by dissolving the photoresist in acetone (Figure 7-1J). The final electrodes were 4 mm long, separated by 1.2 mm, and 6 mm wide. During device operation, the PDMS microfluidic chip is put on top of the electrodes with the 3D structures aligned between the electrodes (Figure 7-1K). In this configuration the electrodes extend across the entire width of the channel. Between experiments, the PDMS microfluidic device can be replaced to maintain sample purity. The two components of the 3D πDEP device are shown in Figure 7-2.

Scanning electron microscopy (SEM) images of the 2 cm long microfluidic channel are shown in Figure 7-3. The main channel has a cross-section which is 2 mm wide and 100 μm deep. In the middle of the channel, there is a 3D obstacle which

constricts to 14 smaller channels. These smaller channels have crossections which are 36 μm wide and 22 μm deep. It is important to note that by using this technique, the fabricated posts/pillars will have a round corner in contrast with sharp edges, typical characteristic of microchannels formed by anisotropic etching of silicon. Thus while change in cross-sectional area is abrupt, no sharp edges are formed.

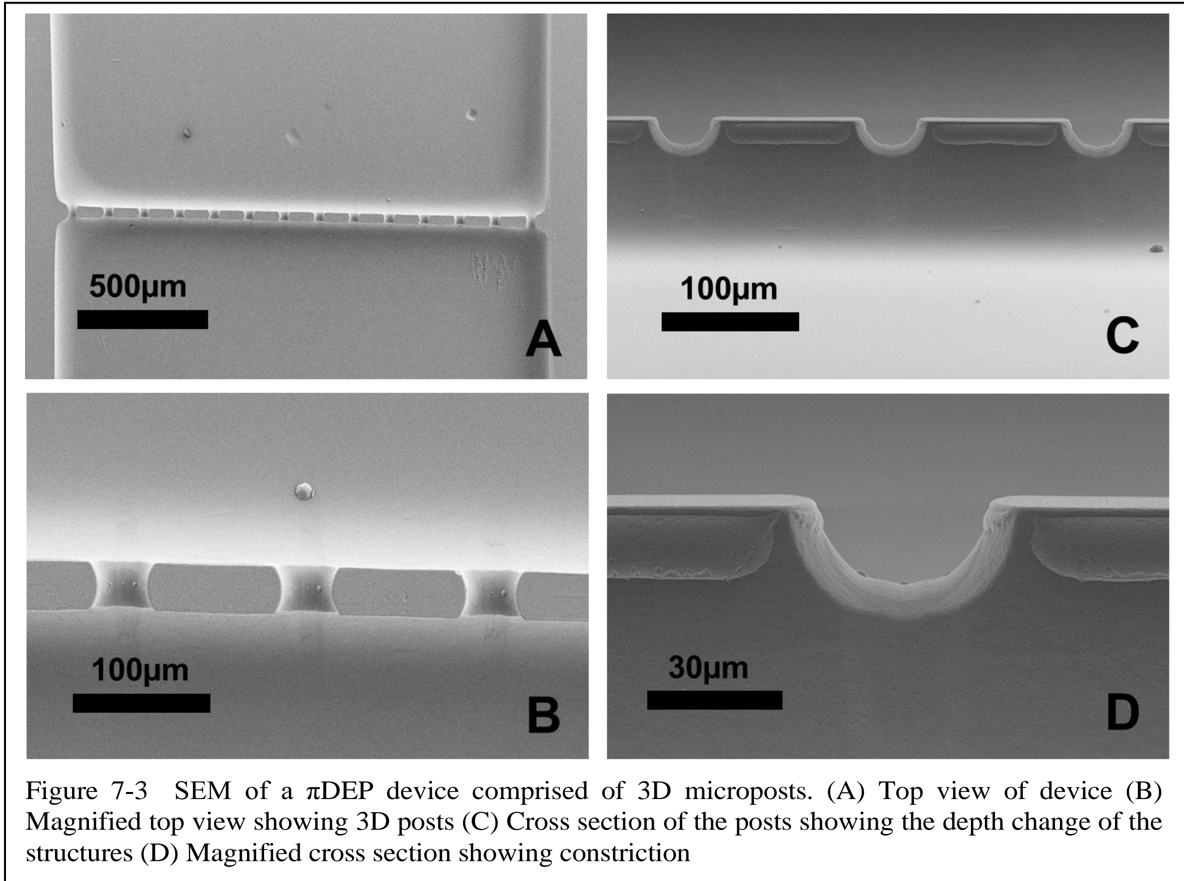

Figure 7-3 SEM of a πDEP device comprised of 3D microposts. (A) Top view of device (B) Magnified top view showing 3D posts (C) Cross section of the posts showing the depth change of the structures (D) Magnified cross section showing constriction

7.3.3 Cell Preparation

Staphylococcus aureus (*S. aureus)* (ATCC 12600) was cultured in brain heart infusion media. *Escherichia coli (E. coli)* K5808 (ATCC 53832) was cultured in trypticase soy media. All controls were cultured in 100 ml of their respective broth medium at 37 °C and 165 rpm to the exponential growth phase (OD600 ~0.5). Cells were transferred into two sterile 50 ml centrifuge tubes and subjected to three washes by centrifugation (5000 × g for 10 min) and resuspension in 1X PBS. Quantification of bacteria was done microscopically using a hemocytometer (counting chamber), and by

colony forming unit (CFU) counting of dilutions where colony numbers ranged between 30 and 300. For all experiments, *E. coli* cells and *S. aureus cells* were centrifuged and resuspended 3 times in DI water with a measured conductivity of 800 μS/m. The DI water conductivity was measured with a solution conductivity meter (SG7, Mettler Toledo, Scherzenbach, Switzerland). The cells were diluted to a final concentration of $1x10^8$ cells/ml.

7.3.4 Experimental Setup

A function generator (4079, BK Precision) was connected to a power amplifier (EW2350, Tegam) which provided an AC signal of 400 V peak to peak (V_{pp}) across a frequency range of DC to 1 MHz. An oscilloscope (DL1300A, Yokogawa) was connected to the monitor output of the amplifier to observe the applied waveforms for distortion. The PDMS-based microfluidic catridges were placed in vacuum for at least 30 min before experiments were run to reduce priming issues. During device operation, the solution was passed through the OπDEP device using a 1 ml syringe connected to syringe pump (NE-1000, New Era Pump Systems Inc) to a waste reservoir. Once the device was primed, fluid was continually moved through the channels at 100 μl/hr for 5 minutes prior to the beginning of the experiments. DEP trapping experiments were observed using an inverted fluorescent microscope (Axio Observer Z1) and videos of all trapping experiments were acquired using either CCD color camera (AxioCam MRc) or a CCD monochrome camera (IDT Ltd. MotionXtra NX-4) for high frame rate capture.

For a single DEP trapping experiment data point, the flow rate of interest would be applied for 15 seconds to stabilize the flow velocity. Then, the electric signal would be switched on and the DEP trapping would be recorded by video. The signal was switched off after 30 seconds and bacteria were released. The microchannels were inspected before every run and cleared of fouled bacteria by increasing the flow rate of the syringe pump when necessary. Thus, each data point included only bacteria trapped during that run.

In order to quantify the effectiveness of the DEP trap in the experiments is the capture efficiency (CE) which is defined as:

$$CE = [(I - O)/I] \times 100\% \qquad (5)$$

where I is the number of incoming bacteria observed on a single frame of the trapping video, O is the number of outgoing or escaped bacteria observed on a single frame of the trapping video. These measurements were made by counting the bacteria upstream (I) and downstream (O) of the trapping region in the individual frames of the videos taken during the experiments. The regions used for counting I and O were the identically sized rectangles and remained constant for the experiments. Ten fluid flow velocity sweeps from 100 μl/hr to 2000 μl/hr were each completed in random order. To obtain a data point representing one flow rate, values of I and O were averaged over the ten flow sweeps. For cases where bacteria remained in clusters after being released, the clusters were assumed to be flat and the size of the cluster was used to estimate the number of bacteria in the cluster. It should be noted that if clusters had multiple bacteria stacked in depth, then this method would underestimate the number of bacteria.

7.4 Results and Discussion

7.4.1 Numerical Modeling

The numerical modeling results are shown in Figure 7-4. $\nabla(\mathbf{E}\bullet\mathbf{E})$ was computed for an applied signal of 400 V_{pp} at 300 kHz. The top view and cross-section view of the slice plot of $\nabla(\mathbf{E}\bullet\mathbf{E})$ are shown in figure 7-4A and figure 7-4B respectively. The peak gradient was found to be 5.28×10^{17} $[(m\bullet kg^2)/(s^6\bullet A^2)]$. This is two orders of magnitude greater than the peak gradients using the exact same input signal in our previous OπDEP devices[181] which only varied in 2 dimensions. As equation 8-1 shows, $\nabla(\mathbf{E}\bullet\mathbf{E})$ is proportional to the DEP force on a particle. Thus the 3D πDEP devices will produce much larger DEP forces for same input than the previous OπDEP devices. It

also should be noted that the electric field gradients found in the 3D πDEP devices, vary in all three dimensions while the gradients in the OπDEP devices only varied

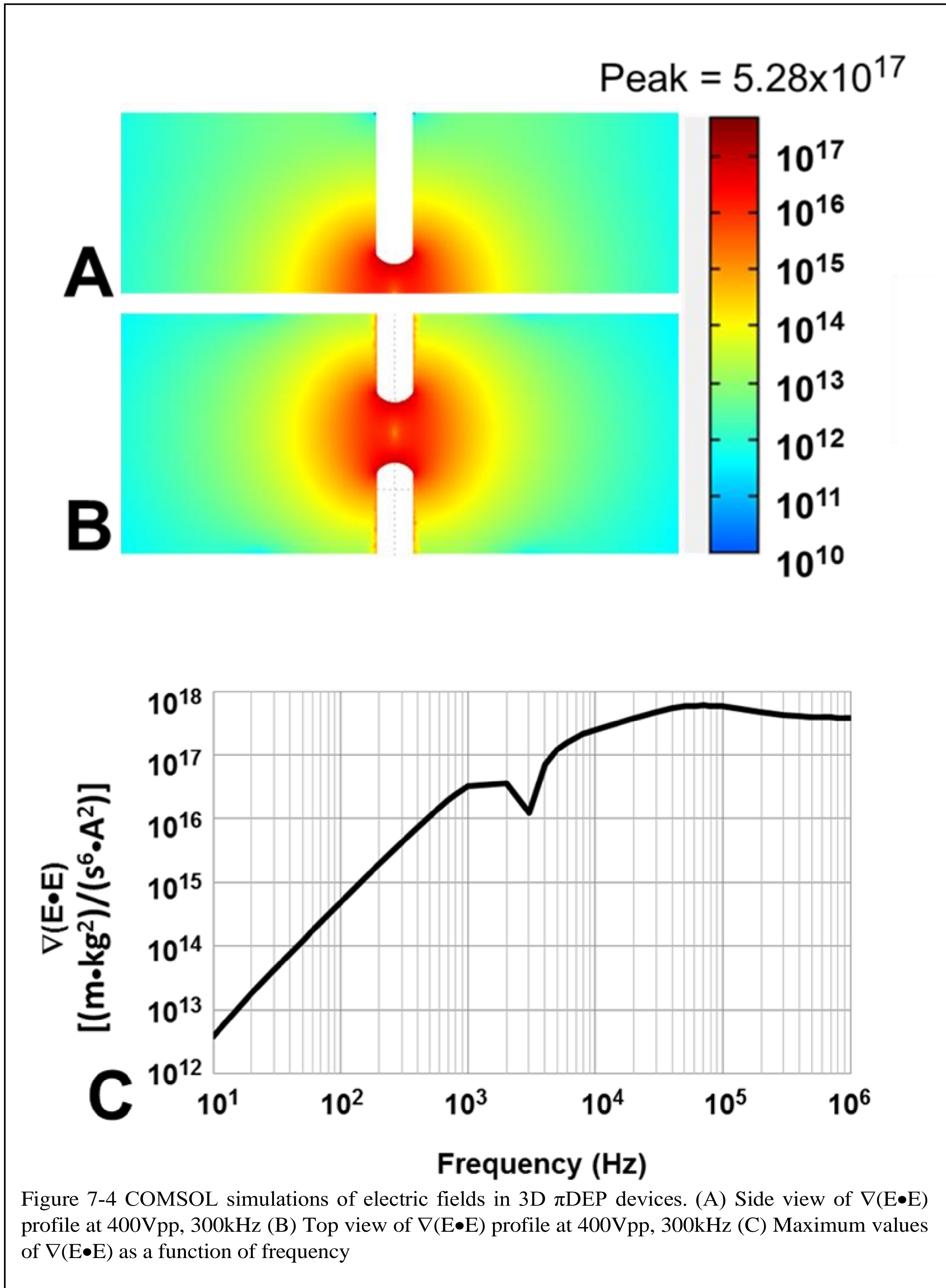

Figure 7-4 COMSOL simulations of electric fields in 3D πDEP devices. (A) Side view of ∇(E•E) profile at 400Vpp, 300kHz (B) Top view of ∇(E•E) profile at 400Vpp, 300kHz (C) Maximum values of ∇(E•E) as a function of frequency

significantly in two dimensions.

Figure 7-4C shows the frequency response of the 3D πDEP device. Since the electric field are capacitively coupled into the device, the response is similar to a high pass filter, with the attenuation increasing as the frequency is lowered. It should be noted however, that the magnitude of the electric field gradient does not dip below 10^{15} $[(m\bullet kg^2)/(s^6\bullet A^2)]$ until the frequency is ~100 Hz. This is significant because all of the trapping with the OπDEP devices was performed at that electric field gradient strength[181]. Thus the model predicts that the 3D πDEP should be able to operate over a wide frequency range, including very low frequencies.

7.4.2 Frequency Response

Trapping experiments of *E. coli* and *S. aureus* was performed with an applied flow rate of 400 µl/hr and the signal amplitude held constant at $400V_{pp}$. Figure 7-5 shows the experimental performance of the device as a function of the applied frequency. Under these conditions, DEP trapping with 100% capture efficiency was observed over a wide range, from 700 Hz to 600 kHz for *S. aureus* and from 800 Hz to 700 kHz for *E. coli*. These results are consistent with the model predictions. Since the 3D πDEP devices produce DEP forces greater than 10^{15} $[(m\bullet kg^2)/(s^6\bullet A^2)]$ over a broad frequency range, trapping is possible over a broad frequency range. It should be noted that the decrease in capture efficiency at the high frequencies is due to the bandwidth limit of the power amplifier that was used.

It was observed that even at the lowest frequency tested, some bacteria were trapped. It was also observed that at low frequencies, the bacteria tended to form longer pearl chains (Figure 7-5). Bioparticles trapping in DEP devices have been previously reported to form pearl chains[103]. However, at high frequencies, the bacteria were trapped into a more compact area. This is due to DEP forces on the entire pearl chain structure. Since at higher frequencies, the DEP forces are larger than at low frequencies, the increased DEP force acts on the entire pearl chain structure. This force pulls the entire pearl chain structure toward the highest electric field gradient in the channel, compressing the area in which cells are trapped. The observed trapping

profiles of the bacteria tested were similar. It should be noted that for all conditions tested, the bacteria were released when the AC signal was removed. Thus the trapping was found to be reversible. Also, although the *E. coli* experiments did produce slightly lower trapping efficiencies at the low frequencies, there was not a frequency where one

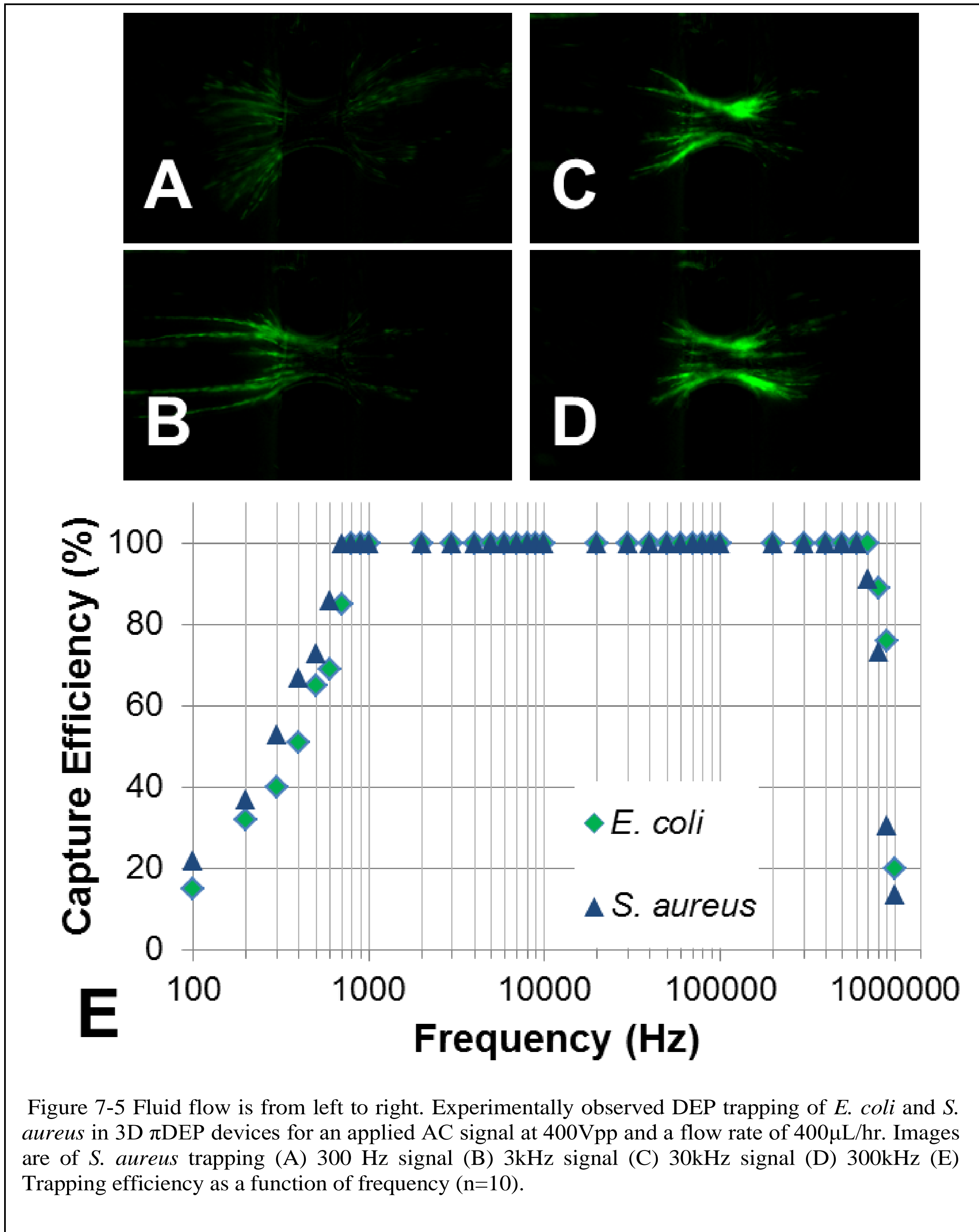

Figure 7-5 Fluid flow is from left to right. Experimentally observed DEP trapping of *E. coli* and *S. aureus* in 3D πDEP devices for an applied AC signal at 400Vpp and a flow rate of 400µL/hr. Images are of *S. aureus* trapping (A) 300 Hz signal (B) 3kHz signal (C) 30kHz signal (D) 300kHz (E) Trapping efficiency as a function of frequency (n=10).

type of bacteria was observed to completely trap but the other was not. This is not surprising as *E. coli* and *S. aureus* was have been shown to behave similarly in DEP trapping experiments[170].

7.4.3 Low Voltage Operation

Voltage sweeps were performed at several frequencies within the experimental determined bandwidth of the device. While holding the flowrate constant at 400 µl/hr, the applied signal amplitude was increased from 0 V until 100% trapping was obtained. The results are shown in Figure 7-6. At 800 Hz, it took nearly to 400 V_{pp} to trap both of the bacteria, however the minimum operating voltage rapidly decreased as the frequency was increased. The minimum voltage that *E. coli* and *S. aureus* were found to trap with 100% trapping efficiency was 49 V_{pp} and 50 V_{pp} respectively with both of these values found. This is an order of magnitude lower than the trapping voltages used in the original OπDEP devices [181]. These values are very low compared to traditional iDEP device which typically require high voltages (~1000 V) to operate [26, 27]. Utilizing 3D constrictions, researchers have reported iDEP devices operating at lower voltages. For example, Braff et al. reported trapping of *E. coli* at 50 V, which is

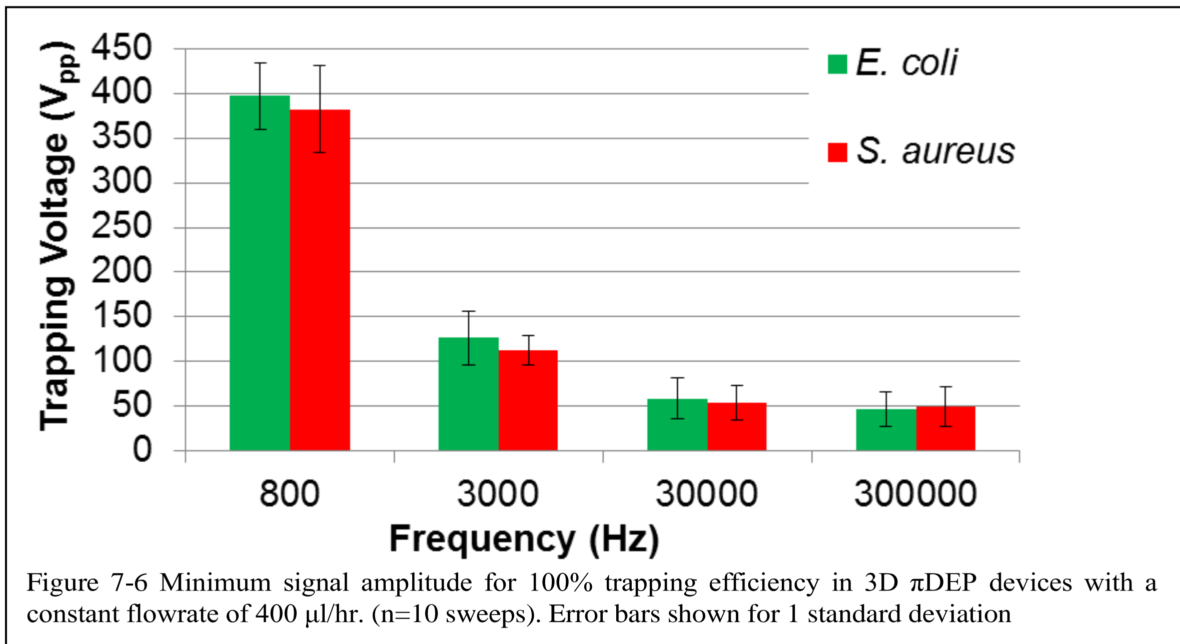

Figure 7-6 Minimum signal amplitude for 100% trapping efficiency in 3D πDEP devices with a constant flowrate of 400 µl/hr. (n=10 sweeps). Error bars shown for 1 standard deviation

the lowest reported for bacteria in an iDEP device[123]. The device they presented was a traditional iDEP device with electrodes directly contacting the solution and providing electoosmotic flow. However, in this work, we have demonstrated bacteria trapping with the same signal amplitude, without any direct contact between the electrodes and the solution. The tradeoff is that the frequency of the applied signal must be high enough to capacitively couple most of the signal into the channel.

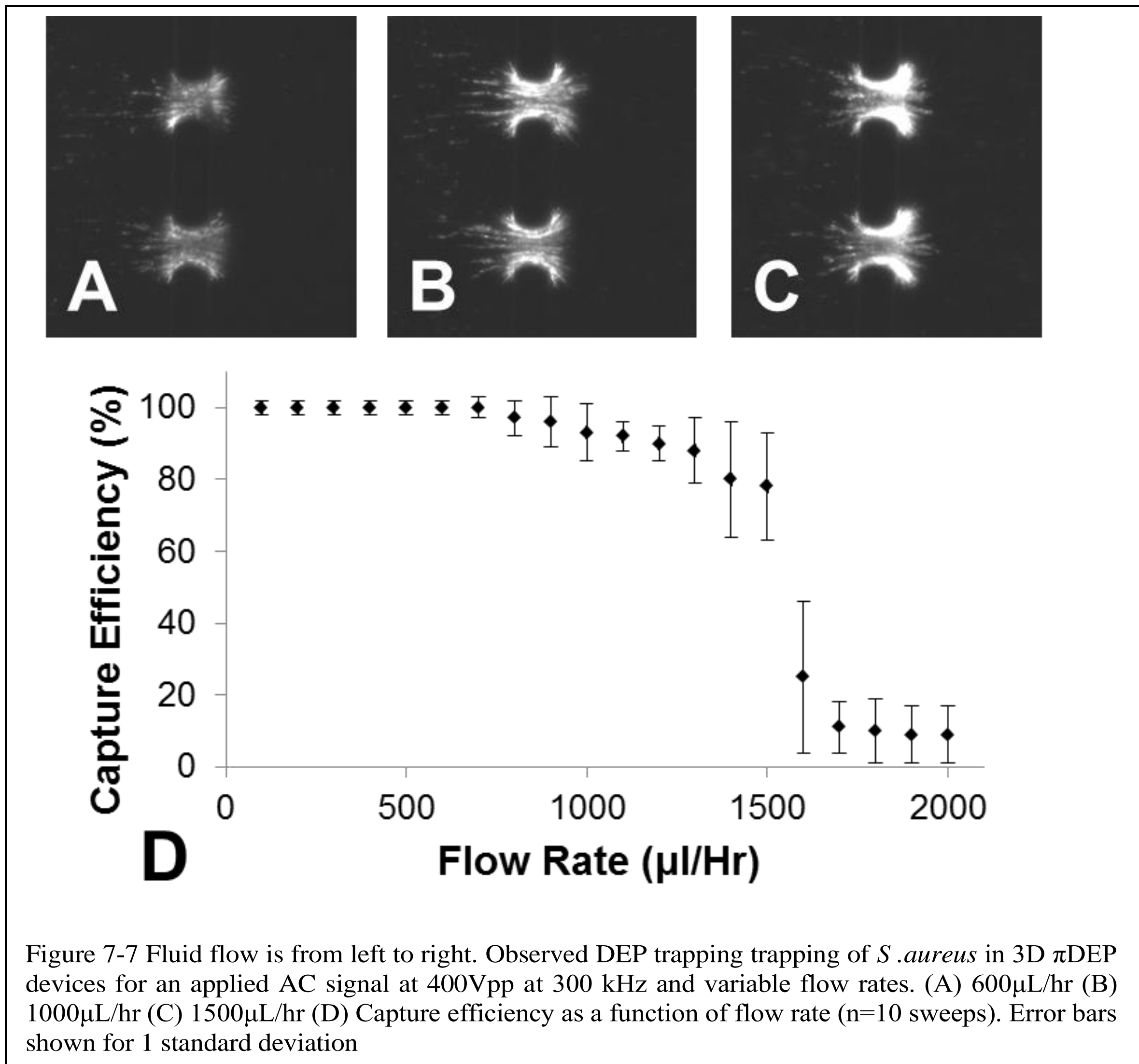

Figure 7-7 Fluid flow is from left to right. Observed DEP trapping trapping of *S .aureus* in 3D πDEP devices for an applied AC signal at 400Vpp at 300 kHz and variable flow rates. (A) 600µL/hr (B) 1000µL/hr (C) 1500µL/hr (D) Capture efficiency as a function of flow rate (n=10 sweeps). Error bars shown for 1 standard deviation

7.4.4 Flow Rate Tests

In order to determine the maximum throughput of the 3D πDEP device, the input signal was held constant at 400 V_{pp} at 300 kHz and the fluid flow rate was varied

from 100 µl/hr to 2000 µl/hr. Figure 7-7 Shows the response of the device capture efficiency as a function of flow rate. It was observed that during the flow sweeps, both of the bacteria performed very similarly with mean values with 5% of each other for the entire sweep. Thus for clarity, Figure 7-7 shows only data from *S. aureus*. The device obtained 100% capture efficiency for flow rates up to 600 µl/hr. It should be noted that some of the experiments at 700 µl/hr resulted in 100% trapping, however it was consistent across all of the trials. The capture efficiency of the device decreased steadily from 700 µl/hr to 1500 µl/hr but remained above 50%. At 1600 µl/hr, the drag force was high enough to strip entire pearl chains of cells from the trap, and consequently the capture efficiency fell to nearly zero. Thus if 100% trapping is necessary, the throughput is 600 µl/hr whereas if only concentration is important, the device can be operated at 1500 µl/hr.

7.5 Conclusion

In this paper we have presented the first reported 3D πDEP device and used it trap the pathogens *E. coli* and *S. aureus*. This technology combines 3D structures with our previously developed OπDEP. As both the numerical and experimental results demonstrate, the 3D structures provided much stronger DEP forces than previous 2D OπDEP designs. This resulted in a significant improvement in the operating bandwidth. Since bioparticles have a frequency dependent response to DEP devices, a wider bandwidth may enable finer control manipulations. Additionally, the stronger DEP forces decreased the operating voltage by an order of magnitude. This decreases joule heating within the device as well as decreases the support electronics complexity. The throughput of the devices increased as well, although not as dramatically. These performance increases were all obtained while maintaining a single etch, polymer mold fabrication. Thus the resulting devices are low cost and rapidly produced. Additionally, this technology enables bioparticle manipulation without any direct contact between the electrodes and the sample, maintain sample purity. These results demonstrate the potential of 3D πDEP devices for cost effective, high throughput, platform for bioparticle manipulation for application ranging from pathogen detection to medical diagnostics. In the future, we plan on studying effect of the slope and shape of the 3D

constriction on a device’s ability to separate bioparticles which are very similar.

8 Conclusions and Future Work

8.1 Summary

Waterborne pathogens kill millions of people every year. The vast majority of these deaths are avoidable; however, the methods to detect these pathogens are expensive, slow, and often not sensitive enough to be effective. In this dissertation, MEMS technology is used to help tackle the problem of inexpensive pathogen detection. The main focus of this work is dielectrophoresis, an electrokinetic technique for particle manipulation which has been very popular in research for the past 20 years. Dielectrophoresis devices manipulated bioparticles with a force that is very sensitive to the material makeup of the particle. It is the objective of this dissertation to develop dielectrophoresis devices which are closer than state of the art devices, to meeting the performance and cost requirements for pathogen detection. This dissertation presented the design, fabrication, numerical modeling, and experiment evaluation of new dielectrophoresis techniques. These dielectrophoresis devices utilize 3D microstructures for enhanced performance and can be fabricated in PDMS or silicon. New fabrication techniques were developed in order to accommodate the need for cost 3D varying microstructures. Additionally, practical concerns such device throughput and maintaining sample purity were addressed. The resulting 3D πDEP devices performed dielectrophoresis manipulation on known pathogens over a wide frequency range, with a low voltage input signal, and with a high throughput. This transformative research leads to the development of pathogen detection on a low-cost MEMS platform.

In order to help direct future research in this area, a few concept devices are presented in this chapter. These devices increase the capabilities of the DEP systems already discussed in the work in different ways. The results presented here show the need and the benefit of future work in this area.

8.2 Off-chip Impedance Sensing

8.2.1 Introduction

In OπDEP devices, particles are trapped and separated in a cartridge based system. The electric fields necessary for operation are capacitively coupled into the

device. However, thus far, the cell detection has been performed by counting the cells released by the DEP trap using fluorescent dyes and a fluorescent microscope. In order to have a complete pathogen detection system, however, there must be another method of sensing the cells trapped and released by DEP. One method of cell detection in a microfluidic device is to sense the change in impedance that occurs when a cell passes between a pair of electrodes in a channel. A microfluidic impedance detection devices with an iDEP concentrator has been previously demonstrated [117]. Here we will demonstrate a DEP preconcentrator and cell impedance detection system that is compatible with the OπDEP device architecture.

8.2.2 Methods and Materials

The device is fabricated using the same process flow as presented in Chapter 6 for the OπDEP devices. Briefly, we created a silicon wafer was patterned with photoresist and etched using an Alcatel AMS-100 Deep Reactive Ion Etcher (DRIE) to obtain the structures. Photoresist was stripped and the wafer was then used as a master mold for PMDS. Liquid PDMS poured onto the silicon mold and cured. Finally, the PDMS was plasma bonded to a #0 micro cover glass forming the microfluidic cartridge. On a separate Pyrex substrate, electrodes were formed using the lift-off technique. During device operation the microfluidic cartridge is placed onto the electrode substrate and aligned such that the insulating structures in the micrchannel are visible between the electrodes. Figure 8-1 shows the device. The operating principle of this device is to concentrate the bacteria at the microposts and then sense the impedance change in the microchannel when the bacteria are released and travel through the small constriction in the channel. The electric current is concentrated through that constriction and thus the system is more sensitive to changes in impedance in the constriction then elsewhere in the channel.

The most significant difference between these experiments and the previous OπDEP experiments, is that the electrodes were connected to a high-voltage, double-pole double-throw (DPDT) relay (G12, Gigavac). This relay switched between the DEP actuation

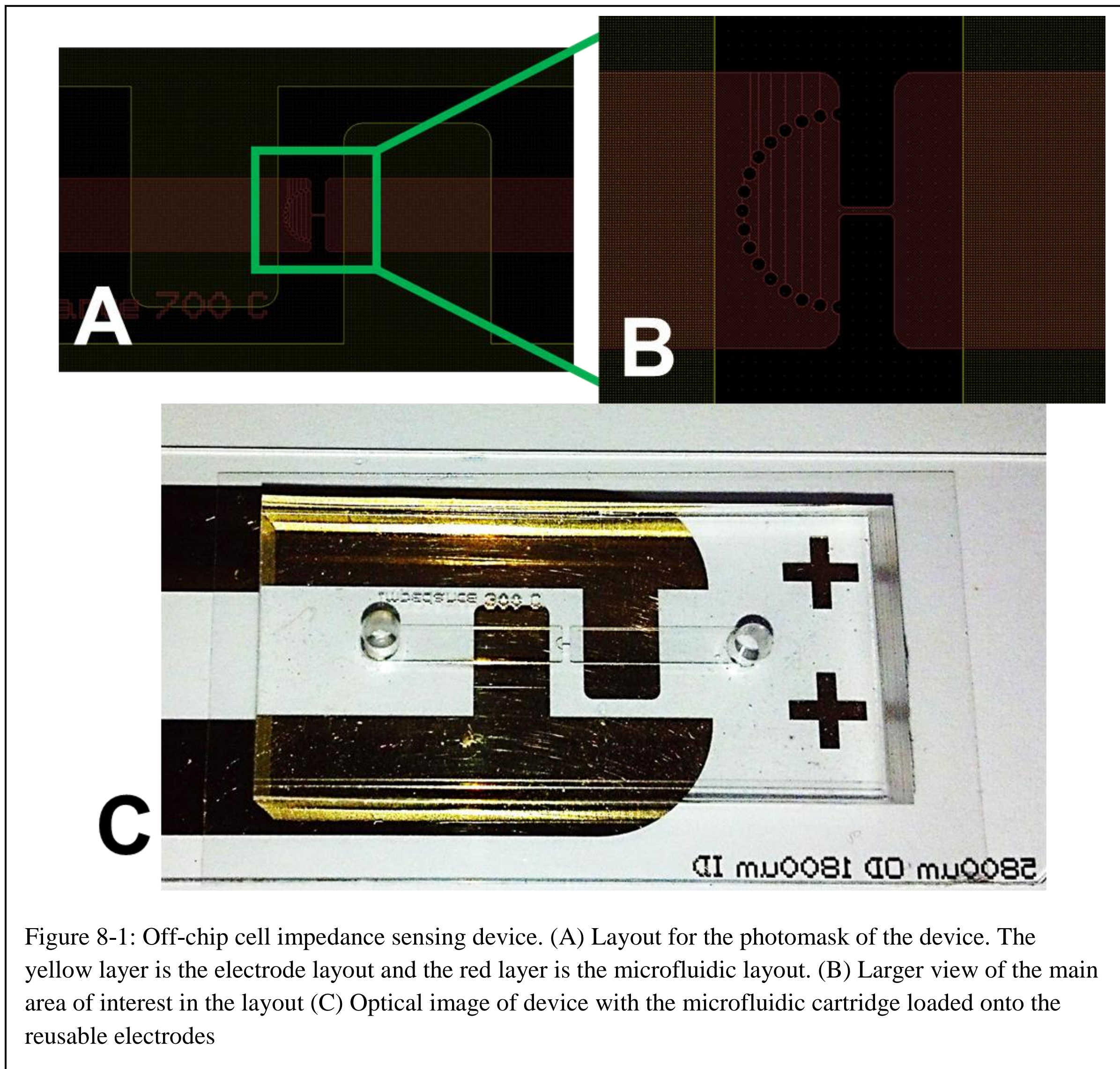

Figure 8-1: Off-chip cell impedance sensing device. (A) Layout for the photomask of the device. The yellow layer is the electrode layout and the red layer is the microfluidic layout. (B) Larger view of the main area of interest in the layout (C) Optical image of device with the microfluidic cartridge loaded onto the reusable electrodes

electronics, which included consisted of a function generator (4079, BK Precision) was connected to a power amplifier (EW2350, Tegam), and the impedance detection electronics, which included an impedance spectroscope (HF21S, Zurich Instruments) connected to a current amplifier (HF2TA, Zurich Instruments). The circuit for this is shown in Figure 8-2. The DEP actuation electronics provided an input signal of 400 V_{pp} at 300 kHz whereas the impedance detection electronics provided an input signal of 10 V_{pp} signal at 700 kHz. During the experiments the electrodes would be connected to either the DEP actuation electronics or the impedance detection electronics depending on the position of the relay.

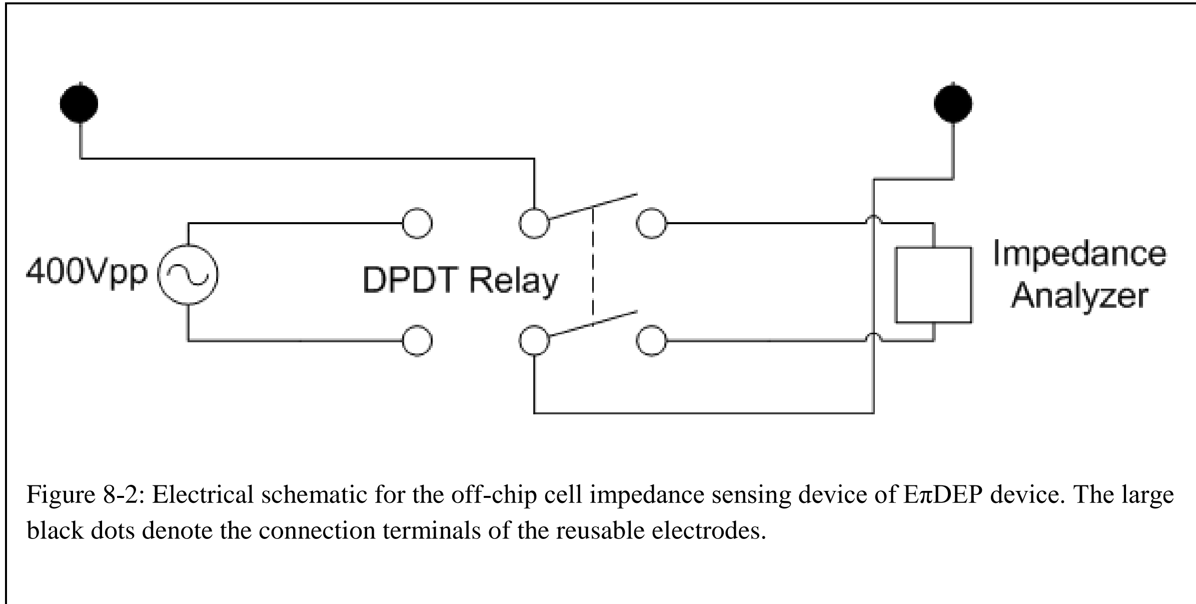

Figure 8-2: Electrical schematic for the off-chip cell impedance sensing device of EπDEP device. The large black dots denote the connection terminals of the reusable electrodes.

8.2.3 Results and Discussion

To test the device, the bacteria were suspended in deionized water with a measured conductivity of 800 μS/m. The experiments were performed with *Escherichia coli* (*E. coli*) strain MG1655 at a concentration of $1x10^6$ cells/ml. During device operation, the solution was passed through the device with a syringe pump at a flow rate of 300 μl/hr. Using a relay, the electrodes were actively switched between the DEP actuation electronics and the impedance detection electronics during the experiment. Figure 8-3 shows the frames of a video of the experiments. First the DEP actuation electronics are connected and the bacteria are concentrated at the microposts for set period of time (Figure 8-3A). Then the bacteria are released by switching the relay to the impedance electronics (Figure 8-3B). At first, the spectroscope does not see any change in the impedance signal. The bacteria then travel away from the microposts and toward a constriction in the channel (Figure 8-3C). When they reach the 20 μm constriction, the impedance spectroscope measured a drop in impedance. The bacteria then continue to travel through the channel. When all of the bacteria have passed through the constriction the measured impedance returned to the original impedance value.

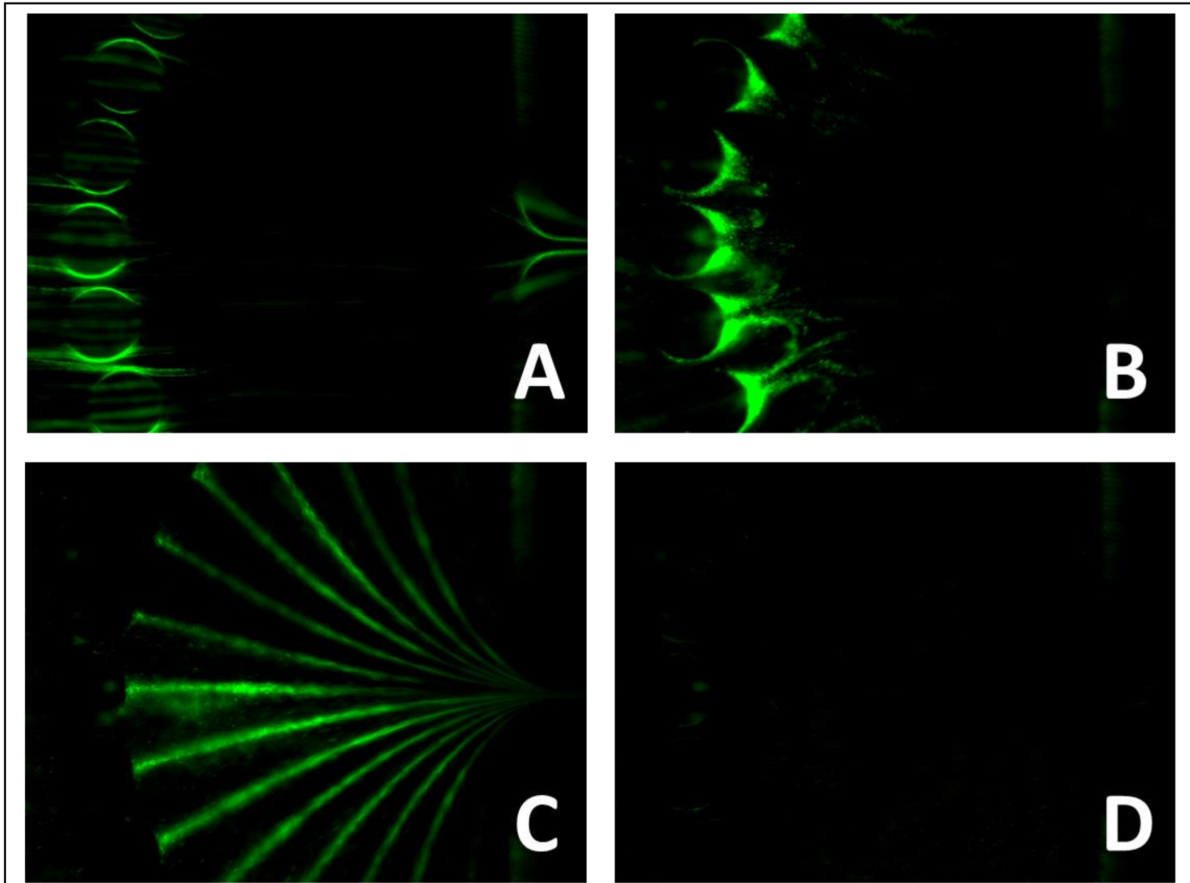

Figure 8-3: Fluorescent microscopy of the off-chip cell impedance sensing device in operation. *E. coli* are stained green. Fluid flow is from left to right. (A) The cells are trapped onto the preconcentrator posts. (B) The relay is switched to the impedance detection electronics and the the bacteria are released from the posts. (C) The bacteria continue down the channel into the narrow constriction and the impedance analyzer registers sees a drop in impedance. (D) All of the bacteria passed through the narrow constriction

By varying the set period of time that the bacteria are allowed trap, the number of cells that are being sensed were varied. Using this method, the resolution of the impedance detection system was evaluated. This assumes 100% trapping DEP trapping and 100% release of the cells trapped. Figure 8-4 shows the measured performance of the impedance detection system. The minimum number of cells that produced a distinguishable signal was just over 300. As the number of cells trapped on the posts was increased, the change in the magnitude of the measured impedance increased.

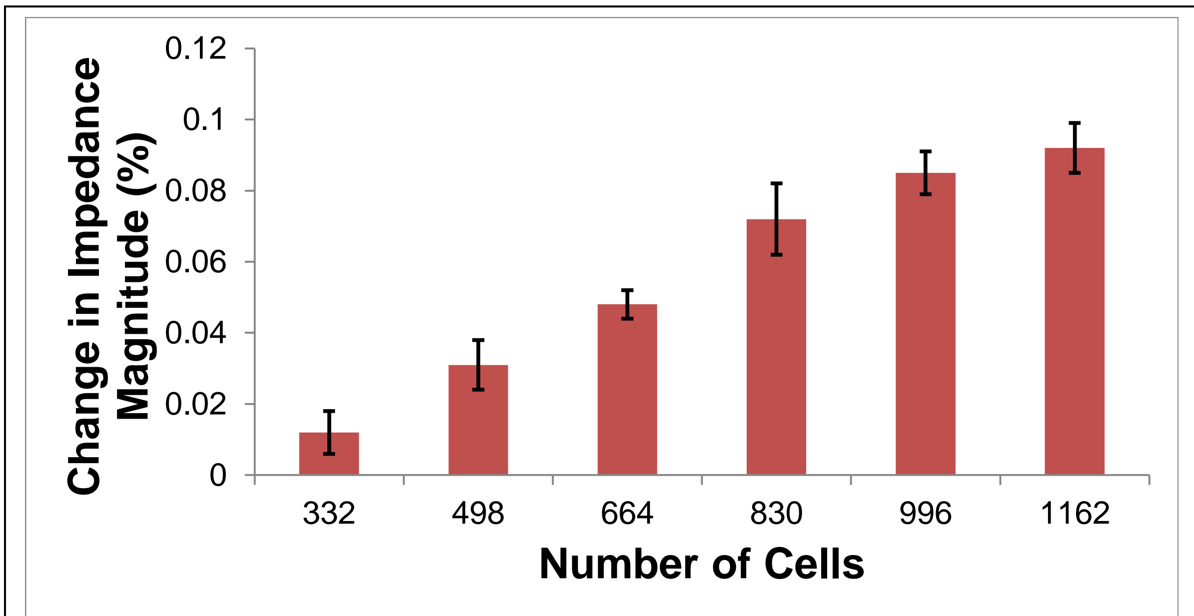

Figure 8-4: Performance of the off-chip cell impedance sensing device. It should be noted that all impedance changes were negative, however the absolute value of the change is displayed here for clarity. Error bars are shown for 1 standard deviation (n=3)

8.2.4 Conclusions and Outlook

These results demonstrate that it is possible to quantify the bacteria in a microfluidic device by detecting the impedance changes with off-chip electrodes. This enables OπDEP devices to count the number of cells that are caught in the DEP traps. It may be possible to improve the resolution of this system by using a smaller constriction, possibly even a 3D constriction if incorporating into a 3D πDEP device. Additionally, the device may be made more robust by adding reference electrode in order to performance a differential measurement.

The most important finding from these experiments is that since the process flow is identical to the OπDEP process flow, this functionality can be added without any additional cost per device. Thus a complete detection system can be created using the OπDEP architecture. Figure 8-5 shows one such proposed integrated pathogen detection system. At a high level the device operates by processing an entire fluid sample, perhaps from a water supply, and then giving an electronic count of the target pathogens that it found in the sample. The device should only count the target pathogen and no other particles or cells found in the system, however, more complex systems

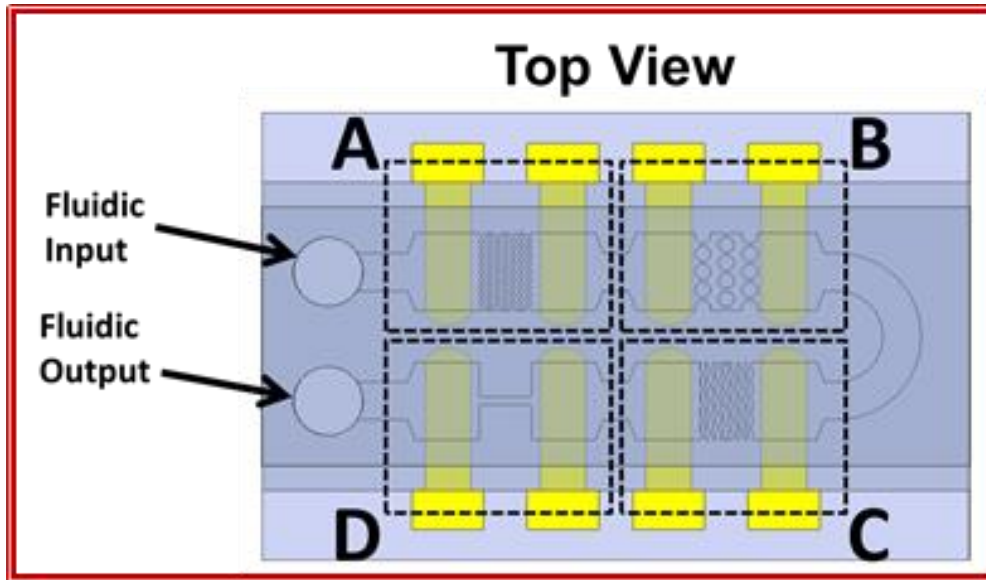

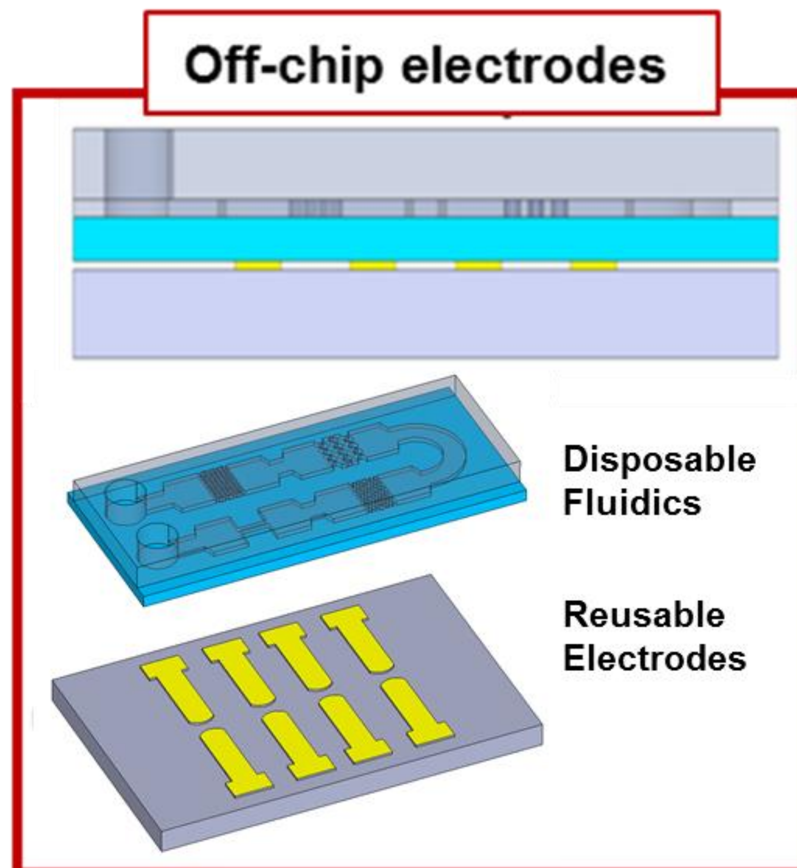

Figure 8-5: Conceptual images of the proposed 3D-πDEP platform for waterborne pathogenic bacteria isolation and enrichment.

could be designed to look for multiple targets. The system has a single fluidic input and output, however it has several functional compartments. A sample running through the device would proceed through each component in order. The compartments are each optimized to perform different task. The first compartment the sample encounters, compartment A, may be optimized for filtering out contaminants and non-target cells. The next compartment, compartment B would be designed for a fine separation of similar cell types. Compartment C would then concentrate the cells for detection. The last compartment, compartment D would then count the target cells by impedance measurement and give an analog output on its electrodes. It should be noted that all of these components are feasible given the results presented throughout this work.

In order to make this proposed system a reality, research must be done on integrating the different compartments. Additionally, the electrical properties of the target pathogens as well as other similar particles which may be present in the sample, must characterized very accurately and very extensively. This is necessary to acquire the parameters needed to separate, sort, and concentrate the target pathogens with a high accuracy. The benefits of this work, however, are great. This proposed system would require no sample prep and no cell labeling to operate. All of the needed functions for sample processing are included on the chip. Another advantage of this system, is that it can all be fabricated using a cartridge based design with disposable components, mold fabricated from polymers and glass. Thus sample purity is maintained and the cost for each test is kept low.

8.3 Embedded Passivated-electrode Insulator-based Dielectrophoresis (EπDEP)

8.3.1 Introduction

In OπDEP devices, the passivation layer attenuates the input signal, decreasing the performance. For applications in which sensitivity is crucial, this could result in the devices becoming ineffective. Thus, it is beneficial to explore the effect of using thinner passivation

In order to briefly study this effect, we will introduce a new technique called Embedded Passivated-electrode Insulator-based Dielectrophoresis (EπDEP). Rather than have electrodes on a separate substrate, these devices have embedded on the

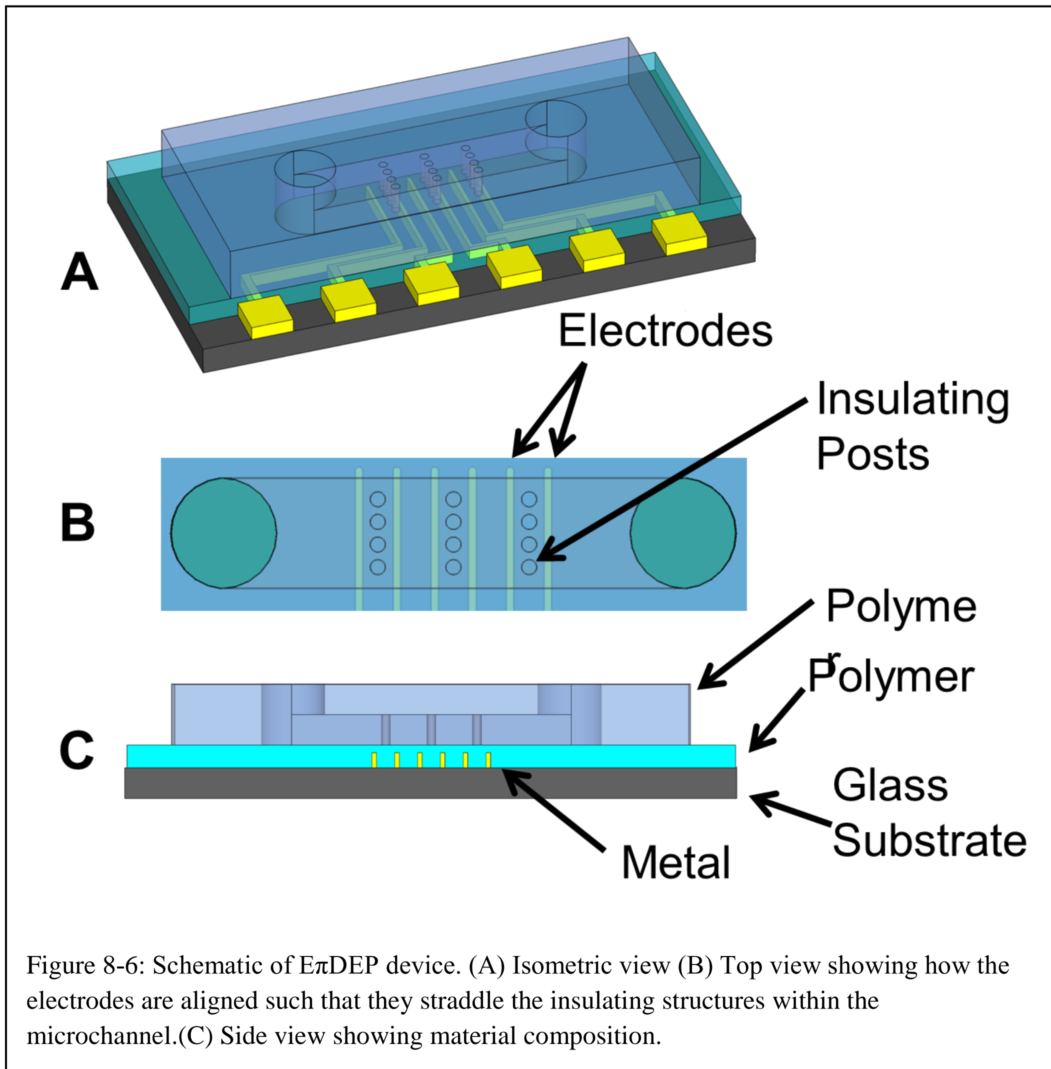

Figure 8-6: Schematic of EπDEP device. (A) Isometric view (B) Top view showing how the electrodes are aligned such that they straddle the insulating structures within the microchannel.(C) Side view showing material composition.

microfluidic substrate. The electrodes are passivated by a layer of PDMS. This layer will be very thin (~4 μm) compared to the 100 μm glass cover slide used for the OπDEP devices. Thus the losses across the layer will be lower and should lead to an improved frequency response and sensitivity. We have previously demonstrated iDEP with passivated off-chip electrodes (OπDEP) that operates at 400 V_{pp} [182]. In this section, we use (EπDEP) devices, which are fabricated with a new process flow and designed to operate at much lower voltages.

8.3.2 Methods and Materials

Figure 8-6 shows a schematic of the EπDEP device which consists of a PDMS microfluidic channel bonded to a substrate with patterned electrodes. To improve the

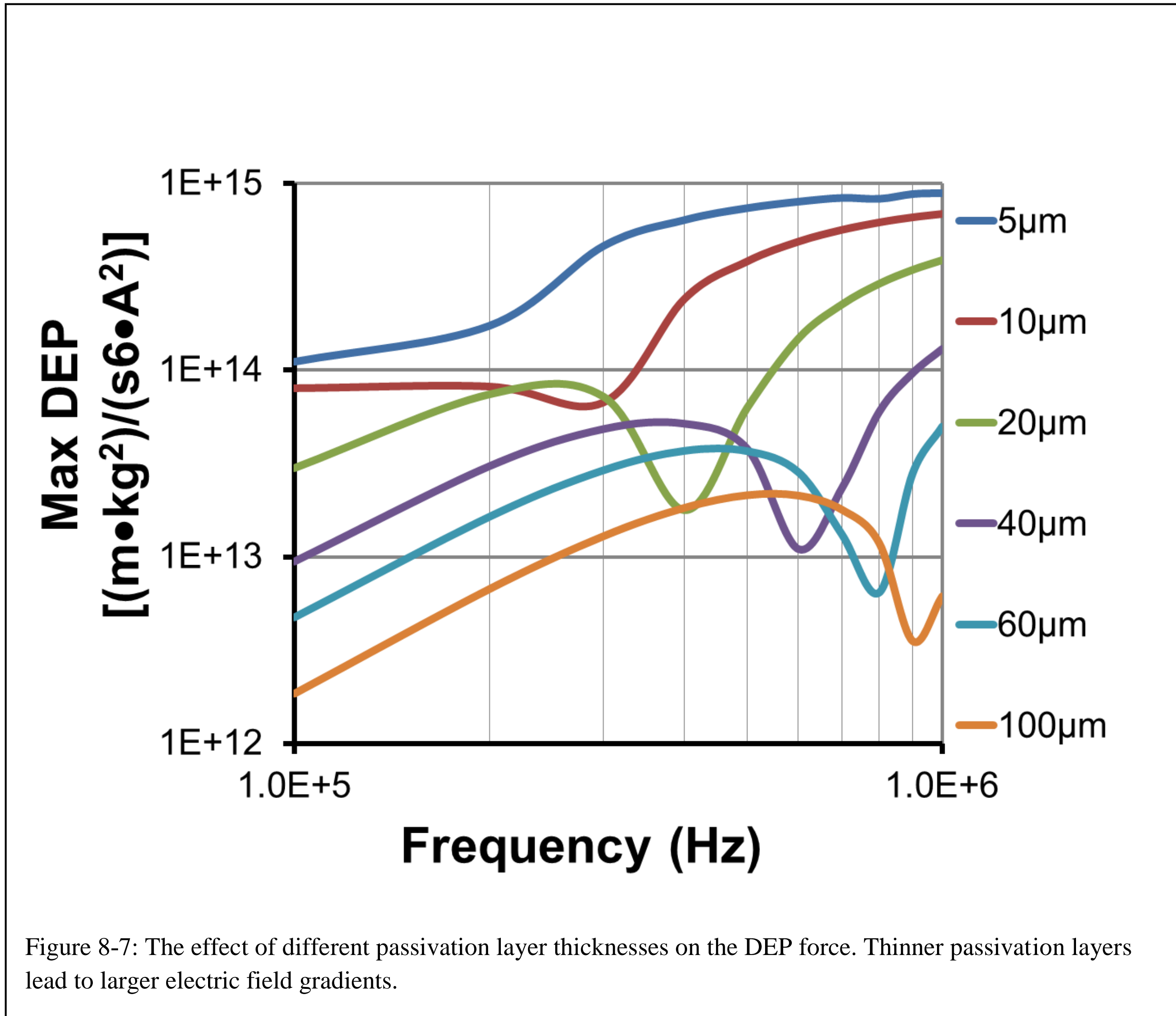

Figure 8-7: The effect of different passivation layer thicknesses on the DEP force. Thinner passivation layers lead to larger electric field gradients.

capacitive coupling between the AC signal and the microchannel and to increase the DEP force for a given voltage, a thinner barrier is desirable. Figure 8-7 shows a COMSOL simulation of the DEP forces generated in an EπDEP device with 10 V_{pp} applied. As the passivation layer decreases in in height, the DEP force increases dramatically.

Similar DEP techniques have been shown which use an insulating wall to separate the electrodes from the channel [60]. However, these techniques are limited to using a ~20 μm passivation wall in order to maintain the integrity of the bond between the wall and the glass substrate while having limited throughput. By contrast, we have used a 4 μm passivation and due to the spinning technique, this layer may be thinned to the dielectric

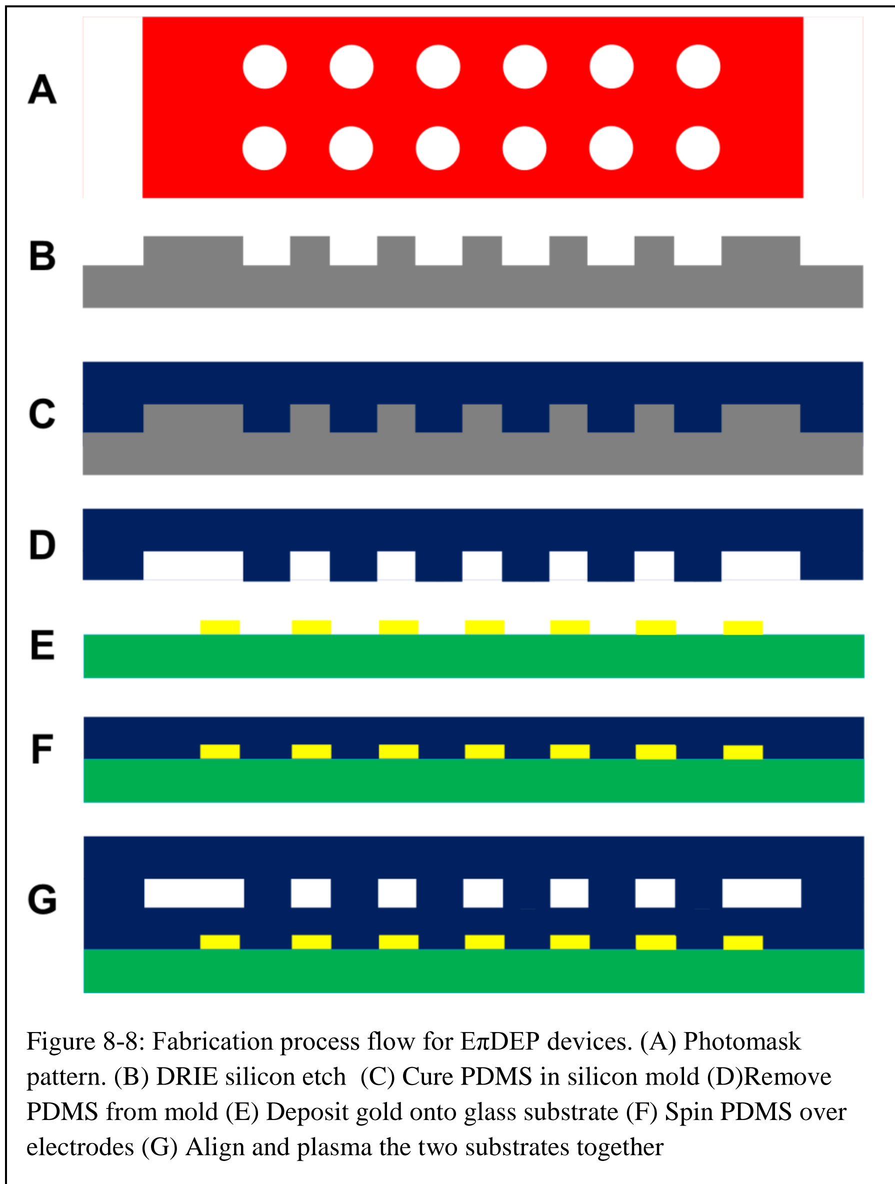

Figure 8-8: Fabrication process flow for EπDEP devices. (A) Photomask pattern. (B) DRIE silicon etch (C) Cure PDMS in silicon mold (D)Remove PDMS from mold (E) Deposit gold onto glass substrate (F) Spin PDMS over electrodes (G) Align and plasma the two substrates together

breakdown limit of the passivating material and can be extended across the channel width, thereby providing the ability to achieve high throughput.

Figure 8-8 shows our process flow for the design and fabrication of EπDEP implemented in PDMS. We created a photomask layout consisting of a microfluidic channel with an array of 100 μm diameter circular posts spaced 50 μm apart. After patterning photoresist, silicon was etched anisotropically using DRIE to form the channel and the embedded posts. After removing photoresist, the silicon substrate is used as a master mold. Liquid PDMS is poured onto the silicon master and cured, resulting in PDMS structures. Electrodes are patterned on a glass substrate using the lift-off technique and then passivated

by spinning and curing a thin PDMS layer on top of the glass substrate. Then, the PDMS substrate containing the insulating structures is plasma bonded directly to the electrode substrate forming a PDMS-PDMS bond.

8.3.3 Results and Discussion

To test the device, the bacteria were suspended in deionized water with a measured conductivity of 800 µS/m. The experiments were performed with *Salmonella typhimurium (S. typhimurium) (ATCC 14028)*. During device operation, the solution was passed through the EπDEP device with a syringe pump. The electrodes were excited with an AC signal of 40 Vpp with frequencies from 1 kHz to 1 MHz. The DEP force on the bacteria was observed to be dependent on the applied frequency (Figure 8-9) with 100% trapping occurring at frequencies of 100 kHz and higher with a flow rate of 400 µl/hr.

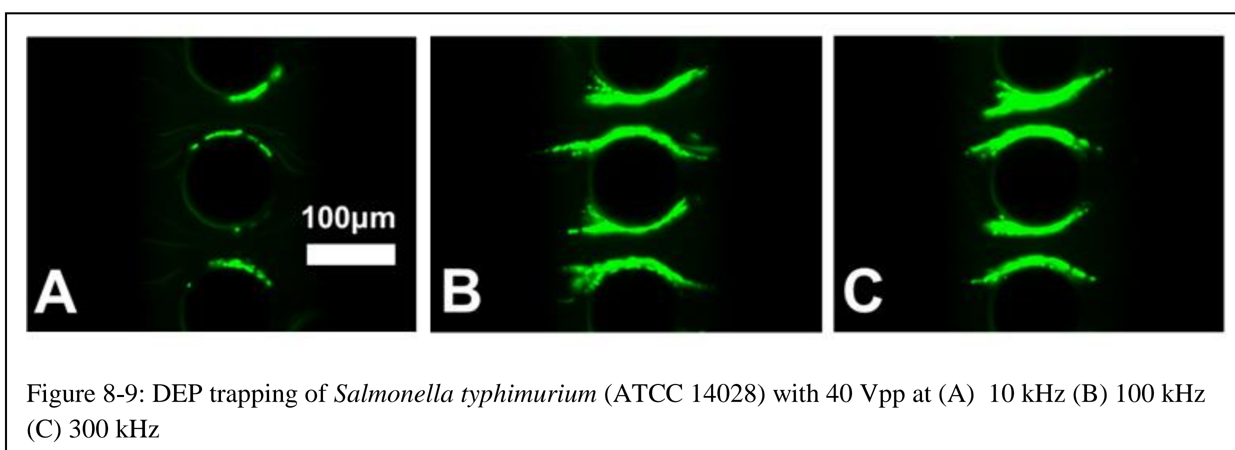

Figure 8-9: DEP trapping of *Salmonella typhimurium* (ATCC 14028) with 40 Vpp at (A) 10 kHz (B) 100 kHz (C) 300 kHz

8.3.4 Conclusions and Outlook

These results demonstrate the performance gains that are possible by decreasing the passivation layer thickness below the 100 µm used in OπDEP devices. The EπDEP device presented here was identical in design to the OπDEP device presented in Chapter 6 (Device 2) with the exception of a dramatically reduced passivation layer. This resulted in the device operating and order of magnitude lower voltage than the OπDEP device. The tradeoff is that the fabrication of these devices is more complicated and more expensive. Nevertheless, these devices may be useful for bioparticle characterization and other research applications where the cost per device is not crucial. Additionally, if OπDEP devices are found to not

operate properly with a certain media and bioparticle combination, EπDEP devices may be used to perform concentration and trapping to a sufficient level.

More importantly, however, these results show that it is worthwhile to experiment with OπDEP designs that allow devices to have reduced passivation layers. If 3D πDEP devices presented in Chapter 7 are given reduced passivation layers, the resulting devices may be able to operate on the order of a single volt. This would all but eliminate the supporting electronics and the input of these devices could be connected to a simple integrated circuit, greatly miniaturizing the full device. Of course, if implemented using OπDEP technique, this problem will be difficult due to the practical concerns of having a cartridge with one wall which is less than 100 μm thick. There are numerous ways to tackle this technical issue, such as using a substrate which is thin in some areas and thick in others. This may present other unforeseen issues however, given the potential benefits, this is a problem worthy of attention.

8.4 Other Future Directions

Dielectrophoresis is technique which is rapidly increasing in popularity. While this work has focused on bacteria manipulation, DEP devices can work on a large variety of bioparticles. Smaller particles such as viruses and proteins are can be difficult to work with as they are very small and thus require large electric field gradient to manipulate. 3D πDEP is ideally suited for these particles as these devices produce very large electric field gradients. Designs with even higher constriction ratios than presented in this work may be used for the smallest proteins to ensure sufficient DEP force.

Additionally larger particles such as mammalian cells may also be manipulated with 3D πDEP devices. The larger size would enable trapping at low voltages without any modifications to the device design. These devices could be used to characterize different cells or even perform fine separations and concentrations. For example the isolation of rare cells such as stem cells or circulation tumor cells, with a sufficient selectivity and throughput, remains a major goal for many researchers today. 3D πDEP may provide a platform to perform such sensitive operations.

8.5 Dissertation Significance and Contribution

8.5.1 Microfabrication Thrust

Within this work, several thrusts were made in microfabrication. These are diagramed in Figure 8-10. The main focus of this work was the development of a fabrication process capable of creating three dimensional microstructures. In order to keep the process cost effect, it was decided that only techniques which use a single photolithographic mask would be used. The only two techniques that fit this criteria are grey scale lithography and reactive ion etch lag. RIE lag was chosen as it is less sensitive to process conditions and thus more robust. Typically RIE lag is used to create channels which are of a fixed depth. However, this project developed a technique to create not only controllable etch depths, but also controllable depth transitions. Additionally, because of the oxide lattice structure which is key to enhancing RIE lag, all of these structures can easily be produced in buried channels. This technique was then extended to polymer devices by creating a negative of the 3D structures with a glass wafer and then using that negative as a mold for PDMS. Thus the 3D structures could then be reproduced using rapid, low cost, mold fabrication. The main microfabrication thrust accomplishments are listed below:

- This project extends the single mask, single etch, RIE lag, 3D fabrication process to include control of the transition region between different depths. **(Journal of Micromechanics and Microengineering 2010)**
- This project demonstrated the first buried channel technology with 3D varying features **(Journal of Micromechanics and Microengineering 2010)**
- This project extends the single mask, single etch, RIE lag, 3D fabrication process to both silicon and PDMS substrates. **(Journal of Microelectromechanical Systems 2012)**

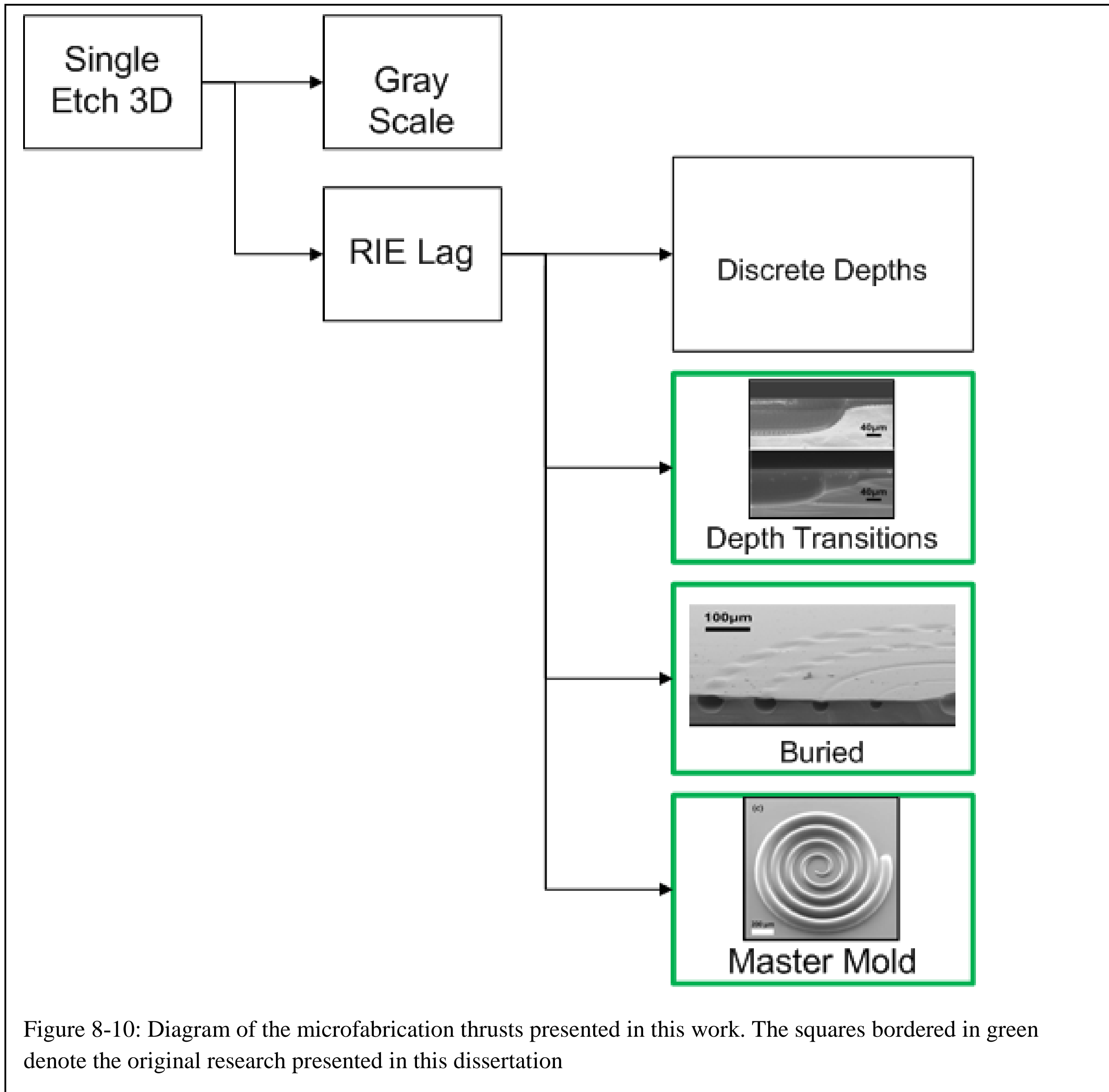

Figure 8-10: Diagram of the microfabrication thrusts presented in this work. The squares bordered in green denote the original research presented in this dissertation

8.5.2 Dielectrophoresis Thrust

The original research performed in this dissertation concerning dielectrophoresis is diagramed in figure 8-11. This research focused on insulator based dielectrophoresis rather than electrode based dielectrophoresis since the chosen application, pathogen detection, requires devices which are low cost and high throughput. Silicon was the first substrate chosen in this work for these devices due to compatibility with microfabrication tools. Previous iDEP designs were fabricated with either glass or

PDMS and suffered from heat buildup issues. This was the first time silicon had been used for iDEP devices, and the heat transfer properties of silicon proved to be very useful. Additionally, the silicon allowed for 3D structures to be easily included in the designs which increased the DEP force while decreasing the operating voltage and Joule heating in the devices. Then, using the 3D PDMS fabrication developed in this work, identical 3D iDEP devices were created in PDMS. These devices were actuated with DC biased AC electric fields, a technique which had not previously been used with bacteria. The resulting devices were very versatile, as the introduction of AC fields allowed them to easily separate a variety of bioparticles.

In order to move the technology toward a realistic device OπDEP, the cartridge based DEP system, was develop. By allowing the reusable electrodes to be on a separate substrate while having the microfluidic components on a very low cost substrate, this technology ensured sample purity in a practical manner. In addition to simpler device operation, this technology enabled an arbitrarily scalable throughput. Additionally, the technology was very flexible as it allowed different reusable electrodes to be used depending on the application requirements. This technology was then enhanced by using the 3D PDMS fabrication process to introduce 3D structures into the microchannel. The 3D structures greatly improved the performance of the devices, leading to benefits in operating bandwidth, operating voltage, and throughput without any added cost per device.

Using the same fabrication process flow as the standard OπDEP devices, a device was developed which contained both dielectrophoretic separation and off-chip impedance detection on the same chip. The impedance detection segment of the chip gave an indication of the amount of cells selectively trapped and released by the DEP portion of the chip. This was the first reported example of quantifying biological cells with impedance electrodes located off of the microfluidic chip. This component enables the development of a complete pathogen detection system, using the OπDEP architecture. Finally, an alternative method of increasing device sensitivity called EπDEP was developed. These devices have very thin passivation layers compared to the OπDEP devices and were shown to perform at reduced operating voltages. However, they had a more expensive process flow. The main dielectrophoresis thrust accomplishments are listed below:

- This project demonstrated the first 3D iDEP device **(Microtechnologies in Medicine and Biology 2009)**
- This project demonstrated the first silicon iDEP device and demonstrated the thermal benefits of using silicon **(Electrophoresis 2012)**
- This project demonstrated the first iDEP device powered by patterned off-chip electrodes (OπDEP) **(Analytical and Bioanalytical Chemistry 2013)**
- This project demonstrated the first use of DC-biased, AC field iDEP on biological samples (*E. coli and S. aureus*) **(Engineering in Medicine and Biology Conference 2012)**
- This project demonstrated the effect of thin passivation layers on πDEP devices, creating the first EπDEP device **(Biomedial Engineering Society Annual Meeting 2013)**
- This project developed the first OπDEP device with three dimensional structures for enhanced sensitivity (3D πDEP).
- This project developed the first OπDEP device with off-chip impedance detection

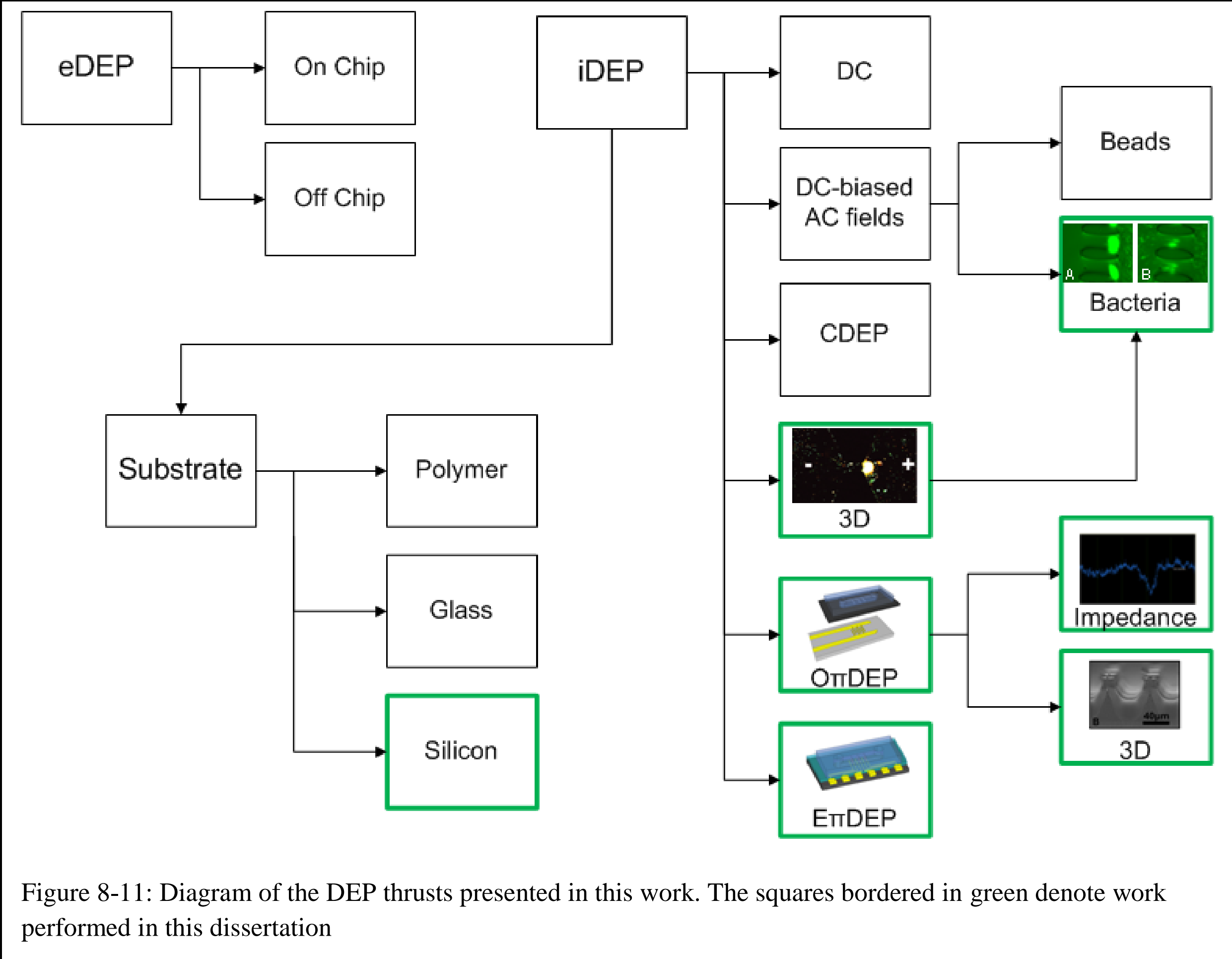

Figure 8-11: Diagram of the DEP thrusts presented in this work. The squares bordered in green denote work performed in this dissertation

Bibliography

1. WHO, *Global Water Supply and Sanitation Assessment 2000 Report*, 2000: Geneva, Switzerland.
2. S. Pedley, J.B., G. Rees, A. Dufour, J. A. Cotruvo, *Pathogenic Mycobacteria in Water*2004, London, UK: IWA Publishing,.
3. Terry, S.C., J.H. Jerman, and J.B. Angell, *A gas chromatographic air analyzer fabricated on a silicon wafer.* Electron Devices, IEEE Transactions on, 1979. **26**(12): p. 1880-1886.
4. Kua, C., Y.C. Lam, C. Yang, and K. Youcef-Toumi, *Review of bio-particle manipulation using dielectrophoresis.* 2005.
5. Irimajiri, A., T. Hanai, and A. Inouye, *A dielectric theory of "multi-stratified shell" model with its application to a lymphoma cell.* Journal of theoretical biology, 1979. **78**(2): p. 251-269.
6. Pohl, H., Appl. Phys., 1951. **22**: p. 869-871.
7. Zhou, R., P. Wang, and H.C. Chang. *Bacteria capture, concentration and detection based on ac dielectrophoresis, electro-osmotic transport and self-assembly of single-wall carbon nanotubes*. in *AICHE Annual Meeting*. 2005.
8. Huang, Y., R. Holzel, R. Pethig, and X.B. Wang, *Differences in the AC electrodynamics of viable and non-viable yeast cells determined through combined dielectrophoresis and electrorotation studies.* Physics in medicine and biology, 2000. **37**(7): p. 1499.
9. Hunt, T. and R. Westervelt, *Dielectrophoresis tweezers for single cell manipulation.* Biomedical Microdevices, 2006. **8**(3): p. 227-230.
10. Grom, F., J. Kentsch, T. Müller, T. Schnelle, and M. Stelzle, *Accumulation and trapping of hepatitis A virus particles by electrohydrodynamic flow and dielectrophoresis.* Electrophoresis, 2006. **27**(7): p. 1386-1393.
11. Hölzel, R., N. Calander, Z. Chiragwandi, M. Willander, and F.F. Bier, *Trapping single molecules by dielectrophoresis.* Physical review letters, 2005. **95**(12): p. 128102.
12. Pohl, H.A. and I. Hawk, *Separation of living and dead cells by dielectrophoresis.* Science (New York, NY), 1966. **152**(3722): p. 647.
13. Pohl, H.A. and J.S. Crane, *Dielectrophoresis of cells.* Biophysical Journal, 1971. **11**(9): p. 711-727.
14. Alazzam, A., I. Stiharu, R. Bhat, and A.-N. Meguerditchian, *Interdigitated comb-like electrodes for continuous separation of malignant cells from blood using dielectrophoresis.* Electrophoresis, 2011. **32**(11): p. 1327-1336.
15. Li, H.B. and R. Bashir, *Dielectrophoretic separation and manipulation of live and heat-treated cells of Listeria on microfabricated devices with interdigitated electrodes.* Sensors and Actuators B-Chemical, 2002. **86**(2-3): p. 215-221.
16. Wang, L., J. Lu, S.A. Marukenko, E.S. Monuki, L.A. Flanagan, and A.P. Lee, *Dual frequency dielectrophoresis with interdigitated sidewall electrodes for microfluidic flow-through separation of beads and cells.* Electrophoresis, 2009. **30**(5): p. 782-791.
17. Hsiung, L.C., C.H. Yang, C.L. Chiu, C.L. Chen, Y. Wang, H. Lee, J.Y. Cheng, M.C. Ho, and A.M. Wo, *A planar interdigitated ring electrode array via dielectrophoresis for uniform patterning of cells.* Biosensors & Bioelectronics, 2008. **24**(4): p. 869-875.
18. Rhoads, J.E., H.A. Pohl, and R.G. Buckner, *The dielectrophoresis of blood platelets as affected by hemophilic traits.* Journal of Biological Physics, 1976. **4**(3): p. 93-108.
19. Ting, I.P., K. Jolley, C. Beasley, and H.A. Pohl, *Dielectrophoresis of chloroplasts.* Biochimica et Biophysica Acta (BBA)-Bioenergetics, 1971. **234**(3): p. 324-329.
20. Markx, G.H., M.S. Talary, and R. Pethig, *Separation of viable and non-viable yeast using dielectrophoresis.* Journal of biotechnology, 1994. **32**(1): p. 29-37.
21. Moon, H., Y. Nam, J. Park, and H. Jung. *Continuous microfluidic airborne bacteria separation using dielectrophoresis*. 2009. IEEE.

22. Doh, I. and Y.H. Cho, *A continuous cell separation chip using hydrodynamic dielectrophoresis (DEP) process.* Sensors and Actuators A: Physical, 2005. **121**(1): p. 59-65.
23. Masuda, S., M. Washizu, and T. Nanba, *Novel method of cell fusion in field constriction area in fluid integration circuit.* Industry Applications, IEEE Transactions on, 1989. **25**(4): p. 732-737.
24. Cummings, E.B. and A.K. Singh, *Dielectrophoresis in microchips containing arrays of insulating posts: theoretical and experimental results.* Analytical Chemistry, 2003. **75**(18): p. 4724-4731.
25. Lapizco-Encinas, B.H., R.V. Davalos, B.A. Simmons, E.B. Cummings, and Y. Fintschenko, *An insulator-based (electrodeless) dielectrophoretic concentrator for microbes in water.* Journal of Microbiological Methods, 2005. **62**(3): p. 317-326.
26. Davalos, R.V., G.J. McGraw, T.I. Wallow, A.M. Morales, K.L. Krafcik, Y. Fintschenko, E.B. Cummings, and B.A. Simmons, *Performance impact of dynamic surface coatings on polymeric insulator-based dielectrophoretic particle separators.* Analytical and Bioanalytical Chemistry, 2008. **390**(3): p. 847-855.
27. Martinez-Lopez, J.I., H. Moncada-Hernandez, J.L. Baylon-Cardiel, S.O. Martinez-Chapa, M. Rito-Palomares, and B.H. Lapizco-Encinas, *Characterization of electrokinetic mobility of microparticles in order to improve dielectrophoretic concentration.* Analytical and Bioanalytical Chemistry, 2009. **394**(1): p. 293-302.
28. Chen, D. and H. Du, *A microfluidic device for rapid concentration of particles in continuous flow by DC dielectrophoresis.* Microfluidics and Nanofluidics, 2010. **9**(2-3): p. 281-291.
29. Ozuna-Chacon, S., B.H. Lapizco-Encinas, M. Rito-Palomares, S.O. Martinez-Chapa, and C. Reyes-Betanzo, *Performance characterization of an insulator-based dielectrophoretic microdevice.* Electrophoresis, 2008. **29**(15): p. 3115-3122.
30. Lapizco-Encinas, B.H., *Dielectrophoretic Concentration and Separation of Live and Dead Baccteria in an Array of Insulators.* Anal. Chem., 2004. **76**: p. 1571-1579.
31. Lapizco-Encinas, B.H., B.A. Simmons, E.B. Cummings, and Y. Fintschenko, *Insulator-based dielectrophoresis for the selective concentration and separation of live bacteria in water.* Electrophoresis, 2004. **25**(10-11): p. 1695-1704.
32. Li, H. and R. Bashir, *Dielectrophoretic separation and manipulation of live and heat-treated cells of Listeria on microfabricated devices with interdigitated electrodes.* Sensors and Actuators B: Chemical, 2002. **86**(2–3): p. 215-221.
33. Markx, G.H., Y. Huang, X.F. Zhou, and R. Pethig, *Dielectrophoretic characterization and separation of micro-organisms.* Microbiology, 1994. **140**(3): p. 585-591.
34. Zellner, P., A. Sahari, Y. Hosseini, B. Behkam, and M. Agah. *Selective E. coli Trapping with 3D Insulator-based Dielectrophoresis using DC-Biased, AC Electric Fields*. in *34th Annual International Conference of the IEEE EMBS (EMBC 2012)*. August 2012. San Diego, CA.
35. Castellarnau, M., A. Errachid, C. Madrid, A. Juárez, and J. Samitier, *Dielectrophoresis as a Tool to Characterize and Differentiate Isogenic Mutants of Escherichia coli.* Biophysical Journal, 2006. **91**(10): p. 3937-3945.
36. Simmons, B., B. Lapizco-Encinas, R. Shediac, J. Hachman, J. Chames, J. Brazzle, J. Ceremuga, G. Fiechtner, E. Cummings, and Y. Fintschenko, *Polymeric insulator-based (electrodeless) dielectrophoresis (iDEP) for the monitoring of water-borne pathogens.* Micro Total Analysis Systems 2004, Vol 2, 2005(297): p. 171-173.
37. Huang, Y., J. Yang, P. Hopkins, S. Kassegne, M. Tirado, A. Forster, and H. Reese, *Separation of Simulants of Biological Warfare Agents from Blood by a Miniaturized Dielectrophoresis Device.* Biomedical Microdevices, 2003. **5**(3): p. 217-225.
38. Morgan, H. and N.G. Green, *AC electrokinetics: colloids and nanoparticles*2003: Research Studies Press.

39. Allsopp, D. and W. Betts, *Dielectrophoretic sensors for microbiological applications.* Selected Topics in Advanced Solid State and Fibre Optic Sensors, 2000. **11**: p. 165.
40. Pethig, R., *Review Article—Dielectrophoresis: Status of the theory, technology, and applications.* Biomicrofluidics, 2010. **4**(2).
41. Polk, C. and E. Postow, *Handbook of biological effects of electromagnetic fields*1996: CRC PressI Llc.
42. Kakutani, T., S. Shibatani, and M. Sugai, *Electrorotation of non-spherical cells: theory for ellipsoidal cells with an arbitrary number of shells.* Bioelectrochemistry and bioenergetics, 1993. **31**(2): p. 131-145.
43. Rice, C. and R. Whitehead, *Electrokinetic flow in a narrow cylindrical capillary.* The Journal of Physical Chemistry, 1965. **69**(11): p. 4017-4024.
44. Cummings, E.B., S. Griffiths, R. Nilson, and P. Paul, *Conditions for similitude between the fluid velocity and electric field in electroosmotic flow.* Analytical Chemistry, 2000. **72**(11): p. 2526-2532.
45. Masuda, S., T. Itagaki, and M. Kosakada, *Detection of extremely small particles in the nanometer and ionic size range.* IEEE Trans. on Industry Applications, 1988. **24**: p. 740-744.
46. Cummings, E.B., B.A. Simmons, R.V. Davalos, G.J. McGraw, B.H. Lapizco-Encinas, and Y. Fintschenko, *Fast and selective concentration of pathogens by insulator-based dielectrophoresis.* Abstracts of Papers of the American Chemical Society, 2005. **230**: p. U404-U405.
47. Davalos, R.V., B.H. Lapizco-Encinas, G.J. Fiechtner, A.K. Singh, B.A. Simmons, Y. Fintschenko, and E.B. Cummings, *A performance comparison of post-and ridge-based dielectrophoretic particle sorters.* Micro Total Analysis Systems 2004, Vol 1, 2005(296): p. 650-652.
48. Lapizco-Encinas, B.H., S. Ozuna-Chacon, and M. Rito-Palomares, *Protein manipulation with insulator-based dielectrophoresis and direct current electric fields.* Journal of Chromatography A, 2008. **1206**(1): p. 45-51.
49. Lapizco-Encinas, B.H., S. Ozuna-Chacon, M. Rito-Palomares, C. Reyes-Betanzo, E. Collado-Arredondo, and S.O. Martinez-Chapa, *Insulator based dielectrophoresis: Effects of bulk medium properties.* Icnmm2007: Proceedings of the 5th International Conference on Nanochannels, Microchannels, and Minichannels, 2007: p. 177-183.
50. Lapizco-Encinas, B.H., B.A. Simmons, E.B. Cummings, and Y. Fintschenko, *Dielectrophoretic concentration and separation of live and dead bacteria in an array of insulators.* Anal Chem, 2004. **76**(6): p. 1571-9.
51. McGraw, G.J., M. Kanouff, J.T. Ceremuga, R.V. Davalos, B.H. Lapizco-Encinas, P. Mela, R. Shediac, J.D. Brazzle, J.T. Hachman, G.J. Fiechtner, E.B. Cummings, Y. Fintschenko, and B.A. Simmons, *A Comparison of Insulator-Based Dielectrophoretic Devices for the Monitoring and Separation of Waterborne Pathogens as a Function of Microfabrication Technique.* Antiterrorism and Homeland Defense: Polymers and Materials, 2007. **980**: p. 133-157.
52. Ozuna-Chacon, S., B.H. Lapizco-Encinas, M. Rito-Palomares, E. Collado-Arredondo, and S.O. Martinez-Chapa, *Insulator-based dielectrophoresis.* Revista Mexicana De Ingenieria Quimica, 2007. **6**(3): p. 329-335.
53. Wang, J.P., H. Hu, Z.Y. Wang, and L.T. Liu, *Numerical analysis and optimization of insulator-based dielectrophoresis devices for cell sorter applications.* 2007 2nd IEEE International Conference on Nano/Micro Engineered and Molecular Systems, Vols 1-3, 2007: p. 814-817.
54. Du, F., M. Baune, and J. Thoming, *Insulator-based dielectrophoresis in viscous media - Simulation of particle and droplet velocity.* Journal of Electrostatics, 2007. **65**(7): p. 452-458.
55. Jen, C.P. and T.W. Chen, *Selective trapping of live and dead mammalian cells using*

insulator-based dielectrophoresis within open-top microstructures. Biomedical Microdevices, 2009. **11**(3): p. 597-607.

56. Jen, C.P. and T.W. Chen, *Trapping of cells by insulator-based dielectrophoresis using open-top microstructures.* Microsystem Technologies-Micro-and Nanosystems-Information Storage and Processing Systems, 2009. **15**(8): p. 1141-1148.
57. Jen, C.P., C.T. Huang, and H.Y. Shih, *Hydrodynamic Separation of Cells Utilizing Insulator-based Dielectrophoresis.* Dtip 2009: Symposium on Design, Test, Integration and Packaging of Mems/Moems, 2009: p. 55-59.
58. Jen, C.P., Y.H. Huang, and T.W. Chen, *Cell Trapping Utilizing Insulator-based Dielectrophoresis in The Open-Top Microchannels.* Dtip 2008: Symposium on Design, Test, Integration and Packaging of Mems/Moems, 2008: p. 289-291.
59. Shaflee, H. and R.V. Davalos, *An Autonomous Cell Type Selective Irreversible Electroporation Microsystem Using Insulator Based Dielectrophoresis (Idep).* Proceedings of the Asme Summer Bioengineering Conference 2008, Pts a and B, 2009: p. 591-592.
60. Shafiee, H., J.L. Caldwell, M.B. Sano, and R.V. Davalos, *Contactless dielectrophoresis: a new technique for cell manipulation.* Biomedical Microdevices, 2009. **11**.
61. Kovacs, G.T.A., N.I. Maluf, and K.E. Petersen, *Bulk micromachining of silicon.* Proceedings of the IEEE, 1998. **86**(8): p. 1536-1551.
62. Frechette, L.G., S.F. Nagle, R. Ghodssi, S.D. Umans, M.A. Schmidt, and J.H. Lang. *An electrostatic induction micromotor supported on gas-lubricated bearings*. in *Micro Electro Mechanical Systems, 2001. MEMS 2001. The 14th IEEE International Conference on*. 2001. IEEE.
63. Chuang-Chia, L., R. Ghodssi, A.A. Ayon, C. Dye-Zone, S. Jacobson, K. Breuer, A.H. Epstein, and M.A. Schmidt. *Fabrication and characterization of a micro turbine/bearing rig*. in *Micro Electro Mechanical Systems, 1999. MEMS '99. Twelfth IEEE International Conference on*. 1999.
64. Bustillo, J.M., R.T. Howe, and R.S. Muller, *Surface micromachining for microelectromechanical systems.* Proceedings of the IEEE, 1998. **86**(8): p. 1552-1574.
65. Waits, C., B. Morgan, M. Kastantin, and R. Ghodssi, *Microfabrication of 3D silicon MEMS structures using gray-scale lithography and deep reactive ion etching.* Sensors and Actuators A: Physical, 2005. **119**(1): p. 245-253.
66. Jansen, H., M. deBoer, R. Wiegerink, N. Tas, E. Smulders, C. Neagu, and M. Elwenspoek. *RIE lag in high aspect ratio trench etching of silicon*. in *Micro and Nano Engineering Conference 1996 (MNE 96)*. 1996. Glasgow, Scotland.
67. Panda, S., R. Ranade, and G.S. Mathad, *Etching high aspect ratio silicon trenches.* Journal of the Electrochemical Society, 2003. **150**(10): p. G612-G616.
68. Chung, C.K., *Geometrical pattern effect on silicon deep etching by an inductively coupled plasma system.* Journal of Micromechanics and Microengineering, 2004. **14**(4): p. 656-662.
69. Chou, T.K.A. and K. Najafi. *Fabrication of out-of-plane curved surfaces in Si by utilizing RIE lag*. in *Micro Electro Mechanical Systems, 2002. The Fifteenth IEEE International Conference on*. 2002. IEEE.
70. Bourouina, T., T. Masuzawa, and H. Fujita. *The MEMSNAS process: Microloading effect for micromachining 3-D structures of nearly all shapes*. in *IEEE/LEOS Optical MEMS Conference*. 2001. Okinawa, JAPAN.
71. Bourouina, T., T. Masuzawa, and H. Fujita, *The MEMSNAS process: microloading effect for micromachining 3-D structures of nearly all shapes.* Microelectromechanical Systems, Journal of, 2004. **13**(2): p. 190-199.
72. Rao, M.P., M.F. Aimi, and N.C. MacDonald, *Single-mask, three-dimensional microfabrication of high-aspect-ratio structures in bulk silicon using reactive ion etching lag and sacrificial oxidation.* Applied Physics Letters, 2004. **85**(25): p. 6281-6283.
73. Gantz, K., L. Renaghan, and M. Agah, *Development of a comprehensive model for RIE-lag-based three-dimensional microchannel fabrication.* Journal of Micromechanics and

Microengineering, 2008. **18**(2).
74. Duffy, D.C., H.L. Gillis, J. Lin, N.F. Sheppard, and G.J. Kellogg, *Microfabricated centrifugal microfluidic systems: Characterization and multiple enzymatic assays.* Analytical Chemistry, 1999. **71**(20): p. 4669-4678.
75. Terray, A., J. Oakey, and D.W.M. Marr, *Microfluidic control using colloidal devices.* Science, 2002. **296**(5574): p. 1841-1844.
76. Agah, M., J.A. Potkay, G. Lambertus, R. Sacks, and K.D. Wise, *High-performance temperature-programmed microfabricated gas chromatography columns.* Journal of Microelectromechanical Systems, 2005. **14**(5): p. 1039-1050.
77. Deng, Z.S., J. Liu, and Ieee. *Capacity evaluation of a MEMS based micro cooling device using liquid metal as coolant*. in *IEEE International Conference of Nano/Micro Engineered and Molecular Systems*. 2006. Zhuhai, PEOPLES R CHINA: Ieee.
78. Thong, J.T.L., W.K. Choi, and C.W. Chong, *TMAH etching of silicon and the interaction of etching parameters.* Sensors and Actuators a-Physical, 1997. **63**(3): p. 243-249.
79. Williams, K.R., K. Gupta, and M. Wasilik, *Etch rates for micromachining processing - Part II.* Journal of Microelectromechanical Systems, 2003. **12**(6): p. 761-778.
80. Williams, K.R. and R.S. Muller, *Etch rates for micromachining processing.* Journal of Microelectromechanical Systems, 1996. **5**(4): p. 256-269.
81. Jansen, H., M. de Boer, R. Wiegerink, N. Tas, E. Smulders, C. Neagu, and M. Elwenspoek, *RIE lag in high aspect ratio trench etching of silicon.* Microelectronic Engineering, 1997. **35**(1-4): p. 45-50.
82. Keil, D. and E. Anderson, *Characterization of reactive ion etch lag scaling.* Journal of Vacuum Science and Technology B: Microelectronics and Nanometer Structures, 2001. **19**(6): p. 2082-2088.
83. Panda, S., R. Ranade, and G.S. Mathad, *Etching high aspect ratio silicon trenches.* Journal of the Electrochemical Society, 2003. **150**(10): p. 612-616.
84. Chung, C.-K., *Geometrical pattern effect on silicon deep etching by an inductively coupled plasma system.* Journal of Micromechanics and Microengineering, 2004. **14**(4): p. 656-662.
85. Zhu, X., D.W. Greve, and G.K. Fedder, *Characterization of silicon isotropic etch by inductively coupled plasma etch in post-CMOS processing.* Proceedings of the IEEE Micro Electro Mechanical Systems (MEMS), 2000: p. 568-573.
86. Larsen, K.P., J.T. Ravnkilde, and O. Hansen, *Investigations of the isotropic etch of an ICP source for silicon microlens mold fabrication.* Journal of Micromechanics and Microengineering, 2005. **15**(4): p. 873-882.
87. Bourouina, T., T. Masuzawa, and H. Fujita, *The MEMSNAS process: Microloading effect for micromachining 3-D structures of nearly all shapes.* Journal of Microelectromechanical Systems, 2004. **13**(2): p. 190-199.
88. de Boer, M.J., R.W. Tjerkstra, J.W. Berenschot, H.V. Jansen, C.J. Burger, J.G.E. Gardeniers, M. Elwenspoek, and A. van den Berg, *Micromachining of buried micro channels in silicon.* Journal of Microelectromechanical Systems, 2000. **9**(1): p. 94-103.
89. Agah, M. and K.D. Wise, *Low-mass PECVD oxynitride gas chromatographic columns.* Journal of Microelectromechanical Systems, 2007. **16**(4): p. 853-860.
90. Chen, J.K. and K.D. Wise, *A high-resolution silicon monolithic nozzle array for inkjet printing.* IEEE Transactions on Electron Devices, 1997. **44**(9): p. 1401-1409.
91. Ray, S.K., C.K. Maiti, S.K. Lahiri, and N.B. Chakrabarti, *TEOS-based PECVD of silicon dioxide for VLSI applications.* Advanced Materials for Optics and Electronics, 1996. **6**(2): p. 73-82.
92. Zellner, P., H. Shafiee, M. Sano, R. Davalos, and M. Agah, *An Insulator-based Dielectrophoresis Silicon Microchip for Cell Trapping*, in *Microtechnologies in Medicine and Biology Conference*2009: Quebec, Canada.
93. Weisenberg, B.A. and D.L. Mooradian, *Hemocompatibility of materials used in microelectromechanical systems: Platelet adhesion and morphology in vitro.* Journal of

Biomedical Materials Research, 2002. **60**(2): p. 283-291.
94. Voskerician, G., M.S. Shive, R.S. Shawgo, H. von Recum, J.M. Anderson, M.J. Cima, and R. Langer, *Biocompatibility and biofouling of MEMS drug delivery devices.* Biomaterials, 2003. **24**(11): p. 1959-1967.
95. Lapizco-Encinas, B.H., *An insulator-based (electrodeless) dielectrophoretic concentrator for microbes in water.* Microbiological Methods, 2005. **62**: p. 317-326.
96. Hawkins, B.G., A.E. Smith, Y.A. Syed, and B.J. Kirby, *Continuous-flow particle separation by 3D insulative dielectrophoresis using coherently shaped, dc-biased, ac electric fields.* Analytical Chemistry, 2007. **79**(19): p. 7291-7300.
97. Tung, Y.C., M. Zhang, C.T. Lin, K. Kurabayashi, and S.J. Skerlos, *PDMS-based opto-fluidic micro flow cytometer with two-color, multi-angle fluorescence detection capability using PIN photodiodes.* Sensors and Actuators B-Chemical, 2004. **98**(2-3): p. 356-367.
98. Lin, C.H., G.B. Lee, S.H. Chen, and G.L. Chang, *Micro capillary electrophoresis chips integrated with buried SU-8/SOG optical waveguides for bio-analytical applications.* Sensors and Actuators a-Physical, 2003. **107**(2): p. 125-131.
99. Bernini, R., E. De Nuccio, F. Brescia, A. Minardo, L. Zeni, P.M. Sarro, R. Palumbo, and M.R. Scarfi, *Development and characterization of an integrated silicon micro flow cytometer (vol 386, pg 2257, 2006).* Analytical and Bioanalytical Chemistry, 2006. **386**(7-8): p. 2257-2257.
100. Jensen, K.F. *Microreaction engineering - is small better?* in *16th International Symposium on Chemical Reaction Engineering*. 2000. Krakow, Poland: Pergamon-Elsevier Science Ltd.
101. Losey, M.W., R.J. Jackman, S.L. Firebaugh, M.A. Schmidt, and K.F. Jensen, *Design and fabrication of microfluidic devices for multiphase mixing and reaction.* Journal of Microelectromechanical Systems, 2002. **11**(6): p. 709-717.
102. Stott, S.L., C.H. Hsu, D.I. Tsukrov, M. Yu, D.T. Miyamoto, B.A. Waltman, S.M. Rothenberg, A.M. Shah, M.E. Smas, G.K. Korir, F.P. Floyd, A.J. Gilman, J.B. Lord, D. Winokur, S. Springer, D. Irimia, S. Nagrath, L.V. Sequist, R.J. Lee, K.J. Isselbacher, S. Maheswaran, D.A. Haber, and M. Toner, *Isolation of circulating tumor cells using a microvortex-generating herringbone-chip.* Proceedings of the National Academy of Sciences of the United States of America, 2010. **107**(43): p. 18392-18397.
103. Shafiee, H., M.B. Sano, E.A. Henslee, J.L. Caldwell, and R.V. Davalos, *Selective isolation of live/dead cells using contactless dielectrophoresis (cDEP).* Lab on a Chip, 2010. **10**(4): p. 438-445.
104. Maruyama, H., K. Kotani, T. Masuda, A. Honda, T. Takahata, and F. Arai, *Nanomanipulation of single influenza virus using dielectrophoretic concentration and optical tweezers for single virus infection to a specific cell on a microfluidic chip.* Microfluidics and Nanofluidics, 2011. **10**(5): p. 1109-1117.
105. Didar, T.F. and M. Tabrizian, *Adhesion based detection, sorting and enrichment of cells in microfluidic Lab-on-Chip devices.* Lab on a Chip, 2010. **10**(22): p. 3043-3053.
106. Rhee, S.W., A.M. Taylor, D.H. Cribbs, C.W. Cotman, and N.L. Jeon, *External force-assisted cell positioning inside microfluidic devices.* Biomedical Microdevices, 2007. **9**(1): p. 15-23.
107. Inatomi, K.I., S.I. Izuo, and S.S. Lee, *Application of a microfluidic device for counting of bacteria.* Letters in Applied Microbiology, 2006. **43**(3): p. 296-300.
108. Chou, C.F., J.O. Tegenfeldt, O. Bakajin, S.S. Chan, E.C. Cox, N. Darnton, T. Duke, and R.H. Austin, *Electrodeless dielectrophoresis of single- and double-stranded DNA.* Biophysical Journal, 2002. **83**(4): p. 2170-2179.
109. Voldman, J., *Electrical forces for microscale cell manipulation.* Annual Review of Biomedical Engineering, 2006. **8**: p. 425-454.
110. Sabounchi, P., D.E. Huber, M.P. Kanouff, A.E. Harris, and B.A. Simmons, *Joule Heating Effects on Insulator-Based Dielectrophoresis*, in *Twelfth International Conferences on Miniaturized Systems for Chemistry and Life Sciences*2008: San Diego, CA, USA. p. 50–52.

111. Muller, T., A. Gerardino, T. Schnelle, S.G. Shirley, F. Bordoni, G. DeGasperis, R. Leoni, and G. Fuhr, *Trapping of micrometre and sub-micrometre particles by high-frequency electric fields and hydrodynamic forces.* Journal of Physics D-Applied Physics, 1996. **29**(2): p. 340-349.
112. Ramos, A., H. Morgan, N.G. Green, and A. Castellanos, *Ac electrokinetics: a review of forces in microelectrode structures.* Journal of Physics D-Applied Physics, 1998. **31**(18): p. 2338-2353.
113. Perch-Nielsen, I.R., N.G. Green, and A. Wolff, *Numerical simulation of travelling wave induced electrothermal fluid flow.* Journal of Physics D-Applied Physics, 2004. **37**(16): p. 2323-2330.
114. Wang, D.Z., M. Sigurdson, and C.D. Meinhart, *Experimental analysis of particle and fluid motion in ac electrokinetics.* Experiments in Fluids, 2005. **38**(1): p. 1-10.
115. Gonzalez, A., A. Ramos, H. Morgan, N.G. Green, and A. Castellanos, *Electrothermal flows generated by alternating and rotating electric fields in microsystems.* Journal of Fluid Mechanics, 2006. **564**: p. 415-433.
116. Hawkins, B.G. and B.J. Kirby, *Electrothermal flow effects in insulating (electrodeless) dielectrophoresis systems.* Electrophoresis, 2010. **31**(22): p. 3622-3633.
117. Sabounchi, P., A.M. Morales, P. Ponce, L.P. Lee, B.A. Simmons, and R.V. Davalos, *Sample concentration and impedance detection on a microfluidic polymer chip.* Biomedical Microdevices, 2008. **10**(5): p. 661-670.
118. Sridharan, S., J. Zhu, G. Hu, and X. Xuan, *Joule heating effects on electroosmotic flow in insulator-based dielectrophoresis.* Electrophoresis, 2011. **32**(17): p. 2274-2281.
119. Erickson, D., *Joule heating and heat transfer in poly(dimethylsiloxane) microfluidic systems.* Lab Chip, 2003. **3**: p. 141-149.
120. Lobo, H. and C. Cohen, *MEASUREMENT OF THERMAL-CONDUCTIVITY OF POLYMER MELTS BY THE LINE-SOURCE METHOD.* Polymer Engineering and Science, 1990. **30**(2): p. 65-70.
121. Lide, D.R., *CRC Handbook of Chemistry and Physics*. 90 Edition ed2009, Boca Raton, FL: CRC Press.
122. Yamasue, E., M. Susa, H. Fukuyama, and K. Nagata, *Thermal conductivities of silicon and germanium in solid and liquid states measured by non-stationary hot wire method with silica coated probe.* Journal of Crystal Growth, 2002. **234**(1): p. 121-131.
123. Braff, W.A., A. Pignier, and C.R. Buie, *High sensitivity three-dimensional insulator-based dielectrophoresis.* Lab on a Chip, 2012. **12**(7): p. 1327-1331.
124. Zellner, P., L. Renaghan, Z. Hasnain, and M. Agah, *A fabrication technology for three-dimensional micro total analysis systems.* Journal of Micromechanics and Microengineering, 2010. **20**(4).
125. Gallo-Villanueva, R.C., V.H. Perez-Gonzalez, R.V. Davalos, and B.H. Lapizco-Encinas, *Separation of mixtures of particles in a multipart microdevice employing insulator-based dielectrophoresis.* Electrophoresis, 2011. **32**(18): p. 2456-2465.
126. Mampallil, D., D. van den Ende, and F. Mugele, *A simple method to determine the surface charge in microfluidic channels.* Electrophoresis, 2010. **31**(3): p. 563-569.
127. Spehar, A.M., S. Koster, V. Linder, S. Kulmala, N.F. de Rooij, E. Verpoorte, H. Sigrist, and W. Thormann, *Electrokinetic characterization of poly(dimethylsiloxane) microchannels.* Electrophoresis, 2003. **24**(21): p. 3674-3678.
128. Ross, D., M. Gaitan, and L.E. Locascio, *Temperature measurement in microfluidic systems using a temperature-dependent fluorescent dye.* Analytical Chemistry, 2001. **73**(17): p. 4117-4123.
129. Seger, U., M. Panayiotou, S. Schnydrig, M. Jordan, and P. Renaud, *Temperature measurements in microfluidic systems: Heat dissipation of negative dielectrophoresis barriers.* Electrophoresis, 2005. **26**(11): p. 2239-2246.
130. Swarts, J.W., A.E.M. Janssen, and R.M. Boom, *Temperature effects during practical*

operation of microfluidic chips. Chemical Engineering Science, 2008. **63**(21): p. 5252-5257.

131. Shah, J.J., M. Gaitan, and J. Geist, *Generalized Temperature Measurement Equations for Rhodamine B Dye Solution and Its Application to Microfluidics.* Analytical Chemistry, 2009. **81**(19): p. 8260-8263.
132. Glawdel, T., Z. Almutairi, S. Wang, and C. Ren, *Photobleaching absorbed Rhodamine B to improve temperature measurements in PDMS microchannels.* Lab on a Chip, 2009. **9**(1): p. 171-174.
133. Castellanos, A., A. Ramos, A. Gonzalez, N.G. Green, and H. Morgan, *Electrohydrodynamics and dielectrophoresis in microsystems: scaling laws.* Journal of Physics D-Applied Physics, 2003. **36**(20): p. 2584-2597.
134. Henslee, E.A., M.B. Sano, A.D. Rojas, E.M. Schmelz, and R.V. Davalos, *Selective concentration of human cancer cells using contactless dielectrophoresis.* Electrophoresis, 2011. **32**(18): p. 2523-2529.
135. Kirby, B.J. and E.F. Hasselbrink, *Zeta potential of microfluidic substrates: 1. Theory, experimental techniques, and effects on separations.* Electrophoresis, 2004. **25**(2): p. 187-202.
136. Xia, Y. and G.M. Whitesides, *Soft Lithography.* Annu. Rev. Mater. Sci. , 1998. **28**: p. 153-184.
137. Abbott, A., *Cell culture: Biology's new dimension.* Nature, 2003. **424**(6951): p. 870–872.
138. Wu, M.-H., C. Park, and G.M. Whitesides, *Fabrication of Arrays of Microlenses with Controlled Profiles Using Gray-Scale Microlens Projection Photolithography.* Langmuir, 2002. **18**: p. 9312-9318.
139. C. M. Waits, A. Modafe, and R. Ghodssi, *Investigation of gray-scale technology for large area 3D silicon MEMS structures.* J. Micromech. Microeng., 2003. **3**: p. 170–177.
140. Therriault, D., S.R. White, and J.A. Lewis, *Chaotic mixing in three-dimensional microvascular networks fabricated by direct-write assembly.* Nature Mater., 2003. **2**: p. 265 - 271.
141. C. N. LaFratta, L. Li, and J.T. Fourkas. *Soft-lithographic replication of 3D microstructures with closed loops*. in *Proc. Ntnl. Acad. Sci. USA*. 2006.
142. Kim, D. and P.T.C. So, *High-throughput three-dimensional lithographic microfabrication.* Opt. Lett., 2010. **35**(10): p. 1602–1604.
143. Y. Hongbin, Z. Guangya, C. Fook Siong, W. Shouhua, and L. Feiwen, *Novel polydimethylsiloxane (PDMS) based microchannel fabrication method for lab-on-a-chip application.* Sens. Act. B, 2009. **137**: p. 754–761.
144. L. K. Fiddes, N. Raz, S. Srigunapalan, E. Tumarkan, C. A. Simmons, A. R. Wheeler, and E. Kumacheva, *A circular cross-section PDMS microfluidics system for replication of cardiovascular flow conditions.* Biomater., 2010. **31**: p. 3459–3464.
145. S.-H. Song, C.-K. Lee, T.-J. Kim, I.-C. Shin, S.-C. Jun, and H.-I. Jung, *A rapid and simple fabrication method for 3-dimensional circular microfluidic channel using metal wire removal process* Microfluid. Nanofluid., 2010. **9**: p. 533–540.
146. Shih, W.-C., S.-G. Kim, and G. Barbastathis, *High-resolution electrostatic analog tunable grating with a single-mask fabrication process.* J. Microelectromech. Syst., 2006. **15**: p. 763–769.
147. Yeh, R., S. Hollar, and K.S.J. Pister, *Single mask, large Force, and large displacement electrostatic linear inchworm motors.* J. Microelectromech. Syst., 2002. **11**: p. 330–336.
148. K. Gantz, L. Renaghan, and M. Agah, *Development of a comprehensive model for RIE-lag-based three-dimensional microchannel Fabrication.* J. Micromech. Microeng., 2008. **18**: p. 025003.
149. P. Zellner, L. Renaghan, Z. Hasnain, and M. Agah, *A fabrication technology for three-dimensional micro total analysis systems.* J. Micromech. Microeng., 2010. **20**: p. 045013.
150. Wang, G.-J., K.-H. Ho, S.-H. Hsu, and K.-P. Wang, *Microvessel scaffold with circular microchannels by photoresist melting.* Biomed Microdevices, 2007. **9**: p. 657–663.

151. Chen, Y.-C., G.-Y. Chen, Y.-C. Lin, and G.-J. Wang, *A lab-on-a-chip capillary network for red blood cell hydrodynamics.* Microfluid. Nanofluid., 2010. **9**: p. 585–591.
152. Pohl, H., *The motion and precipitation of suspensoids in divergent electric fields.* Appl. Phys., 1951. **22**: p. 869–871.
153. Davalos, R.V., G.J. McGraw, T.I. Wallow, A.M. Morales, K.L. Krafcik, Y. Fintschenko, E.B. Cummings, and B.A. Simmons, *Performance impact of dynamic surface coatings on polymeric insulator-based dielectrophoretic particle separators.* Anal. Bioanal. Chem., 2008. **390**: p. 847–855.
154. G. J. McGraw, R. V. Davalos, J. D. Brazzle, J. Hachman, M. C. Hunter, J. Chames, G. J. Fiechtner, E. B. Cummings, Y. Fintschenko, and B.A. Simmons. *Polymeric microfluidic devices for the monitoring and separation of water-borne pathogens utilizing insulative dielectrophoresis*. in *Proc SPIE*. 2005. San Jose, CA.
155. Davalos, R.V., G.J. McGraw, T.I. Wallow, A.M. Morales, K.L. Krafcik, Y. Fintschenko, E.B. Cummings, and B.A. Simmons, *Performance impact of dynamic surface coatings on polymeric insulator-based dielectrophoretic particl sensors.* Anal. Bioanal. Chem., 2007. **389**: p. 1426–1435.
156. Zellner, P., H. Shafiee, M. Sano, R. Davalos, and M. Agah, *An Insulator-based Dielectrophoresis Silicon Microchip for Particle Trapping*, in *Microtechnologies in Medicine and Biology*2009: QC, Canada.
157. W. A. Braff, A. Pignier, and C.R. Buie, *High sensitivity three-dimensional insulator-based dielectrophoresis.* Lab Chip, 2012. **12**(7): p. 1327–1331.
158. Ozuna-Chacon, S., B.H. Lapizco-Encinas, M. Rito-Palomares, S.O. Martinez-Chapa, and C. Reyes-Betanzo, *Performance characterization of an insulator-based dielectrophoretic microdevice.* Electrophoresis, 2008. **29**: p. 3115–3122.
159. Martinez-Lopez, J.I., H. Moncada-Hernandez, J.L. Baylon-Cardiel, S.O. Martinez-Chapa, M. Rito-Palomares, and B.H. Lapizco-Encinas, *Characterization of electrokinetic mobility of microparticles in order to improve dielectrophoretic concentration.* Anal. Bioanal. Chem., 2009. **394**: p. 293–302.
160. Chen, D. and H. Du, *A microfluidic device for rapid concentration of particles in continuous flow by DC dielectrophoresis.* Microfluid. Nanofluid., 2010. **9**: p. 281–291.
161. Gallo-Villanueva, R.C., V.H. Perez-Gonzalez, R.V. Davalos, and B.H. Lapizco-Encinas, *Separation of mixtures of particles in a multipart microdevice employing insulator-based dielectrophoresis.* Electrophoresis, 2011. **32**: p. 2456–2465.
162. Srivastava, S.K., A. Gencoglu, and A.R. Minerick, *DC insulator dielectrophoretic applications in microdevice technology: a review.* Analytical and Bioanalytical Chemistry, 2011. **399**(1): p. 301-321.
163. Rosenthal, A. and J. Voldman, *Dielectrophoretic traps for single-particle patterning.* Biophysical Journal, 2005. **88**(3): p. 2193-2205.
164. Zhu, J. and X. Xuan, *Dielectrophoretic focusing of particles in a microchannel constriction using DC-biased AC flectric fields.* Electrophoresis, 2009. **30**(15): p. 2668-2675.
165. Lewpiriyawong, N., C. Yang, and Y.C. Lam, *Dielectrophoretic manipulation of particles in a modified microfluidic H filter with multi-insulating blocks.* Biomicrofluidics, 2008. **2**(3): p. 11.
166. Lewpiriyawong, N., C. Yang, and Y.C. Lam, *Electrokinetically driven concentration of particles and cells by dielectrophoresis with DC-offset AC electric field.* Microfluidics and Nanofluidics, 2012. **12**(5): p. 723-733.
167. Zellner, P., *An Insulator-based Dielectrophoresis Silicon Microchip for Cell Trapping*, in *MMB*2009: Canada.
168. Zellner, P. and M. Agah, *Silicon insulator-based dielectrophoresis devices for minimized heating effects.* Electrophoresis, 2012. **33**(16): p. 2498-2507.
169. Hosseini, Y., P. Zellner, and M. Agah, *A Single-Mask Process for 3D Microstructure Fabrication in Glass and Elastomers*, in *MEMS 2012*2012: Paris France.

170. Sanchis, A., A. Brown, M. Sancho, G. Martinez, J. Sebastian, S. Munoz, and J. Miranda, *Dielectric characterization of bacterial cells using dielectrophoresis.* Bioelectromagnetics, 2007. **28**(5): p. 393-401.
171. Zhou, R., P. Wang, and H.-C. Chang, *Bacteria capture, concentration and detection by alternating current dielectrophoresis and self-assembly of dispersed single-wall carbon nanotubes.* Electrophoresis, 2006. **27**(7): p. 1376-1385.
172. Park, K., H.J. Suk, D. Akin, and R. Bashir, *Dielectrophoresis-based cell manipulation using electrodes on a reusable printed circuit board.* Lab Chip, 2009. **9**(15): p. 2224-2229.
173. Cho, Y.K., S. Kim, K. Lee, C. Park, J.G. Lee, and C. Ko, *Bacteria concentration using a membrane type insulator-based dielectrophoresis in a plastic chip.* Electrophoresis, 2009. **30**(18): p. 3153-3159.
174. Staton, S.J.R., K.P. Chen, T.J. Taylor, J.R. Pacheco, and M.A. Hayes, *Characterization of particle capture in a sawtooth patterned insulating electrokinetic microfluidic device.* Electrophoresis, 2010. **31**(22): p. 3634-3641.
175. Hosseini, Y., P. Zellner, and M. Agah, *A Single-Mask Process for 3-D Microstructure Fabrication in PDMS.* Journal of Microelectromechanical Systems, 2012. **22**(2): p. 356-361.
176. Suehiro, J., G. Zhou, M. Imamura, and M. Hara, *Dielectrophoretic filter for separation and recovery of biological cells in water.* Industry Applications, IEEE Transactions on, 2003. **39**(5): p. 1514-1521.
177. Demierre, N., T. Braschler, P. Linderholm, U. Seger, H. van Lintel, and P. Renaud, *Characterization and optimization of liquid electrodes for lateral dielectrophoresis.* Lab on a Chip, 2007. **7**(3): p. 355-365.
178. Zhu, J. and X. Xuan, *Curvature-induced dielectrophoresis for continuous separation of particles by charge in spiral microchannels.* Biomicrofluidics, 2011. **5**(2): p. 024111.
179. Sano, M.B., J.L. Caldwell, and R.V. Davalos, *Modeling and development of a low frequency contactless dielectrophoresis (cDEP) platform to sort cancer cells from dilute whole blood samples.* Biosensors and Bioelectronics, 2011. **30**(1): p. 13-20.
180. Pohl, H.A., *The motion and precipitation of suspensoids in divergent electric fields.* Journal of Applied Physics, 1951. **22**(7): p. 869-871.
181. Zellner, P., T. Shake, A. Sahari, B. Behkam, M. Riquelme, A. Pruden, and M. Agah, *Off-chip Pasivated electrode Insulator-based Dielectrophoresis (OπDEP).* Analytical and Bioanalytical Chemistry, 2013 (In Press).
182. Zellner, P., A. Sahari, T. Shake, B. Behkam, and M. Agah. *Off-chip Electrode Insulator Based Dielectrophoresis*. in *IEEE Sensors 2012*. 2012. Taipei, Taiwan.